2009

DEVELOPMENT AND INVESTIGATION OF INTENSITY-MODULATED RADIATION THERAPY TREATMENT PLANNING FOR FOUR-DIMENSIONAL ANATOMY

yelin suh
Virginia Commonwealth University

Humanities and Sciences
Virginia Commonwealth University

This is to certify that the dissertation prepared by Yelin Suh entitled "DEVELOPMENT AND INVESTIGATION OF INTENSITY-MODULATED RADIATION THERAPY TREATMENT PLANNING FOR FOUR-DIMENSIONAL ANATOMY" has been approved by his or her committee as satisfactory completion of the thesis or dissertation requirement for the degree of Doctor of Philosophy.

Dr. Paul J. Keall, Department of Radiation Oncology, Stanford University

Dr. Jeffrey V. Siebers, Department of Radiation Oncology

Dr. Elisabeth Weiss, Department of Radiation Oncology

Dr. Nesrin Dogan, Department of Radiation Oncology

Dr. Sonja Dieterich, Department of Radiation Oncology, Stanford University

Dr. Alison Baski, Chair of the Physics Department

Dr. Fred M. Hawkridge, Dean of the College of Humanities and Sciences

Dr. F. Douglas Boudinot, Dean of the School of Graduate Studies

May 6, 2009

For my family for all the love and support,

especially for Dad and Mom

“DEVELOPMENT AND INVESTIGATION OF

INTENSITY-MODULATED RADIATION THERAPY TREATMENT PLANNING

FOR FOUR-DIMENSIONAL ANATOMY”

A Dissertation submitted in partial fulfillment of the requirements for the degree of Doctor of Philosophy at Virginia Commonwealth University.

by

YELIN SUH
Master of Science, Ewha Womans University, Korea, 2005

Director: Paul J. Keall
Associate Professor, Department of Radiation Oncology, Stanford University

Virginia Commonwealth University
Richmond, Virginia
May 2009

Table of Contents

Page

List of Tables

Page

List of Figures

Page

List of Abbreviations

For clarity, the abbreviations used throughout the text are provided here.

AAPM	American Association of Physicists in Medicine
1D, 2D, 3D, 4D	One-, two-, three-, four-dimensional
AP	Anterior-posterior
BEV	Beam's eye view
COV	Composite objective value
CT	Computed tomography
CTV	Clinical target volume
DMLC	Dynamic MLC
DVH	Dose-volume histogram
GTV	Gross tumor volume
IMRT	Intensity-modulated radiation therapy
IRB	Institutional review board
LR	Left-right
MLC	Multileaf collimator
MU	Monitor units
OAR	Organ at risk
PCA	Principal components analysis
PRV	Planning organ at risk volume
PTV	Planning target volume
RMS	Root-mean-square
SD	Standard deviation
SI	Superior-inferior
SNOPT	Sparse Nonlinear Optimizer

Abstract

DEVELOPMENT AND INVESTIGATION OF

INTENSITY-MODULATED RADIATION THERAPY TREATMENT PLANNING

FOR FOUR-DIMENSIONAL ANATOMY

By Yelin Suh, Ph.D.

A Dissertation submitted in partial fulfillment of the requirements for the degree of Doctor of Philosophy at Virginia Commonwealth University.

Virginia Commonwealth University, 2009

Major Director: Paul J. Keall
Associate Professor, Department of Radiation Oncology, Stanford University

Lung cancer is the leading cause of cancer-related deaths worldwide. Radiotherapy is one of the main treatment modalities of lung cancer. However, the achievable accuracy of radiotherapy treatment is limited for lung-based tumors due to respiratory motion. Four-dimensional radiotherapy explicitly accounts for anatomic motion by characterizing the motion, creating a treatment plan that accounts for this motion, and delivering this plan to the moving anatomy. This thesis focuses on the current problems and solutions throughout the course of four-dimensional radiotherapy. For characterization of respiratory-induced motion, patient tumor motion data were analyzed. It is shown that tumor motion can be

significant during radiotherapy treatment, and its extent, direction, and linearity vary considerably between patients, between treatment fractions, and between respiratory cycles. After this, approaches to four-dimensional intensity-modulated radiation therapy treatment planning were developed and investigated. Among the techniques to manage respiratory motion, tumor tracking using a dynamic multileaf collimator delivery technique was chosen as a promising method. A formalism to solve a general four-dimensional intensity-modulated radiation therapy treatment-planning problem was developed. Specific solutions to this problem accounting for tumor motion initially in one dimension and extending this to three dimensions were developed and investigated using four-dimensional computed tomography planning scans of lung cancer patients. For four-dimensional radiotherapy treatment delivery, accuracy of two-dimensional projection imaging methods was investigated. Geometric uncertainty due to the limitation of two-dimensional imaging in monitoring three-dimensional tumor motion during treatment delivery was quantified. This geometric uncertainty can be used to estimate proper margins when a single two-dimensional projection imager is used for four-dimensional treatment delivery. Lastly, tumor-tracking delivery using a moving average algorithm was investigated as an alternative delivery technique that reduces mechanical motion constraints of a multileaf collimator. Moving average tracking provides an approximate solution that can be immediately implemented for delivery of four-dimensional intensity-modulated radiation therapy treatment. The clinical implementation of four-dimensional guidance, intensity-modulated radiation therapy treatment planning, and dynamic multileaf collimator tracking delivery may have a positive impact on the treatment of lung cancer.

PREFACE

This preface gives an outline of this thesis.

Chapter 1 is an introduction to this thesis and explains the terms in its title, four-dimensional intensity-modulated radiation therapy treatment planning. The literature related to the subjects of the thesis is briefly reviewed; and the rationale is presented. Four-dimensional radiotherapy consists of three tasks: characterization of respiratory-induced motion, creation of a treatment plan, and delivery of the treatment. Chapter 2 is assigned to the first task, quantifying and characterizing respiratory tumor motion; Chapters 3-5 are to the second task, four-dimensional intensity-modulated radiation therapy treatment planning; and Chapters 6 and 7 are to the third task, monitoring anatomic motion during treatment delivery and delivering four-dimensional radiotherapy treatment, respectively.

Chapter 2 shows an analysis of respiratory-induced motion using thoracic and abdominal tumor motion data. This has been published in *Physics in Medicine and Biology* (Appendix A).

Chapter 3 demonstrates the background and significance of four-dimensional intensity-modulated radiation therapy treatment planning using dynamic multileaf collimator tracking and its framework. The literature is reviewed and a formalism to solve a general four-dimensional intensity-modulated radiation therapy treatment-planning problem is presented.

Chapters 4 and 5 show two specific solutions to four-dimensional intensity-modulated radiation therapy treatment planning by extending three-dimensional treatment planning to four-dimensional treatment planning with deliverable constraints. Chapter 4 is a four-dimensional intensity-modulated radiation therapy treatment-planning method to account for one-dimensional tumor motion. This has been published in *Int. J. Radiation Oncology, Biology, Physics* (Appendix B). Chapter 5 is a four-dimensional intensity-modulated radiation therapy treatment-planning method to account for three-dimensional motion. This has been accepted for publication in *Physics in Medicine and Biology* (Appendix C).

Chapter 6 is dedicated to quantification of the geometric uncertainty of two-dimensional projection imaging in monitoring three-dimensional tumor motion. This has been published in *Physics in Medicine and Biology* (Appendix D). Chapter 7 shows an alternative technique of tumor-tracking delivery using a moving average algorithm. This has been published in *Medical Physics* (Appendix E).

Chapter 8 describes ongoing and future work as extension of the work performed in this thesis.

CHAPTER 1 INTRODUCTION

This chapter provides an introduction to this thesis. Several topics are discussed to explain the overall rationale for carrying out the research for the thesis.

A brief description of radiotherapy and four-dimensional (4D) radiotherapy is given; and the subject is narrowed down to the main topics, 4D radiotherapy treatment planning, dynamic multileaf collimator (DMLC) tracking, and intensity-modulated radiation therapy (IMRT). Respiratory-induced motion relevant to radiotherapy and techniques to manage this motion during radiotherapy are reviewed; and lung cancer is briefly discussed as the main clinical application of this research. Then, utilizing respiratory tumor motion as a degree of freedom is shown. Finally, the rationale *to develop and investigate 4D IMRT treatment planning using DMLC tracking* is presented.

1.1. Four-dimensional radiotherapy

Radiotherapy is an important modality in the treatment of cancer. About 50% of all cancer patients are treated with the treatments that include radiotherapy [http://www.cancer.gov].

The goal of radiotherapy is to apply radiation to eradicate a tumor, while sparing normal tissues. This goal is not always achievable due to different types of uncertainties

introduced throughout the course of external beam radiotherapy. These are likely from (1) patient setup, (2) anatomic motion and deformation, and (3) target volume definition due to imaging quality, uncertainty about tumor extent, and/or inter-observer delineation variation. Among these sources of uncertainties originating from the tumor-identifying to the beam-irradiating stage, patient anatomic motion [1, 2] is the primary focus of this thesis. Non-rigid anatomy and physiological motion, such as motion from breathing, heart-beating, or the digestive system, of a patient are possible sources of anatomic motion. The motion complicates tumor localization for external beam radiotherapy; and thus "time" has been introduced as the fourth dimension in radiotherapy and 4D radiotherapy is to explicitly include anatomic motion during imaging, treatment planning, and treatment delivery of radiotherapy [3, 4]. Effective motion management is especially important for the radiotherapy treatment of thoracic and abdominal regions, wherein respiratory-induced motion is shown to contribute most to patient anatomic motion during radiotherapy and to be a significant factor causing geometric uncertainties during imaging, treatment planning, and treatment delivery of radiotherapy [4, 5].

1.2. Four-dimensional radiotherapy treatment planning

Four-dimensional radiotherapy that incorporates anatomic motion consists of three tasks: (1) characterizing the motion, (2) creating a treatment plan that accounts for this motion, and (3) delivering this treatment plan to the moving anatomy. The first task has been greatly facilitated through the increased use of 4D computed tomography (CT) [6, 7]. Four-dimensional CT provides more accurate anatomic motion information than the

conventional CT, and suggests that the motion information can be used to improve accuracy of radiotherapy treatment. However, how to utilize this extra information in an optimal way to create a treatment plan that accounts for anatomic motion remains challenging. The third task has been investigated and/or clinically implemented using different types of motion management techniques (discussed in Section 1.5). For a linear accelerator equipped with a multileaf collimator (MLC), DMLC delivery is shown to be a promising method to deliver 4D radiotherapy treatment [8-22]. However, how to include mechanical constraints of delivery devices in a treatment plan that accounts for anatomic motion also continues to be a challenge.

1.3. Dynamic multileaf collimator tracking

An introduction of a computer-controlled MLC consisting of multiple narrow leaves that can move independently in and out of a radiation beam path allows conformal shaping of the beam to match the border of a tumor. A DMLC delivery technique which dynamically moves MLC leaves during treatment delivery allows the radiation beam to follow a moving tumor by continuously changing both positions and shapes of treatment beam apertures. Tumor tracking using DMLC delivery has been investigated and experimentally demonstrated for rigid or deforming, mobile tumors [8-22]. It is suggested that real-time DMLC tumor tracking has potential to improve radiotherapy treatment by reducing geometric uncertainties of a tumor due to anatomic motion and thus increasing dosimetric accuracy.

1.4. Intensity-modulated radiation therapy

Three-dimensional (3D) conformal radiation therapy focuses on increasing a local tumor control rate and thus a survival rate, by achieving spatial localization of a high-dose irradiation volume [23]. This treatment technique often does not produce a satisfactory treatment plan when a tumor has a complex volume shape or critical structures are in close proximity. Intensity-modulated radiation therapy aims to keep a radiation dose to surrounding normal tissues low by modulating beam intensity within each beam delivery. The improved sparing of normal tissues allows increasing a radiation dose delivered to a tumor. It has been shown that using an IMRT treatment technique increases a tumor control rate and lowers local toxicity and complications associated with high-dose radiation [24-28]. The capability of delivering the highly conformal dose to the tumor with a tighter margin while sparing normal tissues also indicates that IMRT can be more susceptible to anatomic motion.

Delivery of an IMRT treatment has been facilitated by the use of MLCs. Multiple fixed gantry angle IMRT uses a number of fixed beam directions; and at each beam direction, a desired beam intensity pattern is achieved by (1) alternating segments between MLC leaf motion and dose delivery (a step-and-shoot technique) or (2) moving MLC leaves during dose delivery (a sliding-window technique). Modulation of beam intensity may also be achieved by using one or more gantry arcs with continuously varying MLC leaf positions, dose rate, and gantry rotation speed (intensity-modulated arc therapy or volumetric modulated arc therapy) [29].

1.5. Respiratory-induced motion in radiotherapy

Extent of respiratory-induced motion

Many studies show that respiratory motion for thoracic and abdominal tumors can be as large as 2-3 cm, and shows intra- and inter-fractional variations [1, 4, 30, 31]. The American Association of Physicists in Medicine (AAPM) Task Group 76 [4] summarizes lung tumor motion data and finds that the greatest lung tumor motion is generally in the superior-inferior (SI) direction, whereas the least motion is in the left-right (LR) direction. Lung tumor motion tends to increase from the upper lobes to the lower lobes of the lungs. The maximum motion extent documented is 5 cm [32]. Ekberg *et al.* [33] showed relatively small motion in which the mean extent was 0.4 cm at most, while Erridge *et al.* [34] reported relatively large motion with the mean extent being 1.3 cm in the SI direction. The extent and the degree of wide variations in motion are acknowledged in the literature; however, no consensus is apparent regarding respiratory motion management. The AAPM Task Group 76 [4] recommends that respiratory motion management techniques should be considered when the tumor motion range in any direction is greater than 0.5 cm.

Techniques to manage respiratory-induced motion

Several techniques have been developed to manage respiratory tumor motion, such as motion-encompassing, abdominal compression, breath-hold, respiratory-gating, and tumor-tracking techniques [4].

Creating a treatment volume that encompasses the motion of a tumor is the simplest idea to manage respiratory tumor motion [35, 36]. This *motion-encompassing* technique is

agreeable with the aim of radiotherapy in an initial stage, eradicating the tumor. However, with the complications due to excessive irradiation to critical structures, the importance of normal tissue sparing started to be acknowledged. The advent of 4D CT provides accurate information of tumor positions within a respiratory cycle, which helps design more optimal margins [6, 7] compared with conventional margin expansion.

Another simple approach is an *abdominal compression* technique. Pressing down patient's abdomen restricts the amount of abdominal motion and thus reduces respiratory tumor motion. An abdomen-pressing plate with an arc and scaled screw is a commercial abdominal compression device included in Stereotactic Body Frame® (Elekta, Stockholm, Sweden) [37]. For patient immobilization, it is equipped with a rigid-body frame and a vacuum pillow in a body shell, and laser markers attached to the frame. An air-injected blanket also is developed as an abdomen-pressing device [38]. By inflating the urethane pillow that is spread over patient's abdomen, even pressure is applied to the abdominal area to reduce the motion. Abdominal compression techniques are relatively simple and easy to implement, and the device is inexpensive. Patient discomfort can be an issue, and reproducibility of pressure and positions of a device are in question.

Breath-hold techniques minimize respiratory tumor motion by controlling patient's breathing actively or passively. Active breathing control [39, 40] and deep inspiration breath hold [41] make use of filling the lungs with deep inspiration breath holding. This has two benefits. First, deep inspiration increases a lung volume, thus reduces a normal tissue volume in a treatment volume and reproducibly moves a tumor volume away from critical structures. Second, breath holding effectively immobilizes a tumor, thus margins can be

reduced significantly while maintaining a constant lung volume. These techniques require compliance and active participation of patients; and breath holding might not be well tolerated or performed by patients with compromised lung functions, which often happens to lung cancer patients [41, 42]. Also, breath-hold techniques require additional treatment time (17-33 min reported) compared with free-breathing approaches. *Active breathing control* temporarily closes inspiration and expiration paths of an airflow using a ventilator, while a patient breathes only through a mouth with a nose clip on. As a portable system, it can be compatible with any kind of treatment machines and treatment modalities. A commercial system, Active Breathing Coordinator™ (Elekta, Stockholm, Sweden), aids a patient to maintain a consistent and reproducible breath-hold volume by controlling a balloon valve that allows a specified volume of air to be inhaled or exhaled and by showing a patient the respiratory trace on a screen. *Deep inspiration breath hold* involves coaching a patient to reproduce a deep inspiration level. Initially a patient is brought to quiet breathing only through a mouth to a spirometer with a nose clip on, while looking at a screen displaying a volume of air breathed in and out. Then verbal coaching to maneuver deep inspiration breath hold is given to a patient to follow a slow deep inspiration, a slow deep expiration, a second slow deep inspiration, and a breath hold. One more type of a breath-hold technique is *held-breath self gating*, a voluntary breath-hold technique [43]. A patient activates a hand-held buzzer when the patient feels that a breath hold is maintainable; then a therapist activates the treatment beam. Patients perform the functions of a sensor, a detector, and a beam controller, so that this technique requires safety features.

Both a therapist and a patient can inactivate the treatment beam, but only a therapist can activate the beam directly with the patient cooperation.

The last two techniques, respiratory gating and tumor tracking, are relatively new and have been shown to be promising with the advent of image-guided radiation therapy [4]. Given that success of these techniques depends on how accurately a tumor is localized, quantification and characterization of tumor motion is important.

Respiratory-gating techniques synchronize beam exposure with the pre-determined portion of a patient's respiratory cycle [5, 44-47]. To perform this technique, the displacement and the phase of tumor motion within a respiratory cycle needs to be determined; and an external surrogate or internal fiducial markers are used to monitor respiratory tumor motion. Two types of respiratory-gating techniques are available: (1) displacement gating activates the beam only when the displacement of respiratory signals is between the two pre-set displacement limits and (2) phase gating activates the beam only when the phase of respiratory signals is between the two pre-set phase limits. That is, imaging or delivery devices are triggered according to the displacement or the phase of a patient's respiratory trace monitored. This technique does not cause patient discomfort as patients do not need to hold their breaths; but "gating" increases treatment time considerably as the beam repeatedly turns on and off, and it requires accurate information on the internal tumor position as the beam is on within the pre-set gating window only.

Finally, a technique to synchronously follow a tumor with the radiation beam has been suggested as an optimal solution to manage respiratory tumor motion, compared with all other techniques discussed above [48-50]. By continuously tracking a moving tumor, the

tumor can remain static in a beam's eye view (BEV). Consequently, there is potential to yield a more accurate treatment within less time as the beam is always on and follows the tumor with a smaller margin than when the aforementioned techniques are used. This technique is first implemented in a robotic radiosurgery system using a robotic arm to move the entire linear accelerator to track the tumor [50-56]. Tumor tracking can also be performed by repositioning the radiation beam using an MLC [8-22] or a treatment couch [57]. The requirements for a tumor-tracking technique include accurate and fast detection of tumor positions during treatment delivery (to follow the tumor in real time) and/or good reproducibility of a patient's respiratory pattern (to overcome the mechanical time delay to reposition the beam) [12]. This is obvious because the information on internal tumor positions is crucial to track the moving tumor. Then again, it reveals that if accurate tumor positions are not provided, tumor tracking may result in a worse outcome than when no motion management techniques are used. In this regard, there have been studies to train or force a patient to achieve regular and reproducible breathing [22, 58-61]. This helps reduce the problems of free breathing for tumor tracking, such as residual motion and baseline shifts. Regular and reproducible breathing also is helpful for a respiratory-gating technique providing accurate information on internal tumor motion.

1.6. Lung cancer

Cancer occurs when cells in a part of the body begin to grow out of control, and lung cancer is a cancer that starts in the lungs. Lung cancer is the leading cause of cancer deaths in the United States and worldwide for both men and women, even though prostate cancer for men and breast cancer for women are most diagnosed [62]. According to American Cancer Society Cancer Facts and Figures 2008, it was estimated that there were 215 020 new lung cancer cases (114 690 in men and 100 330 in women) and 161 840 deaths from lung cancer (90 810 men and 71 030 women) in 2008. The average chance in a lifetime that a person will develop lung cancer is about 1/13 for a man and 1/16 for a woman. The five-year survival rate, an estimate of the cancer prognosis, is only 15% for all stages of lung cancer, compared with more than 60% for all cancer sites.

The most common treatment options of lung cancer include: (1) surgery to remove the tumor; (2) chemotherapy to use anti-cancer drugs injected onto a vein or taken by mouth; and (3) radiotherapy to kill or shrink cancerous cells with ionizing radiation. More than one kind of treatment modality may be used.

1.7. Utilizing respiratory-induced motion as a degree of freedom

The objective of this thesis is to utilize anatomic motion to benefit radiotherapy treatment instead of seeing the motion as an obstacle to radiotherapy.

Figure 1-1 shows a tumor with normal anatomy at two different respiratory phases in two different beam angles. The first column is from a beam angle where the tumor projection overlaps spinal cord, while the second column is where the tumor projection

overlaps esophagus. While targeting a moving tumor with the radiation beam, a dose from a given beam angle can be spread over different parts of normal anatomy; thus, without compromising the tumor dose, the maximum dose to normal tissues is lower than when the other treatment approaches, such as motion-encompassing or respiratory-gating techniques, are used. The treatments using these two techniques would give approximately same amount of a radiation dose to normal tissues as the tumor from the particular beam angle, and therefore do not have flexibility to spare normal anatomy within a single beam delivery. This is particularly beneficial for serial structures such as spinal cord or esophagus.

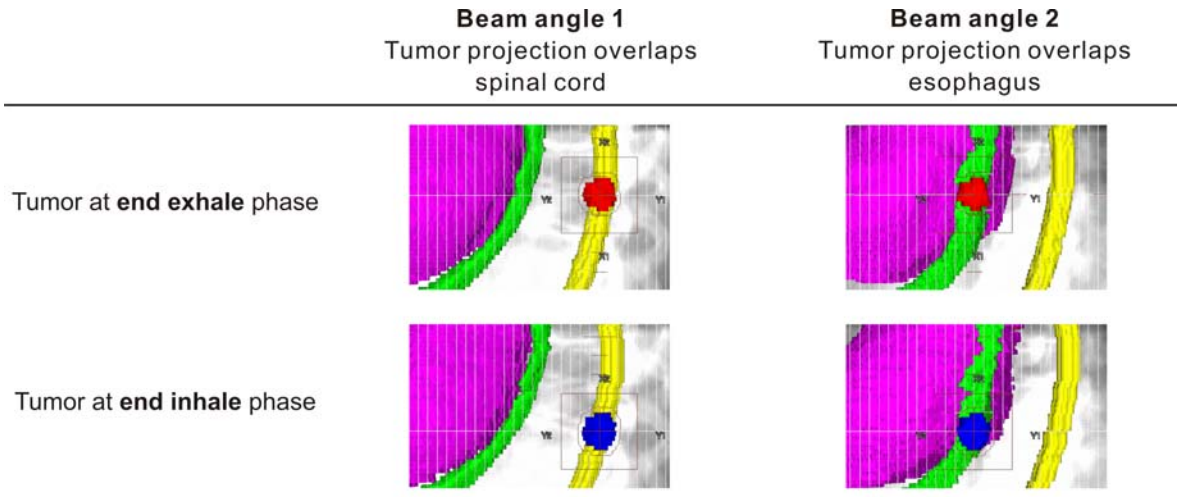

Figure 1-1. A tumor (red at end exhale phase and blue at end inhale phase) with normal anatomy (spinal cord in yellow, esophagus in green, and heart in pink) at two different respiratory phases in two different beam angles: the tumor projection overlaps spinal cord in beam angle 1 and the tumor projection overlaps esophagus in beam angle 2.

To demonstrate a principle of utilizing anatomic motion as a degree of freedom to improve radiotherapy treatment, a highly constrained IMRT treatment plan was designed, in that three beam angles were chosen with beam angle arrangement of the first beam passing through spinal cord to the tumor, the second through esophagus to the tumor, and the third through the tumor only. For a single lung cancer patient 4D CT planning scan (tumor motion of 2.1 cm and tumor volume of 3 cm^3), treatment planning was performed using three different treatment approaches: (1) a respiratory-gating technique at end exhale (exhale gating) or at end inhale (inhale gating) with the target on end exhale phase or on end inhale phase CT image, respectively (Figure 1-1); (2) a motion-encompassing technique with the target encompassing the gross tumor volumes (GTVs) for all phases of the 4D CT planning scan (Figure 1-2); and (3) a 4D approach, where 50% of the treatment is performed on end exhale phase and the rest 50% on end inhale phase (Figure 1-2). The IMRT treatment plan using the 4D approach was created by accumulating the resultant doses from the IMRT treatment plans on end exhale phase and on end inhale phase onto the reference phase CT image using deformable dose summation [63-68].

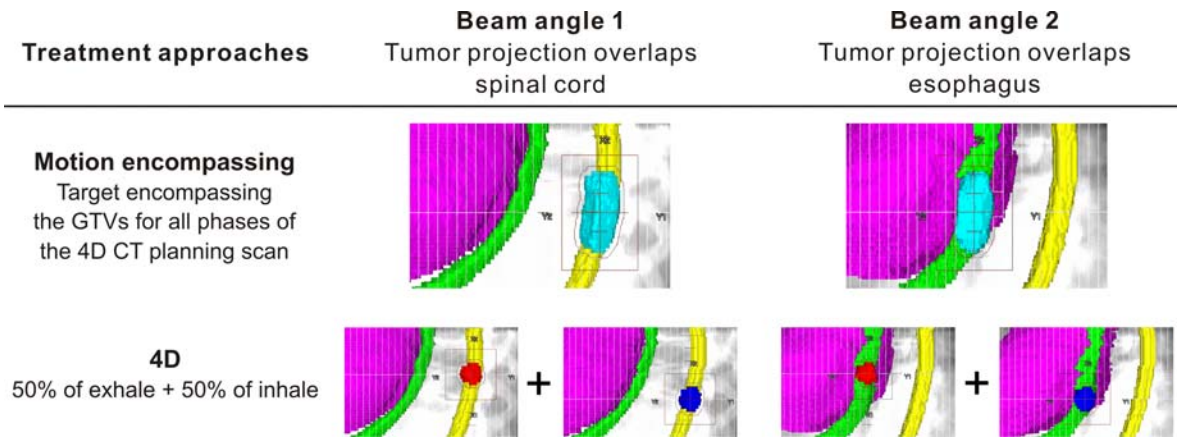

Figure 1-2. Treatment approaches shown at two different respiratory phases in two different beam angles. For a motion-encompassing technique, a target is defined to cover the GTVs for all phases of the 4D CT planning scan (shown in sky-blue with normal anatomy of spinal cord in yellow, esophagus in green, and heart in pink). A 4D approach is defined as 50% of the treatment to be delivered on end exhale phase and the rest on end inhale phase.

The mean and maximum doses to serial structures are significantly decreased in the IMRT treatment plan using the 4D approach compared with the plans using other methods, as shown in dose-volume histograms (DVHs) in Figure 1-3. Dose received by 5% of the volume, $D_{5\%}$, is reduced by 38%, 40%, and 36% for spinal cord and by 29%, 33%, and 35% for esophagus, compared with the plans using exhale-gating, inhale-gating, and motion-encompassing techniques, respectively. This improvement is likely highest for small, mobile tumors as those found in lung stereotactic body radiotherapy (as in this example case), so that it is not a general conclusion; rather it shows a single data point illustrating potential of including anatomic changes in time as an additional degree of freedom to improve radiotherapy treatment by maximizing tumor dose and minimizing normal tissue doses [16, 69].

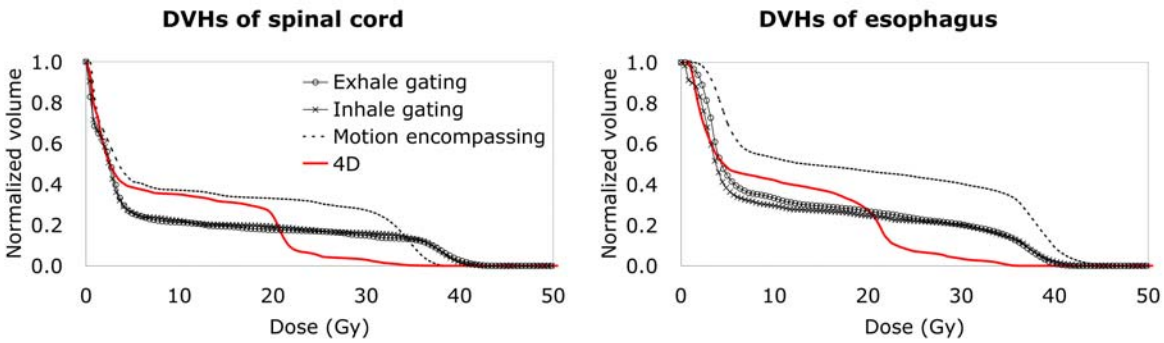

Figure 1-3. DVHs of serial structures, spinal cord and esophagus, for the IMRT treatment plans using different treatment approaches, showing significant decrease of the maximum dose when utilizing anatomic motion as a degree of freedom.

The results reveal that anatomic motion does not have to hinder radiotherapy treatment, but it can be seen as an opportunity to improve the treatment. That is, considering anatomic changes in time as an additional degree of freedom and including the motion as a function of time in radiotherapy treatment planning has potential to improve the treatment plans.

1.8. Rationale

Lung cancer is clinically significant but the overall prognosis is poor (Section 1.6). Although it is reported that increasing a radiation dose helps achieve a better local control rate and an improved survival rate for lung cancer patients [70-72], it is also shown that administering a higher radiation dose results in an increased risk of lung toxicity and complications [73-76]. An IMRT treatment technique is a good candidate for the treatment of lung cancer, because of its highly conformal tumor coverage allowing more sparing of surrounding normal tissues (Section 1.4) [77, 78]. However, lungs are one of the sites affected most by respiratory-induced motion, which compromises the quality of an IMRT treatment by causing geometric and dosimetric uncertainties (Sections 1.1 and 1.5).

Although the recent advances in imaging and treatment delivery techniques show potential to manage anatomic motion in radiotherapy, how to utilize these to improve treatment planning has yet to be fully resolved (Section 1.2).

Tumor motion management has been actively studied for the last decade. Especially, the first four techniques in Section 1.5 have been intensively investigated and/or implemented. Despite technical difficulties to be overcome and quality assurance issues to be solved, there has been much attention to tumor tracking using a DMLC delivery technique as a promising method (Sections 1.3 and 1.5).

This thesis presents the issues and the solutions in 4D radiotherapy mainly focusing on methods of 4D IMRT treatment planning using DMLC tracking for 4D CT image sets of lung cancer patients.

CHAPTER 2 QUANTIFICATION OF THE EXTENT OF RESPIRATORY-INDUCED MOTION

2.1. Introduction

Four-dimensional radiotherapy starts at quantification and characterization of respiratory-induced motion. It is important to quantify the extent of anatomic motion, as it is one of potential sources of geometric uncertainties during imaging, treatment planning, and treatment delivery of radiotherapy. Anatomic motion information is necessary for both designing a treatment plan that accounts for the motion and delivering the treatment to the moving anatomy. This chapter presents how substantial and how regular (or irregular) respiratory tumor motion is for a large patient population over an extended time period.

The aim of this study was to analyze more than 70 hours of thoracic and abdominal tumor motion for stereotactic body radiotherapy patients. The details of this chapter have been published in *Physics in Medicine and Biology*, which is included as Appendix A [31].

2.2. Methods and materials

Tumor motion data from 143 treatment fractions for 42 thoracic and abdominal cancer patients treated with Cyberknife Synchrony (G3 System with delivery software version 6.2.3, Accuray Incorporated, Sunnyvale, CA) in Georgetown University Hospital from July 2005 to January 2006 were used in this study. The use of the data for research purposes was approved by the Georgetown Institutional Review Board (IRB, 2005-309). In order to compensate for tumor motion, Synchrony, the tracking system, estimates internal tumor positions by a correlation between external patient motion and internal fiducial locations, as well as by a prediction algorithm. That is, the patient tumor motion data used in this study were derived from the external/internal correlation model and recorded at 25 Hz by the tracking system.

It is important to note that the tumor motion analyzed is not actual but estimated from the correlation model of the tracking system that is based on periodic stereoscopic x-ray images. The uncertainty of the tracking system motion data was assessed by estimation errors of the correlation model, which the Synchrony system recorded every time two orthogonal x-ray images were acquired and internal fiducial locations were measured. The vector error for each internal fiducial was quantified: the mean and the standard deviation (SD) of 3D positional estimation root-mean-square (RMS) errors of the tracking system over 143 treatment fractions is 1.5 ± 0.8 mm. The estimation errors could be due to inaccuracy of the correlation model, or temporal variations in the correlation model between measurements [55, 79, 80].

Creation of a database of patient tumor motion

The tracking system motion data included portions that might be from sources other than tumor motion, so that these data were processed to extract the estimated tumor motion from the tracking system motion data; and subsequently, for each of 143 treatment fractions, the *longest single contiguous data set* was created by excluding (1) data points showing no motion, (2) significantly large motion at the beginning of the tracking system motion data, (3) large time intervals (more than 5 s) where no data were recorded, and (4) data points showing the large motion change in one direction only out of three directions.

Separation of individual respiratory cycles

To break the respiratory tumor motion data into individual cycles, the system noise was first removed by filtering the tracking system motion data using the first-order Butterworth low-pass filter with a cut-off frequency of 2.5 Hz. Then, the respiratory-induced peak-to-trough distance and period were determined by (1) generating smoothed data (with a moving average over 1 s) and a moving average baseline (with a moving average over 8 s) from the filtered tracking system motion data, (2) searching intersections between the two curves, (3) determining peaks and troughs between the intersections, and (4) calculating peak-to-trough distance and period (Figure 2-1).

Analysis of respiratory motion data

Once separated into individual respiratory cycles, the tumor motion data were analyzed to obtain useful information on respiratory tumor motion: (1) respiratory-induced peak-to-

trough distance, (2) respiratory period, (3) per cent contributions to 3D motion from motion in the LR, anterior-posterior (AP), and SI directions, and (4) motion nonlinearity and hysteresis.

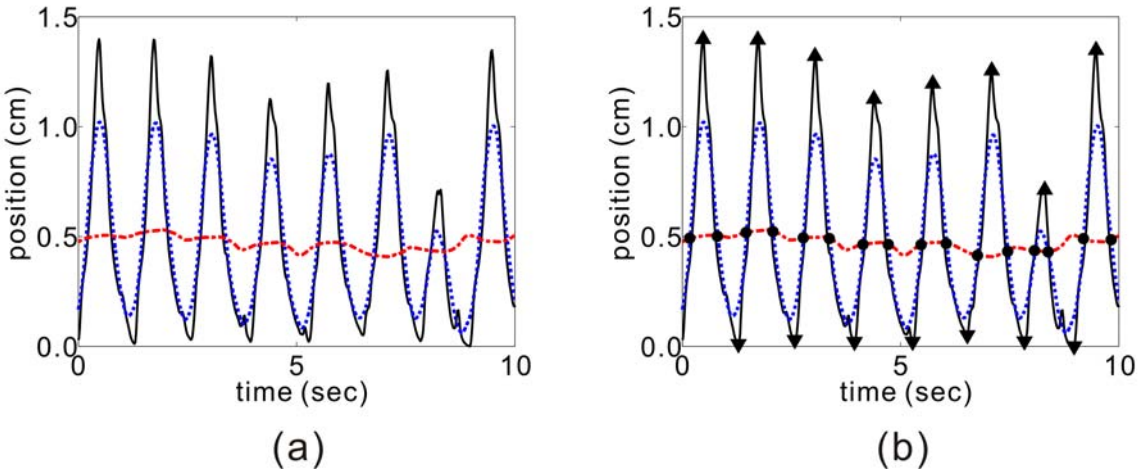

Figure 2-1. Separation of individual respiratory cycles: (a) the black solid curve represents the filtered tracking system motion data, the blue dashed curve represents the smoothed data (moving average over 1 s), and the red dot-dashed curve represents a moving average baseline (moving average over 8 s); (b) the circles mark intersections between the blue dashed and red dot-dashed curves, and the triangles and inverted triangles represent peak and trough points, which are the maximum and minimum points between adjacent intersections, respectively.

2.3. Results and discussion

Creation of a database of patient tumor motion

The mean duration time of the extracted motion data is 30 min (5-86 min), and the total duration time is approximately 72 hours. The mean ratio of duration time in the tracking system motion data and that in the extracted motion data is 0.42 (0.07-0.99).

Separation of individual respiratory cycles

Due to substantial temporal changes in respiratory tumor motion, developing a robust algorithm to separate individual respiratory cycles is challenging. The moving average curves, which can remove the effect of possible signal drifts and noises, were used for the algorithm to separate individual respiratory cycles. For all treatment fractions, 70 218 individual respiratory cycles were examined after separating individual cycles and used to further characterize respiratory tumor motion.

Analysis of respiratory motion data

Figure 2-2 summarizes the information on the respiratory-induced tumor motion data analyzed. The overall mean respiratory-induced peak-to-trough distance is 0.48 cm, with individual treatment fraction means ranging from 0.02 to 1.44 cm. The overall mean respiratory period is 3.8 s, with individual treatment fraction means ranging from 2.2 to 6.4 s. The mean of individual treatment fraction SDs for the peak-to-trough distance and period is 0.15 cm (0.01-0.73 cm) and 0.8 s (0.2-1.7 s), respectively [Figures 2-2(a) and (b)].

One of the conditions where respiratory management techniques should be considered in regard to the recommendations made by the AAPM Task Group 76 [4] is when the tumor motion range in any direction is greater than 0.5 cm. Fifty-seven treatment fractions (40%) show the mean peak-to-trough distance to be greater than 0.5 cm: 44 (42% of all lung tumor fractions) from 16 lung patients and 13 (34% of all retroperitoneal tumor fractions) from 7 retroperitoneal patients.

Twenty-six treatment fractions (18%) show the dominant RL motion, 32 (22%) show the dominant AP motion, and 85 (60%) show the dominant SI motion. Individual treatment fraction means for per cent contributions to 3D motion from the LR, AP, and SI motion range 3-73%, 8-84%, and 5-77%, respectively [Figure 2-2(c)].

Motion nonlinearity and hysteresis are important characteristics of respiratory tumor motion, but no consensus on how to quantify their extent has been reached. In this study, principal components analysis (PCA) is applied to quantify the motion nonlinearity and hysteresis. The first principal component that PCA generates is expressed as a normalized percentage (ranging from 33 to 100%), where 100% indicates pure linear motion, and the lower the percentage, the more nonlinear motion and/or more hysteresis. Given that for many of the treatment fractions the mean of the first principal component is greater than 90%, the motion nonlinearity and hysteresis usually are not significant; however, they are not negligible, either [Figure 2-2(d)].

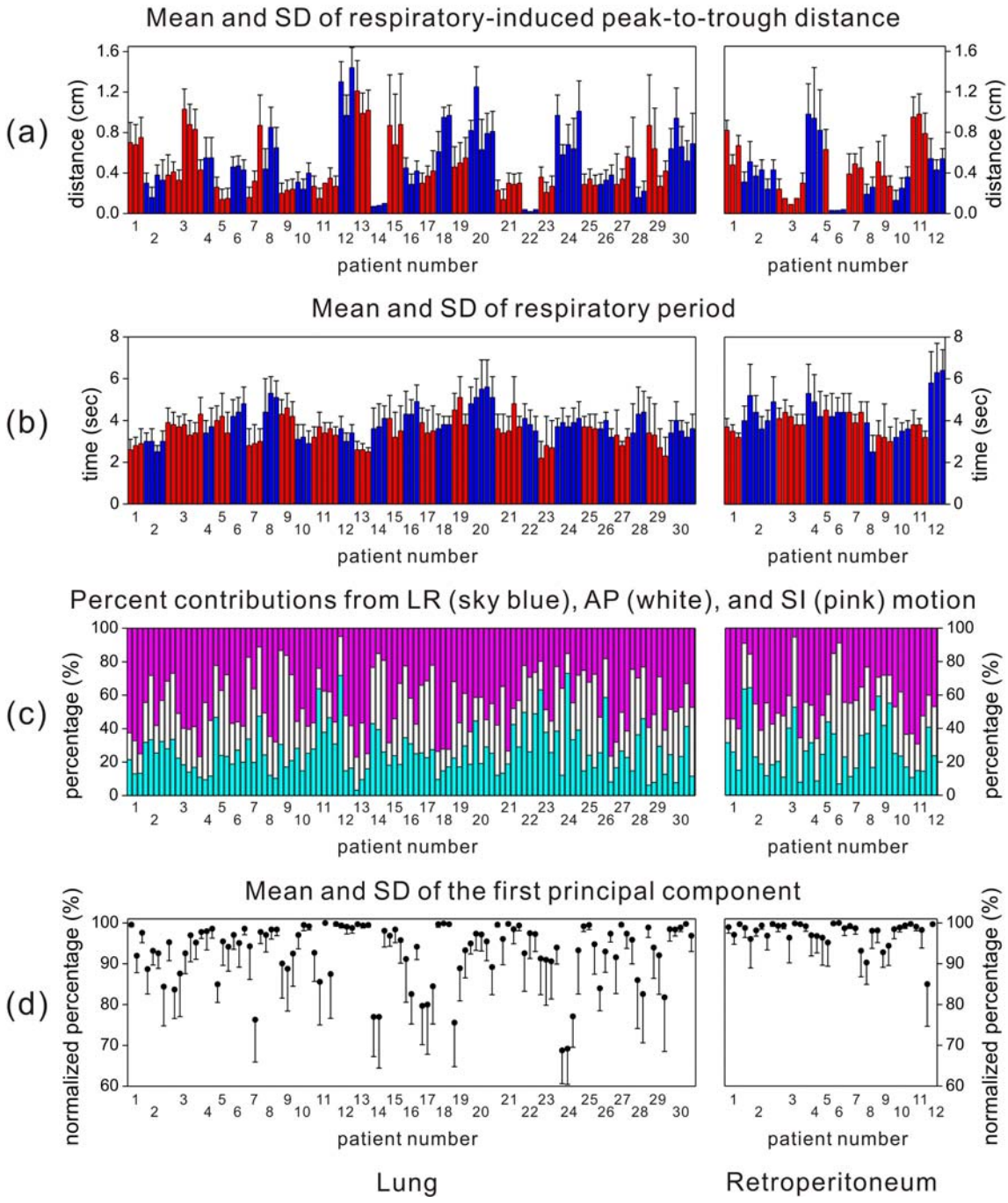

Figure 2-2. Summary of the information on the respiratory-induced tumor motion analyzed: for each of 30 lung patients (left) and 12 retroperitoneal patients (right), (a) mean and SD of the respiratory-induced peak-to-trough distance, (b) mean and SD of the respiratory period, (c) mean of the per cent contributions to 3D motion from the motion in the LR (sky blue), AP (white), and SI (pink) directions, and (d) mean and SD of the first principal component (normalized percentage) showing motion nonlinearity and hysteresis.

2.4. Conclusions

This study shows that (1) respiratory-induced tumor motion can be a significant factor of accuracy for the radiotherapy treatment of thoracic and abdominal tumors and (2) for the extent, direction, and linearity of the motion, large variations are observed from patient to patient, from fraction to fraction, and from cycle to cycle.

Due to normal tissue dose tolerances, accommodating the variable tumor position merely by adding large margins around the tumor limits the therapeutic dose that can be delivered. A potential solution for this is to both plan and deliver the 4D radiotherapy treatment for the tumors that move with respiration.

CHAPTER 3 FOUR-DIMENSIONAL INTENSITY-MODULATED RADIATION THERAPY TREATMENT PLANNING, A GENERAL SOLUTION

3.1. Introduction

Intensity-modulated radiation therapy is shown to have better normal tissue sparing and target coverage compared with 3D conformal radiation therapy treatment techniques [25-27]. For IMRT treatment delivery, a DMLC technique is being used as it is reliable and efficient [81-83]. However, IMRT is known to be more susceptible to the motion of tumor and normal structures because the motion limits knowledge of both the position of the anatomy and the dose received by the anatomy [26]. This is especially the case with an IMRT treatment delivered using a DMLC technique [25, 27]. In addition, DMLC IMRT delivered to moving anatomy results in variations in the delivered dose distribution from the planned due to the interplay between anatomic motion and MLC leaf motion [84-91]. Dosimetric impact from the interplay may be insignificant for IMRT with multiple treatment fractions, but it increases with motion extent [84, 87, 89, 91].

A DMLC technique has been investigated for delivery of a 4D IMRT treatment, and several techniques to incorporate positional changes of anatomy into an IMRT

treatment delivered using a DMLC technique have been proposed (discussed later in this section). However, the finite mechanical motion capabilities of an MLC impose constraints on leaf sequencing for a 4D IMRT treatment because during treatment delivery MLC leaves need to both follow tumor motion (4D) and modulate beam intensity (IMRT). Besides, a constraint on 4D IMRT treatment planning, which is not found in 3D IMRT cases, is that leaf sequences need to be specifically designed such that the maximum leaf dynamics (velocity and acceleration/deceleration) are not exceeded when tracking anatomic motion using an MLC. This mechanical leaf motion constraint adds additional complexity in IMRT treatment planning on 4D CT image sets. Therefore, how to create DMLC leaf sequences to generate an IMRT treatment plan in the presence of moving anatomy has not been developed yet.

A 4D IMRT treatment-planning optimization and its delivery using a DMLC technique has been investigated in the literature.

Trofimov *et al*. compared different 4D IMRT optimization schemes with respect to a full optimization and sorted them by increasing complexity of delivery: (1) using an internal target volume on the basis of a 4D CT scan, (2) using the convolution of a pencil beam kernel that describes dose deposition from individual beamlets with a probability density function that describes tumor motion, to compensate for respiratory motion, (3) respiratory gating, and (4) tumor tracking [92]. They showed that tumor tracking was better than the other techniques; and provided a good framework of formulating 4D IMRT treatment-planning optimization problems. They did not investigate a robustness of the optimization methods with respect to the delivery methods, thus their study did not create

leaf sequences nor include mechanical limitations of a treatment machine, such as MLC leaf motion constraints.

Webb *et al*. developed motion-compensated DMLC techniques to deliver an IMRT treatment. They initially proposed practical methods to account for one-dimensional (1D) rigid-body translation in the MLC leaf travel direction [93] and two-dimensional (2D) rigid-body translation [11], which was based on a modification of the DMLC IMRT technique whereby MLC leaves were arranged to change according to the patient respiratory pattern. It is shown that applying these techniques to tumor-tracking delivery benefits improvement of tumor dose conformality and reduction of PTV margins. They then implemented strategies to find leaf trajectories that minimized geometric mismatch between MLC leaf and non-rigid anatomic locations in one dimension [94] and in two dimensions [8], including the maximum leaf velocity constraint. Their strategy was not a full 4D optimization as it matched geometric mismatch, not dosimetric mismatch, and they did not yet demonstrate implementation with a cohort of patients.

Papiez *et al*. developed algorithms for optimized DMLC IMRT delivery for mobile, deforming targets. They demonstrated DMLC leaf sequencing for target motion in real time and when *a priori* motion information was available in one dimension, but as of yet not for three dimensions [10, 14-18, 20]. Recently, they applied a real-time DMLC leaf-pair optimal control algorithm for IMRT treatment delivery to targets moving two-dimensionally in a BEV, using a leaf-pair shifting technique [9, 19]. Their optimization algorithms were designed to deliver the given radiation beam intensity, to minimize the beam-on time, and not to exceed the maximum MLC leaf velocity. Their investigations

focused on real-time delivery of an IMRT treatment, and thus they did not perform treatment planning for DMLC IMRT.

Zhang *et al.* incorporated respiratory tumor motion and deformation into a treatment-planning optimization for helical tomotherapy delivery [66]. For a beamlet-based optimization, beamlets can be calculated using 4D CT. For each beamlet, time-dependent dose calculation was performed. Then, a set of deformed beamlets was obtained by mapping the calculated dose back to the primary phase, and an optimization incorporating motion was performed. This method provided breathing-correlated delivery as the correlation between treatment delivery and a respiratory cycle was set in treatment planning; thus with the help of guided breathing, this optimization method on a moving tumor resulted in a highly conformal dose distribution. Their study was based on a binary MLC, and limited to a phantom and one lung case.

Schlaefer *et al.* showed an approach to consider the relative motion of organs to avoid overdoses during treatment planning for robotic radiosurgery [95]. On the basis of the periodic nature of respiratory motion, organ motion can be described as the organ position at each state in a respiratory cycle. That is, the relative motion of organs is handled by discretizing the motion in the temporal or spatial dimensions and computing dose coefficients for each discrete state separately. Then these dose coefficients are incorporated into the optimization of beam weights to take into account the motion of both the organs and the beams. This method resulted in improved conformality of the treatment without increasing the overall dose and the treatment time considerably, and has been

clinically released. Their study did not include MLC motion constraints as their system does not have an MLC, and it was restricted to a phantom case.

Alasti *et al*. suggested a 4D-weighted radiotherapy by using a weighting factor to account for tumor motion during treatment planning and delivery [96]. The 4D-weighted MLC treatment field was a weighted sum of the MLC position for the static field and the dynamic MLC position for the 4D dynamic field, which allowed MLC leaves to follow a moving tumor. The weighting factor was chosen depending on the reliability of patient respiration and the limitations of the delivery system. They provided a simple 4D radiotherapy treatment planning and delivery method that reduced PTV margins and the irradiated lung volume, and thus this method may benefit safe application of IMRT. Their 4D MLC leaf sequence was not created by optimal leaf sequencing, rather by a weighted sum of leaf positions for the static and dynamic field, thus it was not a full 4D optimization. Their study was phantom-based.

Tewatia *et al*. proposed procedures of treatment planning for a breathing-synchronized delivery technique and its delivery [97]. Motion was directly overlaid to the DMLC leaf position, and violations of the mechanical limitations of the hardware were avoided during treatment planning. Their results showed that the delivered dose distribution was similar to the planned by compensating respiratory tumor motion without requiring hardware modification, and thus breathing-synchronized delivery can be easily applied in clinic. As motion is incorporated into treatment planning after a plan optimization by superimposing target displacement on the leaf positions, their method was not a full 4D optimization. This study was also phantom-based.

To date, no other groups have reported techniques that develop leaf sequences as a function of respiratory phase; and thus a DMLC IMRT treatment-planning method for 4D CT image sets, which includes MLC leaf motion constraints and is robust to the variations of fractional time spent in respiratory phases within a 4D CT scan has yet to be developed.

3.2. Specific aim

The aim of this study was to develop and investigate 4D IMRT treatment planning with DMLC tracking including MLC leaf motion constraints, which takes respiratory-induced anatomic motion into account and is robust to the variations of fractional time spent in respiratory phases within a given 4D CT planning scan. Reducing phase-to-phase variation in dose distributions is an advantage during treatment delivery, because it would result in dose distributions close to the planned dose distributions even when a patient spends a different fraction of time in each respiratory phase from the planned (as in a 4D CT planning scan).

Variables not included (outside the scope of this thesis, but might affect the final clinical implementation) in the analysis are as follows.

- Day-to-day and cycle-to-cycle variation of patient respiratory motion was not included, as there was no further information about the patient respiratory motion beyond a single 4D CT planning scan. Thus, only the changes in respiratory motion within one respiratory cycle from a 4D CT image set for a given patient were included, whereas variables such as day-to-day and cycle-to-cycle changes in tumor positions with respect to skeletal anatomy or out-of-phase variation were not.
- Dose calculation was performed with a superposition-convolution algorithm using a commercial radiotherapy treatment-planning system, as it is the "most-accurate easily-available" method. Dose calculation using other methods like Monte Carlo was not included in the analysis. The aim was to develop and investigate 4D IMRT treatment-planning methods. Changing dose calculation algorithms, more specifically, using a Monte Carlo dose calculation may slightly change the resulted dose distributions, but it should not significantly affect relative plan rankings for the five 4D IMRT treatment-planning methods studied.
- Deformable registration between a 4D image set for dose summation was performed using a single algorithm and assumed to be accurate. Comparing different displacement vector fields, registration algorithms, or dose summation methods was beyond the scope of this study.
- Dose-mass histograms were not included in the analysis. Only DVHs were used for comparing and evaluating treatment plans.

3.3. Research design

Treatment scenario

Three-dimensional IMRT treatment planning is to create a treatment plan from one CT image, resulting in an MLC leaf sequence, L, as a function of monitor units (MU), i.e., $L(MU)$. Four-dimensional IMRT, wherein modulating the radiation beam to temporally changing anatomy is explicitly included, aims to create a treatment plan on a CT image set of multiple respiratory phases, resulting in an MLC leaf sequence as a function of MU and respiratory phase, θ, i.e., $L(MU, \theta)$. A 4D radiotherapy treatment scenario investigated is to obtain a 4D treatment plan from a 4D CT planning scan and to have delivery flexible enough to account for changes in tumor positions, tumor drifts, and/or respiratory patterns during treatment delivery.

It is important to note that like currently available 3D radiotherapy, some approximations are being made for 4D radiotherapy treatment planning and delivery. Four-dimensional radiotherapy treatment planning is based on a single 4D CT planning scan, which is usually taken long before actual delivery of treatment. Guckenberger *et al*. showed that respiratory motion assessed by a single 4D CT image set was reproducible during a time period corresponding to a high-dose stereotactic treatment, and concluded that for the majority of lung cancer patients studied, treatment planning on the basis of a 4D CT planning scan appeared to be reliable [98]. On the other hand, Minn *et al*. showed that a 4D CT planning scan cannot accurately predict pancreatic tumor motion during treatment delivery for radiosurgery [99]. That is, it is not always true that a single 4D CT image set represents the location and the motion of patient's anatomy during treatment

delivery; rather, the anatomic motion pattern would likely change between imaging and delivery. Nevertheless, the patient anatomic motion during the 4D CT planning scan is at this time the best possible estimation for what it will be during treatment delivery. Beyond one single 4D CT planning scan, no further information on the anatomic motion pattern is known as it is often the case in clinic, this estimation is necessary. If 4D cone-beam CT [100-102] or 4D magnetic resonance imaging [103, 104] is available, the most recent information on the patient anatomic location can be used. Even when the updated information is available, the assumption to correlate the anatomic location during imaging to that during delivery is still required. With a 4D radiotherapy treatment plan, 4D radiotherapy treatment delivery assumes that during delivery there exists real-time information on both the tumor location and the respiratory phase of tumor motion, which is from either measurement or estimation.

A general framework

Figure 3-1 shows various approaches to 4D radiotherapy treatment planning. The most general approach to determine radiotherapy treatment planning for 4D anatomy is to allow MLC leaves to vary as a function of dose delivered (i.e., *MU*) and time (i.e., respiratory phase), while also allowing for beam on/off at different respiratory phases. This is a gated 4D IMRT treatment-planning method. When posed in this manner, other approaches to 4D radiotherapy treatment planning become subsets of a solution space of the gated 4D IMRT as in Figure 3-1. Thus, a main challenge is to solve the gated 4D IMRT treatment-planning optimization problem. Once this problem is solved, limiting the degrees of

freedom (or adding additional constraints) and reducing the solution space further to solve for other methods described in Figure 3-1 can be straightforward.

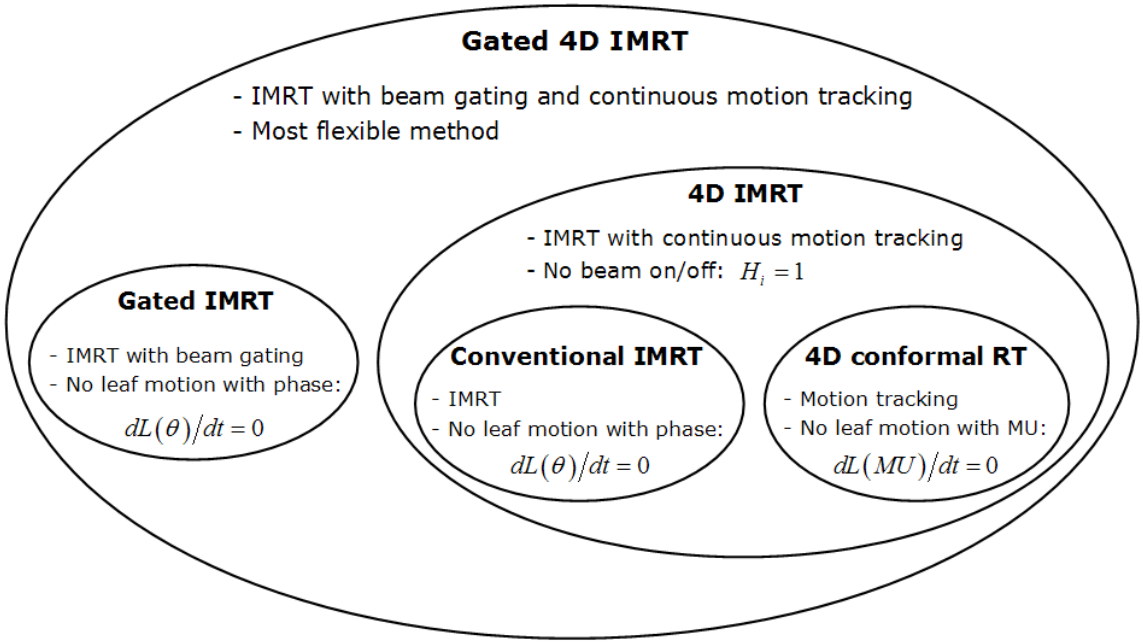

Figure 3-1. Solution space of 4D radiotherapy treatment planning and delivery methods: gated IMRT and conventional IMRT are currently available. RT = radiation therapy.

A general framework is to solve and investigate the contributions of the various degrees of freedom of a 4D radiotherapy treatment-planning optimization problem shown in Figure 3-1, including (1) MLC leaf motion as a function of respiratory phase (4D IMRT vs. conventional IMRT), (2) MLC leaf motion as a function of *MU* (4D IMRT vs. 4D conformal radiation therapy), and (3) beam on/off at different respiratory phases (4D IMRT vs. gated IMRT).

While a 3D optimization of IMRT treatment planning results in $L(MU)$, optimizing IMRT treatment planning for 4D anatomy adds an extra variable of respiratory phase, resulting in $L(MU,\theta)$. A mathematical description of a 4D IMRT treatment-planning optimization is then to find a deliverable leaf sequence as a function of MU and θ, $L(MU,\theta)$, and beam on/off status, H, to satisfy

$$\min\left\{ f\left[D\left(L(MU,\theta), H\right)\right]\right\}, \qquad (1)$$

where the 4D dose distribution to be delivered, D, is as follows:

$$D = \sum_{i=1}^{P} H_i \lambda_i D_i\left(I_i, I_{ref}, u(\theta_i), L(MU,\theta_i)\right), \qquad (2)$$

with the nomenclature used shown in Table 3-1. A dose of each respiratory phase, D_i, is computed on a given phase image, I_i, on the basis of $L(MU,\theta_i)$, and then deformed to the reference phase image, I_{ref}, by the displacement vector field, $u(\theta_i)$, using a tri-linear dose interpolation algorithm [64, 67, 68]. All individual phase doses computed are accumulated on I_{ref} using deformable dose summation [63-66], and a deformable dose-summed 4D dose is obtained.

Compared to a 3D IMRT treatment-planning optimization, additional complexities for a 4D IMRT treatment-planning optimization are as follows.

- The optimization is performed over a number of CT images.
- The MLC leaf motion is constrained by the maximum leaf velocity.

Table 3-1. Description and typical type, range, and size of the variables used in a general framework to solve 4D IMRT treatment-planning optimization problems.

	Description	**Typical type, range, and size**
f	*Mathematical cost function* representation of a clinical objective	An arbitrary form for evaluating the dose in segmented anatomy, typically on the basis of dose, dose-volume, or estimated outcome
i	*Respiratory phase index* from 1 to maximum phase number, P	Discrete index of typical size 10, i.e., $P = 10$
I	*4D CT image set*, where I_i represents the CT image for phase i and I_{ref} is the reference phase CT image, which is used for deformable dose summation	4D density distribution of typically 10^7 voxels at P time points
$u(\theta_i)$	*Displacement vector field* for phase i, which is computed using a deformable image registration mapping I_i to I_{ref}	3D vector field of typically 10^7 vectors
D_i	*Dose distribution of a treatment plan on* I_i	3D density distribution of typically 10^6 voxels
D	*Deformable-summed dose distribution, or 4D dose*	3D density distribution of typically 10^6 voxels
H_i	*Heavyside function* for phase i, which indicates beam on/off status for the given phase	Binary; $H_i = 0$ corresponds to beam-off and $H_i = 1$ to beam-on
λ_i	*Fractional time spent* per each phase, which is normalized such that $\sum_{i=1}^{P} H_i \lambda_i = 1$	Continuous variable of typical size 10, assumed to be the same for all respiratory phases
L	*Leaf sequence consisting of the position of each MLC leaf tip* for each beam planned, which can change with MU for each respiratory phase.	Continuous variable for each of the respiratory phases (typically, 10 phases), the beams (typically, 5-9 beams), the MU control points (typically, 5-200 control points), the MLC leaves (typically, 80-160 leaves)

Multileaf collimator leaf velocity constraints

Because MLC leaf acceleration, which has been measured to be about 50 cm s^{-2}, is assumed to be sufficient for a currently used DMLC leaf-sequencing algorithm [11, 105], only maximum leaf velocity, measured to be 3.3-3.9 cm s^{-1} [105], is used as a constraint for leaf sequencing. For the current leaf-sequencing algorithms where MLC leaf positions vary with MU, leaf velocity is constrained to the maximum leaf velocity, $v_{\max}$, i.e., $dL(MU)/dt \le v_{\max}$. For Equation (2), $dL(MU,\theta_i)/dt \le v_{\max}$ is an additional complexity for the phases where the beam is on, i.e., $H_i = 1$. It is important to note that this constraint is not just for motion along the MLC leaf travel direction, but also for motion perpendicular to the leaf travel direction; hence adjacent leaf ends should not be further apart than the maximum leaf velocity in a given phase transition. This constraint has been studied [8, 10] and is similar to synchronization to reduce the MLC tongue-and-groove effects [11, 20]. The addition of beam hold allows this constraint to be violated when a dosimetric penalty of the constraint is too high.

Given this complexity, the current practice to decouple dose calculation and leaf sequencing is undesirable because the planned dose distribution with the constraints may be quite different from those without constraints. Despite an additional computational burden, coupling dose calculation and leaf sequencing ensures that coupled plans are at least as good as decoupled plans. Also, so-called "optimized" plans prior to leaf sequencing, which cannot be delivered, are not used for plan evaluation.

`

For the phase i, leaf j, and control point k, leaf velocity constraint in terms of MU is as follows:

$$L_{i,j,k} - L_{i,j,k-1} < v_{\max} \cdot \Delta MU \cdot (t / MU), \qquad (3)$$

where ΔMU is MU difference between control points of $k-1$ and k. Leaf velocity constraint in terms of *phase* is divided into two constraints, which are constraints for parallel and perpendicular to the target motion:

$$\begin{array}{ll} \text{Parallel constraint:} & L_{i,j} - L_{i-1,j} < v_{\max} \cdot \lambda_i \\ \text{Perpendicular constraint:} & L_{i,j} - L_{i,j-1} < v_{\max} \cdot \lambda_i \end{array}. \qquad (4)$$

Note that violating these constraints occasionally is acceptable, although it results in lower efficiency (longer treatment time); however it is better not to violate the constraints often.

In this study, the maximum MLC leaf velocity is assumed to be 3.3 cm s^{-1}, which is a reasonable measurement-base estimate [105]. Given that the mean patient respiratory period is about 4 s (ranging 1 to 8 s) [31, 106], the time interval between the adjacent respiratory phases is assumed to be 0.4 s. Consequently, the maximum possible leaf motion range from one phase to the next is 1.32 cm.

Besides the maximum velocity of MLC leaves, the constraints from using an MLC are as follows.

- Two opposing leaves should not be overlapped.
- If two opposing leaves are open, any of the two should not move behind the jaws.

`

Deliverables

Main deliverables of this research are:

- to develop a formalism for a general 4D IMRT treatment-planning optimization, and
- to develop and investigate specific solutions for 4D IMRT treatment planning.

3.4. Methods and materials

Patient four-dimensional computed tomography data

The 4D CT image sets of 12 lung cancer patients acquired on a 16-slice CT scanner in a cine mode (GE Healthcare Technologies, Waukesha, WI) were used [107, 108]. The acquisition was performed as a part of an IRB-approved study (protocol 00-202) at the University of Texas M. D. Anderson Cancer Center. On the basis of the respiratory signals from a respiration monitoring system (Real-time Position Management™, Varian Medical Systems, Palo Alto, CA), a respiratory cycle of a patient was divided into 10 phases of equal duration. The respiratory phase indices of 0 and 5 represent the end inhale phase and the end exhale phase, respectively. The tumor classifications ranged from T1N0 to T4N0, and the tumors were located in the upper lobes for 9 patients and in the lower lobes for 3 patients with peripheral (3 patients) and central (9 patients) tumor localizations. The means of volume and centroid motion extent of the GTV were 49.2 cm^3 and 0.7 cm, respectively (Table 3-2).

`

Table 3-2. Volume and centroid motion extent of the GTV quantified from 4D CT planning scans for 12 patients.

Patient	GTV volume (cm^3)	GTV centroid motion (cm)
1	3.0	2.1
2	61.0	0.4
3	12.5	0.5
4	1.0	0.6
5	20.4	0.1
6	5.2	0.4
7	323.6	0.2
8	23.0	0.3
9	6.1	0.2
10	7.5	0.5
11	119.2	1.3
12	7.5	1.1
Mean (minimum, maximum)	49.2 (1.0, 323.6)	0.7 (0.1, 2.1)

Anatomy segmentation, treatment-planning preparation, and plan evaluation

Anatomy segmentation, treatment-planning preparation, and plan evaluation were performed using a commercially available treatment-planning system (Pinnacle 7.9 and 8.1; Philips Healthcare, Milpitas, CA). On the basis of the manually segmented contours on Phase 0, contours on the other phases of the 4D CT scan were automatically generated using the large deformation diffeomorphic image registration algorithm developed at the University of North Carolina [64, 67, 68]. The clinical target volume (CTV) enclosed the GTV with an isotropic 0.8-cm margin [109], and a 0.5-cm margin was added to create the planning

target volume (PTV). Further details, reviews, and analyses of the manual and automatically-generated contours are described elsewhere [108, 110, 111].

For the IMRT treatment plans of lung tumors, the prescribed dose was 74 Gy (2 Gy per fraction, 5 times per week) to cover at least 95% of the PTV, within a dose range of 90 to 120% of the prescribed dose. For the organs at risk (OARs), the plan objective was designed to limit the maximum or minimum dose or DVH with the corresponding weighting factor for each OAR or planning OAR volume (PRV; OAR with margins for setup and/or organ motion): (1) no more than 45 Gy to the spinal cord PRV; (2) no more than 20 Gy (V_{20}) to 30% of the normal lung volume (both lungs without the GTV); (3) no more than 55 Gy (V_{55}) to 30% of the esophagus PRV; (4) no more than 40 Gy (V_{40}) to 50% of the heart volume; and (5) no more than 80 Gy to the entire normal thorax (entire thorax without the PTV). The objectives for lung IMRT treatment plans used in this study are summarized in Table 3-3. Beam arrangements were six coplanar, non-opposed, predominantly anterior-posterior, with beam angles adjusted depending on the tumor locations. Objectives and details about IMRT treatment plans have been reviewed by one radiation oncologist and described elsewhere [107].

`

Table 3-3. Objectives for lung IMRT treatment plans and plan evaluation for the PTV and each OAR or PRV.

Regions of interest	Type	Dose (Gy)	Volume (%)	Weighting factor
PTV	Minimum DVH	74	95	100
	Maximum dose	74	-	10
	Minimum dose	74	-	10
	Minimum dose	66.6	-	40
	Maximum dose	88.8	-	40
Spinal cord PRV	Maximum dose	45	-	50
Normal lung	Maximum DVH	20	30	20
	Maximum DVH	20	15	1
Esophagus PRV	Maximum DVH	55	30	40
	Maximum DVH	40	30	1
Heart	Maximum DVH	40	50	20
	Maximum DVH	40	25	1
Entire normal thorax	Maximum dose	80	-	100

The same GTV motion in three dimensions has different 2D motion from the BEVs of different beam angles as shown in Figure 3-2. On the basis of the GTV centroid position for each respiratory phase quantified from a 4D CT planning scan, a major axis of tumor motion was automatically determined for each BEV using a least-squares fit. Then, for each beam, the collimator was rotated to align the MLC leaf travel direction parallel to the major axis. This was performed because of the known decrease in delivery efficiency for the motion perpendicular to the MLC leaf travel direction [21].

`

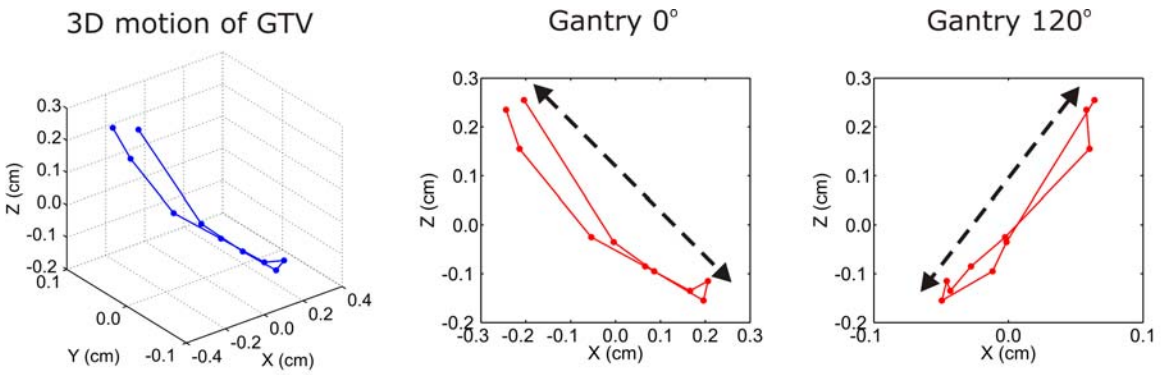

Figure 3-2. Collimator rotation: the same GTV motion in three dimensions has different 2D motion from the BEVs of different beam angles, such as gantry angles of 0^o and 120^o. On the basis of the GTV centroid positions in a given BEV, a major axis (dashed arrows) of tumor motion is determined for each beam: collimator angles are 41^o and 106^o for the gantry angle of 0^o and 120^o, respectively.

To calculate a 4D dose distribution, D, in Equation (2), a deformable dose-summed 4D plan was created by accumulating the resultant doses from all individual phase plans on the reference phase CT image (Phase 0) using deformable dose summation [64, 67, 68, 112-115].

Individual phase plans and deformable dose-summed 4D plans were evaluated and compared using composite objective values (COVs) and dose-volume evaluation metrics derived from DVHs. As being calculated on the basis of the plan objectives in Table 3-3, the COV, a single number, is an indicator of plan quality that takes into account the actually achieved dose distribution for the PTV and OARs/PRVs after the plan optimization, relative to the initial constraints [107]. The COV is the only single quantitative metric that is considered during the IMRT treatment-planning optimization. The smaller the COV, the better the treatment plan.

3.5. Specific solutions

An "ideal" 4D IMRT treatment-planning method would be one optimized over the continuous motion of target and surrounding normal structures, which may be deliverable; however, there are no solutions for this type of deliverable-based optimization yet. Before solving the general solution to 4D IMRT treatment planning, two specific solutions, which extend 3D IMRT treatment planning to 4D IMRT treatment planning with deliverable constraints, have been proposed. The reason for taking this approach is that it provides feasible solutions that use the current planning technology (performed using Pinnacle treatment-planning system), and therefore it has a clear path to clinical application. In the solution space in Figure 3-1, these solutions are the subsets of "4D IMRT." The specific solutions are to account for 1D motion along the major axis and 3D motion by applying a DMLC motion-tracking algorithm, respectively (Figure 3-3). The first solution is to show that accounting for 1D tumor translation is practical and also provides a reasonable approximation to compensating complex tumor motion and deformation (presented in Chapter 4); and the second solution is to show that accounting for more complex, 3D tumor motion yields better results and integrating deliverable treatment planning with DMLC tumor-tracking delivery has a clear path to clinical implementation (presented in Chapter 5). The patient 4D CT image sets described in this chapter were used for treatment planning in Chapters 4 and 5, with the same details on anatomy segmentation, treatment-planning preparation, and plan evaluation.

`

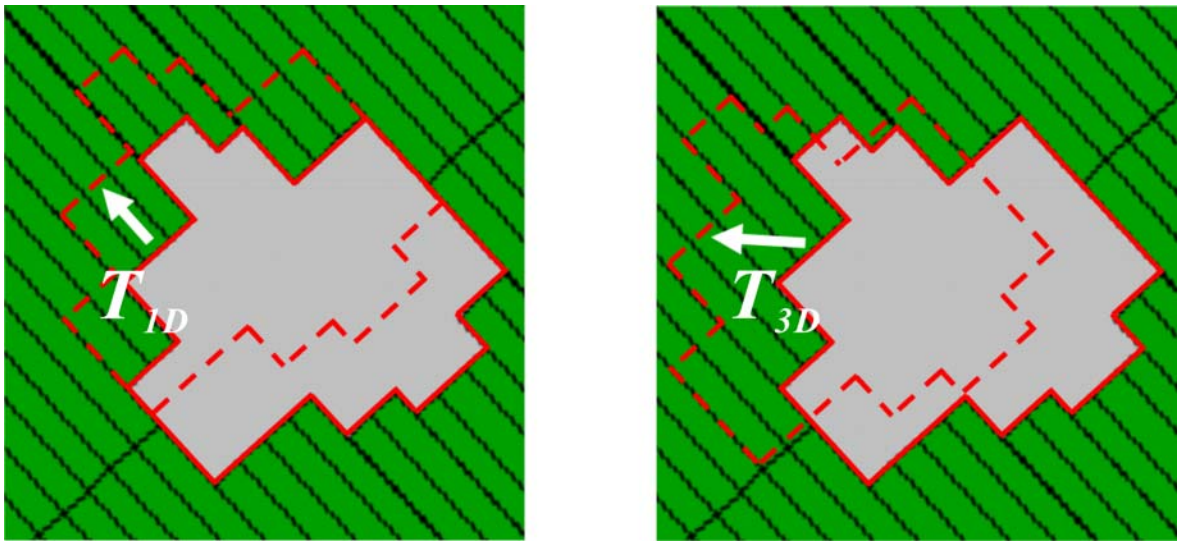

Figure 3-3. Comparison of two specific solutions to 4D IMRT treatment planning by extending 3D IMRT treatment planning with deliverable constraints: using 1D translation of MLC leaves from the reference phase (solid red) to a given phase (dashed red) (left) and using a DMLC motion-tracking algorithm to move MLC leaves to track 3D tumor motion (right). For the first solution, only the motion along the MLC leaf travel direction, T_{1D}, is accounted for (left), whereas for the second solution, 3D tumor motion, T_{3D}, is accounted for (right).

CHAPTER 4 FOUR-DIMENSIONAL INTENSITY-MODULATED RADIATION THERAPY TREATMENT PLANNING, A SPECIFIC SOLUTION I: *Extending 3D IMRT Treatment Planning to 4D IMRT Treatment Planning by Accounting for 1D Motion*

4.1. Introduction

As one of the specific solutions to 4D IMRT treatment planning that extend 3D IMRT treatment planning to 4D with deliverable constraints, this chapter presents a method to account for 1D motion. The method incorporates MLC leaf motion constraints into 4D IMRT treatment planning by accounting for 1D translation of rigid-body tumor motion along the major axis of a tumor trajectory. After rotating the collimator (as discussed in Figure 3-2), only tumor motion along the MLC leaf travel direction is considered, whereas tumor motion in the other directions from tumor deformation or rotation and nonlinear motion or hysteresis is ignored. This simplification is reasonable because respiratory tumor motion is predominantly linear as shown in Chapter 2.

The aim of this study was to develop a deliverable 4D IMRT treatment-planning method for DMLC tumor-tracking delivery. The details of this chapter have been

published in *Int. J. Radiation Oncology, Biology, Physics*, which is included as Appendix B [116].

4.2. Methods and materials

A framework to solve

A deliverable 4D IMRT treatment-planning method to solve Equation (2) is to account for rigid-body tumor motion along the MLC leaf travel direction only, as well as to ensure that MLC leaf motion does not exceed the maximum leaf velocity [105]. The deliverable method first finds a deliverable leaf sequence on the reference phase CT image, $L(MU,\theta_{ref})$, to satisfy Equation (1) with $H=1$ for all the respiratory phases (beam is always on): $\min\left\{ f\left[D\left(L(MU,\theta_{ref})\right)\right]\right\}$, where $D = D_{ref}\left(I_{ref}, L(MU,\theta_{ref})\right)$. For rigid-body tumor translation, the solutions for other respiratory phases then become $L(MU,\theta_i) = L(MU,\theta_{ref}) + g(\theta_i)$, where $g(\theta_i)$ is tumor centroid displacement from the reference phase to phase i along the major axis of tumor motion in a given BEV.

A benchmark method is a 3D optimal treatment-planning scheme, which finds an optimal leaf sequence for each respiratory phase independently, i.e., to find $L(MU,\theta_i)$ to satisfy $\min\left\{ f\left[D_i\left(L(MU,\theta_i)\right)\right]\right\}$. The 3D optimal approach accounts for tumor deformation or rotation and nonlinear motion or hysteresis but ignores MLC leaf motion constraints; and thus it is deliverable only if the MLC leaf velocity is infinite. It is important to note that the sum of individually optimized dose distributions does not

guarantee an optimal dose distribution (i.e., an optimal 4D treatment plan) because $\min\left\{ f\left[D\left(L(MU,\theta) \right) \right] \right\}$ is a subset of $\sum_{i=1}^{P} \min\left\{ f\left[D_i\left(L(MU,\theta_i) \right) \right] \right\}$.

Four-dimensional intensity-modulated radiation therapy treatment planning

Figure 4-1 shows the deliverable and 3D optimal method of 4D IMRT treatment planning. For 12 patient 4D CT image sets described in Chapter 4, the two methods were applied.

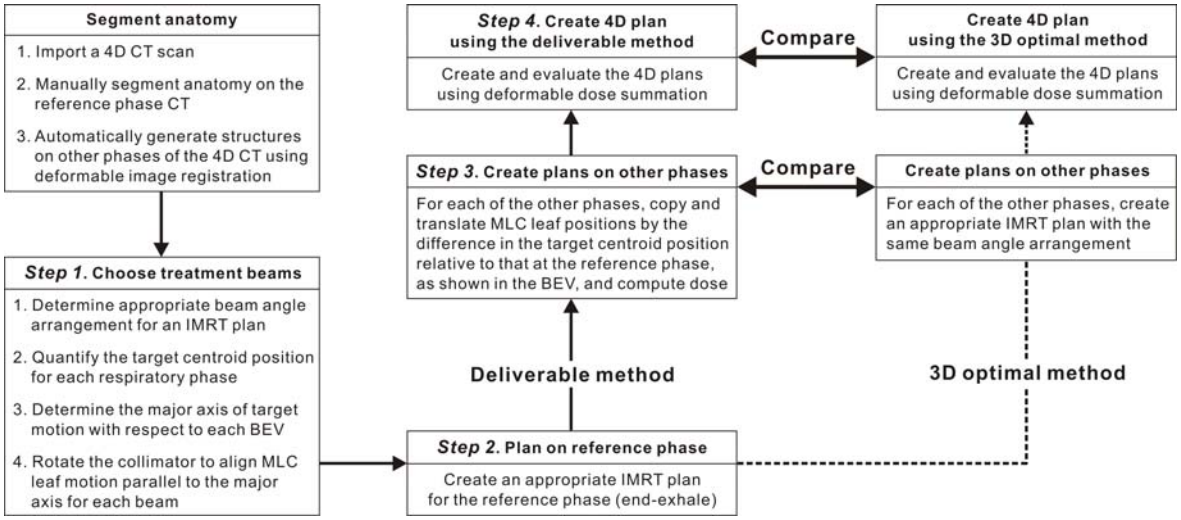

Figure 4-1. Methods of deliverable and 3D optimal IMRT treatment planning on the 4D CT image sets.

For individual phase plans, the mean and SD of dose-volume metric ratios were averaged over all 10 phases for all 12 patients:

$$\overline{\overline{X_{opt}^{del}}} = \frac{\sum_{i}^{M}\sum_{j}^{N} X_{del}^{i,j} / X_{opt}^{i,j}}{M \cdot N} \text{ and } \sigma_{\overline{\overline{X_{opt}^{del}}}} = \sqrt{\frac{\sum_{i}^{M}\sum_{j}^{N}\left(X_{del}^{i,j} / X_{opt}^{i,j} - \overline{\overline{X_{opt}^{del}}}\right)^2}{M \cdot N}},$$

where X is a dose-volume metric computed from the DVHs of plans using the deliverable (X_{del}) or 3D optimal (X_{opt}) methods, i is a patient number, and j is a phase number. For deformable dose-summed 4D plans, the mean and SD of dose-volume metric ratios were averaged over all 12 patients:

$$\overline{X_{opt}^{del}} = \frac{\sum_{i}^{M} X_{del}^{i} / X_{opt}^{i}}{M} \text{ and } \sigma_{\overline{X_{opt}^{del}}} = \sqrt{\frac{\sum_{i}^{M}\left(X_{del}^{i} / X_{opt}^{i} - \overline{X_{opt}^{del}}\right)^2}{M}}.$$

A one-tailed Student's *t*-test with the null hypothesis of $H_0 : X_{opt} = X_{del}$ and the alternative hypothesis of $H_A : X_{opt} > X_{del}$ was used to evaluate whether the two methods were statistically different (statistically different if $p < 0.05$).

`

4.3. Results and discussion

Figure 4-2 and Figures 4-3 and 4-4 show the COVs and the DVHs, respectively, of all 10 individual phase plans and deformable dose-summed 4D plans using the deliverable and 3D optimal methods. The two Phase 5 plans using each method are identical. For the other phase plans and deformable dose-summed 4D plans, the 3D optimal method always yields better plans. Variation in plan quality is generally larger for phase-to-phase compared with that for method-to-method. The deformable dose-summed 4D plan is similar to an average over individual phase plans.

The outliers are Patients 1, 4, and 11. Patients 1 and 4 show significant discrepancy in quality of individual phase plans using the deliverable method due to the artifacts in the 4D CT image set and the largest tumor volume variation during the respiratory cycle, respectively. Patient 1 also shows degraded 4D plans for both methods due to large gradients of the displacement vector field across the PTV. Patient 11 shows the most method-to-method and phase-to-phase discrepancy in the DVHs, which is due to the tumor with the most hysteresis, the second most motion, and the second biggest volume.

`

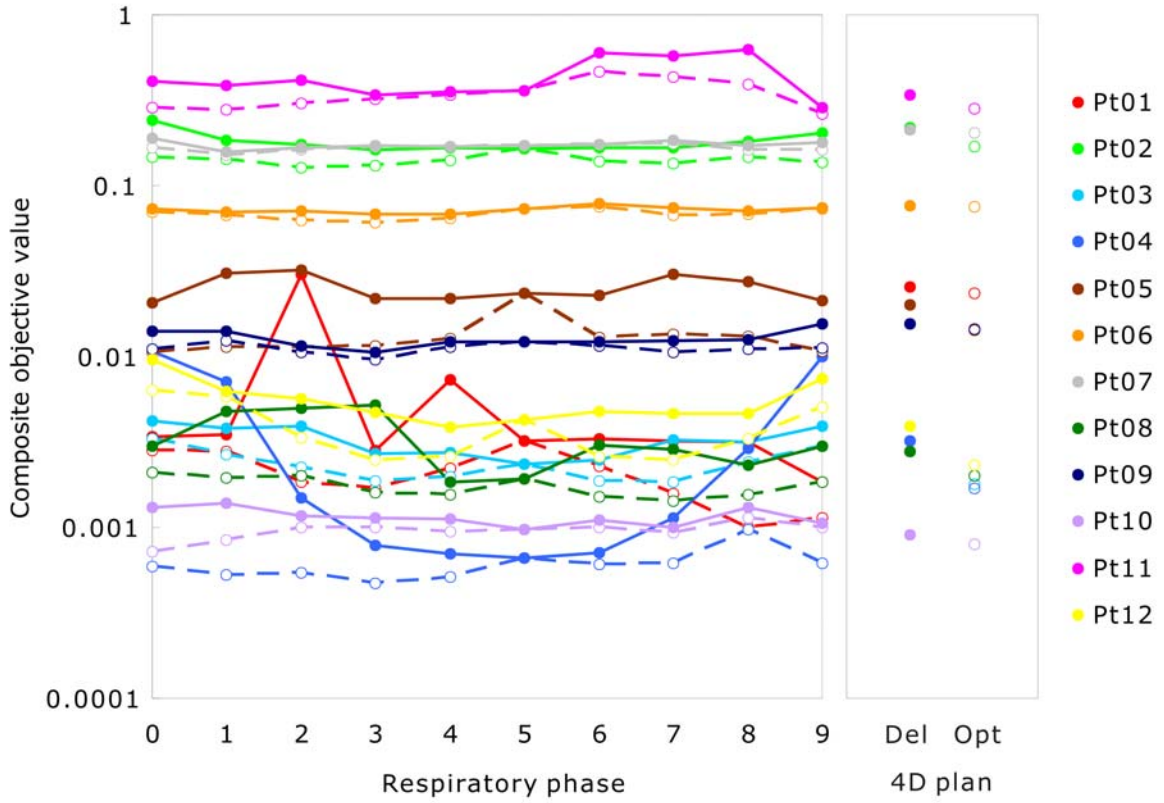

Figure 4-2. Overall plan quality (COVs) of individual phase plans using the deliverable (solid) and 3D optimal (dashed) methods and those of deformable dose-summed 4D plans using the deliverable (Del, filled circles) and 3D optimal (Opt, empty circles) method for each of 12 patients. The smaller the COV, the better the treatment plan. The two methods have identical COVs for Phase 5. For the other phases, the 3D optimal method always yields better plans. The COV of a deformable dose-summed 4D plan for each method is an approximate average value over all individual phase plans per patient.

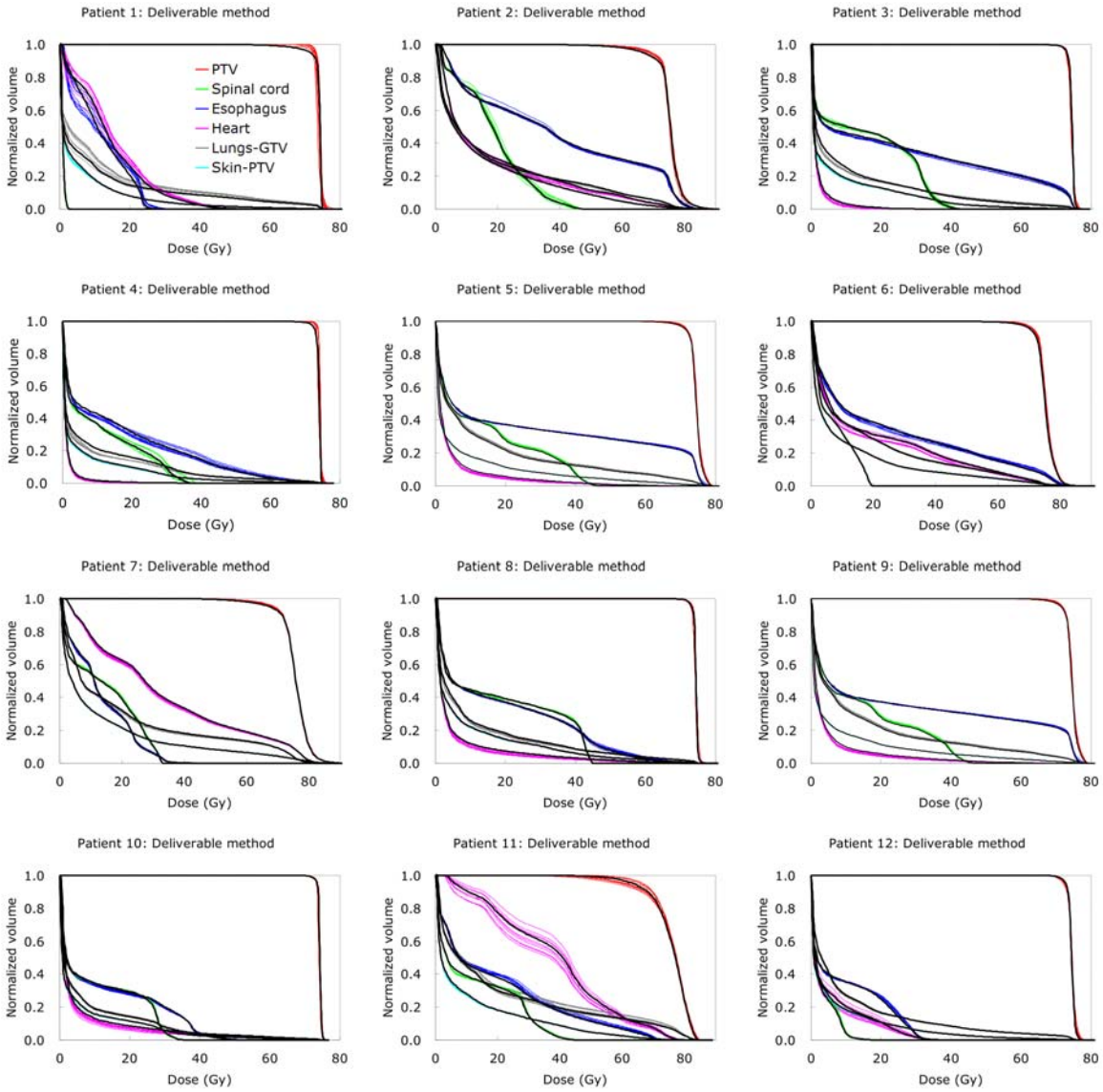

Figure 4-3. DVHs of individual phase plans (thin colored) and a deformable dose-summed 4D plan (black thick) using the deliverable method for each of 12 patients.

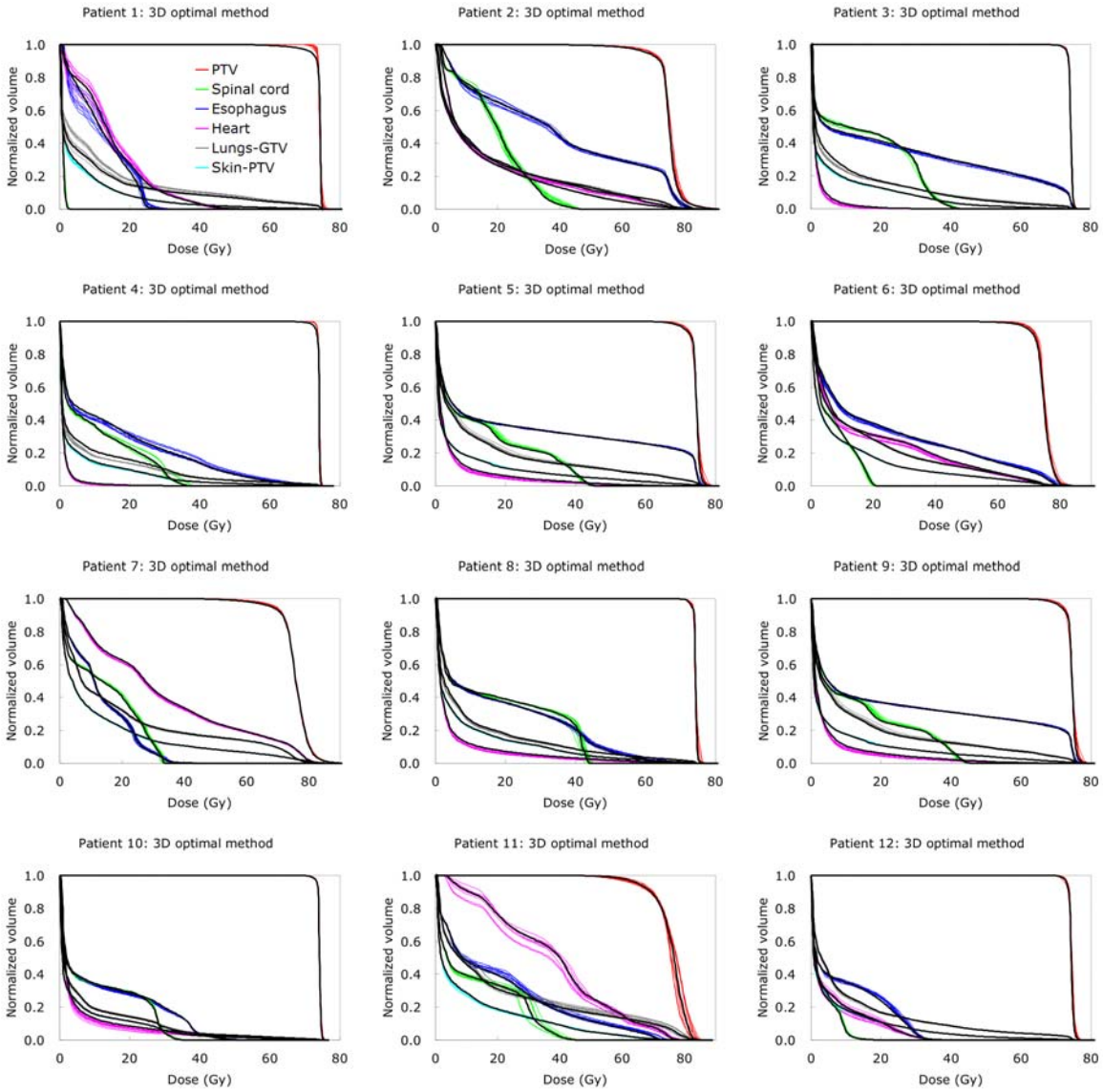

Figure 4-4. DVHs of individual phase plans (thin colored) and a deformable dose-summed 4D plan (black thick) using the 3D optimal method for each of 12 patients.

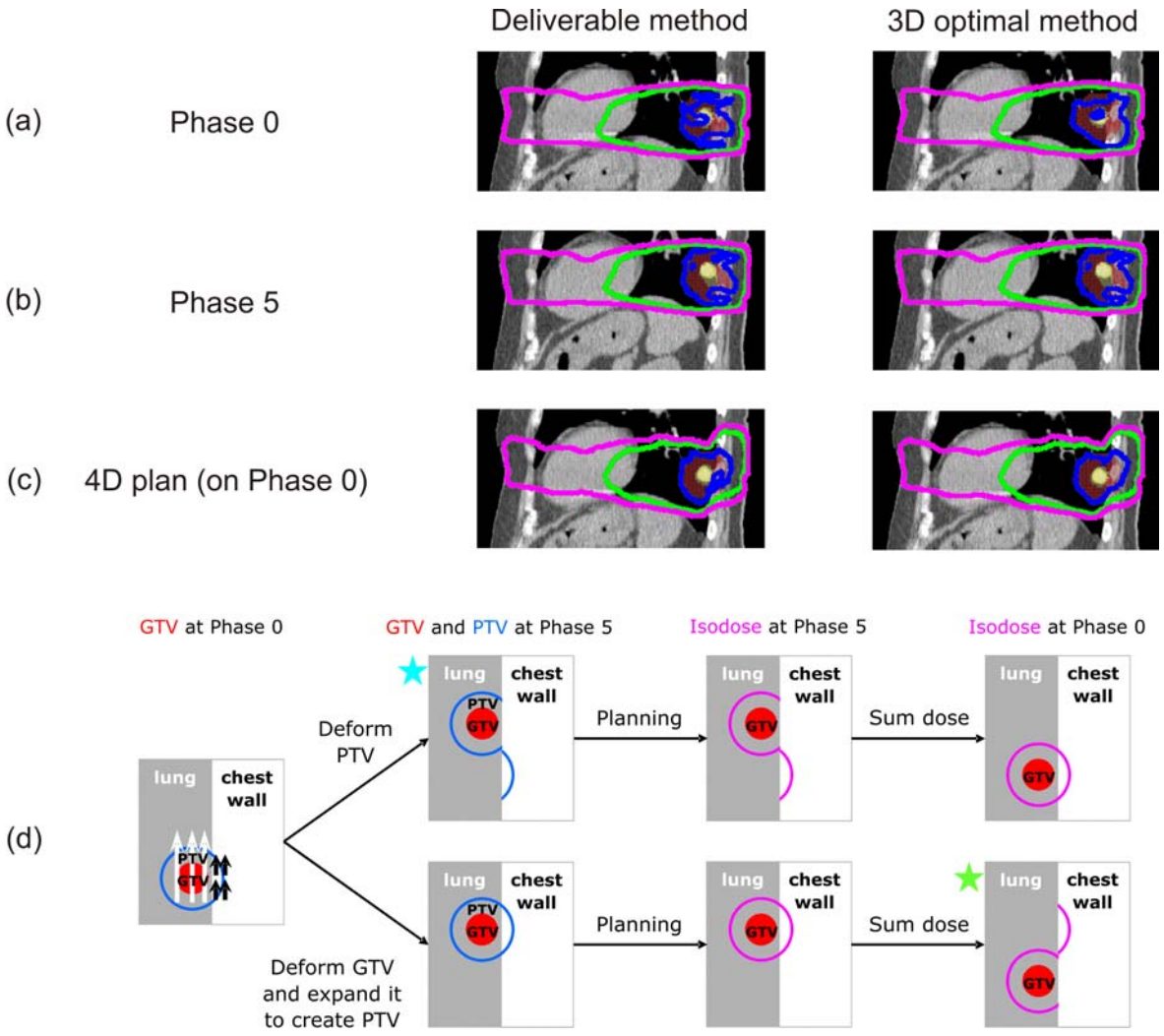

Figure 4-5. Issues due to large gradients of the displacement vector field across the PTV in deformable registration: isodose distributions for (a) Phase 0 plans and (b) Phase 5 plans, and (c) 4D plans (on Phase 0 CT image) using the deliverable and 3D optimal method in a sagittal view for Patient 1. Note that Phase 5 plans are identical for both methods. Whereas dose distributions of Phase 0 and Phase 5 plans look reasonable, the 4D plans have inconsistent dose distributions for both methods. (d) This is due to large gradients of the displacement vector field across the PTV. Because the vector field is large in the lungs (white arrows) and small in the chest wall (black arrows), deforming the PTV generates unrealistic appearance of the PTV after deformable image registration (aqua star). Deforming the GTV and expanding it to create the PTV results in inconsistent dose distributions after deformable dose summation (green star). In (a)-(c), the GTV is shaded in yellow and the PTV in red, and blue isodose curves indicate 74 Gy, green 40 Gy, and pink 20 Gy. In (d), the GTV is shaded in red, blue indicates the PTV, and pink illustrates the isodose curves.

`

Two important findings are as follows.

- The deliverable method is dosimetrically robust to the variations of fractional time spent within respiratory phases on a 4D CT planning scan. Given that the dose distributions of individual phase plans using the deliverable method are very similar to one another, the deliverable method would result in the dose distribution close to the planned dose distribution, even when a patient spends more time on one phase (*e.g.*, end exhale) than the other phases during treatment delivery. In addition, for deformable dose-summed 4D plans, the deliverable method yields dosimetric values statistically similar to those with the 3D optimal method ($p > 0.05$ for all dose-volume metrics compared). This indicates not only that the deliverable method is dosimetrically robust but also that the target deformation or rotation and nonlinear motion or hysteresis generally have little dosimetric impact for the 12-patient series studied.
- Both methods are affected by high vector field variations from deformable registration. The deformable dose-summed 4D plans for Patient 1 are significantly inferior to individual phase plans for both methods, mostly due to PTV coverage. Although the dose distributions for Phase 0 and Phase 5 plans look reasonable, 4D plans have inconsistent dose distributions for both methods (Figure 4-5). This is explained by large gradients of the displacement vector field across the PTV. Because the tumor of Patient 1 is next to the chest wall and moves 2.1 cm, the vector field, which differs significantly across the PTV, is used for deformable image registration and dose summation. The vector field tends to be large in the lungs

(white arrows) and small in the chest wall (black arrows) as in Figure 4-5. As a result, some portion of the PTV (in the chest wall) deforms differently from its other portion (in the lungs). Thus, deforming the PTV differs from deforming the GTV and expanding it to create the PTV, because the former may generate unrealistic appearance of the PTV after deformable image registration; however, when the dose is deformed back to Phase 0, the latter may result in inconsistent dose distributions after deformable dose summation, as shown in Figure 4-5(d).

4.4. Conclusions

A deliverable 4D IMRT treatment-planning method that involves aligning the MLC leaf travel direction parallel to the major axis of a tumor trajectory and translating MLC leaf positions by the difference in the tumor centroid position between respiratory phases of the 4D CT scan has been developed. It shows that accounting for 1D tumor translation is practical and provides a reasonable approximation to compensating complex tumor motion and deformation. The 1D approach yields a planning scheme that is not optimal but, importantly, is deliverable with currently available technology.

A simplification of 3D motion of a deforming, rotating tumor to 1D rigid-body tumor translation is sensible; however, since tumor motion is known to exhibit nonlinear behavior and hysteresis as shown in Chapter 2, incorporating more complex, 3D tumor motion into 4D IMRT treatment-planning might provide a better solution.

CHAPTER 5 FOUR-DIMENSIONAL INTENSITY-MODULATED RADIATION THERAPY TREATMENT PLANNING, A SPECIFIC SOLUTION II: *Extending 3D IMRT Treatment Planning to 4D IMRT Treatment Planning by Accounting for 3D Motion*

5.1. Introduction

The other specific solution to 4D IMRT treatment planning that extends 3D IMRT treatment planning to 4D with deliverable constraints is a method to account for 3D tumor motion. This method utilizes an algorithm developed for real-time DMLC motion tracking [21] in an offline manner to create 4D IMRT treatment plans. It allows 4D radiotherapy treatment planning and delivery using the same underlying algorithm. A treatment plan created using this algorithm explicitly accounts for 3D tumor motion and consequently nonlinear motion and hysteresis [31, 117], and it also is deliverable on a treatment machine.

The aim of this study was to develop a 4D IMRT treatment-planning method by modifying and applying a DMLC motion-tracking algorithm. The details of this chapter are accepted for publication in *Physics in Medicine and Biology*, which is included as Appendix C.

`

5.2. Methods and materials

A dynamic multileaf collimator motion-tracking algorithm

A DMLC motion-tracking algorithm [21] is designed to (a) read initial MLC leaf positions as a function of *MU* from an MLC leaf sequence derived from a treatment plan; (b) dynamically calculate MLC leaf positions to account for target position changes using real-time 3D target location data from a position-monitoring system; (c) generate new MLC leaf positions as a function of *MU* and 3D target location using (a) and (b); and (d) send the generated MLC leaf sequence to a treatment machine to reposition the beam in real time. For 4D treatment planning, the DMLC motion-tracking algorithm was modified to include the respiratory phase as an additional parameter and to be used in an offline mode.

Four-dimensional intensity-modulated radiation therapy treatment planning

The DMLC motion-tracking algorithm requires two inputs: an initial MLC leaf sequence and real-time 3D target location and phase information.

- An initial MLC leaf sequence is derived from an IMRT treatment plan created on the reference phase CT image.
- From the delivery perspective, real-time target location and phase information is necessary to reposition the beam in real time; for planning purposes, 3D offsets of the tumor centroid position for each phase *i* relative to that for the reference phase are calculated as the motion parallel to the major axis, the motion perpendicular to the major axis, and the motion along the beam direction, $T_i(x, y, z \mid \theta_i)$.

`

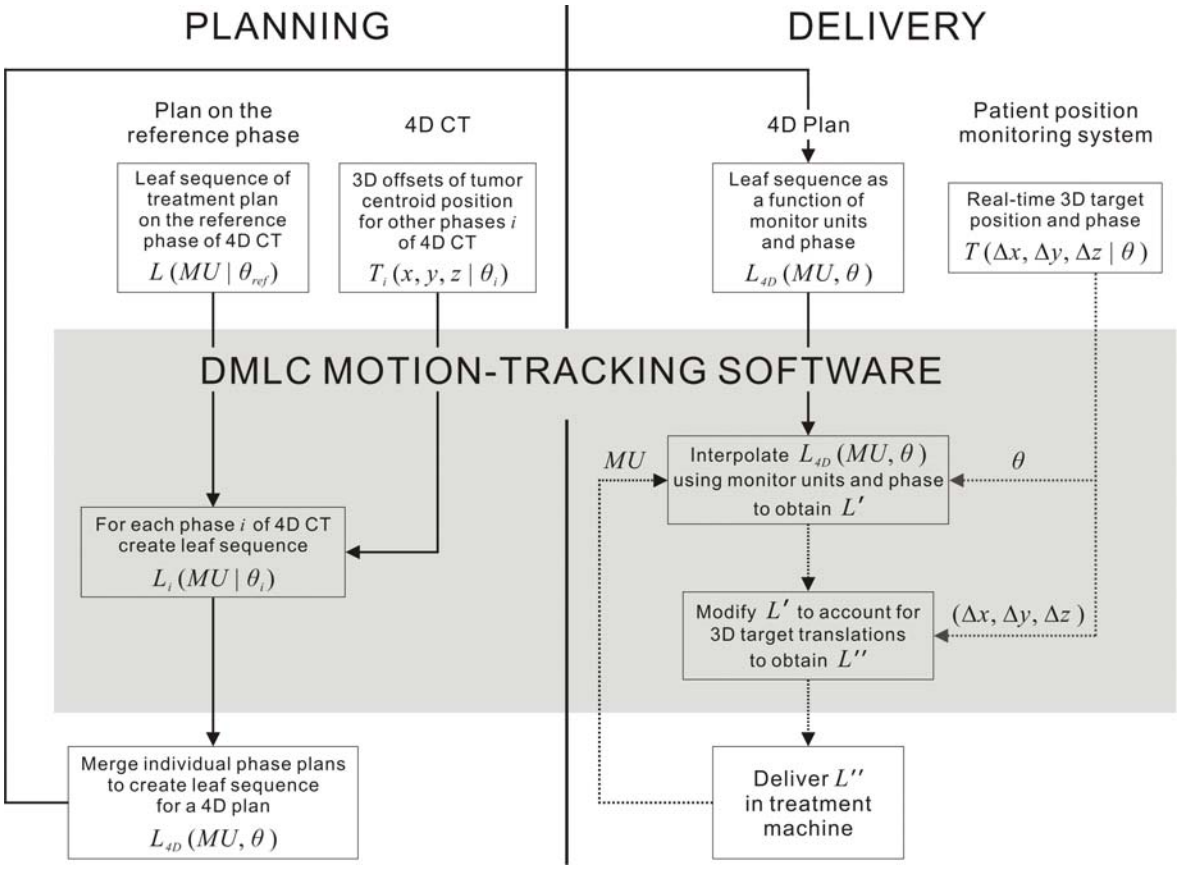

Figure 5-1. Use of a DMLC motion-tracking algorithm for both planning and delivery of 4D radiotherapy treatment, where T is 3D target position and phase information. Dashed lines indicate real-time processes and solid lines are not real time.

Figure 5-1 shows a flow diagram of using the same algorithm for both planning and delivery of 4D radiotherapy treatment, and how a 4D IMRT treatment plan is created using the DMLC motion-tracking algorithm. The DMLC motion-tracking software generates a set of MLC leaf sequences for each phase, which is used to create plans for individual phases; then the leaf sequences of individual phase plans are merged to create a leaf sequence for a 4D plan, $L_{4D}(MU, \theta)$ (bottom left in Figure 5-1), which is used as an initial

leaf sequence on the delivery side. For 12 patient 4D CT image sets described in Chapter 4, the 4D IMRT treatment-planning method using a DMLC motion-tracking algorithm was applied.

5.3. Results and discussion

Figures 5-2 and 5-3 show the DVHs and the COVs, respectively, of all 10 individual phase plans with a deformable dose-summed 4D plan generated using the DMLC motion-tracking algorithm. In general, individual phase plans have similar overall quality (COVs) to the reference phase plans, as well as to a deformable dose-summed 4D plan; and a deformable dose-summed 4D plan for each patient is similar to an average over individual phase plans. The DVHs of the PTV show similar target coverage from phase to phase, whereas the DVHs for OARs show variation. This variation is due to an intrinsic drawback of all tumor-tracking methods, which only track the tumor motion, not the motion of whole patient anatomy [108]. That is, individual phase plans generated using the DMLC motion-tracking algorithm do not account for the phase-to-phase positional changes of OARs with respect to the tumor and/or to the BEV.

Using this method, the DVHs and isodose distributions of an IMRT treatment plan for every phase of the 4D CT scan were, in general, similar to those of the reference phase plan, as well as the deformable dose-summed 4D plan, for each patient. This indicates that the method is dosimetrically robust to the variations of fractional time spent in respiratory phases on a given 4D CT planning scan.

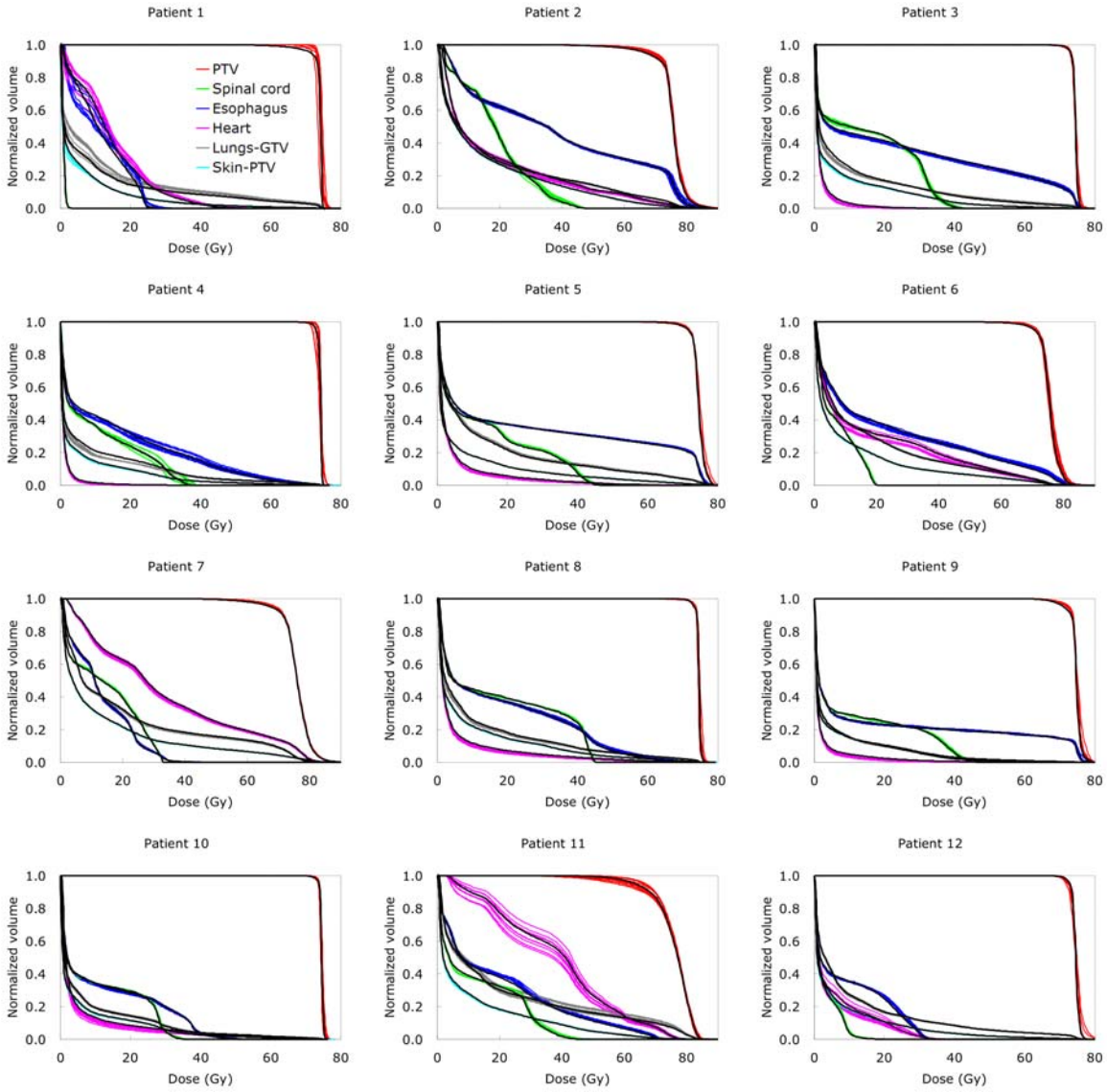

Figure 5-2. DVHs of individual phase plans (thin colored) and a deformable dose-summed 4D plan (black thick) for each of 12 patients.

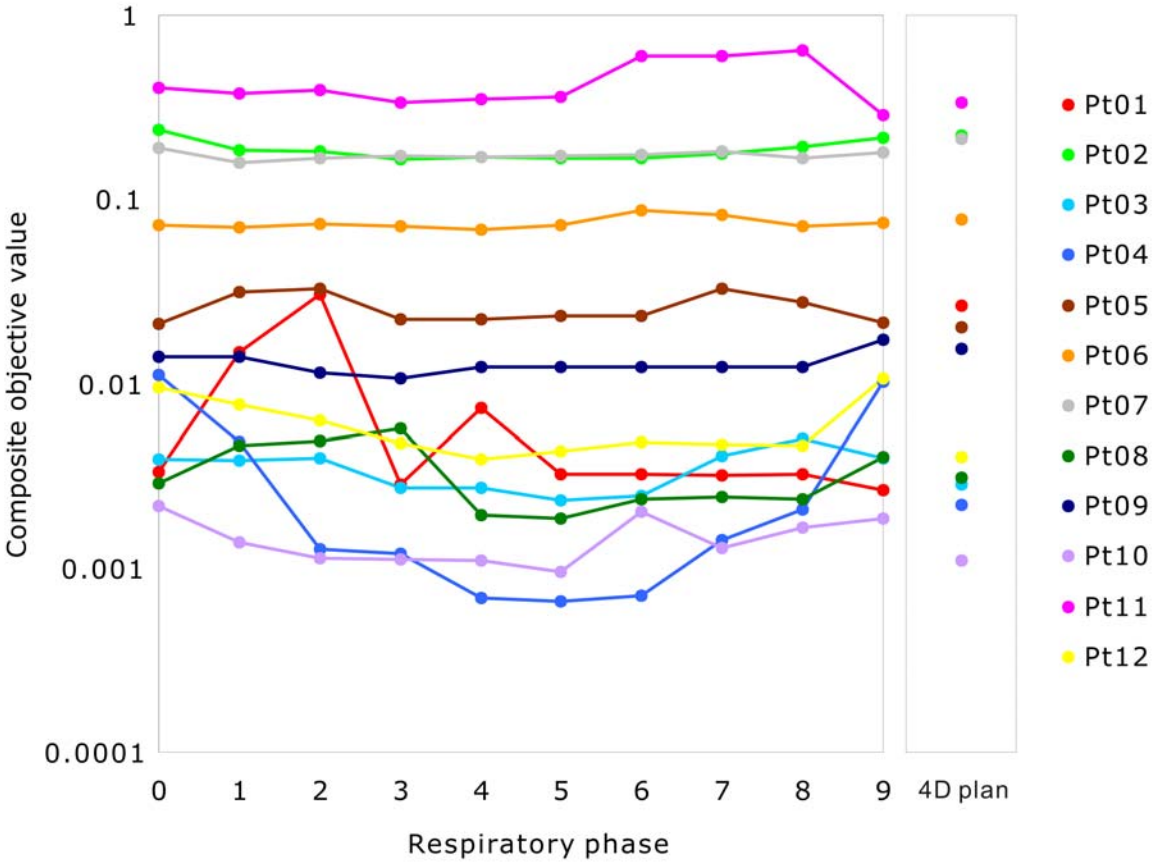

Figure 5-3. Overall plan quality (COVs) of individual phase plans and a deformable dose-summed 4D plan for each of 12 patients. The smaller the COV, the better the treatment plan. The COV of a deformable dose-summed 4D plan for each patient is an approximate average value over all individual phase plans per patient.

In two patients out of twelve, this method was affected by the tumor volume changes from phase to phase. These changes can be attributed to either artifacts in the 4D CT image set as in Patient 1, or tumor volume variations throughout the respiratory phases as in Patient 4. Also, large gradients of the displacement vector field across the PTV deteriorate target coverage resulting in a deformable dose-summed 4D plan much worse than all individual phase plans for Patient 1 (as described in Chapter 4). Patient 11 shows the most phase-to-phase discrepancy in the DVHs of both the PTV and OARs. The tumor of Patient 11 shows the most hysteresis, the second most motion, and the second biggest volume, all of which cause phase-to-phase variations in treatment plans. The tumor motion and hysteresis change the geometric relation between the tumor and normal anatomy from phase to phase, which affects the resulted treatment plans; and the large tumor volume makes an optimization algorithm difficult to be balanced with given optimization constraints, which causes variations in the treatment plans from phase to phase.

5.4. Conclusions

A 4D IMRT treatment-planning method using a DMLC motion-tracking algorithm that creates a treatment plan to explicitly account for 3D tumor motion and thus nonlinear motion and hysteresis, and to be deliverable on a treatment machine has been developed. This method allows the same algorithm to be used for both planning and delivery of 4D radiotherapy treatment. This symmetry between planning and delivery for determining MLC leaf sequences lends itself to clinical viability. This method integrates deliverable 4D IMRT treatment planning with DMLC tumor-tracking delivery, and thus has a clear path to clinical implementation.

Accounting for 3D tumor motion (including nonlinear motion and hysteresis) gives a better solution than accounting for 1D tumor translation (Chapter 4); yet, the results show little advantages to adding an additional degree of freedom because nonlinear motion and hysteresis are not significant in the patient 4D CT image sets available for this study. The greater the nonlinear motion and the hysteresis, the greater the improvement in a resultant treatment plan will be when the off-axis motion of tumor is taken into account. In addition, as this treatment-planning method is based on the assumptions that a tumor is rigid and does not undergo deformation and in- or out-plane rotation, and that the entire anatomy moves, deformation and rotation of a tumor within a respiratory cycle and the relative motion between a tumor and normal anatomy are not accounted for. Therefore, a general solution to 4D IMRT treatment-planning, which is a full 4D optimization to account for all of the above, is being investigated as an extension of the specific solutions (Chapter 8).

`

CHAPTER 6 DETECTION OF ANATOMIC MOTION DURING RADIOTHERAPY TREATMENT DELIVERY

6.1. Introduction

A 4D radiotherapy treatment scenario involves delivering a 4D treatment plan, but with flexibility to account for changes in tumor positions, tumor drifts, or respiratory patterns during actual treatment delivery (Chapter 3). That is, there should be some kind of monitoring methods to observe tumor motion and/or to acquire tumor positions during treatment delivery. This chapter presents the limitation of acquiring tumor position information with a single 2D x-ray imager for the patients with implanted markers.

If 3D tumor motion is monitored with 2D projection imaging, there is unresolved motion because 2D projection is limited in its ability to resolve the motion along the imaging beam axis [118-120]. As 2D projection imaging, two different geometric relationships between the imaging beam and the treatment beam were considered as shown in Figure 6-1: (1) an inline orientation, where the imaging beam is parallel to the treatment beam, and (2) an orthogonal orientation, where the imaging beam is orthogonal (by a 90^o gantry rotation) to the treatment beam. When gantry and couch angles are set to 0^o, a 2D imager in the inline orientation is limited to resolving AP tumor motion as this motion is in the

imaging beam axis, while for a 2D imager in the orthogonal orientation LR tumor motion cannot be resolved.

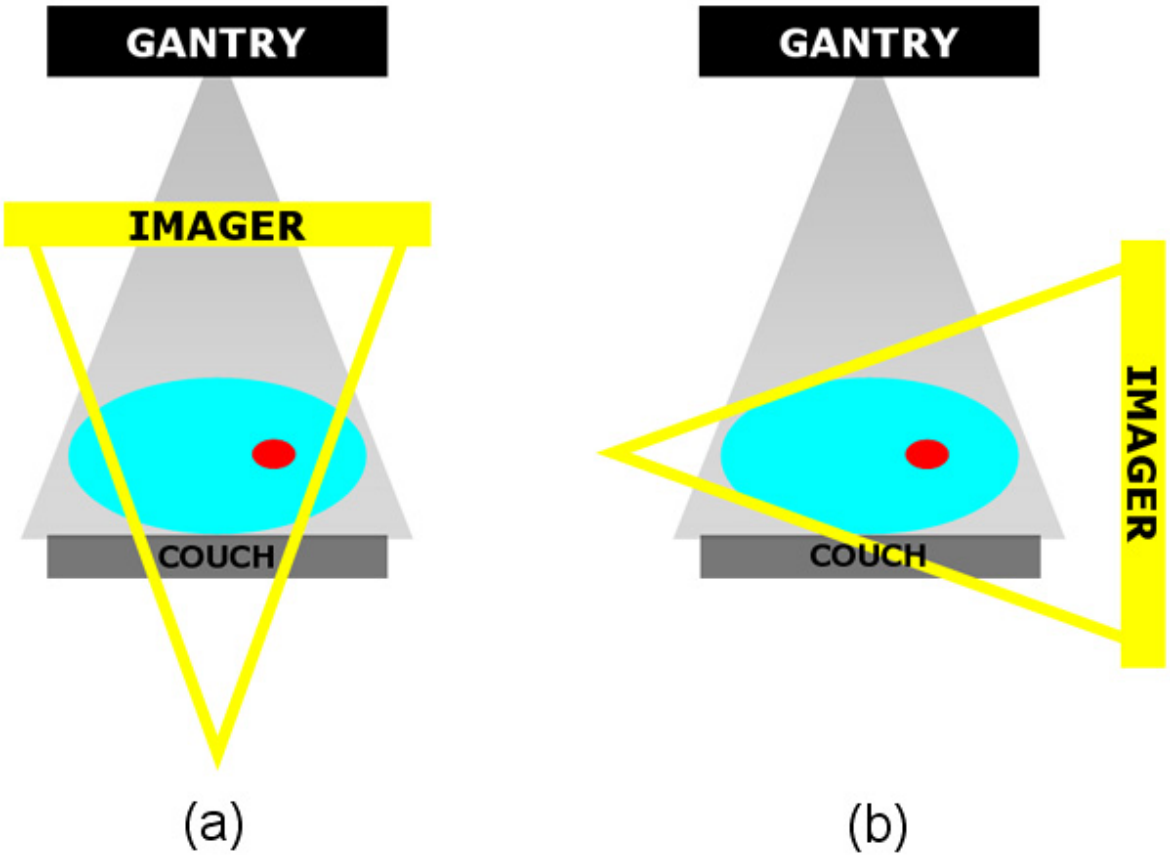

Figure 6-1. Two different geometric relationships between the imaging beam and the treatment beam: (a) an inline orientation, where the imaging beam is parallel to the treatment beam, and (b) an orthogonal orientation, where the imaging beam is orthogonal (by a 90^{o} gantry rotation) to the treatment beam.

The aim of this study was to investigate the accuracy of 2D projection imaging methods in 3D tumor motion monitoring by evaluating the motion that 2D imagers in each of the two orientations, inline and orthogonal, fail to resolve, which can be one important error source in respiratory motion management. The details of this chapter have been published in *Physics in Medicine and Biology*, which is included as Appendix D [121].

6.2. Methods and materials

This study relies on two assumptions, common to the work by Nill *et al.* [120]:

- The setup error will be very small since a possible setup correction on the basis of the acquired images could be performed prior to treatment delivery. This assumption is necessary to set a common 2D to 3D framework from which to analyze the limitations of 2D imaging.
- For a given imaging beam angle, a 2D projection system fails to detect one direction of 3D tumor motion.

Calculation of the unresolved motion

From the 3D tumor motion data of 160 treatment fractions for 46 thoracic and abdominal cancer patients analyzed in Chapter 2, the unresolved motion (i.e., motion in the imaging beam axis) due to the limitation of 2D projection imaging to monitor motion in three dimensions was calculated for each treatment fraction. The geometric uncertainty is shown schematically in Figure 6-2 for a tumor moving only in the AP direction and a 2D projection imager in an inline orientation to monitor the motion. If gantry and couch

angles are 0^o as in Figure 6-2(a), the tumor looks static for the imager in this orientation as shown in the imager's view even though the tumor is moving. If the gantry angle is 90^o and the couch angle is 0^o as in Figure 6-2(c), the imager resolves the full motion of the tumor.

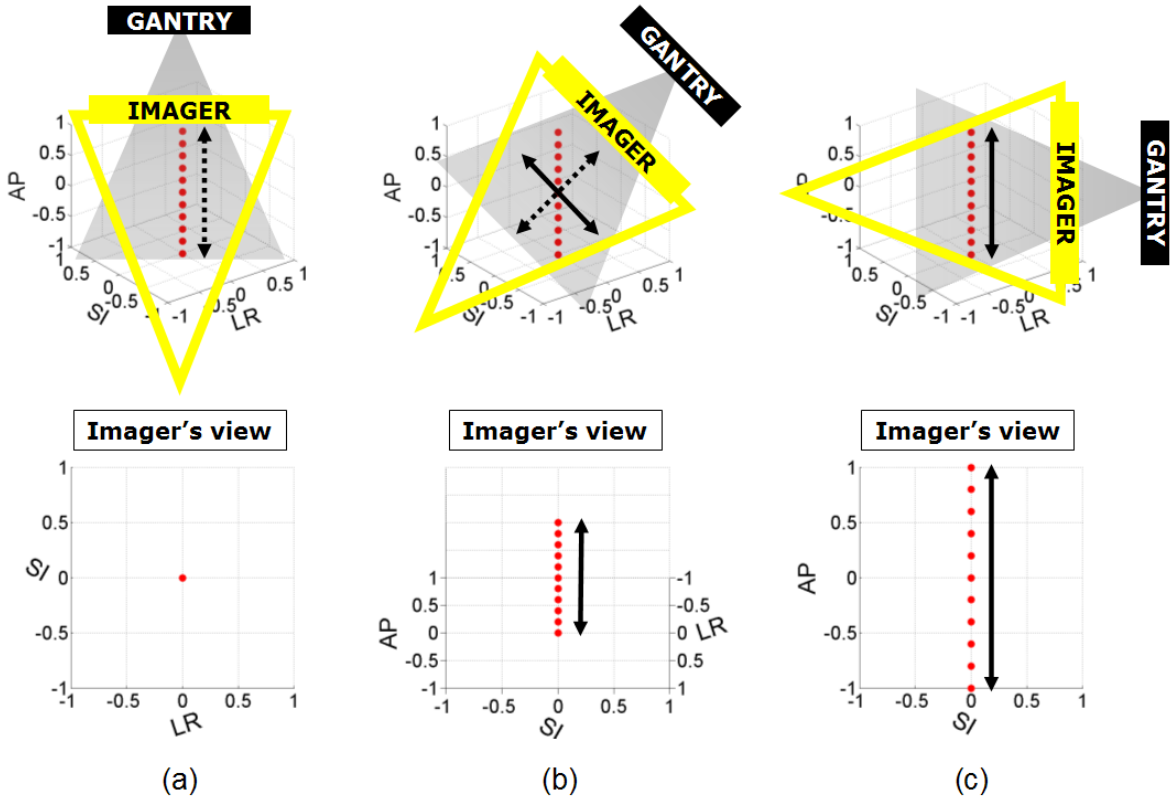

Figure 6-2. Unresolved motion from the limitation of 2D projection imaging to monitor 3D motion: red dots indicate the tumor motion (only AP motion for example), dashed arrows the unresolved motion, and solid arrows the resolved motion for an inline orientation. (a) When gantry and couch angles are 0^o, the tumor looks static for the imager in this orientation as shown in an imager's view even though it is moving (no solid arrow). However, (c) when gantry angle is 90^o and couch angle is 0^o, the imager resolves the full motion (no dashed arrow). (b) If gantry angle is 45^o with couch angle 0^o, the imager resolves part of the motion (solid arrow) while failing to detect the motion in the imaging beam axis (dashed arrow). All plots are in arbitrary units.

As for different treatment beam-patient alignments, 216 beam angles were considered (24 gantry angles from 0^o to 360^o in 15^o increments and 9 couch angles from -60^o to 60^o in 15^o increments). The unresolved motion as a function of only gantry angle while couch angle is 0^o was also calculated as most conventional thoracic and abdominal treatments are coplanar. Also, to look at the unresolved motion for different time intervals, 0-1, 0-10, and 0-30 min, were considered.

Quantification of the geometric uncertainty

The geometric uncertainty in monitoring 3D tumor motion with a 2D projection imager due to the unresolved motion was statistically quantified using the RMS uncertainty of the unresolved motion. To investigate the geometric uncertainty for the cohort of patients studied, let U be the unresolved motion of 2D projection imaging: $U(g, c=0)$ is the unresolved motion as a function of gantry angle for coplanar treatments (zero couch angle) and $U(g, c)$ is the unresolved motion as a function of gantry and couch angle for non-coplanar treatments, where couch angles vary from -60^o to 60^o. For each fraction i, the RMS uncertainty of $U(g, c=0)$, which is $R_{g,t,i}$, and the RMS uncertainty of $U(g, c)$, which is $R_{g,c,t,i}$, for each of the time intervals t, where t is 0-1, 0-10, and 0-30 min, were calculated. Then, the RMS, minimum, and maximum values of $R_{g,t,i}$ and $R_{g,c,t,i}$ were calculated, respectively, and these were repeated for the fractions whose average respiratory peak-to-trough distances were more than 0.5 cm, in regard to the recommendations by the AAPM Task Group 76 [4]. As shown in Figure 6-3, and obvious

from Figure 6-1, the geometric uncertainty of 2D projection imaging in the orthogonal orientation from the treatment beam perspective is simply a 90^o gantry rotation from that in the inline orientation; so $R^{orthogonal}_{g,c,t,i} = R^{inline}_{g+90^o,c,t,i}$.

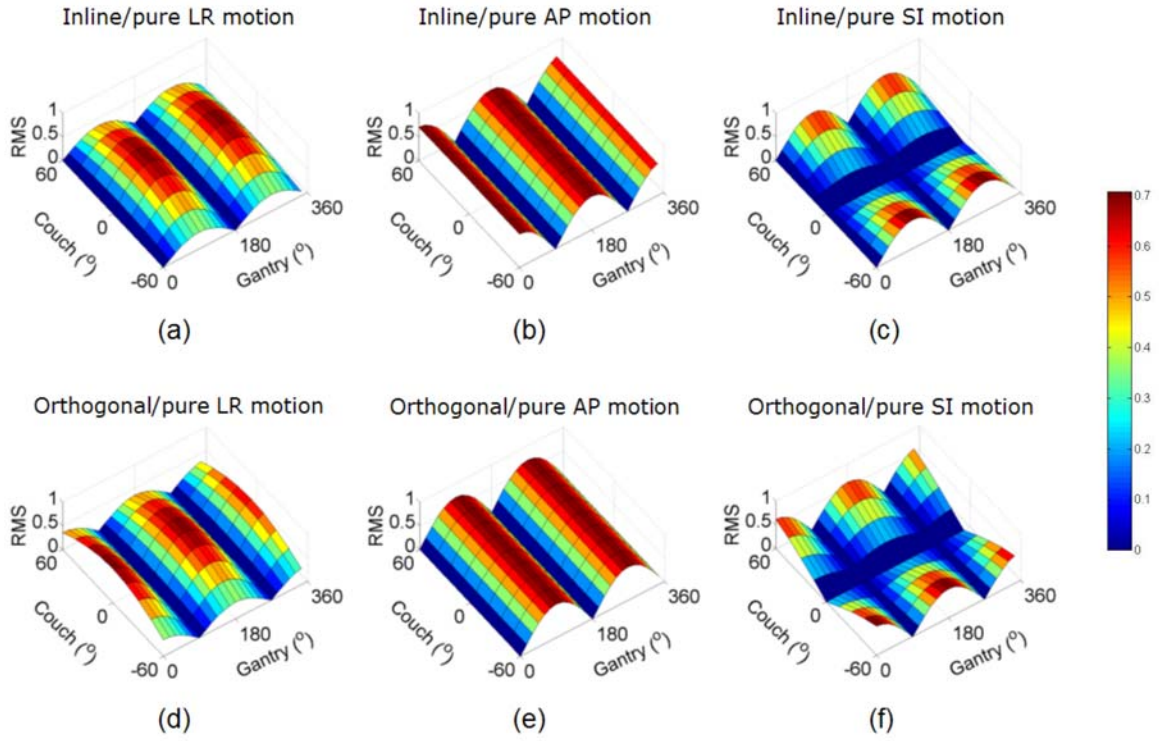

Figure 6-3. RMS uncertainty of the unresolved motion for uni-directional unit amplitude sinusoidal motion: (a) LR, (b) AP, and (c) SI motion for an inline orientation and (d) LR, (e) AP, and (f) SI motion for an orthogonal orientation. Note that plots for an orthogonal orientation are simply rotated by 90^o in the axis of gantry angle from those for an inline orientation. The red color indicates the higher value and the blue is the lower value as in a color bar. All plots are in arbitrary units.

6.3. Results and discussion

Figure 6-3 shows the RMS uncertainty of the unresolved motion as a function of gantry and couch angle for theoretical motion (uni-directional unit amplitude sinusoidal motion) for 2D projection imaging for each orientation. If there is only LR motion as in Figure 6-3(a), the 2D projection in the inline orientation can resolve the LR motion for the case when gantry and couch angles are 0^o, so there is no uncertainty; but for the case when gantry angle is 90^o while couch angle is 0^o, the 2D projection in this orientation cannot resolve the LR motion, so the uncertainty is the highest.

Given that all three plots for the orthogonal orientation are shifted by 90^o in the gantry angle axis from those for the inline orientation, the geometric uncertainty for both orientations is the same. However, in the orthogonal orientation the geometric uncertainty from the unresolved motion can be in a high dose gradient direction, whereas in the inline orientation it is along the dose fall-off in the beam direction where the gradient is lower. Therefore, the dosimetric impact of the unresolved motion is generally higher for the orthogonal orientation.

Overall RMS values of the RMS uncertainty of the unresolved motion was around 0.13 cm for all treatment fractions, 0.10 cm for all coplanar treatment fractions, 0.18 cm for the fractions whose average respiratory peak-to-trough distances were more than 0.5 cm, and 0.13 cm for coplanar treatment fractions whose average respiratory peak-to-trough distances were more than 0.5 cm.

Figure 6-4 shows the cumulative probability of the distributions of the RMS of $R_{g,c,t,i}$ or $R_{g,t,i}$ for different time intervals. All four plots show the similar patterns for the

different time intervals, still showing a tendency that the shorter the time interval the smaller the RMS, in general. One noticeable thing is that patient-to-patient variations are much larger than variations from different time intervals.

6.4. Conclusions

Geometric uncertainty of 2D projection imaging due to the unresolved motion is 0.13 cm for all treatment fractions and 0.18 cm for the treatment fractions whose average respiratory peak-to-trough distances are more than 0.5 cm; and it is smaller for coplanar treatments than non-coplanar treatments, as SI tumor motion, the predominant motion from patient respiration, is always resolved for coplanar treatments. Geometric uncertainty varies depending on the tumor site, tumor motion extent, time interval, and beam angle, as well as between patients, between fractions, and within a fraction.

Geometric uncertainty of 2D imaging methods quantified in this study can be used to estimate proper margins when a single 2D projection imager is used for 4D radiotherapy treatment delivery. In order to have delivery flexible enough to account for any changes that are occurred during actual treatment delivery, but not incorporated into treatment planning, various types of monitoring systems may be used; and the use of a single 2D imager to monitor internal tumor positions will require margins of the order of 0.3 cm, which is about twice the RMS of $R_{g,c,t,i}$ or $R_{g,t,i}$.

`

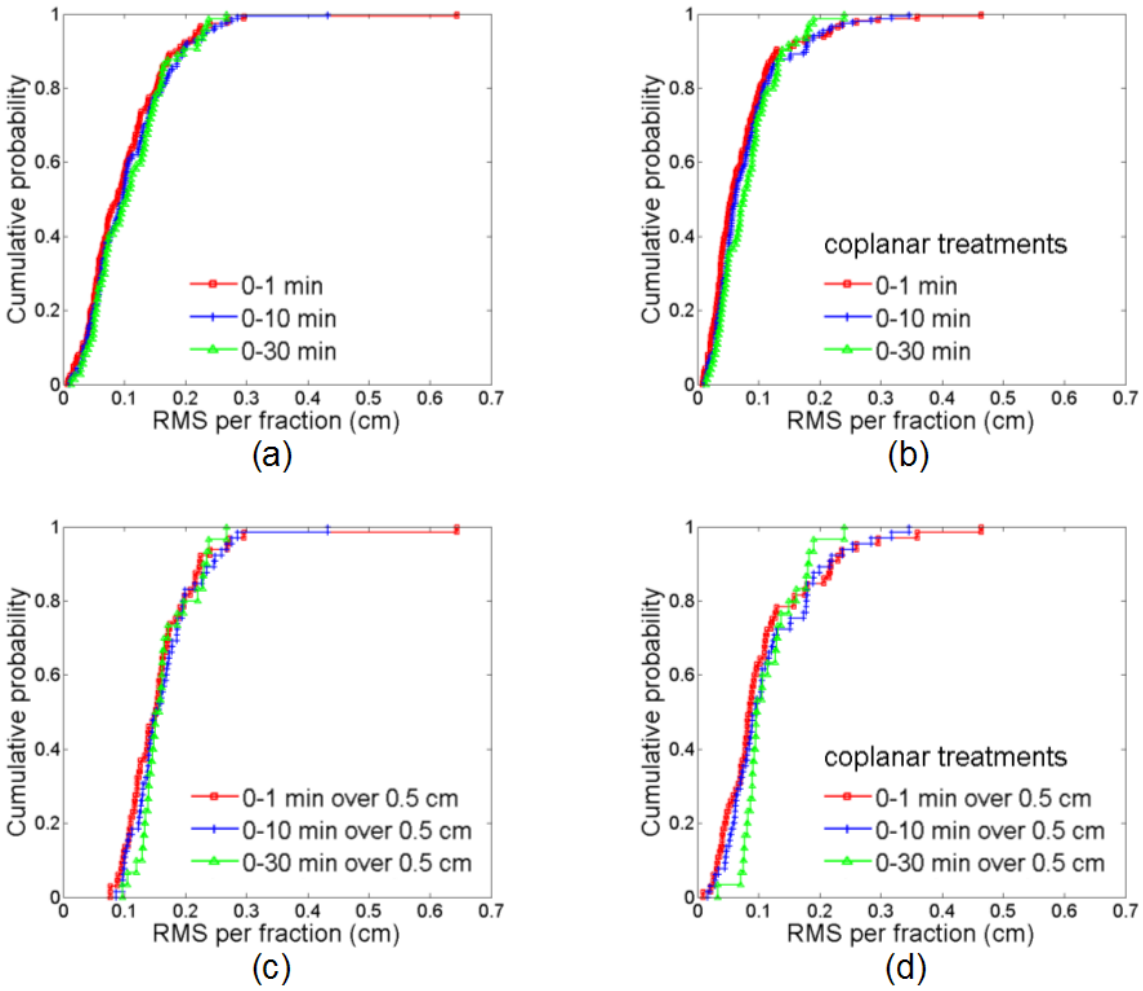

Figure 6-4. Cumulative probability of the distributions of the RMS of $R_{g,c,t,i}$ (RMS uncertainty of the unresolved motion for each fraction i and for each time interval t for non-coplanar treatments) [(a) and (c)] and of $R_{g,t,i}$ (RMS uncertainty of the unresolved motion for each fraction i and for each time interval t for coplanar treatments) [(b) and (d)] for 0-1 (red), 0-10 (blue), and 0-30 (green) min for an inline orientation: (a) all fractions for non-coplanar treatments, (b) all fractions for coplanar treatments, (c) fractions whose average respiratory peak-to-trough distances are more than 0.5 cm for non-coplanar treatments, and (d) fractions whose average respiratory peak-to-trough distances are more than 0.5 cm for coplanar treatments.

CHAPTER 7 DELIVERY OF FOUR-DIMENSIONAL RADIOTHERAPY TREATMENT

7.1. Introduction

Real-time tumor tracking using DMLC delivery is shown to have potential to improve radiotherapy treatment by reducing positional uncertainties due to anatomic motion and thus increasing dosimetric accuracy. Current limitations for an MLC to continuously align the radiation beam with a moving tumor include mechanical motion constraints. In addition, Sawant *et al*. shows that efficiency of IMRT delivery for the tumor motion perpendicular to the MLC leaf travel direction is significantly lower than that for the motion parallel to the MLC leaf travel direction [21].

Using a moving average algorithm for tumor-tracking delivery eliminates a systematic tracking error and treats respiratory motion as a residual random error. In addition, tumor tracking using a moving average algorithm significantly reduces mechanical requirements on an MLC compared with real-time tumor tracking, and can be combined with a respiratory-gating technique.

`

The aim of this study was to investigate an alternative technique of radiotherapy treatment delivery for tumor tracking that uses a moving average algorithm. The details of this chapter have been published in *Medical Physics*, which is included as Appendix E [122].

7.2. Methods and materials

Two sets of respiratory motion data were used.

- External respiratory motion data: 331 four-minute abdominal wall AP motion traces from 24 lung cancer patients using a Real-time Position Management™ system. Each patient was initially asked to breathe without any instructions, which is called free breathing, and the respiratory motion was recorded. Then, audio coaching was given followed by audio-visual biofeedback on the basis of the displacement and the period of respiratory motion during the free-breathing session. Therefore the data consist of (1) free-breathing, (2) audio-coaching, and (3) audio-visual biofeedback sessions.
- Implanted fiducial motion data: 3D tumor motion data from 160 treatment fractions for 46 thoracic and abdominal cancer patients analyzed in Chapter 2.

Different treatment delivery scenarios

Figure 7-1 shows the five different radiotherapy treatment delivery scenarios compared. It is assumed that a real-time tumor position-monitoring system is present for all scenarios.

Moving average tracking. The beam position at time t is calculated as the mean tumor position during the past m s (15 s was chosen as it represents an average amount of time that a patient takes to settle on a treatment table and breathes normally). The number of points included in a moving average was $m \times f$, where f is a sampling frequency (30 Hz for the external respiratory motion data and 25 Hz for the implanted fiducial motion data). The estimated tumor position, x_{est}, at time t for moving average tracking is

$$x_{est}(t) = \frac{\sum_{i=t-m\times f-RT}^{t-RT} x_{act}(i)}{m \times f},$$

where x_{act} is an actual position, i indicates an increment of the points from 1 to $m \times f$, and RT is the number of sample points during a system response time (0.16 s). That is, the beam position is calculated as the mean of the past 15 s of the tumor position information.

Real-time tracking. Without any prediction algorithm, the estimated tumor position at time t for real-time tracking is the beam position after a system response time:

$$x_{est}(t) = x_{act}(t - RT).$$

Respiratory gating at exhale and at inhale. A duty cycle of 40% is utilized for a respiratory-gating technique: 30-70% for exhale gating and 80-20% for inhale gating. The beam position at time t is calculated as the mean tumor position in a gating

window during the first n s. The estimated tumor position at time t for respiratory gating at both exhale and inhale is calculated by

$$x_{est}(t) = \frac{\sum_{i=1}^{n\times f} x_{act}(i) \times H}{\sum_{i=1}^{n\times f} H},$$

where H is a Heavyside function that equals 1 when a respiratory phase is within the gating window and 0 otherwise. That is, the beam position is calculated as the mean of the first n s of the tumor position information within the duty cycle.

Moving average gating at exhale and inhale. Moving average gating uses a moving average algorithm over the respiratory motion in a gating window. The estimated tumor position at time t for moving average gating at both exhale and inhale is

$$x_{est}(t) = \frac{\sum_{i=t-m\times f-RT}^{t-RT} x_{act}(i) \times H}{\sum_{i=t-m\times f-RT}^{t-RT} H}.$$

The tumor position is updated every 15 s similar to moving average tracking. That is, the beam position is calculated as the mean of the most recent n s (i.e., from $t - m \times f - RT$ to $t - RT$) of the tumor position information within the duty cycle.

Static beam delivery with online pre-treatment tumor-beam alignment. The first n s of the tumor position information is used to align the beam with the tumor before treatment, but the beam does not respond to the tumor motion during treatment

delivery. The tumor position at time t for static beam delivery is determined as the mean tumor position during the first n s:

$$x_{est}(t) = \frac{\sum_{i=1}^{n \times f} x_{act}(i)}{n \times f}.$$

That is, the beam position is calculated as the mean of the first n s of the tumor position information.

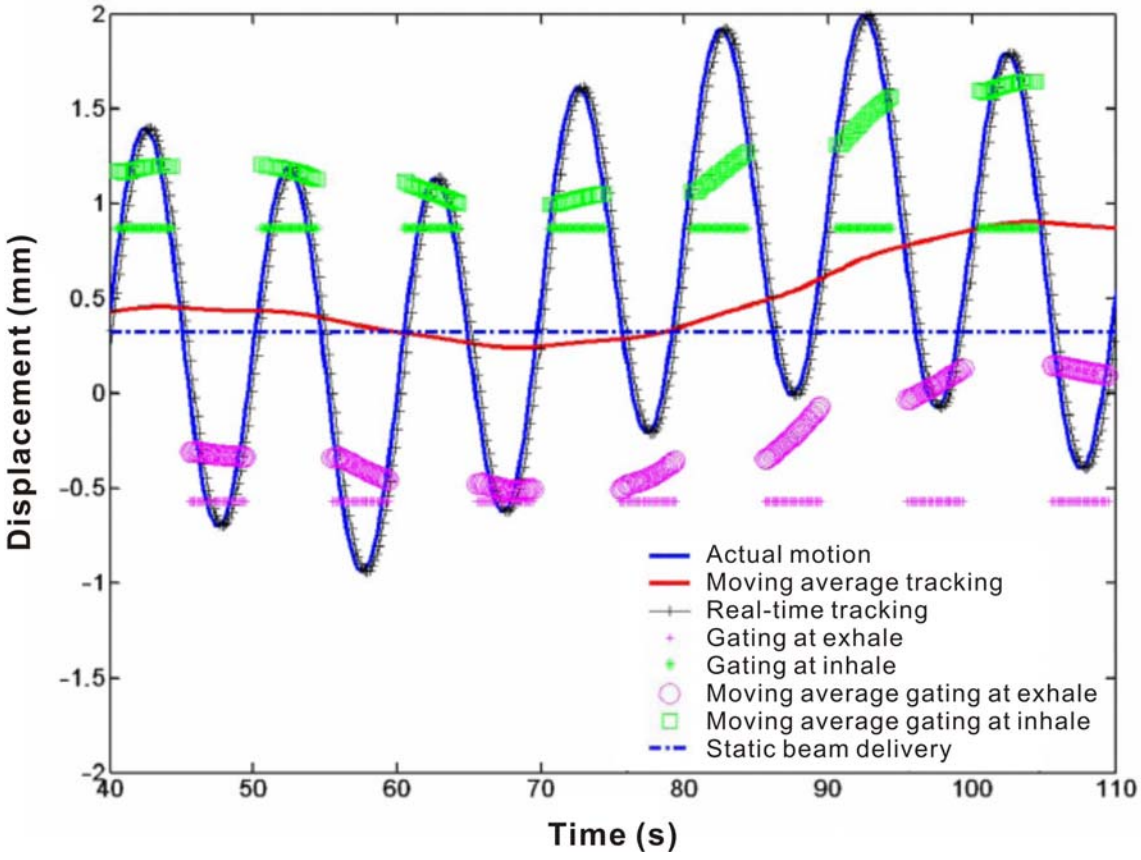

Figure 7-1. Different treatment delivery scenarios compared: (1) moving average tracking, (2) real-time tracking, (3) gating at exhale and at inhale, (4) moving average gating at exhale and at inhale, and (5) static beam delivery.

The metrics evaluated to compare the five treatment delivery scenarios are the group systematic error, M, the SD of the systematic error, Σ, and the RMS of the random error, σ, calculated as in Table 7-1 [123].

Table 7-1. Formalisms to calculate the group systematic error, M, the SD of the systematic error, Σ, and the RMS of the random error, σ, where Δ is displacement between the beam and the tumor at a given time and $\Delta(P_j, F_i)$ is a set of displacement for a given fraction F_i for a given patient P_j.

	Patient 1	Patient 2	...	**Formalisms**
Fraction 1	$\Delta(P_1, F_1)$	$\Delta(P_2, F_1)$		
Fraction 2	$\Delta(P_1, F_2)$	$\Delta(P_2, F_2)$		
...				
				$M = \overline{\Delta(P_1 ... P_M, F_1 ... F_N)}$
Mean	$\overline{\Delta(P_1, F_1 ... F_N)}$	$\overline{\Delta(P_2, F_1 ... F_N)}$		$\Sigma = SD\left(\Delta(P_1 ... P_M, F_1 ... F_N)\right)$
SD	$SD\left(\Delta(P_1, F_1 ... F_N)\right)$	$SD\left(\Delta(P_2, F_1 ... F_N)\right)$		$\sigma = RMS\left(\Delta(P_1 ... P_M, F_1 ... F_N)\right)$

Margin calculations

For the implanted fiducial motion data, margins were calculated using the formula by Stroom *et al.* [123]: (1) optimistic case, when no other error contributions, $2\Sigma + 0.7\sigma$, and (2) realistic case, when 0.3-cm systematic and 0.3-cm random error contributions from other sources, $2(\Sigma^2 + 0.3^2) + 0.7(\sigma^2 + 0.3^2)$.

`

7.3. Results and discussion

External respiratory motion

For real-time tracking, moving average tracking, and moving average gating, M and Σ are negligible (Tables 7-2 and 7-3). Moving average gating improves gating at both exhale and inhale. Real-time tracking and moving average tracking have slightly lower σ than static beam delivery. Moving average gating results in improved σ compared with moving average tracking.

Implanted fiducial motion

For moving average tracking, M and Σ are negligible compared with static beam delivery (Tables 7-2 and 7-3). Moving average gating results in improved σ compared with moving average tracking over the entire respiratory traces. On the basis of margin calculations without error, the different treatment delivery scenarios is ranked as follows: (1) real-time tracking; (2) moving average gating at exhale; (3) moving average gating at inhale; (4) moving average tracking; (5) gating at exhale; (6) static beam delivery with online pre-treatment tumor-beam alignment; and (7) gating at inhale.

Margin calculations

The cumulative probability plots in Figure 7-2 show how appropriate (or inappropriate) applying a population margin to an individual patient is, indicating a proper amount of a margin for each patient. These cumulative probability plots are useful to determine what percentage of the patients fall into a particular margin range.

`

Table 7-2. Group systematic error calculated for different treatment delivery techniques.

Treatment delivery techniques	Group systematic error, M (cm)			
	External respiratory motion			Implanted fiducial motion
	Free breathing	Audio coaching	Audio-visual biofeedback	
Moving average tracking	-0.01	-0.01	0.00	0.00
Real-time tracking	0.00	0.00	0.00	0.00
Gating at exhale	-0.11	-0.05	-0.03	-0.05
Gating at inhale	-0.16	-0.12	-0.02	0.16
Moving average gating at exhale	-0.01	-0.01	0.00	0.00
Moving average gating at inhale	-0.01	0.00	0.00	0.00
Static beam delivery	-0.13	-0.17	-0.06	0.02

Table 7-3. SD of the systematic error and RMS of the random error calculated for different treatment delivery techniques. In parentheses are the minimum and maximum values.

Treatment delivery techniques	SD of the systematic error, Σ (cm)			
	External respiratory motion			Implanted fiducial motion
	Free breathing	Audio coaching	Audio-visual biofeedback	
Moving average tracking	0.01 (-0.03-0.02)	0.01 (-0.03-0.01)	0.01 (-0.03-0.01)	0.00 (-0.01-0.01)
Real-time tracking	0.00 (0.00-0.00)	0.00 (0.00-0.00)	0.00 (0.00-0.00)	0.00 (0.00-0.00)
Gating at exhale	0.18 (-0.52-0.48)	0.12 (-0.28-0.25)	0.06 (-0.18-0.11)	0.17 (-0.73-0.60)
Gating at inhale	0.23 (-0.64-0.41)	0.18 (-0.52-0.21)	0.07 (-0.19-0.15)	0.26 (-0.53-1.23)
Moving average gating at exhale	0.01 (-0.03-0.04)	0.01 (-0.03-0.01)	0.01 (-0.03-0.01)	0.00 (-0.01-0.01)
Moving average gating at inhale	0.02 (-0.04-0.05)	0.01 (-0.03-0.02)	0.01 (-0.02-0.03)	0.00 (-0.02-0.01)
Static beam delivery	0.21 (-0.52-0.45)	0.24 (-0.55-0.36)	0.18 (-0.77-0.12)	0.16 (-0.56-0.84)

Treatment delivery techniques	RMS of the random error, σ (cm)			
	External respiratory motion			Implanted fiducial motion
	Free breathing	Audio coaching	Audio-visual biofeedback	
Moving average tracking	0.46 (0.14-0.80)	0.53 (0.22-0.90)	0.54 (0.23-0.88)	0.22 (0.01-0.63)
Real-time tracking	0.13 (0.07-0.25)	0.14 (0.06-0.26)	0.16 (0.08-0.32)	0.07 (0.00-0.18)
Gating at exhale	0.30 (0.11-0.58)	0.29 (0.14-0.50)	0.27 (0.13-0.49)	0.15 (0.01-0.75)
Gating at inhale	0.44 (0.15-0.77)	0.44 (0.21-0.67)	0.36 (0.13-0.68)	0.23 (0.01-0.83)
Moving average gating at exhale	0.21 (0.08-0.43)	0.21 (0.09-0.31)	0.22 (0.12-0.37)	0.10 (0.00-0.53)
Moving average gating at inhale	0.35 (0.13-0.57)	0.35 (0.17-0.58)	0.32 (0.12-0.61)	0.17 (0.01-0.68)
Static beam delivery	0.47 (0.18-0.81)	0.54 (0.21-0.86)	0.55 (0.23-0.88)	0.24 (0.01-0.82)

`

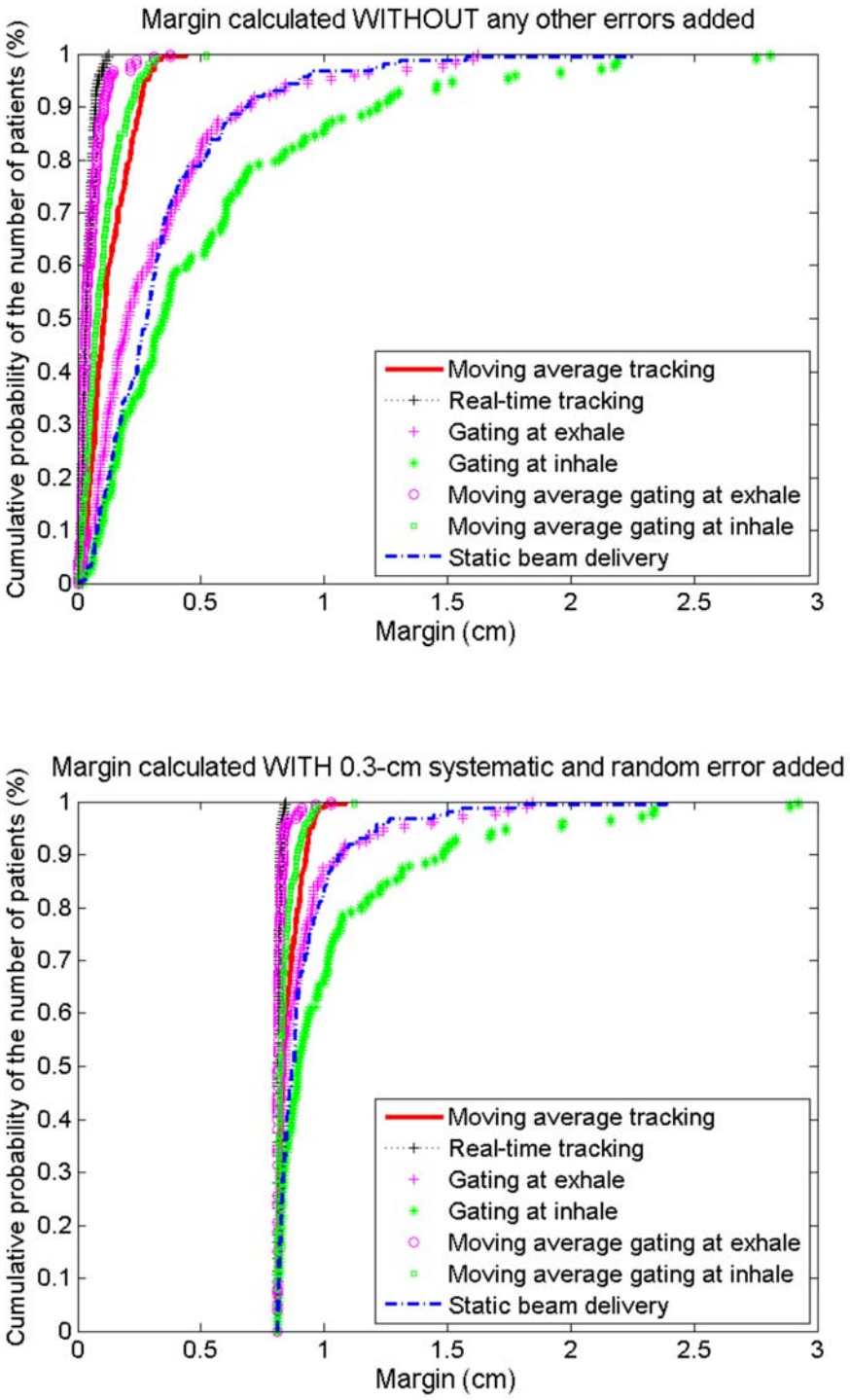

Figure 7-2. Margins calculated for different treatment scenarios for implanted fiducial motion, without other error components and with the addition of 0.3-cm systematic and 0.3-cm random error contribution from other sources.

`

7.4. Conclusions

Tumor-tracking delivery using a moving average algorithm has been developed as an alternative technique of radiotherapy treatment delivery for tumor tracking. Moving average tracking accounts for variations in the average tumor position; but tumor position variations about this average due to respiratory motion are ignored during treatment delivery and can be treated as a random error during treatment planning. Moving average tracking shows (1) margin reduction compared with gating and static beam delivery with online pre-treatment beam-tumor alignment, (2) practical advantages over real-time tracking as the motion is slower and smoother, (3) mechanical advantages over real-time tracking when the beam is aligned to the tumor, and (4) patient compliance advantages over real-time tracking when the tumor is align to the beam.

Mechanical constraints of an MLC may hinder delivery of 4D radiotherapy treatment. This can be worse for delivery of 4D IMRT treatment, because MLC leaves need to both follow tumor motion and modulate beam intensity during treatment delivery. Using a moving average algorithm to deliver a 4D IMRT treatment plan provides an approximate solution that can be immediately implemented. Moving average tracking will require an additional margin compared with real-time tracking. For moving average tracking, population margins calculated are 0.15 cm (without any other errors) and 0.86 cm (with 0.3-cm systematic and 0.3-cm random error contributions from other sources), compared with 0.05 cm and 0.82 cm, respectively, for real-time tracking.

`

CHAPTER 8 ONGOING AND FUTURE WORK

8.1. Ongoing work to solve a general solution

The ongoing work is to investigate a general 4D IMRT treatment-planning optimization by solving Equation (1) in Chapter 3. The framework for solving the general solution will be used to solve for other approaches in the solution space in Figure 3-1, by removing degrees of freedom. Solving all of the treatment approaches proposed within a common framework has an advantage, in that the only difference between the approaches being compared is the variable of interest. For the 4D CT planning scans of lung cancer patients, 4D IMRT treatment planning will be performed using the different treatment approaches, and the results will be compared and evaluated.

An optimization tool

The planned optimization tool to solve the optimization problems is SNOPT (Sparse Nonlinear OPTimizer) from Stanford Systems Optimization Lab [124, 125]. SNOPT is a general-purpose system to solve optimization problems involving many variables and constraints. It is suitable for *large-scale* linear and nonlinear programming and for linearly *constrained* optimization; and especially effective for nonlinear problems whose objective

and/or constraint functions and their gradients are expensive to evaluate. This is why SNOPT is chosen for a probable method to solve the 4D IMRT treatment-planning optimization problem, which deals with *constrained* MLC leaf sequences due to the MLC leaf velocity constraint and is a *large scale involving many variables* to handle the 4D problem.

SNOPT is implemented as a library of Fortran 77 subroutines. The Fortran source code can be converted to C code by a f2c translator [126]. The **snOptA** interface minimizes a linear or nonlinear objective function, $F_{obj}(x)$, subject to constant bounds, l and u, on both variables, x, and a number of sparse linear and/or nonlinear constraint functions, $F(x)$:

$$\begin{array}{ll} \underset{x}{\text{minimize}} & F_{obj}(x) \\ \text{subject to} & l_x \le x \le u_x \quad \text{and} \quad l_F \le F(x) \le u_F \end{array}.$$

Suppose $\{F_i(x)\}$ is a set of problem functions that includes both the objective and constraint functions. Ideally, the first derivatives (gradients) of all $F_i(x)$ are coded and provided by the user; but if not all gradients are known, **snOptA** estimates the missing ones by finite differences.

In general, $F_i(x)$ is a sum of linear and nonlinear functions, such that $F_i(x) = f_i(x) + \sum_{j=1}^{n} A_{ij}\, x_j$, where $f_i(x)$ is a nonlinear function and A_{ij} is a constant. Then,

`

the Jacobian of $F_i(x)$ is $F_i'(x) = f_i'(x) + A_{ij}$. Let $G_i(x) = f_i'(x)$ and $\{A_{ij}\}$ is a matrix with the elements of A_{ij}, i.e., G_i and $\{A_{ij}\}$ are two sparse matrices of the same size, then $F_i'(x) = G_i(x) + A_{ij}$. In a user-coded function, x, $\{F_i(x)\}$, and the nonzero elements of $\{A_{ij}\}$ and G_i (as many as possible) should be provided to **snOptA**.

To solve the nonlinear problems, a sparse sequential quadratic programming (SQP) method [124, 127] is applied. The SQP algorithm basically involves major and minor iterations. The major iterations generate a sequence of iterations that satisfy the linear constraints and converge to a point satisfying the nonlinear constraints and the first-order conditions for optimality. At each of this iteration, the SQP algorithm obtains search directions towards the next iteration from a sequence of minor iterations, quadratic programming (QP) sub-problems. Each QP sub-problem minimizes a quadratic model of a certain Lagrangian function subject to a linearization of the constraints. An augmented Lagrangian merit function is reduced along each search direction to ensure convergence from any starting point. After a QP sub-problem is solved, new estimates of the nonlinear problem solution are computed using a line-search on the augmented Lagrangian merit function.

`

Optimization

For a general 4D IMRT treatment-planning optimization problem, the variables to be solved are H_i and $L(MU,\theta_i)$. For the treatment efficiency, beam should be on for the minimum of four adjacent respiratory phases during treatment, i.e., $\sum_i H_i \geq 4$. Due to mechanical constraints, MLC leaf motion is limited by the maximum leaf velocity, $v_{\max}$, i.e., $\frac{dL(MU,\theta_i)}{dt} \leq v_{\max}$ when $H_i = 1$, where t is time in second and $\frac{d(MU)}{dt}$ is the pre-planned dose rate.

To find H_i, whether the beam is on or not for each phase has to be decided. To decide if the beam is on for phase k, the f values from $D = \frac{\sum_{i=1}^{P} D_i}{P}$ and $D^k = \frac{\sum_{i=1}^{P} D_i - D_k}{P-1}$ (i.e., D^k is a deformable-summed dose except for phase k plan dose) are compared. If the f value from D is greater than the f value from D^k, then phase k is used for the treatment. To find $L(MU,\theta_i)$ with the variables of respiratory phases, beams, control points, and MLC leaves in Equation (1), SNOPT is used to minimize f.

An intensity map of an MLC-based IMRT treatment plan can be decomposed into a set of MLC-formed beam apertures. Thus, an IMRT treatment plan to be delivered using a DMLC technique is basically a series of MLC leaf positions, i.e., MLC leaf sequences as a function of MU. The MLC leaf sequence is recorded in a computer file, which is then used to control the MLC leaf motion to deliver the treatment plan. In the research system of Pinnacle, MLC leaf sequence files can be imported into a certain treatment plan; with all

other requirements for dose computation set, a dose for the treatment plan with imported MLC leaf sequences can be computed.

Therefore, the tool to solve 4D IMRT treatment-planning optimization problems is developed by integrating Pinnacle and SNOPT as in Figure 8-1. SNOPT performs the optimization to find the two variables, L and H, and passes those to Pinnacle after each iteration; in Pinnacle, on the basis of L and H passed from SNOPT, the doses for individual phase plans are computed and summed to yield a deformable dose-summed 4D plan; then, Pinnacle passes the information on dose-volume evaluation metrics and plan quality (*e.g.*, COVs) of individual phase plans and a deformable dose-summed 4D plan to SNOPT; with the information passed from Pinnacle, SNOPT decides to continue the optimization or not.

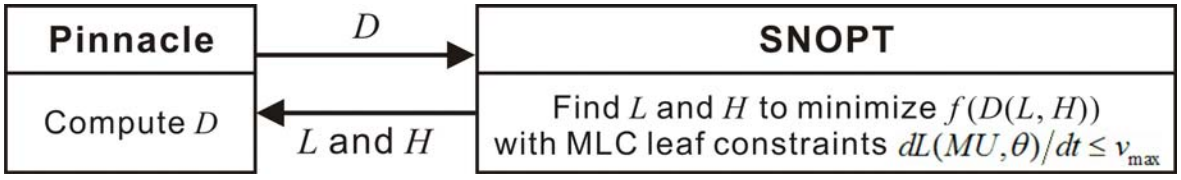

Figure 8-1. Integration of Pinnacle and SNOPT for a 4D IMRT treatment-planning optimization.

For initialization of the optimization, the MLC leaf sequences, $L(MU,\theta_i)$, from the deliverable IMRT treatment plans (presented in Chapter 4) are used; and H_i is set to 1 for all respiratory phases, so that beam is always on. The maximum field size is defined on

the basis of both tumor size and tumor motion extent quantified from the 4D CT planning scan for each patient. Then the openings of the carriages and the jaws are decided, which limit the number of leaves to be used and the possible motion ranges of those leaves during the optimization. The jaw positions are adjusted to cover the PTVs in all respiratory phases of the 4D CT planning scan with 1-cm margin added for penumbra.

8.2. Future outlook

The longer term goal of this work is the conjecture on the need for clinical studies to assess the clinical benefit of the 4D IMRT treatment-planning method with DMLC tracking for the radiotherapy treatment of thoracic and abdominal tumors. The framework can be further extended for online adaptive 4D radiotherapy planning, and potentially real-time adaptation.

`

REFERENCES

1. Langen, K. M.; Jones, D. T. L., Organ motion and its management. *Int J Radiat Oncol Biol Phys* **2001,** 50, 265-78.
2. Webb, S., Motion effects in (intensity modulated) radiation therapy: a review. *Phys Med Biol* **2006,** 51, R403-25.
3. Keall, P. J.; Chen, G. T. Y.; Joshi, S.; Mackie, T. R.; Stevens, C. W., Time-the fourth dimension in radiotherapy (ASTRO Panel discussion). *Int J Radiat Oncol Biol Phys* **2003,** 57, S8-9.
4. Keall, P. J.; Mageras, G. S.; Balter, J. M.; Emery, R. S.; Forster, K. M.; Jiang, S. B.; Kapatoes, J. M.; Low, D. A.; Murphy, M. J.; Murray, B. R.; Ramsey, C. R.; van Herk, M. B.; Vedam, S. S.; Wong, J. W.; Yorke, E., The management of respiratory motion in radiation oncology report of AAPM Task Group 76. *Med Phys* **2006,** 33, 3874-900.
5. Ozhasoglu, C.; Murphy, M. J., Issues in respiratory motion compensation during external-beam radiotherapy. *Int J Radiat Oncol Biol Phys* **2002,** 52, 1389-99.
6. Keall, P. J.; Starkschall, G.; Shukla, H.; Forster, K. M.; Ortiz, V.; Stevens, C. W.; Vedam, S. S.; George, R.; Guerrero, T.; Mohan, R., Acquiring 4D thoracic CT scans using a multislice helical method. *Phys Med Biol* **2004,** 49, 2053-67.
7. Vedam, S. S.; Keall, P. J.; Kini, V. R.; Mostafavi, H.; Shukla, H. P.; Mohan, R., Acquiring a four-dimensional computed tomography dataset using an external respiratory signal. *Phys Med Biol* **2003,** 48, 45-62.
8. McClelland, J. R.; Webb, S.; McQuaid, D.; Binnie, D. M.; Hawkes, D. J., Tracking 'differential organ motion' with a 'breathing' multileaf collimator: magnitude of problem assessed using 4D CT data and a motion-compensation strategy. *Phys Med Biol* **2007,** 52, 4805-26.
9. McMahon, R.; Berbeco, R.; Nishioka, S.; Ishikawa, M.; Papiez, L., A real-time dynamic-MLC control algorithm for delivering IMRT to targets undergoing 2D rigid motion in the beam's eye view. *Med Phys* **2008,** 35, 3876-88.

`

10. McMahon, R.; Papiez, L.; Rangaraj, D., Dynamic-MLC leaf control utilizing on-flight intensity calculations: A robust method for real-time IMRT delivery over moving rigid targets. *Med Phys* **2007,** 34, 3211-23.
11. McQuaid, D.; Webb, S., IMRT delivery to a moving target by dynamic MLC tracking: delivery for targets moving in two dimensions in the beam's eye view. *Phys Med Biol* **2006,** 51, 4819-39.
12. Neicu, T.; Berbeco, R.; Wolfgang, J.; Jiang, S. B., Synchronized moving aperture radiation therapy (SMART): improvement of breathing pattern reproducibility using respiratory coaching. *Phys Med Biol* **2006,** 51, 617-36.
13. Neicu, T.; Shirato, H.; Seppenwoolde, Y.; Jiang, S. B., Synchronized moving aperture radiation therapy (SMART): average tumour trajectory for lung patients. *Phys Med Biol* **2003,** 48, 587-98.
14. Papiez, L., DMLC leaf-pair optimal control of IMRT delivery for a moving rigid target. *Med Phys* **2004,** 31, 2742-54.
15. Papiez, L., The leaf sweep algorithm for an immobile and moving target as an optimal control problem in radiotherapy delivery. *Mathematical and Computer Modelling* **2003,** 37, 735-45.
16. Papiez, L.; McMahon, R.; Timmerman, R., 4D DMLC leaf sequencing to minimize organ at risk dose in moving anatomy. *Med Phys* **2007,** 34, 4952-6.
17. Papiez, L.; Rangaraj, D., DMLC leaf-pair optimal control for mobile, deforming target. *Med Phys* **2005,** 32, 275-85.
18. Papiez, L.; Rangaraj, D.; Keall, P. J., Real-time DMLC IMRT delivery for mobile and deforming targets. *Med Phys* **2005,** 32, 3037-48.
19. Rangaraj, D.; Palaniswaamy, G.; Papiez, L., DMLC IMRT delivery to targets moving in 2D in beam's eye view. *Med Phys* **2008,** 35, 3765-78.
20. Rangaraj, D.; Papiez, L., Synchronized delivery of DMLC intensity modulated radiation therapy for stationary and moving targets. *Med Phys* **2005,** 32, 1802-17.
21. Sawant, A.; Venkat, R.; Srivastava, V.; Carlson, D.; Povzner, S.; Cattell, H.; Keall, P., Management of three-dimensional intrafraction motion through real-time DMLC tracking. *Med Phys* **2008,** 35, 2050-61.
22. Suh, Y.; Yi, B.; Ahn, S.; Kim, J.; Lee, S.; Shin, S.; Shin, S.; Choi, E., Aperture maneuver with compelled breath (AMC) for moving tumors: a feasibility study with a moving phantom. *Med Phys* **2004,** 31, 760-6.
23. Purdy, J., 3D treatment planning and intensity-modulated radiation therapy. *Oncology* **1999,** 13, 10 Suppl. 5: 155-68.
24. Teh, B.; Woo, S.; Butler, E., Intensity modulated radiation therapy (IMRT): a new promising technology in radiation oncology. *The Oncologist* **1999,** 4, 433-42.
25. Bortfeld, T., IMRT: a review and preview. *Phys Med Biol* **2006,** 51, R363-79.
26. Ezzell, G. A.; Galvin, J. M.; Low, D.; Palta, J. R.; Rosen, I.; Sharpe, M. B.; Xia, P.; Xiao, Y.; Xing, L.; Yu, C. X., Guidance document on delivery, treatment planning, and clinical implementation of IMRT: Report of the IMRT subcommittee of the AAPM radiation therapy committee. *Med Phys* **2003,** 30, 2089-115.

27. Webb, S., IMRT delivery techniques. In *Image-guided IMRT*, Bortfeld, T.; Schmidt-Ullrich, R. K.; DeNeve, W., Eds. Springer-Verlag: Heidelberg, 2006; pp 73-90.
28. Tubiana, M.; Eschwege, F., Conformal radiotherapy and intensity-modulated radiotherapy. *Acta Oncol* **2000,** 39, 555-67.
29. Otto, K., Volumetric modulated arc therapy: IMRT in a single gantry arc. *Med Phys* **2008,** 35, 310-7.
30. Ahn, S.; Yi, B.; Suh, Y.; Kim, J.; Lee, S.; Shin, S.; Shin, S.; Choi, E., A feasibility study on the prediction of tumour location in the lung from skin motion. *Br J Radiol* **2004,** 77, 588-96.
31. Suh, Y.; Dieterich, S.; Cho, B.; Keall, P. J., An analysis of thoracic and abdominal tumour motion for stereotactic body radiotherapy patients. *Phys Med Biol* **2008,** 53, 3623-40.
32. Chen, Q.-S.; Weinhous, M. S.; Deibel, F. C.; Ciezki, J. P.; Macklis, R. M., Fluoroscopic study of tumor motion due to breathing: Facilitating precise radiation therapy for lung cancer patients. *Med Phys* **2001,** 28, 1850-6.
33. Ekberg, L.; Holmberg, O.; Wittgren, L.; Bjelkengren, G.; Landberg, T., What margins should be added to the clinical target volume in radiotherapy treatment planning for lung cancer? *Radiother Oncol* **1998,** 48, 71-7.
34. Erridge, S. C.; Seppenwoolde, Y.; Muller, S. H.; Van Herk, M.; Jaeger, K. D.; Belderbos, J. S.; Boersma, L. J.; Lebesque, J. V., Portal imaging to assess set-up errors, tumor motion and tumor shrinkage during conformal radiotherapy of non-small cell lung cancer. *Radiother Oncol* **2003,** 66, 75-85.
35. Koste, R. d.; Lagerwaard, F. J.; Boer, H. C. d.; Nijssen-Visser, M. R.; Senan, S., Are multiple CT scans required for planning curative radiotherapy in lung tumors of the lower lobe? *Int J Radiat Oncol Biol Phys* **2003,** 55, 1394-9.
36. Lagerwaard, F. J.; Koste, J. R. V. S. d.; Nijssen-Visser, M. R.; Schuchhard-Schipper, R. H.; Oei, S. S.; Munne, A.; Senan, S., Multiple "slow" CT scans for incorporating lung tumor mobility in radiotherapy planning. *Int J Radiat Oncol Biol Phys* **2001,** 51, 932-7.
37. Negoro, Y.; Nagata, Y.; Aoki, T.; Mizowaki, T.; Araki, N.; Takayama, K.; Kokubo, M.; Yano, S.; Koga, S.; Sasai, K.; Shibamoto, Y.; Hiraoka, M., The effectiveness of an immobilization device in conformal radiotherapy for lung tumor: Reduction of respiratory tumor movement and evaluation of the daily setup accuracy. *Int J Radiat Oncol Biol Phys* **2001,** 50, 889-98.
38. Ko, Y.; Suh, Y.; Ahn, S.; Lee, S.; Kim, S. S. J.; Choi, E.; Yi, B., Immobilization effect of air-injected blanket (AIB) for abdomen fixation. *Med Phys* **2005,** 32, 3363-6.
39. Dawson, L. A.; Brock, K. K.; Kazanjian, S.; Fitch, D.; McGinn, C. J.; Lawrence, T. S.; Haken, R. K. T.; Balter, J., The reproducibility of organ position using active breathing control (ABC) during liver radiotherapy. *Int J Radiat Oncol Biol Phys* **2001,** 51, 1410-21.

40. Wong, J. W.; Sharpe, M. B.; Jaffray, D. A.; Kini, V. R.; Robertson, J. M.; Stromberg, J. S.; Martinez, A. A., The use of active breathing control (ABC) to reduce margin for breathing motion. *Int J Radiat Oncol Biol Phys* **1999,** 44, 911-9.
41. Rosenzweig, K. E.; Hanley, J.; Mah, D.; Mageras, G.; Hunt, M.; Toner, S.; Burman, C.; Ling, C. C.; Mychalczak, B.; Fuks, Z.; Leibel, S. A., The deep inspiration breath-hold technique in the treatment of inoperable non small-cell lung cancer. *Int J Radiat Oncol Biol Phys* **2000,** 48, 81-7.
42. Mah, D.; Hanley, J.; Rosenzweig, K. E.; Yorke, E.; Braban, L.; Ling, C. C.; Leibel, S. A.; Mageras, G., Technical aspects of the deep inspiration breath-hold technique in the treatment of thoracic cancer. *Int J Radiat Oncol Biol Phys* **2000,** 48, 1175-85.
43. Kim, D. J.; Murray, B. R.; Halperin, R.; Roa, W. H., Held-breath self-gating technique for radiotherapy of non-small-cell lung cancer: A feasibility study. *Int J Radiat Oncol Biol Phys* **2001,** 49, 43-9.
44. Giraud, P.; Reboul, F.; Clippe, S.; Garcia, R.; Carrie, C.; Campana, F.; Dubray, B.; Rosenwald, J. C.; Cosset, J. M., Respiration-gated radiotherapy: current techniques and potential benefits. *Cancer Radiother* **2003,** 7, Suppl 1: 15s-25s.
45. Hugo, G. D.; Agazaryan, N.; Solberg, T. D., The effects of tumor motion on planning and delivery of respiratory-gated IMRT. *Med Phys* **2003,** 30, 1052-66.
46. Kubo, H. D.; Wang, L., Introduction of audio gating to further reduce organ motion in breathing synchronized radiotherapy. *Med Phys* **2002,** 29, 345-50.
47. Vedam, S. S.; Keall, P. J.; Kini, V. R.; Mohan, R., Determining parameters for respiration-gated radiotherapy. *Med Phys* **2001,** 28, 2139-46.
48. Keall, P. J.; Kini, V. R.; Vedam, S. S.; Mohan, R., Motion adaptive x-ray therapy: a feasibility study. *Phys Med Biol* **2001,** 46, 1-10.
49. Yu, C. X.; Jaffray, D. A.; Wong, J. W., The effects of intra-fraction organ motion on the delivery of dynamic intensity modulation. *Phys Med Biol* **1998,** 43, 91-104.
50. Adler, J. R.; Chang, S. D.; Murphy, M. J.; Doty, J.; Geis, P.; Hancock, S. L., The Cyberknife: a frameless robotic system for radiosurgery. *Stereotact Funct Neurosurg* **1997,** 69, 124-8.
51. Dieterich, S., Dynamic tracking of moving tumors in stereotactic radiosurgery. In *Robotic radiosurgery*, Mould, R. F.; Schulz, R. A.; Bucholz, R. D.; Gagnon, G. J.; Gerszten, P. C.; Kresl, J. J.; Levendag, P. C.; Schulz, R. A., Eds. The Cyberknife Society Press: Sunnyvale, 2005; Vol. 1, pp 51-63.
52. Schweikard, A.; Glosser, G.; Bodduluri, M.; Martin, J. M.; Adler, J. R., Robotic motion compensation for respiratory movement during radiosurgery. *Computer Aided Surgery* **2000,** 5, 263-77.
53. Schweikard, A.; Schiomi, H.; Adler, J., Respiration tracking in radiosurgery. *Med Phys* **2004,** 31, 2738-41.
54. Wong, K. H.; Dieterich, S.; Tang, J.; Cleary, K., Quantitative measurement of Cyberknife robotic arm steering. *Technology in Cancer Research and Treatment* **2007,** 6, 1-6.
55. Murphy, M. J., Tracking moving organs in real time. *Semin Radiat Oncol* **2004,** 14, 91-100.

56. Dieterich, S.; Suh, Y., Tumor motion ranges due to respiration and respiratory motion characteristics. In *Robotic radiosurgery: Treating tumors that move with respiration*, Urschel, H. C.; Kresl, J. J.; Luketich, J. D.; Papiez, L.; Timmerman, R. D.; Schulz, R. A., Eds. Springer: Heidelberg, 2007; pp 3-13.
57. D'Souza, W. D.; Naqvi, S. A.; Yu, C. X., Real-time intra-fraction motion tracking using the treatment couch: A feasibility study. *Phys Med Biol* **2005,** 50, 4021-33.
58. George, R.; Chung, T. D.; Vedam, S. S.; Ramakrishnan, V.; Mohan, R.; Weiss, E.; Keall, P. J., Audio-visual biofeedback for respiratory-gated radiotherapy: impact of audio instruction and audio-visual biofeedback on respiratory-gated radiotherapy. *Int J Radiat Oncol Biol Phys* **2006,** 65, 924-33.
59. Kini, V. R.; Vedam, S. S.; Keall, P. J.; Patil, S.; Chen, C.; Mohan, R., Patient training in respiratory-gated radiotherapy. *Med Dosim* **2003,** 28, 7-11.
60. Lim, S.; Park, S.; Ahn, S.; Suh, Y.; Shin, S.; Lee, S.; Kim, J.; Choi, E.; Yi, B.; Kwon, S.; Kim, S.; Jeung, T., Guiding curve based on the normal breathing as monitored by thermocouple for regular breathing. *Med Phys* **2007,** 34, 4514-8.
61. Venkat, R. B.; Sawant, A.; Suh, Y.; George, R.; Keall, P. J., Development and preliminary evaluation of a prototype audiovisual biofeedback device incorporating a patient-specific guiding waveform. *Phys Med Biol* **2008,** 53, N197-208.
62. Jemal, A.; Siegel, R.; Ward, E.; Hao, Y.; Xu, J.; Murray, T.; Thun, M. J., Cancer statistics. *CA Cancer J Clin* **2008,** 58, 71-96.
63. Christensen, G.; Joshi, S.; Miller, M., Volumetric transformation of brain anatomy. *IEEE Trans Med Imaging* **1997,** 16, 864-77.
64. Foskey, M.; Davis, B.; Goyal, L.; Chang, S.; Chaney, E.; Strehl, N.; Tomei, S.; Rosenman, J.; Joshi, S., Large deformation three-dimensional image registration in image-guided radiation therapy. *Phys Med Biol* **2005,** 50, 5869-92.
65. Keall, P. J.; Siebers, J. V.; Joshi, S.; Mohan, R., Monte Carlo as a four-dimensional radiotherapy treatment-planning tool to account for respiratory motion. *Phys Med Biol* **2004,** 49, 3639-48.
66. Zhang, T.; Jeraj, R.; Keller, H.; Lu, W.; Olivera, G. H.; McNutt, T. R.; Mackie, T. R.; Paliwal, B., Treatment plan optimization incorporating respiratory motion. *Med Phys* **2004,** 31, 1576-86.
67. Christensen, G.; Rabbitt, R.; Miller, M., 3D brain mapping using a deformable neuroanatomy. *Phys Med Biol* **1994,** 39, 609-18.
68. Joshi, S.; Pizer, S.; Fletcher, P.; Yushkevich, P.; Thall, A.; Marron, J., Multiscale deformable model segmentation and statistical shape analysis using medial descriptions. *IEEE Trans Med Imaging* **2002,** 21, 538-50.
69. McMahon, R.; Papiez, L.; Sandison, G., Addressing relative motion of tumors and normal tissue during dynamic MLC tracking delivery. *Australas Phys Eng Sci Med* **2007,** 30, 331-6.
70. Choi, N.; Doucette, J., Improved survival of patients with unresectable non-small-cell bronchogenic carcinoma by an innovated high-dose en-bloc radiotherapeutic approach. *Cancer* **1981,** 48, 101-9.

71. Martel, M.; Ten Haken, R.; Hazuka, M.; Kessler, M.; Strawderman, M.; Turrisi, A.; Lawrence, T.; Fraass, B.; Lichter, A., Estimation of tumor control probability model parameters from 3-D dose distributions of non-small cell lung cancer patients. *Lung Cancer* **1999,** 24, 31-7.
72. Vijayakumar, S.; Myrianthopoulos, L.; Rosenberg, I.; Halpern, H.; Low, N.; Chen, G., Optimization of radical radiotherapy with beam's eye view techniques for non-small cell lung cancer. *Int J Radiat Oncol Biol Phys* **1991,** 21, 779-88.
73. Graham, M.; Purdy, J.; Emami, B.; Harms, W.; Bosch, W.; Lockett, M.; Perez, C., Clinical dose-volume histogram analysis for pneumonitis after 3D treatment for non-small cell lung cancer (NSCLC). *Int J Radiat Oncol Biol Phys* **1999,** 45, 323-9.
74. Hayman, J.; Martel, M.; Ten Haken, R.; Normolle, D.; Todd, R. r.; Littles, J.; Sullivan, M.; Possert, P.; Turrisi, A.; Lichter, A., Dose escalation in non-small-cell lung cancer using three-dimensional conformal radiation therapy: update of a phase I trial. *J Clin Oncol* **2001,** 19, 127-36.
75. Kwa, S.; Lebesque, J.; Theuws, J.; Marks, L.; Munley, M.; Bentel, G.; Oetzel, D.; Spahn, U.; Graham, M.; Drzymala, R.; Purdy, J.; Lichter, A.; Martel, M.; Ten Haken, R., Radiation pneumonitis as a function of mean lung dose: an analysis of pooled data of 540 patients. *Int J Radiat Oncol Biol Phys* **1998,** 42, 1-9.
76. Yorke, E.; Jackson, A.; Rosenzweig, K.; Merrick, S.; Gabrys, D.; Venkatraman, E.; Burman, C.; Leibel, S.; Ling, C., Dose-volume factors contributing to the incidence of radiation pneumonitis in non-small-cell lung cancer patients treated with three-dimensional conformal radiation therapy. *Int J Radiat Oncol Biol Phys* **2002,** 54, 329-39.
77. Liu, H. H.; Wang, X.; Dong, L.; Wu, Q.; Liao, Z.; Stevens, C. W.; Guerrero, T. M.; Komaki, R.; Cox, J. D.; Mohan, R., Feasibility of sparing lung and other thoracic structures with intensity-modulated radiotherapy for non-small-cell lung cancer. *Int J Radiat Oncol Biol Phys* **2004,** 58, 1268-79.
78. Murshed, H.; Liu, H. H.; Liao, Z.; Barker, J. L.; Wang, X.; Tucker, S. L.; Chandra, A.; Guerrero, T.; Stevens, C.; Change, J. Y.; Jeter, M.; Cox, J. D.; Komaki, R.; Mohan, R., Dose and volume reduction for normal lung using intensity-modulated radiotherapy for advanced-stage non-small-cell lung cancer. *Int J Radiat Oncol Biol Phys* **2004,** 58, 1258-67.
79. Korreman, S. S.; Juhler-Nøttrup, T.; Boyer, A. L., Respiratory gated beam delivery cannot facilitate margin reduction, unless combined with respiratory correlated image guidance. *Radiother Oncol* **2008,** 86, 61-8.
80. Nishioka, S.; Nishioka, T.; Kawahara, M.; Tanaka, S.; Hiromura, T.; Tomita, K.; Shirato, H., Exhale fluctuation in respiratory-gated radiotherapy of the lung: a pitfall of respiratory gating shown in a synchronized internal/external marker recording study. *Radiother Oncol* **2008,** 86, 69-76.
81. Spirou, S. V.; Chui, C. S., Generation of arbitrary intensity profiles by dynamic jaws or multileaf collimators. *Med Phys* **1994,** 21, 1031-41.

`

82. Stein, J.; Bortfeld, T.; Dorschel, B.; Schlegel, W., Dynamic x-ray compensation for conformal radiotherapy by means of multileaf collimation. *Radiother Oncol* **1994,** 32, 163-73.
83. Svensson, R.; Kallman, P.; A, B., Analytical solution for the dynamic control of multileaf collimators. *Phys Med Biol* **1994,** 39, 37-61.
84. Bortfeld, T.; Jokivarsi, K.; Goitein, M.; Kung, J.; Jiang, S. B., Effects of intra-fraction motion on IMRT dose delivery: statistical analysis and simulation. *Phys Med Biol* **2002,** 47, 2203-20.
85. Chui, C.; Yorke, E.; Hong, L., The effects of intra-fraction organ motion on the delivery of intensity-modulated field with a multileaf collimator. *Med Phys* **2003,** 30, 1736-46.
86. Court, L. E.; Wagar, M.; Ionascu, D.; Berbeco, R.; Chin, L., Management of the interplay effect when using dynamic MLC sequences to treat moving targets. *Med Phys* **2008,** 35, 1926-31.
87. Duan, J.; Shen, S.; Fiveash, J.; Popple, R.; Brezovich, I., Dosimetric and radiobiological impact of dose fractionation on respiratory motion induced IMRT delivery errors: A volumetric dose measurement study. *Med Phys* **2006,** 33, 1380-7.
88. Jiang, S.; Pope, C.; Al Jarrah, K.; Kung, J.; Bortfeld, T.; Chen, G., An experimental investigation on intra-fractional organ motion effects in lung IMRT treatments. *Phys Med Biol* **2003,** 48, 1773-84.
89. Schaefer, M.; Münter, M.; Thilmann, C.; Sterzing, F.; Haering, P.; Combs, S.; Debus, J., Influence of intra-fractional breathing movement in step-and-shoot IMRT. *Phys Med Biol* **2004,** 49, N175–9.
90. Liu, Q.; McDermott, P.; Burmeister, J., Effect of respiratory motion on the delivery of breast radiotherapy using SMLC intensity modulation. *Med Phys* **2007,** 34, 347-51.
91. George, R.; Keall, P. J.; Kini, V. R.; Vedam, S. S.; Siebers, J. V.; Wu, Q.; Lauterbach, M. H.; Arthur, D. W.; Mohan, R., Quantifying the effect of intrafraction motion during breast IMRT planning and dose delivery. *Med Phys* **2003,** 30, 552-62.
92. Trofimov, A.; Rietzel, E.; Lu, H. M.; Martin, B.; Jiang, S.; Chen, G. T.; Bortfeld, T., Temporo-spatial IMRT optimization: concepts, implementation and initial results. *Phys Med Biol* **2005,** 50, 2779-98.
93. Webb, S., The effect on IMRT conformality of elastic tissue movement and a practical suggestion for movement compensation via the modified dynamic multileaf collimator (dMLC) technique. *Phys Med Biol* **2005,** 50, 1163-90.
94. Webb, S.; Binnie, D. M., A strategy to minimize errors from differential intrafraction organ motion using a single configuration for a 'breathing' multileaf collimator. *Phys Med Biol* **2006,** 51, 4517-31.
95. Schlaefer, A.; Fisseler, J.; Dieterich, S.; Shiomi, H.; Cleary, K.; Schweikard, A., Feasibility of four-dimensional conformal planning for robotic radiosurgery. *Med Phys* **2005,** 32, 3786-92.

96. Alasti, H.; Cho, Y. B.; Vandermeer, A. D.; Abbas, A.; Norrlinger, B.; Shubbar, S.; Bezjak, A., A novel four-dimensional radiotherapy method for lung cancer: imaging, treatment planning and delivery. *Phys Med Biol* **2006,** 51, 3251–67.
97. Tewatia, D.; Zhanga, T.; Tome, W.; Paliwal, B.; Metha, M., Clinical implementation of target tracking by breathing synchronized delivery. *Med Phys* **2006,** 33, 4330-6.
98. Guckenberger, M.; Wilbert, J.; Meyer, J.; Baier, K.; Richter, A.; Flentje, M., Is a single respiratory correlated 4D CT study sufficient for evaluation of breathing motion? *Int J Radiat Oncol Biol Phys* **2007,** 67, 1352-9.
99. Minn, A. Y.; Schellenberg, D.; Maxim, P.; Suh, Y.; McKenna, S.; Cox, B.; Dieterich, S.; Xing, L.; Graves, E.; Goodman, K. A.; Chang, D.; Koong, A. C., Pancreatic tumor motion on a single planning 4D-CT does not correlate with intrafraction tumor motion during treatment. *American Journal of Clinical Oncology* **2009,** 32.
100. Sonke, J.; Zijp, L.; Remeijer, P.; van Herk, M., Respiratory correlated cone beam CT. *Med Phys* **2005,** 32, 1176-86.
101. Li, T.; Schreibmann, E.; Yang, Y.; Xing, L., Motion correction for improved target localization with on-board cone-beam computed tomography. *Phys Med Biol* **2006,** 51, 253-67.
102. Li, T.; Xing, L.; Munro, P.; McGuinness, C.; Chao, M.; Yang, Y.; Loo, B.; Koong, A., Four-dimensional cone-beam computed tomography using an on-board imager. *Med Phys* **2006,** 33, 3825-33.
103. Remmert, G.; Biederer, J.; Lohberger, F.; Fabel, M.; Hartmann, G. H., Four-dimensional magnetic resonance imaging for the determination of tumour movement and its evaluation using a dynamic porcine lung phantom. *Phys Med Biol* **2007,** 52, N401-15.
104. von Siebenthal, M.; Székely, G.; Gamper, U.; Boesiger, P.; Lomax, A.; Cattin, P., 4D MR imaging of respiratory organ motion and its variability. *Phys Med Biol* **2007,** 52, 1547-64.
105. Wijesooriya, K.; Bartee, C.; Siebers, J. V.; Vedam, S. S.; Keall, P. J., Determination of maximum leaf velocity and acceleration of a dynamic multileaf collimator: implications for 4D radiotherapy. *Med Phys* **2005,** 32, 932-41.
106. George, R.; Vedam, S. S.; Chung, T. D.; Ramakrishnan, V.; Keall, P. J., The application of the sinusoidal model to lung cancer patient respiratory motion. *Med Phys* **2005,** 32, 2850-61.
107. Weiss, E.; Siebers, J. V.; Keall, P. J., An analysis of 6-MV versus 18-MV photon energy plans for intensity-modulated radiation therapy (IMRT) of lung cancer. *Radiother Oncol* **2007,** 82, 55-62.
108. Weiss, E.; Wijesooriya, K.; Dill, S. V.; Keall, P. J., Tumor and normal tissue motion in the thorax during respiration: Analysis of volumetric and positional variations using 4D CT. *Int J Radiat Oncol Biol Phys* **2007,** 67, 296-307.
109. Giraud, P.; Antoine, M.; Larrouy, A.; Milleron, B.; Callard, P.; De Rycke, Y.; Carette, M.; Rosenwald, J.; Cosset, J.; Housset, M.; Touboul, E., Evaluation of

microscopic tumor extension in non-small-cell lung cancer for three-dimensional conformal radiotherapy planning. *Int J Radiat Oncol Biol Phys* **2000,** 48, 1015-24.
110. Weiss, E.; Wijesooriya, K.; Ramakrishnan, V.; Keall, P. J., Comparison of intensity-modulated radiotherapy planning based on manual and automatically generated contours using deformable image registration in four-dimensional computed tomography of lung cancer patients. *Int J Radiat Oncol Biol Phys* **2008,** 70, 572-81.
111. Wijesooriya, K.; Weiss, E.; Dill, V.; Dong, L.; Mohan, R.; Joshi, S.; Keall, P. J., Quantifying the accuracy of automated structure segmentation in 4D CT images using a deformable image registration algorithm. *Med Phys* **2008,** 35, 1251-60.
112. Christensen, G.; Joshi, S.; Miller, M., Volumetric transformation of brain anatomy. *IEEE Trans Med Imaging* **1997,** 16, 864-77.
113. Foskey, M.; Davis, B.; Goyal, L.; Chang, S.; Chaney, E.; Strehl, N.; Tomei, S.; Rosenman, J.; Joshi, S., Large deformation three-dimensional image registration in image-guided radiation therapy. *Phys Med Biol* **2005,** 50, 5869-92.
114. Keall, P. J.; Siebers, J. V.; Joshi, S.; Mohan, R., Monte Carlo as a four-dimensional radiotherapy treatment-planning tool to account for respiratory motion. *Phys Med Biol* **2004,** 49, 3639-48.
115. Zhang, T.; Jeraj, R.; Keller, H.; Lu, W.; Olivera, G. H.; McNutt, T. R.; Mackie, T. R.; Paliwal, B., Treatment plan optimization incorporating respiratory motion. *Med Phys* **2004,** 31, 1576-86.
116. Suh, Y.; Weiss, E.; Zhong, H.; Fatyga, M.; Siebers, J.; PJ, K., A deliverable four-dimensional intensity-modulated radiation therapy-planning method for dynamic multileaf collimator tumor tracking delivery. *Int J Radiat Oncol Biol Phys* **2008,** 71, 1526-36.
117. Seppenwoolde, Y.; Shirato, H.; Kitamura, K.; Shimizu, S.; van Herk, M.; Lebesque, J. V.; Miyasaka, K., Precise and real-time measurement of 3D tumor motion in lung due to breathing and heartbeat, measured during radiotherapy. *Int J Radiat Oncol Biol Phys* **2002,** 53, 822-34.
118. Berbeco, R. I.; Jiang, S. B.; Sharp, G. C.; Chen, G. T. Y.; Mostafavi, H.; Shirato, H., Integrated radiotherapy imaging system (IRIS): design considerations of tumour tracking with linac gantry-mounted diagnostic x-ray systems with flat-panel detectors. *Phys Med Biol* **2004,** 49, 243-55.
119. Gilhuijs, K. G. A.; van de Ven, P. J. H.; van Herk, M., Automatic three-dimensional inspection of patient setup in radiation therapy using portal images, simulator images, and computed tomography data. *Med Phys* **1996,** 23, 389-99.
120. Nill, S.; Unkelbach, J.; Dietrich, L.; Oelfke, U., Online correction for respiratory motion: evaluation of two different imaging geometries. *Phys Med Biol* **2005,** 50, 4087-96.
121. Suh, Y.; Dieterich, S.; Keall, P. J., Geometric uncertainty of 2D projection imaging in monitoring 3D tumor motion. *Phys Med Biol* **2007,** 52, 3439-54.

122. George, R.; Suh, Y.; Murphy, M.; Williamson, J.; Weiss, E.; Keall, P. J., On the accuracy of a moving average algorithm for target tracking during radiation therapy treatment delivery. *Med Phys* **2008,** 35, 2356-65.
123. Stroom, J. C.; de Boer, H. C.; Huizenga, H.; Visser, A. G., Inclusion of geometrical uncertainties in radiotherapy treatment planning by means of coverage probability. *Int J Radiat Oncol Biol Phys* **1999,** 43, 905-19.
124. Gill, P. E.; Murray, W.; Saunders, M. A., SNOPT: An SQP algorithm for large-scale constrained optimization. *SIAM Review* **2005,** 47, 99-131.
125. Gill, P. E.; Murray, W.; Saunders, M. A., *User's guide for SNOPT Version 7: Softward for large-scale nonlinear programming*. 2006.
126. Feldman, S. I.; Gay, D. M.; Maimone, M. W.; Schryer, N. L. *A Fortran-to-C converter*; AT&T Bell Laboratories: Murray Hill, NJ, 1990.
127. Gill, P. E.; Murray, W.; Saunders, M. A., SNOPT: An SQP algorithm for large-scale constrained optimization. *SIAM J Optim* **2002,** 12, 979-1006.

VITA

Yelin Suh was born on September 7th, 1976 in Seoul, Korea. She received her Bachelor of Science in 1999 and Master of Science in 2005 in Physics from Ewha Womans University. She received her Doctor of Philosophy in Medical Physics from Virginia Commonwealth University in 2009.

List of Publications

Primary Authorship Publications

1. **Y. Suh**, A. Sawant, R. Venkat, and P. J. Keall, "4D IMRT treatment planning using a DMLC motion-tracking algorithm," *Phys Med Biol* (In press)

2. **Y. Suh**, E. Weiss, H. Zhong, M. Fatyga, J. V. Siebers, and P. J. Keall, "A deliverable four-dimensional intensity-modulated radiation therapy-planning method for dynamic multileaf collimator tumor tracking delivery," *Int J Radiat Oncol Biol Phys* 71:1526-36, 2008

3. **Y. Suh**, S. Dieterich, B. Cho, and P. J. Keall, "An analysis of thoracic and abdominal tumour motion for stereotactic body radiotherapy patients," *Phys Med Biol* 53:3623-40, 2008

4. **Y. Suh**, S. Dieterich, and P. J. Keall, "Geometric uncertainty of 2D projection imaging in monitoring 3D tumor motion," *Phys Med Biol* 52:3439-54, 2007

Secondary Authorship Publications

1. V. Srivastava, A. Sawant, **Y. Suh**, R. Venkat, and P. J. Keall, "Prediction of abdominal and thoracic tumor motion using a modified linear adaptive filter," *Phys Med Biol* (Under review)

2. A. Y. Minn, D. Schellenberg, P. Maxim, **Y. Suh**, S. McKenna, B. Cox, S. Dieterich, L. Xing, E. Graves, K. A. Goodman, D. Chang, and A. C. Koong, "Pancreatic tumor motion on a single planning 4D-CT does not correlate with intrafraction tumor motion during treatment," *American Journal of Clinical Oncology* 32, 2009

3. R. D. Wiersma, N. Riaz, S. Dieterich, **Y. Suh**, and L. Xing, "Use of MV and kV imager correlation for maintaining continuous real-time 3D internal marker tracking during beam interruptions," *Phys Med Biol* 54:91-105, 2009

4. R. George, **Y. Suh**, M. Murphy, J. Williamson, E. Weiss, and P. J. Keall, "On the accuracy of a moving average algorithm for target tracking during radiation therapy treatment delivery," *Med Phys* 35:2356-65, 2008

5. R. B. Venkat, A. Sawant, **Y. Suh**, R. George, and P. J. Keall, "Development and preliminary evaluation of a prototype audiovisual biofeedback device incorporating a patient-specific guiding waveform," *Phys Med Biol* 53:N197-208, 2008

6. B. Cho, **Y. Suh**, S. Dieterich, and P. J. Keall, "A monoscopic method for real-time tumour tracking using combined occasional x-ray imaging and continuous respiratory monitoring," *Phys Med Biol* 53:2837-55, 2008

7. S. Lim, S. Park, S. Ahn, **Y. Suh**, S. Shin, S. Lee, J. Kim, E. Choi, B. Yi, S. Kwon, S. Kim, and T. Jeung, "Guiding curve based on the normal breathing as monitored by thermocouple for regular breathing," *Med Phys* 34: 4514-8, 2007

Book Chapter

1. S. Dieterich and **Y. Suh**. 2007, Tumor motion ranges due to respiration and respiratory motion characteristics, in Robotic radiosurgery: Treating tumors that move with respiration, ed Harold C. Urschel, John J. Kresl, James D. Luketich *et al.* (Heidelberg: Springer), p. 3-13

`

APPENDICES

A AN ANALYSIS OF THORACIC AND ABDOMINAL TUMOR MOTION FOR STEREOTACTIC BODY RADIOTHERAPY PATIENTS

B A DELIVERABLE FOUR-DIMENSIONAL INTENSITY-MODULATED RADIATION THERAPY-PLANNING METHOD FOR DYNAMIC MULTILEAF COLLIMATOR TUMOR-TRACKING DELIVERY

C FOUR-DIMENSIONAL IMRT TREATMENT PLANNING USING A DMLC MOTION-TRACKING ALGORITHM

D GEOMETRIC UNCERTAINTY OF 2D PROJECTION IMAGING IN MONITORING 3D TUMOR MOTION

E ON THE ACCURACY OF A MOVING AVERAGE ALGORITHM FOR TARGET TRACKING DURING RADIATION THERAPY TREATMENT DELIVERY

Appendix A

AN ANALYSIS OF THORACIC AND ABDOMINAL TUMOR MOTION FOR STEREOTACTIC BODY RADIOTHERAPY PATIENTS

Yelin Suh

Sonja Dieterich

Byung Chul Cho

Paul J. Keall

Physics in Medicine and Biology 53(13), 2008

IOP PUBLISHING PHYSICS IN MEDICINE AND BIOLOGY

Phys. Med. Biol. **53** (2008) 3623–3640 doi:10.1088/0031-9155/53/13/016

An analysis of thoracic and abdominal tumour motion for stereotactic body radiotherapy patients

Yelin Suh[1,2], Sonja Dieterich[2,3], Byungchul Cho[2] and Paul J Keall[1,2]

[1] Department of Radiation Oncology, Virginia Commonwealth University, Richmond, VA, USA
[2] Department of Radiation Oncology, Stanford University, 875 Blake Wilbur Drive, Stanford, CA 94305-5847, USA
[3] Department of Radiation Medicine, Georgetown University Hospital, Washington, DC, USA

E-mail: ysuh@stanford.edu

Received 26 December 2007, in final form 4 April 2008
Published 17 June 2008
Online at stacks.iop.org/PMB/53/3623

Abstract

An analysis of thoracic and abdominal tumour motion for stereotactic body radiotherapy patients was performed using more than 70 h of tumour motion estimated from the correlation between the external and internal motion for 143 treatment fractions in 42 patients. The tumour sites included lungs (30 patients) and retroperitoneum (12 patients). The overall mean respiratory-induced peak-to-trough distance was 0.48 cm, with individual treatment fraction means ranging from 0.02 to 1.44 cm. The overall mean respiratory period was 3.8 s, with individual treatment fraction means ranging from 2.2 to 6.4 s. In 57 treatment fractions (40%), the mean respiratory-induced peak-to-trough distance was greater than 0.5 cm. In general, tumour motion was predominantly superior–inferior (60% of all the treatment fractions), while anterior–posterior and left–right motion were 22% and 18%, respectively. The motion was predominantly linear, and the overall mean of the first principal component was 94%. However, for motion magnitude, direction and linearity, large variations were observed from patient to patient, fraction to fraction and cycle to cycle.

(Some figures in this article are in colour only in the electronic version)

1. Introduction

During the course of radiotherapy, patient motion results in anatomic changes that complicate targeted treatment of tumours. Among possible sources of motion, respiration is a significant factor causing uncertainty during imaging, planning and delivery of radiotherapy, particularly for thoracic and abdominal tumours. Several techniques have been developed to manage respiratory tumour motion, such as motion encompassing, breath holding, respiratory gating and tumour tracking (Keall *et al* 2006). Respiratory gating and tumour tracking are relatively

new and more promising techniques with the advent of image-guided radiotherapy. Given that the success of these techniques depends on precisely localizing the tumour, an accurate characterization of tumour motion is important during imaging and delivery of radiotherapy.

Many studies show that respiratory tumour motion can be up to 2–3 cm, and it varies with intra- and inter-fractional motion. Both the AAPM Task Group 76 report (Keall *et al* 2006) and a study by Langen and Jones (2001) summarize tumour motion data in the literature. Although the extent and degree of wide variations in motion were acknowledged in these reports, no consensus was apparent regarding respiratory tumour motion management.

Tumour motion data for a large population of patients over a long period of time have not yet been published. In this study, the tumour motion data estimated from the correlation between the external and internal motion for 143 treatment fractions in 42 patients over time periods corresponding to stereotactic body radiotherapy were used. The aim of this work was to analyse thoracic and abdominal tumour motion for a large patient population over an extended period of time.

2. Materials and methods

This study was divided into three main tasks. First, a database of patient tumour motion was created from input tracking system motion data; second, the tumour motion data were separated into individual respiratory cycles; third, patient respiratory tumour motion was analysed.

2.1. Creation of a database of patient tumour motion

2.1.1. Tracking system motion data. Tumour motion data from 143 treatment fractions for 42 thoracic and abdominal cancer patients treated with the Cyberknife Synchrony (G3 System with delivery software version 6.2.3, Accuray Incorporated, Sunnyvale, CA) in Georgetown University Hospital from July 2005 to January 2006 were used in this study. The tumour locations were lungs (30 patients) and retroperitoneum (12 patients) with one to seven treatment fractions for each patient. The use of the data for research purposes was approved by the Georgetown Institutional Review Board (IRB-2005-309). Synchrony is a subsystem of respiratory tumour tracking in the Cyberknife system (Adler *et al* 1997, Murphy *et al* 2000, Schweikard *et al* 2000, 2004, Murphy 2004, Dieterich 2005, Seppenwoolde *et al* 2007). In order to compensate for tumour motion, the tracking system estimates internal tumour positions by a correlation between the external patient motion and internal fiducial locations, as well as by a prediction algorithm. For the external patient motion, charge-coupled device (CCD) cameras are used to monitor the multiple light emitting diodes (LEDs) on the patient's chest and abdomen at 32 frames per second. For the internal fiducial locations, two orthogonal diagnostic x-ray systems monitor the implanted markers periodically (e.g., every 30 s or every two beams). The patient tumour motion data used in this study were derived from the correlation model and recorded at 25 Hz by the tracking system. The data contained patient four-dimensional (4D) tumour motion information (3D positions of the tumour versus time) with the format of $t{:}x\,y\,z$, where t is time in seconds and x, y and z are tumour positions estimated from the correlation model in millimetres (mm). The system accuracy is on the order of 0.5 mm with the uncertainty of 0.3 mm for an end-to-end test on a motion platform, which is the difference between the centre of the planned dose distribution and that of the delivered dose distribution measured by a film (Wong *et al* 2007). The technical tracking accuracy is much better (i.e. on the order of 0.6 mm), while fluctuations in the correlation model on the

timescale of minutes add much more uncertainty clinically. Typically, the correlation model is rebuilt if an error is 3 mm or more for two images in a row.

It is important to note that the tumour motion analysed in this study is not actual but estimated from the correlation model of the tracking system that is based on periodic stereoscopic x-ray images. The uncertainty of the tracking system motion data was assessed by estimation errors of the correlation model, which the Synchrony system recorded every time two orthogonal x-ray images were acquired and internal fiducial locations were measured. The vector error for each internal fiducial is quantified. The mean and standard deviation (SD) of 3D positional estimation root-mean-square (RMS) errors of the tracking system over 143 treatment fractions was 1.5 ± 0.8 mm. The estimation errors could be due to inaccuracy of the correlation models of the tracking system, or temporal variations in the internal/external correlation model between measurements (Murphy 2004, Korreman *et al* 2008, Nishioka *et al* 2008). The uncertainty obtained for the current data set (1.5 ± 0.8 mm) is consistent with the values published by Seppenwoolde *et al* (2007), who simulated the Synchrony method using respiratory and orthogonal fluoroscopic measured data in an eight-patient study. They concluded from their data that the systematic error of the position estimation was less than 1 mm for all patients and the mean 3D error was less than 2 mm for over 80% of the time.

2.1.2. Creation of a database. The tracking system motion data included portions with either no motion or significantly large motion, gaps or spikes that might be from sources other than tumour motion (explained in detail in section 2.1.3). These data were processed to extract the estimated tumour motion from the tracking system motion data and subsequently, the *longest single contiguous data set* was created according to the criteria for each of 143 treatment fractions. Aside from tumour motion, other possible sources of motion included the motion of a patient or a couch, fiducial mistracking or non-tracking, all of which led to stopping treatment and/or rebuilding or resetting the correlation model, and the learning time of the internal tumour position estimator.

2.1.3. Criteria to create a database. Each of the tracking system motion data was visually inspected to identify possible areas of exclusion and to select the longest single contiguous data set among the remaining data. The data exclusion criteria were as follows.

(1) Data points showing no motion, which may indicate that the treatment was stopped or the correlation was reset (figure 1(a)).
(2) Significantly large motion at the beginning of the tracking system motion data, which may reflect the learning time of the internal tumour position estimator (figure 1(b)).
(3) Large time intervals (more than 5 s) where no data were recorded, which may indicate that the treatment was stopped or paused, problems with the external imaging occurred or the system might be unable to track the fiducials (e.g., maybe something was in the way of the tracking beam) (figure 1(c)).
(4) Data points showing the large motion change in one direction only out of three directions because there possibly were large changes in couch motion, or fiducials were mistracked or not tracked (figure 2(a)). Note that data points showing the large motion changes in two directions simultaneously while maintaining the motion in the third direction were included (figure 2(b)).

2.2. Separation of individual respiratory cycles

The starting point in analysing the respiratory tumour motion data begins with breaking the data into individual respiratory cycles to obtain the information on motion, such as a

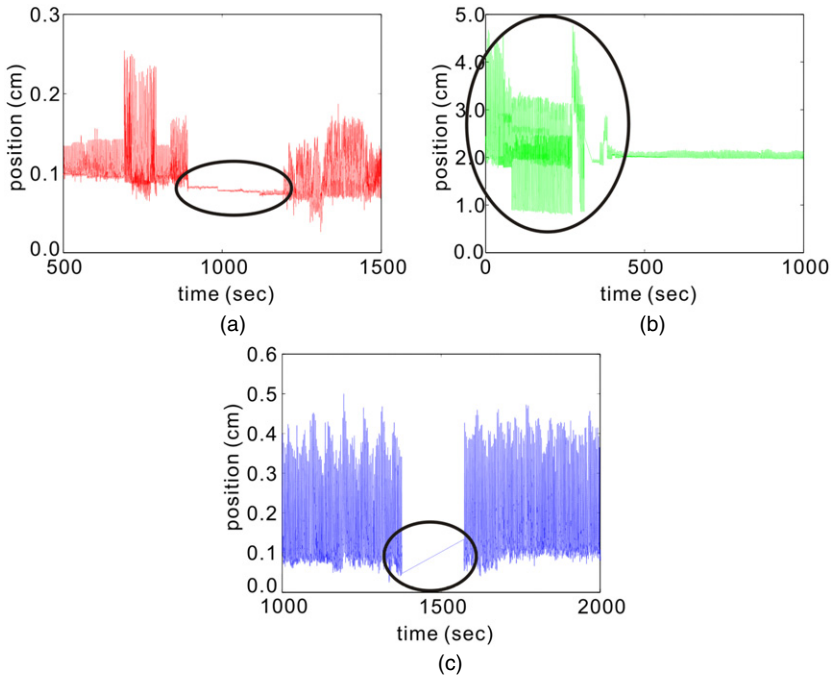

Figure 1. Examples of data exclusion criteria in a new data set: data points showing (a) no motion, (b) significantly large motion at the beginning of the tracking system motion data and (c) large time intervals where no data were recorded.

respiratory-induced peak-to-trough distance and period. First of all, the system noise was removed by filtering the tracking system motion data using the first-order Butterworth low-pass filter with a cut-off frequency of 2.5 Hz, assuming that anything greater than ten times average respiratory frequency (∼0.25 Hz) (Seppenwoolde *et al* 2002, George *et al* 2005) was noise or due to sources other than respiration. High-frequency noise was also evident in the data. To separate individual respiratory cycles, 3D tumour motion, $R = \sqrt{\mathrm{LR}^2 + \mathrm{AP}^2 + \mathrm{SI}^2}$, where LR was motion in the left–right (LR) direction, AP in the anterior–posterior (AP) direction and SI in the superior–inferior (SI) direction, was calculated. This approach is more reasonable than using either LR, AP or SI motion, since the correlation coefficients between any two of them are not always one. Before calculating R, a new coordinate system was determined in which the correlations between each two motion directions were positive and the minimum values of LR, AP and SI motion corresponded to zero. The motion data in each direction were then moved to a new coordinate system where inhalation corresponded to maximum R and exhalation to minimum R, and all motion was positive. Then, the respiratory-induced peak-to-trough distance and period were determined as follows.

(1) *Generating smoothed data and a moving average baseline from the filtered tracking system motion data.* In figure 3(a), the black solid curve is the filtered tracking system motion data versus time and the blue dashed curve is the smoothed data versus time. The smoothed data were created by smoothing the filtered tracking system data (recorded 25 times per second) with the moving average of 25 points that correspond to 1 s (∼minimum period of patient free breathing). This idea is from Seppenwoolde *et al* (2002) and Neicu *et al* (2003), where the raw data (recorded 30 times per second) were filtered with the 30-point median filter. The red dot-dashed curve is a moving average

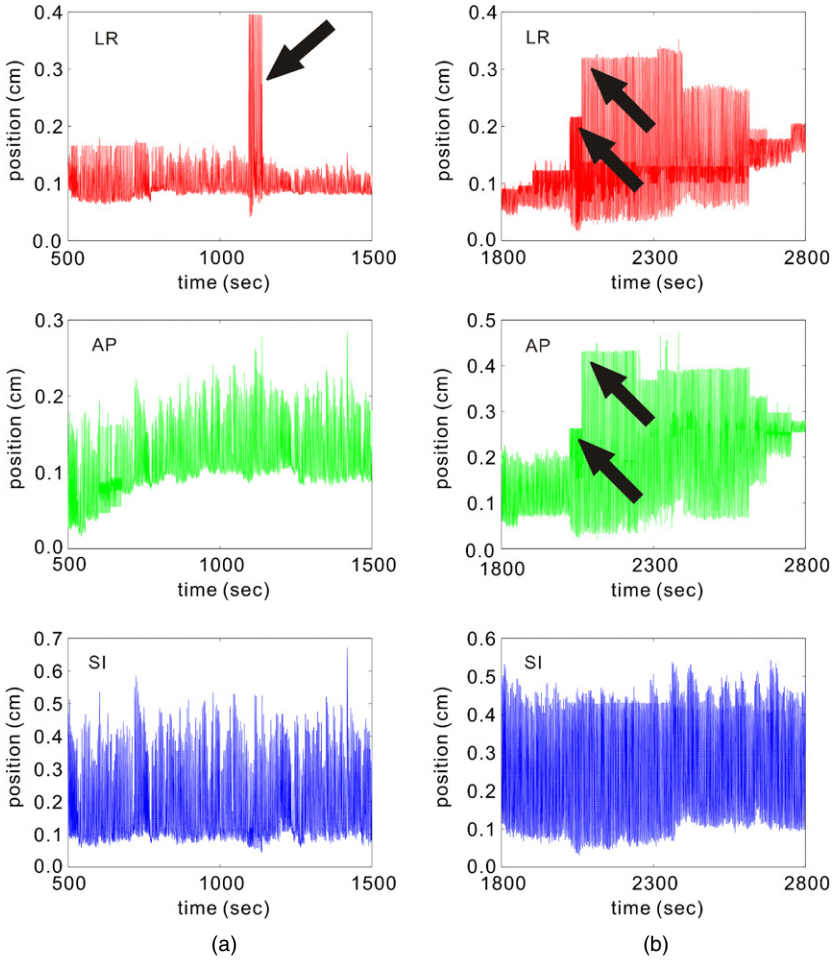

Figure 2. Examples of data exclusion and inclusion criteria in a new data set: data points showing (a) large motion change in one direction only (see an arrow) out of three directions were excluded, but (b) large motion changes in two directions simultaneously (see two arrows) while maintaining the motion in the third direction were included. Tumour motion in the same timescale is shown in the left–right (LR) (top), anterior–posterior (AP) (middle) and superior–inferior (SI) (bottom) directions.

baseline versus time (figure 3(a)), which was created by smoothing the filtered tracking system data with the moving average of 200 points that correspond to 8 s (∼double the mean period of patient free breathing) (Lu *et al* 2006).

(2) *Searching intersections between the two curves*. To find intersections of the smoothed data (blue dashed curve) and the moving average baseline (red dot-dashed curve), the differences between them were calculated. By using the signs of displacement differences, intersections of the blue dashed and red dot-dashed curves were found (circled in figure 3(b)).

(3) *Determining peaks and troughs between the intersections.* Once intersections were found, peaks (triangles) as maximum points and troughs (inverted triangles) as minimum points were determined between adjacent intersections (circles), as shown in figure 3(b). When searching peaks and troughs, only time intervals of more than 0.4 s from a peak to a trough

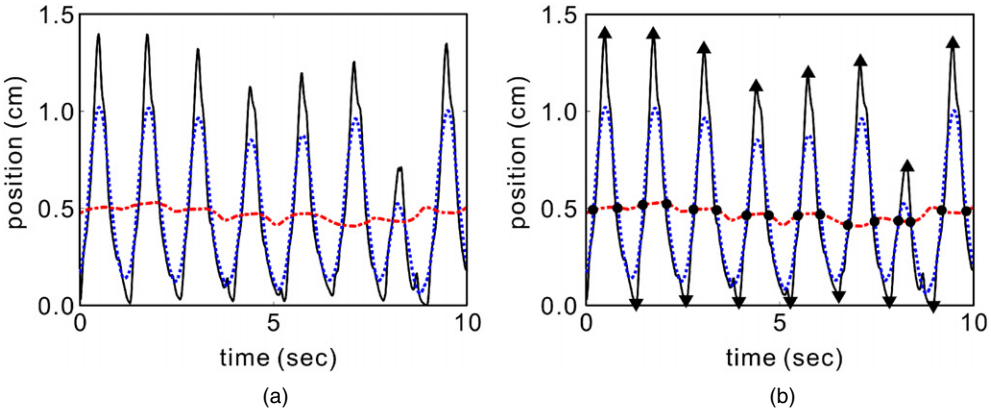

Figure 3. Separation of individual respiratory cycles: (a) the black solid curve represents the filtered tracking system motion data, the blue dashed curve represents the smoothed data and the red dot-dashed curve represents a moving average baseline; (b) the circles mark intersections between the blue dashed and red dot-dashed curves, and the triangles and inverted triangles represent peak and trough points, which are the maximum and minimum points between adjacent intersections, respectively.

or from a trough to a peak were accepted, assuming that the patient minimum breathing period was around 0.8 s. Otherwise, the peaks and troughs were ignored because they were considered not to be real peaks or troughs, but instead they were regarded as errors, such as small bumps or unremoved noise. This minimum breathing period is based on the patient population data from George *et al* (2005), who stated that the mean period for free breathing was 3.8 s and that the fifth percentile of the variations of this period was 2.13 s (i.e. twice the SD from the mean). Extrapolating 3 SD from the mean gave 0.8 s or 0.4 s for each of inhalation and exhalation. Varying this value from 0.4 s to either 0.3 or 0.5 s had little impact on the overall results, which indicated moderate insensitivity to the choice of parameter values. If more than one maximum or one minimum point existed between adjacent intersections (same y values, but different x values in the figure 3 plots), the time values were averaged to minimize the effect on calculating the respiratory period.

(4) *Calculating peak-to-trough distance and period.* The respiratory-induced peak-to-trough distance was calculated as the displacement difference between the consecutive peak and trough points and the respiratory period as the time difference from one peak to the next peak.

2.3. Analysis of respiratory motion data

Once separated into individual respiratory cycles, the patient tumour motion data were analysed to obtain useful information on respiratory tumour motion for large patient population data. The data analysed in this study were as follows: (1) respiratory-induced peak-to-trough distance, (2) respiratory period, (3) per cent contributions to 3D motion (R) from motion in the LR, AP and SI directions and (4) motion nonlinearity and hysteresis.

Tumour motion hysteresis occurs when a tumour follows different paths between inhale and exhale phases during a respiratory cycle (Seppenwoolde *et al* 2002, Manke *et al* 2003, Mageras *et al* 2004, Blackall *et al* 2006, Wolthaus *et al* 2006, Boldea *et al* 2007, Mori *et al* 2007). Nonlinearity and hysteresis of patient tumour motion were quantified using principal component analysis (PCA). The first principal component that PCA generates is a single axis

in space. When each data point is projected on that axis, the resulting values form a new variable, and the variance of this new variable is the maximum among all possible choices of the first axis (Jackson 1991, Wall *et al* 2003). The first principal component was expressed as a normalized percentage (ranging from 33% to 100%), where 100% indicated pure linear motion, and the lower the percentage, the more nonlinear motion and/or more hysteresis. For each of 143 treatment fractions, the first principal components of individual respiratory cycles were calculated.

3. Results

3.1. Creation of a database of patient tumour motion

Extracted motion data are the longest single contiguous data set selected for each of 143 treatment fractions. The mean duration time of the extracted data is 30 min, ranging from 5 to 86 min, and the total duration time is approximately 72 h. The mean ratio of duration time in the tracking system motion data and that in the extracted motion data is 0.42, and ranges from 0.07 to 0.99.

3.2. Separation of individual respiratory cycles

Figure 4 illustrates typical respiratory tumour motion, where the algorithm correctly determines peaks and troughs. By using the smoothed data and the moving average baseline, even very irregular respiratory tumour motion is correctly separated into individual cycles. The algorithm successfully separates the respiratory traces with significant fluctuations (figure 4(c)), considerable noise (figures 4(d) and (e)) or a large peak (figure 4(f)) into individual respiratory cycles. However, there are some cases where the algorithm fails to determine correct peaks or troughs, as shown in figure 5. When there are repeated very small peaks and troughs (figure 5(a)) or very fast respiratory cycles (figure 5(b)), the algorithm fails to separate the motion data into individual cycles correctly.

Using the intersections of the smoothed curves and the moving average baseline curves alone, 70 696 individual respiratory cycles are detected for all treatment fractions analysed. By enforcing the minimum 0.4 s peak-to-trough or trough-to-peak rule, 478 cycles are removed, leaving 70 218 cycles for further analyses. Included in the final respiratory cycles are three cycles with negative peak-to-trough distances, as well as 27 cycles with a trough-to-peak time of less than 0.4 s, despite shorter cycles being removed by the previous rule. These are explained by the design of an algorithm used to separate the tumour motion into individual cycles. The algorithm initializes from a peak and locates the following trough and peak. Only when the time intervals between the initial peak and trough and between the trough and the next peak are more than 0.4 s, the algorithm accepts *the initial peak and the trough as a pair.*

3.3. Analysis of respiratory motion data

The overall mean respiratory-induced peak-to-trough distance is 0.48 cm, with individual treatment fraction means ranging from 0.02 to 1.44 cm. The overall mean respiratory period is 3.8 s, with individual treatment fraction means ranging from 2.2 to 6.4 s. The mean of the individual treatment fraction SDs for the peak-to-trough distance and period is 0.15 cm (0.01–0.73) and 0.8 s (0.2–1.7), respectively. Detailed statistics are given in appendix A.

Tables 1 and 2 show the mean of individual treatment fraction means and SDs for the peak-to-trough distance and respiratory period for each of 30 lung and 12 retroperitoneal tumour patients, respectively. On average, the peak-to-trough distance is slightly larger for

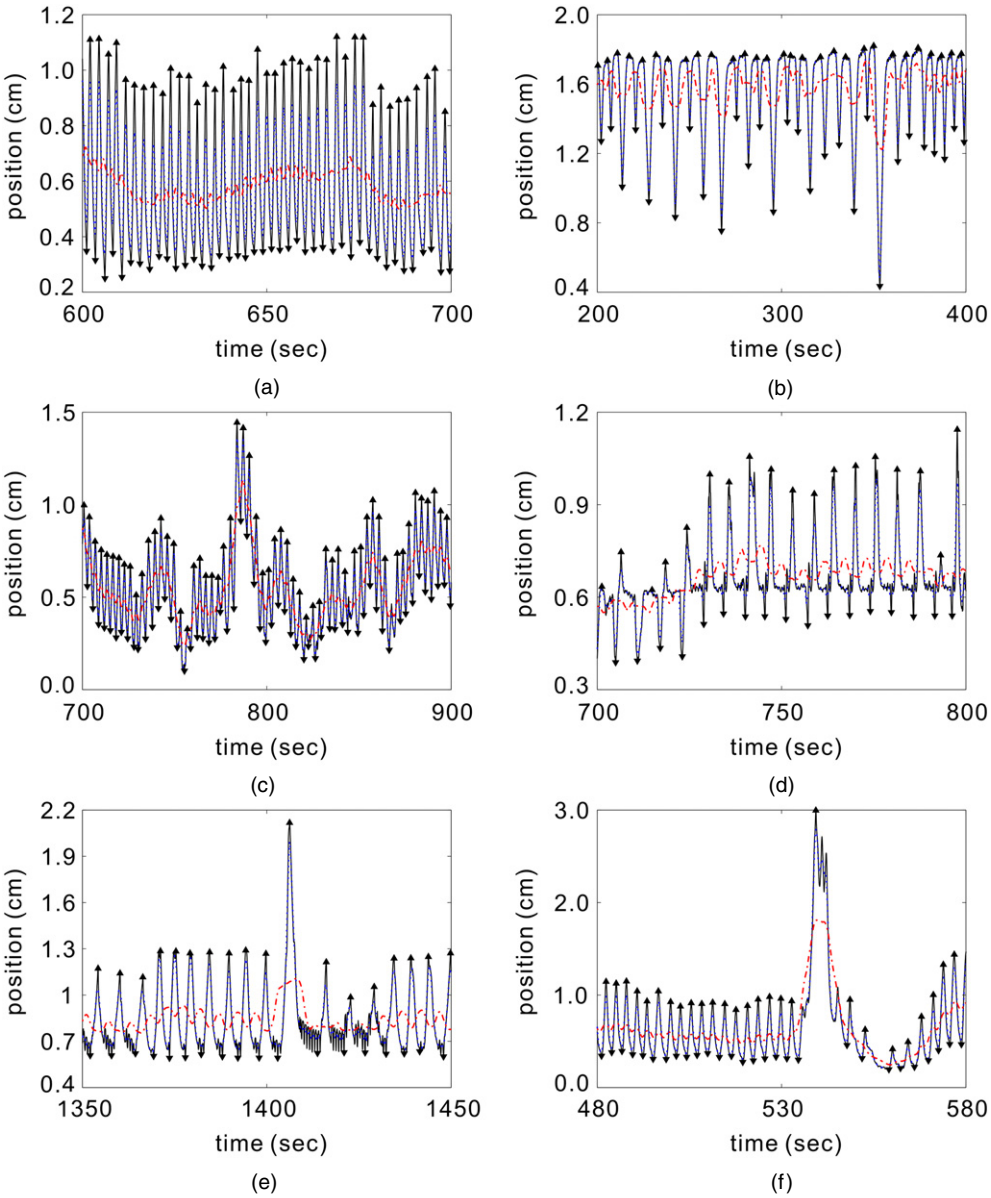

Figure 4. Examples of respiratory tumour motion where the algorithm correctly determines peaks and troughs and thus separates the motion data into individual cycles despite significant respiratory irregularity: typical respiratory tumour motion ((a) and (b)), irregular motion, which represents the respiratory traces with (c) significant fluctuations, (d) and (e) considerable noise and (f) a large peak. The black solid curve is the filtered tracking system motion data, the blue dashed curve is the smoothed data and the red dot-dashed curve is a moving average baseline. The triangles and inverted triangles are peak and trough points, respectively.

lung tumours, while the period is slightly longer for retroperitoneal tumours. However, the differences of the peak-to-trough distance and period between lung and retroperitoneal tumours are not significant; rather these vary from patient to patient, as shown in figures 6(a) and (b).

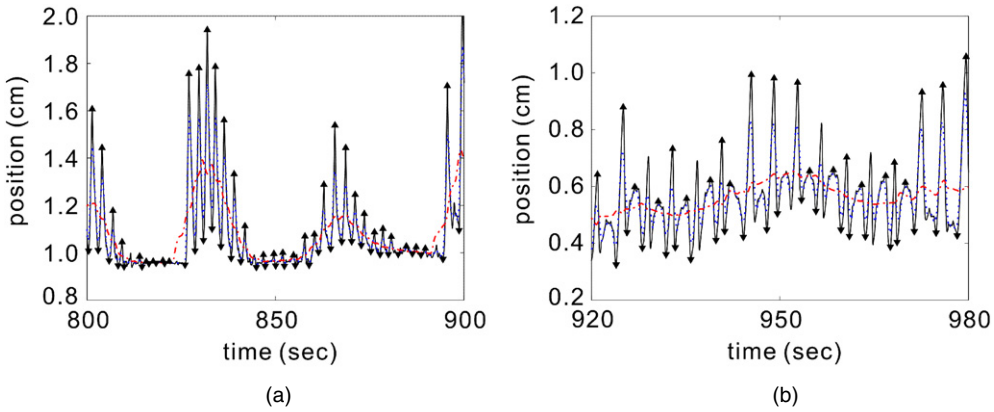

Figure 5. Examples of respiratory tumour motion where the algorithm fails to separate the motion data into individual cycles correctly: the respiratory traces with (a) repeated small peaks and troughs and (b) fast respiratory cycles. The black solid curve is the filtered tracking system motion data, the blue dashed curve is the smoothed data and the red dot-dashed curve is a moving average baseline. The triangles and inverted triangles are peak and trough points, respectively.

Table 3 shows patient tumour motion data sorted by motion extent. Out of 143 treatment fractions, 57 show the mean peak-to-trough distance to be greater than 0.5 cm (40%): 44 treatment fractions (42% of all lung tumour fractions) from 16 lung tumour patients and 13 fractions (34% of all retroperitoneal tumour fractions) from 7 retroperitoneal patients. The mean of individual fraction means for the peak-to-trough distance for lung and retroperitoneal tumours is 0.81 cm and 0.74 cm, respectively, for motion greater than 0.5 cm, and 0.28 cm and 0.27 cm, respectively, for motion less than/equal to 0.5 cm. The lung tumours are sorted to seven different tumour locations in the lungs, as shown in table 4. As expected, tumours in the lower lobes of the lungs show more motion than those in the upper lobes.

The respiratory period, however, does not show any trends dependent on motion extent or tumour sites. The longest mean period (6.1 s) occurs in a retroperitoneal tumour patient, whose three treatment fractions are the top three individual treatment fraction means for the respiratory period (6.4, 6.3 and 5.8 s) (table 2). The second and third longest mean periods are from lung tumour patients (5.2 and 5.1 s) (table 1). The details for tables 1–3 are given in appendices B and C.

Figure 6(c) shows the mean per cent contributions to 3D motion (R) from motion in the LR, AP and SI directions for each of 30 lung and 12 retroperitoneal tumour patients. Out of 143 treatment fractions, 26 fractions (18%) show the dominant RL motion, 32 fractions (22%) show the dominant AP motion and 85 fractions (60%) show the dominant SI motion. The per cent contributions do not show any trends dependent on motion extent or tumour sites. The RL motion is dominant in 16% of 105 lung tumour treatment fractions, the AP motion is in 27% and the SI motion is in 57%. For 38 retroperitoneal treatment fractions, the RL motion is dominant in 24% of the fractions, the AP motion is in 10% and the SI motion is in 66%. For all 143 treatment fractions, the individual treatment fraction means for per cent contributions from the LR, AP and SI motion range 3–73%, 8–84% and 5–77%, respectively. There are no noticeable differences between the lung and retroperitoneal tumours in terms of per cent contribution. The individual treatment fraction means for lung tumours range 3–73% in the LR motion, 8–67% in the AP motion and 5–77% in the SI motion, and those

Table 1. Tumour motion data for each of 30 lung tumour patients: the mean of individual treatment fraction means and standard deviations (SD) for the peak-to-trough distance and period. Note that patients 5 and 27 included more than one tumour sites.

Patient	Number of treatments	Peak-to-trough distance (cm) Mean ± SD	Period (s) Mean ± SD
Patient 1	3	0.71 ± 0.18	2.8 ± 0.6
Patient 3	4	0.29 ± 0.09	2.9 ± 0.4
Patient 5	3/7	0.37 ± 0.14	3.8 ± 0.6
	3/7	0.91 ± 0.20	3.5 ± 0.6
	1/7	0.43 ± 0.12	4.3 ± 0.8
Patient 6	2	0.55 ± 0.19	3.5 ± 0.7
Patient 8	3	0.18 ± 0.07	3.8 ± 0.9
Patient 9	3	0.45 ± 0.13	4.4 ± 0.8
Patient 10	3	0.45 ± 0.17	2.9 ± 0.8
Patient 11	3	0.65 ± 0.19	4.9 ± 1.0
Patient 12	3	0.22 ± 0.09	4.3 ± 0.7
Patient 13	3	0.32 ± 0.11	3.1 ± 0.7
Patient 14	5	0.27 ± 0.07	3.5 ± 0.5
Patient 15	3	1.24 ± 0.18	3.3 ± 0.5
Patient 19	3	1.07 ± 0.24	2.6 ± 0.3
Patient 20	3	0.08 ± 0.03	3.8 ± 0.9
Patient 21	3	0.81 ± 0.46	3.6 ± 1.2
Patient 22	3	0.39 ± 0.09	4.5 ± 0.9
Patient 23	3	0.37 ± 0.14	3.6 ± 1.0
Patient 25	3	0.84 ± 0.15	3.7 ± 0.5
Patient 26	3	0.50 ± 0.18	4.5 ± 0.8
Patient 27	4/5	0.87 ± 0.21	5.2 ± 1.1
	1/5	0.81 ± 0.23	5.1 ± 1.0
Patient 28	5	0.25 ± 0.07	3.8 ± 0.8
Patient 29	3	0.03 ± 0.01	3.8 ± 0.7
Patient 30	3	0.28 ± 0.11	2.6 ± 1.2
Patient 31	5	0.78 ± 0.22	3.9 ± 0.6
Patient 32	3	0.30 ± 0.11	3.7 ± 0.6
Patient 33	3	0.33 ± 0.07	3.6 ± 0.4
Patient 35	3	0.40 ± 0.15	3.1 ± 0.6
Patient 37	3	0.31 ± 0.18	4.0 ± 1.3
Patient 39	4	0.55 ± 0.35	2.9 ± 1.3
Patient 40	5	0.69 ± 0.25	3.5 ± 0.7
Total	105	0.50 ± 0.16	3.7 ± 0.8

for retroperitoneal tumours range 7–64% in the LR motion, 11–84% in the AP motion and 5–69% in the SI motion.

Figure 6(d) shows the mean and SD of the first principal component (normalized percentage) showing motion nonlinearity and hysteresis for each treatment fraction. The overall mean of the first principal component for all treatment fractions is 94%, with individual treatment fraction means ranging from 69% to 100%. The overall mean and range of the first principal component for lung and retroperitoneal tumours are 93% (69–100) and 98% (85–100), respectively. Only seven treatment fractions out of 143 (5%) have the means of the first principal component less than 80%, all of which are from four lung tumour patients. On the other hand, 89 treatment fractions (62%) have the means of the first principal component greater than 95%. These are from 56 treatment fractions (53% of all lung tumour

Table 2. Tumour motion data for each of 12 retroperitoneal tumour patients: the mean of individual treatment fraction means and standard deviations (SD) for the peak-to-trough distance and period.

Patient	Number of treatments	Peak-to-trough distance (cm) Mean ± SD	Period (s) Mean ± SD
Patient 2	3	0.65 ± 0.09	3.5 ± 0.3
Patient 4	6	0.38 ± 0.12	4.4 ± 0.9
Patient 7	5	0.19 ± 0.05	4.1 ± 0.5
Patient 16	3	0.91 ± 0.39	4.8 ± 1.3
Patient 17	1	0.63 ± 0.25	4.5 ± 0.7
Patient 18	3	0.03 ± 0.02	4.3 ± 0.9
Patient 24	3	0.44 ± 0.18	4.2 ± 0.6
Patient 34	2	0.22 ± 0.06	3.2 ± 0.9
Patient 36	3	0.38 ± 0.21	3.1 ± 1.0
Patient 38	3	0.24 ± 0.09	3.4 ± 0.6
Patient 41	3	0.91 ± 0.20	3.6 ± 0.4
Patient 42	3	0.50 ± 0.14	6.1 ± 1.3
Total	38	0.44 ± 0.14	4.1 ± 0.8

Table 3. Tumour motion data sorted by motion extent (greater than 0.5 cm or less than/equal to 0.5 cm): the mean of individual treatment fraction means and standard deviations (SD) for the peak-to-trough distance and period. There are 44 treatment fractions from 16 lung patients and 13 treatment fractions from 7 retroperitoneal patients whose mean peak-to-trough distance is greater than 0.5 cm.

	Peak-to-trough distance (cm) Mean ± SD	Period (s) Mean ± SD
Lungs		
>0.5 cm	0.81 ± 0.24	3.7 ± 0.8
⩽0.5 cm	0.28 ± 0.10	3.6 ± 0.8
Retroperitoneum		
>0.5 cm	0.74 ± 0.22	4.4 ± 0.9
⩽0.5 cm	0.27 ± 0.09	4.0 ± 0.7

Table 4. Tumour motion data sorted by tumour sites in the lungs with the number of treatment fractions: the mean of individual treatment fraction means and standard deviations (SD) for the peak-to-trough distance and period.

	Peak-to-trough distance (cm) Mean ± SD	Period (s) Mean ± SD
Left lower lobe (10)	0.73 ± 0.23	3.7 ± 0.7
Left upper lobe (35)	0.36 ± 0.15	3.7 ± 0.8
Right lower lobe (15)	0.87 ± 0.18	3.1 ± 0.6
Right middle lobe (13)	0.36 ± 0.12	3.7 ± 0.7
Right upper lobe (15)	0.39 ± 0.16	3.5 ± 0.7
Hilum (15)	0.54 ± 0.13	4.1 ± 0.9
Others (2)	0.62 ± 0.18	4.7 ± 0.9

fractions) from 22 lung tumour patients and 33 fractions (87% of all retroperitoneal tumour fractions) from 11 retroperitoneal patients. Figure 7 shows the examples of motion nonlinearity

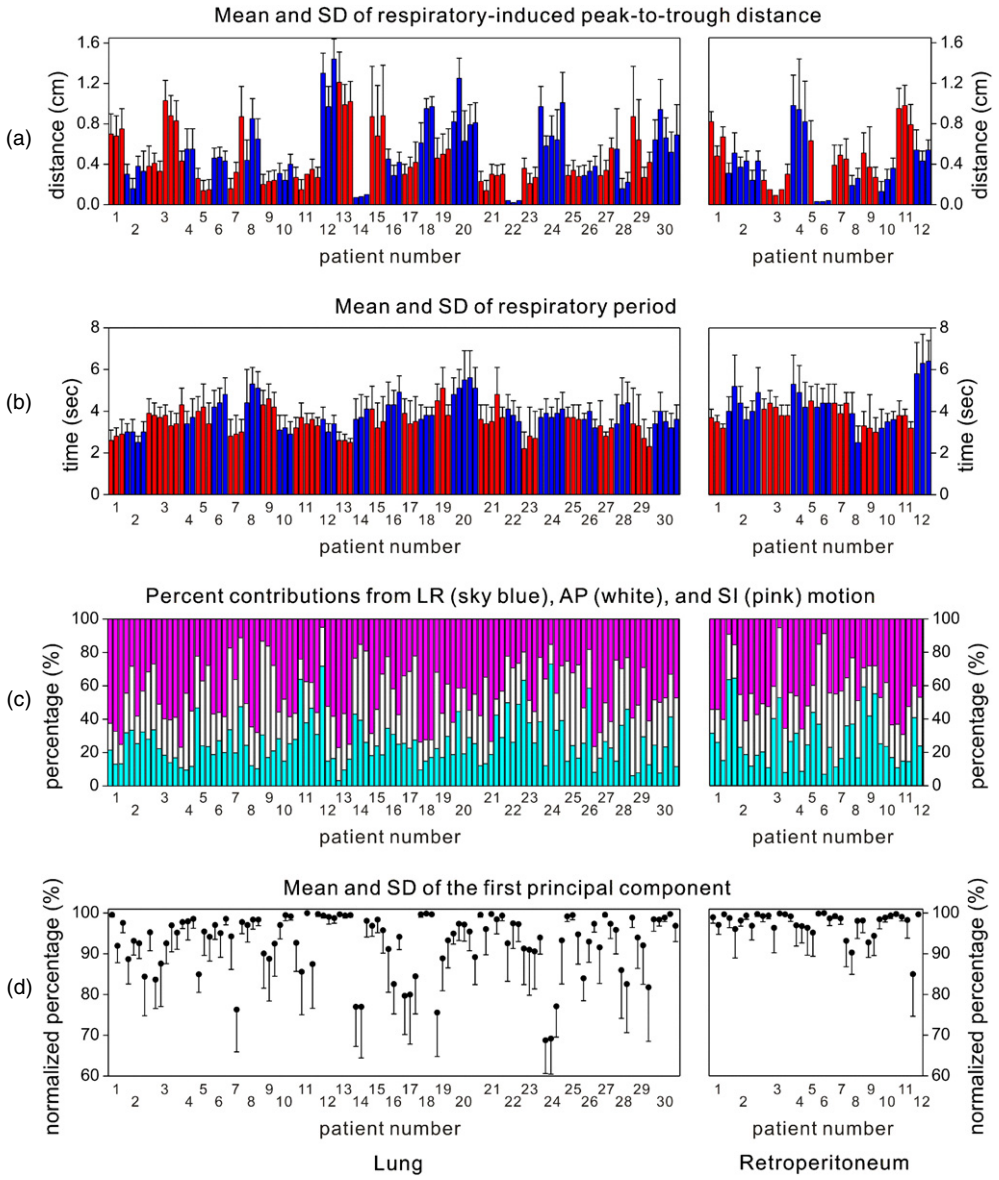

Figure 6. For each of 30 lung tumour patients (left) and 12 retroperitoneal tumour patients (right), (a) mean and standard deviation (SD) of the respiratory-induced peak-to-trough distance, (b) mean and SD of the respiratory period, (c) mean of the per cent contributions to 3D motion (R) from the motion in the LR (sky blue), AP (white) and SI (pink) directions, and (d) mean and SD of the first principal component (normalized percentage) showing motion nonlinearity and hysteresis.

and hysteresis during individual respiratory cycles. The normalized percentages of the first principal component are 100% for linear tumour motion with no hysteresis (figure 7(a)), 97% for nonlinear tumour motion with no hysteresis (figure 7(b)), and between 95% and 69% for tumour motion with hysteresis (figures 7(c)–(f)).

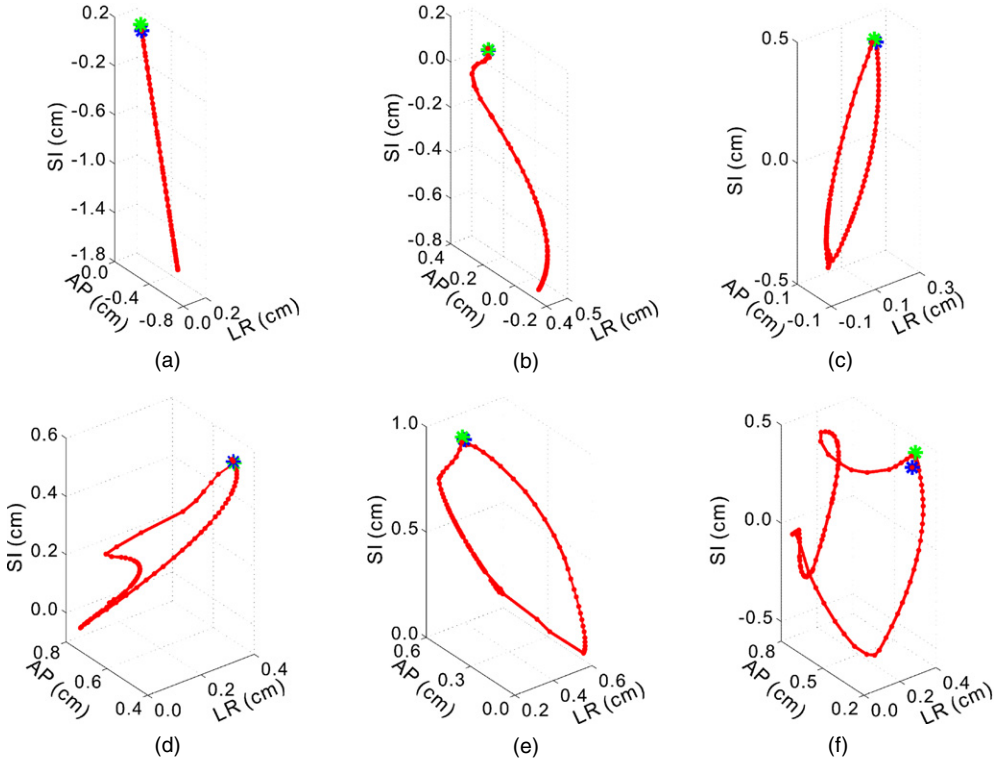

Figure 7. Examples of motion nonlinearity and hysteresis during individual respiratory cycles: (a) linear motion with no hysteresis, (b) nonlinear motion with no hysteresis and (c)–(f) motion with hysteresis. Individual cycles start at green asterisks and end at blue asterisks. The normalized percentages of the first principal component are (a) 100%, (b) 97%, (c) 95%, (d) 90%, (e) 79% and (f) 69%.

4. Discussion

The respiratory-induced tumour motion estimated from the correlation between the external and internal motion for a large patient population over long time periods was analysed and characterized. The algorithm to separate individual respiratory cycles is similar to that presented by Lu *et al* (2006), which makes use of moving average curves to identify the intersections. Similar to their conclusions, this study shows that using the moving average curves instead of the derivatives can remove the effect of possible signal drift and noise. Lu *et al* showed a 99% success rate in detection of the extremes, but this only represents 307 peaks and troughs. In this study, 70 218 respiratory cycles were examined after separating individual cycles and used to further characterize respiratory tumour motion. The algorithm worked well, even for the significant irregularity of respiratory tumour motion (figure 4); however, it failed in some cases (figure 5), which indicated that separating the individual cycles is a complex problem. Due to substantial temporal changes in respiratory tumour motion, developing a robust algorithm to separate the individual respiratory cycles is challenging.

The AAPM Task Group 76 (Keall *et al* 2006) summarized lung tumour motion and showed that the greatest lung tumour motion is generally in the SI direction, whereas the least motion

is in the LR direction. The lung tumour motion tends to increase from the upper lobes to the lower lobes. The maximum extent of the motion documented was 5 cm (Chen *et al* 2001). Ekberg *et al* (1998) showed relatively small motion in which the mean extent was 0.4 cm at the most, while Erridge *et al* (2003) reported relatively large motion with the mean extent being 1.3 cm in the SI direction. In our study, the mean extent of lung tumour motion is 0.50 cm (0.02–1.44) (appendix B), which is comparable to that reported in the literature. As shown in table 4, the mean extent of lung tumour motion in the lower lobes is more than twice as much as that in the middle and upper lobes. The mean tumour motion extent in the hilum is 0.54 cm, which is between that in the middle/upper lobes and that in the lower lobes (table 4).

For retroperitoneal tumour motion, two older studies showed similar extent of motion in which the mean was 2 cm (1–3) from a large patient population (36 subjects (Bryan *et al* 1984) and 50 subjects (Suramo *et al* 1984)). The mean extent of retroperitoneal tumour motion observed in our study (38 treatment fractions for 12 patients) is 0.44 cm (0.03–0.98) (appendix B). This result is somewhat smaller than the observations made in the older studies mentioned above; however, it is comparable to a more recent published study by Gierga *et al* (2004) that reported the mean tumour motion of 0.7 cm in the SI direction and 0.4 cm in the AP direction.

Three studies included the period of respiratory motion: one reported 16 5-min respiratory tumour motion traces for each of 20 lung cancer patients (Seppenwoolde *et al* 2002) that showed that the mean period was 3.6 ± 0.8 s (SD). George *et al* (2005) reported that the mean period was 3.8 ± 1.1 s (SD) from 331 4-min respiratory motion traces for 24 free-breathing lung cancer patients. Lu *et al* (2006) showed that the respiratory waveforms (575.3 s long) for 20 thoracic or upper abdominal cancer patients resulted in the mean respiratory period of 4.1 ± 0.9 s (SD). The overall mean respiratory period of lung tumour in our study is 3.7 ± 0.8 s (SD), which is comparable to that cited in the literature. Unlike the peak-to-trough distance, the respiratory period does not show any trends that are dependent on the location of tumour sites in the lungs; instead, they are similar to one another, with individual treatment fraction means ranging from 2.2 to 5.6 s (table 4).

The signal complexity and non-stationarity of respiratory tumour motion result in a phase difference in the motion in each of the three directions. Thus, the correlation coefficients between tumour motion in any two directions are not one. This shows that the respiratory period resulting from each of the three directions may be different from one another if the tumour motion is treated separately in the LR, AP and SI directions. To avoid ambiguity, the period was computed from the 3D motion vector. Therefore, this study presents the 3D extent of tumour motion (R), while most studies tend to report tumour motion along the separate 1D components of direction (LR, AP and SI motion).

Still, the per cent contributions to 3D motion (R) from the motion extent in each of the three directions are important, and so they are also presented in this study. A recent study by Britton *et al* (2007) showed that tumour motion from the 4D computed tomography (4D CT) data sets was mostly in the SI direction. The findings of Britton *et al* are also consistent with data presented in the other literature in which the greatest respiratory tumour motion was in the SI direction.

Likewise in our study, the mean per cent contribution to 3D motion from the SI motion is the greatest in 85 out of 143 treatment fractions (60%) when compared to the AP (22%) and LR (18%) motion, which is the smallest. However, the ranges of individual treatment fraction means for three motion directions are similar (from 5% to 75%), and show the large individual variations in the directions and extent of motion. Although it is true that respiratory tumour motion is generally the greatest in the SI direction, some patient treatment fractions show predominate motion in the LR or AP direction, as shown in figure 6(c).

These findings were discussed in a previous work using the same tumour motion data (Suh *et al* 2007), where substantial patient-to-patient respiratory tumour motion variation was observed.

One of the conditions where the respiratory management techniques should be considered in regard to the recommendations made by the AAPM Task Group 76 (Keall *et al* 2006) is when the tumour motion range in any direction is greater than 0.5 cm. Thus, tumour motion data are sorted by the motion extent that is either greater than 0.5 cm or less than/equal to 0.5 cm, as shown in table 3. Fifty-seven (57) treatment fractions out of 143 show motion extent greater than 0.5 cm, with the mean of individual treatment fraction means for the peak-to-trough distance being 0.81 cm for lung tumours and 0.74 cm for retroperitoneal tumours (table 3). Again, the means of the respiratory period are similar between the motion extent greater than 0.5 cm and that less than/equal to 0.5 cm.

The motion nonlinearity and hysteresis are important characteristics of respiratory tumour motion, but no consensus on how to quantify their extent has been reached. Seppenwoolde *et al* (2002) calculated the hysteresis as a phase difference between the fitted parameterized curves of the average breathing cycles of two directions. From 3D tumour trajectories, they showed that the hysteresis ranged from 0.1 to 0.5 cm for 10 out of 21 tumours. Based on these findings, Seppenwoolde *et al* concluded that the extent of hysteresis remained rather constant during the treatment. In our study, PCA is used to quantify the motion nonlinearity and hysteresis. Another application of PCA in radiotherapy includes quantification of the variability in a data set of dose–volume histograms (Dawson *et al* 2005, Bauer *et al* 2006, Skala *et al* 2007, Sohn *et al* 2007). Figure 7 shows the motion nonlinearity and hysteresis of individual respiratory cycles with the corresponding first principal components of PCA. As the normalized percentages of the first principal components become smaller, the motion nonlinearity and hysteresis increase. The two paths of tumour, one from exhale to inhale and the other from inhale to exhale, are often quite different and show motion hysteresis. Given that for many of the treatment fractions the means of the first principal component are greater than 90%, the motion nonlinearity and hysteresis usually are not significant; however, they are not negligible, either. PCA can be used to separate nonlinear and hysteresis motion from linear motion, but it cannot be used to differentiate between motion nonlinearity and hysteresis, which is one weakness in using this method.

5. Conclusions

The analysis and characterization of patient respiratory tumour motion were performed using more than 70 h of tumour motion data for 143 treatment fractions in 42 stereotactic body radiotherapy patients. Individual treatment fraction means of tumour motion ranged from 0.02 to 1.44 cm and were greater than 0.5 cm in 57 (40%) of the treatment fractions. Generally, tumour motion was predominantly SI (60% of all the treatment fractions) while predominant AP and LR motion being 22% and 18%, respectively. The motion was predominantly linear, with the overall mean of the first principal component being 94%. However, for motion magnitude, direction and linearity, large variations were observed from patient to patient, fraction to fraction and cycle to cycle. Beyond the quantification and analysis of the tumour motion, there are a number of ongoing uses of this data set, including the use of monoscopic imaging to quantify motion (Suh *et al* 2007), along with the development and continuing investigations of motion prediction. In addition to this ongoing work, there are many further potential applications of the data. For investigators wishing to pursue novel applications of the data, it is available from one of the authors, Sonja Dieterich, by request.

Acknowledgments

This research was supported by NCI Grant No. R01 CA 93626. The authors thank Leslie J Fiedler and Elizabeth Roberts for carefully reviewing and significantly improving the clarity of this manuscript.

Appendix A

Tumour motion data from 70 218 respiratory cycles for 143 treatment fractions in 42 stereotactic body radiotherapy patients: mean and range of individual treatment fraction means, standard deviations (SD), maximums (max), minimums (min) and root mean squares (RMS) for the peak-to-trough distance and period.

	Peak-to-trough distance (cm)	Period (s)
Mean	0.48 (0.02–1.44)	3.8 (2.2–6.4)
SD	0.15 (0.01–0.73)	0.8 (0.2–1.7)
Max	1.36 (0.06–5.12)	8.1 (4.3–19.5)
Min	0.13 (0.00–0.71)	1.9 (1.0–3.4)
RMS	0.51 (0.02–1.45)	3.9 (2.3–6.4)

Appendix B

Tumour motion data of 30 lung and 12 retroperitoneal tumour patients: mean and range of individual treatment fraction means, standard deviations (SD), maximums (max), minimums (min) and root mean squares (RMS) for the peak-to-trough distance and period (details for tables 1 and 2).

Lungs	Peak-to-trough distance (cm)	Period (s)
Mean	0.50 (0.02–1.44)	3.7 (2.2–5.6)
SD	0.16 (0.01–0.73)	0.8 (0.2–1.7)
Max	1.43 (0.08–5.12)	8.0 (4.3–19.5)
Min	0.14 (0.00–0.71)	1.8 (1.0–3.3)
RMS	0.53 (0.02–1.45)	3.8 (2.3–5.7)
Retroperitoneum	**Peak-to-trough distance (cm)**	**Period (s)**
Mean	0.44 (0.03–0.98)	4.1 (2.5–6.4)
SD	0.14 (0.01–0.46)	0.8 (0.2–1.6)
Max	1.19 (0.06–4.07)	8.4 (4.5–16.0)
Min	0.11 (0.00–0.44)	2.1 (1.1–3.4)
RMS	0.46 (0.03–1.05)	4.2 (2.6–6.4)

Appendix C

Tumour motion data of lung and retroperitoneal tumour patients sorted by motion extent (greater than 0.5 cm or less than/equal to 0.5 cm): mean and range of individual treatment fraction means, standard deviations (SD), maximums (max), minimums (min) and root mean squares (RMS) for the peak-to-trough distance and period (details for table 3).

Lungs > 0.5 cm	Peak-to-trough distance (cm)	Period (s)
Mean	0.81 (0.50–1.44)	3.7 (2.5–5.6)
SD	0.24 (0.12–0.73)	0.8 (0.2–1.7)
Max	2.29 (5.12–0.97)	8.0 (5.3–14.2)
Min	0.24 (0.00–0.71)	1.9 (1.0–3.3)
RMS	0.85 (0.53–1.45)	3.8 (2.5–5.7)
Lungs $\leqslant$ 0.5 cm	Peak-to-trough distance (cm)	Period (s)
Mean	0.28 (0.02–0.47)	3.6 (2.2–4.9)
SD	0.10 (0.01–0.25)	0.8 (0.2–1.6)
Max	0.80 (0.08–2.90)	8.0 (4.3–19.5)
Min	0.07 (0.00–0.25)	1.7 (1.0–3.1)
RMS	0.30 (0.02–0.49)	3.7 (2.3–5.0)
Retroperitoneum > 0.5 cm	Peak-to-trough distance (cm)	Period (s)
Mean	0.74 (0.51–0.98)	4.4 (3.2–6.4)
SD	0.22 (0.06–0.46)	0.9 (0.2–1.5)
Max	1.69 (0.71–2.84)	8.4 (4.8–12.6)
Min	0.16 (0.02–0.44)	2.2 (1.2–3.4)
RMS	0.78 (0.54–1.05)	4.5 (3.2–6.4)
Retroperitoneum $\leqslant$ 0.5 cm	Peak-to-trough distance (cm)	Period (s)
Mean	0.27 (0.03–0.49)	4.0 (2.5–6.3)
SD	0.09 (0.01–0.38)	0.7 (0.3–1.6)
Max	0.92 (0.06–4.07)	8.3 (4.5–16.0)
Min	0.09 (0.00–0.31)	2.1 (1.1–3.1)
RMS	0.29 (0.03–0.53)	4.1 (2.6–6.4)

References

Adler J R, Chang S D, Murphy M J, Doty J, Geis P and Hancock S L 1997 The Cyberknife: a frameless robotic system for radiosurgery *Stereotact. Funct. Neurosurg.* **69** 124–8

Bauer J, Jackson A, Skwarchuk M and Zelefsky M 2006 Principal component, varimax rotation and cost analysis of volume effects in rectal bleeding in patients treated with 3D-CRT for prostate cancer *Phys. Med. Biol.* **51** 5105–23

Blackall J M, Ahmad S, Miquel M E, McClelland J R, Landau D B and Hawkes D J 2006 MRI-based measurements of respiratory motion variability and assessment of imaging strategies for radiotherapy planning *Phys. Med. Biol.* **51** 4147–69

Boldea V, Sharp G, Jiang S and Sarrut D 2007 Lung motion modeling with deformable registration: non-linearity and hysteresis estimation *15th Int. Conf. on the Use of Computers in Radiation Therapy (ICCR) (Toronto, Canada)* pp 53–7

Britton K R, Starkschall G, Tucker S L, Pan T, Nelson C, Chang J Y, Cox J D, Mohan R and Komaki R 2007 Assessment of gross tumor volume regression and motion changes during radiotherapy for non-small-cell lung cancer as measured by four-dimensional computed tomography *Int. J. Radiat. Oncol. Biol. Phys.* **68** 1036–46

Bryan P J, Custar S, Haaga J R and Balsara V 1984 Respiratory movement of the pancreas: an ultrasonic study *J. Ultrasound Med.* **3** 317–20

Chen Q-S, Weinhous M S, Deibel F C, Ciezki J P and Macklis R M 2001 Fluoroscopic study of tumor motion due to breathing: facilitating precise radiation therapy for lung cancer patients *Med. Phys.* **28** 1850–6

Dawson L, Biersack M, Lockwood G, Eisbruch A, Lawrence T and Ten Haken R 2005 Use of principal component analysis to evaluate the partial organ tolerance of normal tissues to radiation *Int. J. Radiat. Oncol. Biol. Phys.* **62** 829–37

Dieterich S 2005 Dynamic tracking of moving tumors in stereotactic radiosurgery *Robotic Radiosurgery* vol 1 ed Richard F Mould *et al* (Sunnyvale: The Cyberknife Society Press) pp 51–63

Ekberg L, Holmberg O, Wittgren L, Bjelkengren G and Landberg T 1998 What margins should be added to the clinical target volume in radiotherapy treatment planning for lung cancer? *Radiother. Oncol.* **48** 71–7

Erridge S C, Seppenwoolde Y, Muller S H, Van Herk M, Jaeger K D, Belderbos J S, Boersma L J and Lebesque J V 2003 Portal imaging to assess set-up errors, tumor motion and tumor shrinkage during conformal radiotherapy of non-small cell lung cancer *Radiother. Oncol.* **66** 75–85

George R, Vedam S S, Chung T D, Ramakrishnan V and Keall P J 2005 The application of the sinusoidal model to lung cancer patient respiratory motion *Med. Phys.* **32** 2850–61

Gierga D P, Chen G T Y, Kung J H, Betke M, Lombardi J and Willett C G 2004 Quantification of respiration-induced abdominal tumor motion and its impact on IMRT dose distributions *Int. J. Radiat. Oncol. Biol. Phys.* **58** 1584–95

Jackson J 1991 *A User's Guide to Principal Components* (Hoboken, NJ: Wiley)

Keall P J *et al* 2006 The management of respiratory motion in radiation oncology report of AAPM Task Group 76 *Med. Phys.* **33** 3874–900

Korreman S S, Juhler-Nøttrup T and Boyer A L 2008 Respiratory gated beam delivery cannot facilitate margin reduction, unless combined with respiratory correlated image guidance *Radiother. Oncol.* **86** 61–8

Langen K M and Jones D T L 2001 Organ motion and its management *Int. J. Radiat. Oncol. Biol. Phys.* **50** 265–78

Lu W, Nystrom M M, Parikh P J, Fooshee D R, Hubenschmidt J P, Bradley J D and Low D A 2006 A semi-automatic method for peak and valley detection in free-breathing respiratory waveforms *Med. Phys.* **33** 3634–6

Mageras G S *et al* 2004 Measurement of lung tumor motion using respiration-correlated CT *Int. J. Radiat. Oncol. Biol. Phys.* **60** 933–41

Manke D, Nehrke K and Bornert P 2003 Novel prospective respiratory motion correction approach for free-breathing coronary MR angiography using a patient-adapted affine motion model *Magn. Reson. Med.* **50** 122–31

Mori S, Endo M, Komatsu S, Yashiro T, Kandatsu S and Baba M 2007 Four-dimensional measurement of lung tumor displacement using 256-multi-slice CT-scanner *Lung Cancer* **56** 59–67

Murphy M J 2004 Tracking moving organs in real time *Semin. Radiat. Oncol.* **14** 91–100

Murphy M J, Adler J R, Bodduluri M, Dooley J, Forster K, Hai J, Le Q, Luxton G, Martin D and Poen J 2000 Image-guided radiosurgery for the spine and pancreas *Comput. Aided Surg.* **5** 278–88

Neicu T, Shirato H, Seppenwoolde Y and Jiang S B 2003 Synchronized moving aperture radiation therapy (SMART): average tumour trajectory for lung patients *Phys. Med. Biol.* **48** 587–98

Nishioka S, Nishioka T, Kawahara M, Tanaka S, Hiromura T, Tomita K and Shirato H 2008 Exhale fluctuation in respiratory-gated radiotherapy of the lung: a pitfall of respiratory gating shown in a synchronized internal/external marker recording study *Radiother. Oncol.* **86** 69–76

Schweikard A, Glosser G, Bodduluri M, Martin J M and Adler J R 2000 Robotic motion compensation for respiratory movement during radiosurgery *Comput. Aided Surg.* **5** 263–77

Schweikard A, Schiomi H and Adler J 2004 Respiration tracking in radiosurgery *Med. Phys.* **31** 2738–41

Seppenwoolde Y, Berbeco R I, Nishioka S, Shirato H and Heijmen B 2007 Accuracy of tumor motion compensation algorithm from a robotic respiratory tracking system: a simulation study *Med. Phys.* **34** 2774–84

Seppenwoolde Y, Shirato H, Kitamura K, Shimizu S, Van Herk M, Lebesque J V and Miyasaka K 2002 Precise and real-time measurement of 3D tumor motion in lung due to breathing and heartbeat, measured during radiotherapy *Int. J. Radiat. Oncol. Biol. Phys.* **53** 822–34

Skala M, Rosewall T, Dawson L, Divanbeigi L, Lockwood G, Thomas C, Crook J, Chung P, Warde P and Catton C 2007 Patient-assessed late toxicity rates and principal component analysis after image-guided radiation therapy for prostate cancer *Int. J. Radiat. Oncol. Biol. Phys.* **68** 690–8

Sohn M, Alber M and Yan D 2007 Principal component analysis-based pattern analysis of dose-volume histograms and influence on rectal toxicity *Int. J. Radiat. Oncol. Biol. Phys.* **69** 230–9

Suh Y, Dieterich S and Keall P J 2007 Geometric uncertainty of 2D projection imaging in monitoring 3D tumor motion *Phys. Med. Biol.* **52** 3439–54

Suramo I, Paivansalo M and Myllyla V 1984 Cranio-caudal movements of the liver, pancreas and kidneys in respiration *Acta Radiol. Diagn.* **25** 129–31

Wall M, Rechtsteiner A and Rocha L 2003 Singular value decomposition and principal component analysis *A Practical Approach to Microarray Data Analysis* ed D Berrar, W Dubitzky and M Granzow (Norwell, MA: Kluwer)

Wolthaus J W H, Schneider C, Sonke J-J, Van Herk M, Belderbos J S A, Rossi M M G, Lebesque J V and Damen E M F 2006 Mid-ventilation CT scan construction from four-dimensional respiration-correlated CT scans for radiotherapy planning of lung cancer patients *Int. J. Radiat. Oncol. Biol. Phys.* **65** 1560–71

Wong K H, Dieterich S, Tang J and Cleary K 2007 Quantitative measurement of Cyberknife robotic arm steering *Technol. Cancer Res. Treat.* **6** 1–6

Appendix B

A DELIVERABLE FOUR-DIMENSIONAL INTENSITY-MODULATED RADIATION THERAPY-PLANNING METHOD FOR DYNAMIC MULTILEAF COLLIMATOR TUMOR-TRACKING DELIVERY

Yelin Suh

Elisabeth Weiss

Hualiang Zhong

Mirek Fatyga

Jeffrey V. Siebers

Paul J. Keall

Int. J. Radiation Oncology, Biology, Physics 71(5), 2008

Int. J. Radiation Oncology Biol. Phys., Vol. 71, No. 5, pp. 1526–1536, 2008

0360-3016/08/$–see front matter

ELSEVIER

doi:10.1016/j.ijrobp.2008.04.018

PHYSICS CONTRIBUTION

A DELIVERABLE FOUR-DIMENSIONAL INTENSITY-MODULATED RADIATION THERAPY-PLANNING METHOD FOR DYNAMIC MULTILEAF COLLIMATOR TUMOR TRACKING DELIVERY

YELIN SUH, M.S.,*† ELISABETH WEISS, M.D.,* HUALIANG ZHONG, PH.D.,* MIREK FATYGA, PH.D.,* JEFFREY V. SIEBERS, PH.D.,* AND PAUL J. KEALL, PH.D.†

*Department of Radiation Oncology, Virginia Commonwealth University, Richmond, VA; and †Department of Radiation Oncology, Stanford University, Stanford, CA

Purpose: To develop a deliverable four-dimensional (4D) intensity-modulated radiation therapy (IMRT) planning method for dynamic multileaf collimator (MLC) tumor tracking delivery.
Methods and Materials: The deliverable 4D IMRT planning method involves aligning MLC leaf motion parallel to the major axis of target motion and translating MLC leaf positions by the difference in the target centroid position between respiratory phases of the 4D CT scan. This method ignores nonlinear respiratory motion and deformation. A three-dimensional (3D) optimal method whereby an IMRT plan on each respiratory phase of the 4D CT scan was independently optimized was used for comparison. For 12 lung cancer patient 4D CT scans, individual phase plans and deformable dose-summed 4D plans using the two methods were created and compared.
Results: For each of the individual phase plans, the deliverable method yielded similar isodose distributions and dose–volume histograms. The deliverable and 3D optimal methods yielded statistically equivalent dose–volume metrics for both individual phase plans and 4D plans ($p > 0.05$ for all metrics compared). The deliverable method was affected by 4D CT artifacts in one case. Both methods were affected by high vector field variations from deformable registration.
Conclusions: The deliverable method yielded similar dose distributions for each of the individual phase plans and statistically equivalent dosimetric values compared with the 3D optimal method, indicating that the deliverable method is dosimetrically robust to the variations of fractional time spent in respiratory phases on a given 4D CT scan. Nonlinear target motion and deformation did not cause significant dose discrepancies. © 2008 Elsevier Inc.

Lung cancer, IMRT, 4D CT, DMLC tracking.

INTRODUCTION

Radiation treatment that explicitly accommodates temporal changes of anatomy, called four-dimensional (4D) radiotherapy, is an intense area of study in radiation oncology (1, 2). Recent development of 4D computed tomography (CT) provides better understanding of anatomic motion. How to use this extra information to further improve target coverage and spare normal tissue in an optimal way is still a challenge.

Intensity-modulated radiation therapy (IMRT) is shown to have better normal tissue sparing and target dose conformality compared with conventional treatment techniques (3), and use of the dynamic multileaf collimator (DMLC) is shown to be a reliable and efficient IMRT delivery technique (4). Dynamic MLC also has been investigated to deliver 4D IMRT, and several techniques to incorporate anatomic changes into DMLC IMRT have been proposed (5–21). However, the finite mechanical motion capabilities of an MLC impose constraints on the leaf sequence of 4D radiotherapy because the MLC leaves need to both follow the tumor motion during treatment and move to modulate the beam fluence to perform IMRT.

The complexity of IMRT using the DMLC delivery technique on 4D CT data sets has been investigated (5–21). Trofimov *et al*. (16) compared different 4D IMRT optimization schemes, with respect to the full optimization, and showed tumor tracking to be marginally better than other techniques. They showed a good framework of formulating a 4D IMRT planning problem. However, their investigations did not account for the design specifications of delivery devices and additional complexities of leaf motion constraints.

Reprint requests to: Yelin Suh, M.S., Department of Radiation Oncology, Stanford University, 875 Blake Wilbur Drive, Stanford, CA 94305-5847. Tel: (650) 725-6713; Fax: (650) 498-5008; E-mail: ysuh@stanford.edu

Supported in part by NCI R01 CA93626 and NCI-NIH P01 CA116602.

Conflict of interest: none.

Acknowledgment—The authors thank Drs. Lei Dong and Radhe Mohan from the University of Texas M. D. Anderson Cancer Center for the lung cancer patient four-dimensional CT data used for this study; and Dr. Ivaylo Mihaylov for the tool to translate the multileaf collimator leaves.

Received Sept 19, 2007, and in revised form April 14, 2008. Accepted for publication April 14, 2008.

Webb *et al.* (6, 8, 17–19) showed strategies to find the optimal leaf trajectories by minimizing the geometric mismatch of MLC leaf and organ motion in one dimension and two dimensions, including leaf motion constraints for the motion-compensated DMLC IMRT planning. They applied their strategies to a motion model constructed from a patient 4D CT but did not demonstrate implementation beyond a single patient. Papiez *et al.* (7, 10–14) developed algorithms for DMLC leaf-pair optimal control IMRT delivery to moving and deforming targets. They demonstrated their algorithms for the target motion in real time and when *a priori* motion information is known for one dimension, but as of yet not for three dimensions. Zhang *et al.* (20, 21) investigated plan optimization incorporating respiratory target motion and deformation with helical tomotherapy but with only one lung case. Schlaefer *et al.* (15) showed the feasibility of an approach to consider the relative motion of organs during treatment planning for robotic radiosurgery. Their study was based on the assumptions of perfect target tracking and regular respiratory motion and was not applied to real patients. Because of the complexity of the 4D IMRT problem, an optimal IMRT planning method based on the 4D CT scan that combines MLC leaf motion constraints and MLC transport characteristics with an approach robust to respiratory-induced motion during treatment has not yet been developed.

To incorporate the MLC leaf motion constraints into 4D IMRT planning using DMLC, this study is focused on a simplification of rigid body target translation. Only target motion along the MLC leaf motion direction is considered, whereas target motion perpendicular to the MLC leaf motion caused by target deformation/rotation and motion nonlinearity/hysteresis is ignored. This approach yields a planning scheme that is not optimal but, importantly, is deliverable with currently available technology. For comparison, a three-dimensional (3D) optimal scheme also is shown, in which the dose distribution in each phase of the 4D CT scan is independently optimized. A given phase represents what could be achieved using respiratory gating. The 3D optimal approach accounts for target deformation/rotation and motion nonlinearity/hysteresis but ignores MLC leaf motion constraints and thus is deliverable only if the MLC leaf velocity is infinite.

METHODS AND MATERIALS

Formalism for 4D IMRT planning optimization

The aim of 4D IMRT planning optimization for DMLC tumor tracking is to find the deliverable leaf sequence, $L(MU,\theta)$, as a function of monitor unit, MU, and respiratory phase, θ, to satisfy min $\{f[D(L(MU,\theta))]\}$, where f is a mathematical cost function representation of a clinical objective, and D is the prescribed dose distribution:

$$D = \sum_{\theta=0}^{P} \lambda_\theta \; D_\theta\big(I(\theta), I_{ref}, u(\theta), L(MU,\theta)\big), \qquad (1)$$

where λ_θ is time spent per each phase, D_θ is dose for a given phase, I is a 4D CT image of anatomy where $I(\theta)$ represents a given 3D instance for phase θ and I_{ref} the image used for dose summation, and u is a displacement vector field computed using deformable registration mapping images from a given to the reference phase. To obtain D_θ, the dose is computed on $I(\theta)$ on the basis of $L(MU,\theta)$ and then deformed to I_{ref} using $u(\theta)$.

A deliverable 4D IMRT planning method to solve Eq. (1) proposed in this study is to account for rigid body target motion along the MLC leaf direction only, as well as to ensure that MLC leaf motion does not exceed the maximum leaf velocity (22). The deliverable method finds the deliverable leaf sequence on the reference phase, $L(MU,\theta_{ref})$, to satisfy $\min\{f[D(L(MU,\theta_{ref}))]\}$, where $D = D_{\theta_{ref}}(I_{ref}, L(MU,\theta_{ref}))$ and θ_{ref} is the reference phase. For the rigid body target translation, the solutions for other phases become $L(MU,\theta) = L(MU,\theta_{ref}) + g(\theta)$, where $g(\theta)$ is the target centroid displacement from the reference phase to phase θ along the major axis of target motion in a given beam's eye view (BEV).

A benchmark method is a 3D optimal method, which finds the optimal leaf sequence, $L(MU,\theta)$, to satisfy $\min\{f[D_\theta(L(MU,\theta))]\}$ for each phase independently.

4D CT data and patient characteristics

The 4D CT data of 12 lung cancer patients acquired on a 16-slice CT scanner in a cine mode (GE Healthcare Technologies, Waukesha, WI) were used (23, 24). The acquisition was performed as a part of an institutional review board–approved study (protocol 00-202) at the University of Texas M. D. Anderson Cancer Center. On the basis of the respiratory signal from a respiration monitoring system (RPM; Varian Medical Systems, Palo Alto, CA), the respiratory cycle was divided into 10 phases of equal duration, with Phase 0 representing end-inhale and Phase 5 approximately end-exhale. The tumor classifications ranged from T1N0 to T4N0, and tumors were located in the upper lobes for 9 patients and in the lower lobes for 3 patients with peripheral (3 patients) and central (9 patients) tumor localizations. The means of gross tumor volume (GTV) and GTV centroid motion range were 49.2 cm^3 and 0.7 cm, respectively (Table 1).

Contouring and IMRT planning

Contouring and planning were performed using a commercially available planning system (Pinnacle 7.9; Philips Medical Systems, Milpitas, CA). On the basis of the manually segmented contours on Phase 0, the contours on the other 9 phases of the 4D CT scan were automatically generated using large deformation diffeomorphic image registration (25, 26). The GTV was expanded by an 8-mm margin to yield the clinical target volume (27), and a 5-mm margin was added to create the planning target volume (PTV). The prescribed dose to PTV was 74 Gy, and beam arrangements were six coplanar, non-opposed, predominantly anterior–posterior, with beam angles adjusted depending on the tumor locations. Further details for planning and optimization are described elsewhere (23).

Methods of the deliverable and 3D optimal IMRT planning on the 4D CT scans

The deliverable 4D IMRT planning method involves four steps for each patient (Fig. 1). From Steps 1 through 3, individual phase plans were created, and in Step 4 deformable dose-summed 4D plans were created.

Step 1. The appropriate beam angle arrangement for an IMRT plan was determined. The target centroid position for each phase was quantified from a 4D CT image set. The major axis of target motion was determined in each BEV. Then, for each beam, the collimator was rotated to align MLC leaf motion parallel to the major axis. Figure 2 shows this key step in the deliverable 4D IMRT planning method. The same target motion in 3D (Fig. 2a) has different

Table 1. Patient gross tumor volume (GTV), GTV centroid motion range, and motion range in major axis

Patient no.	GTV volume (cm^3)	GTV centroid motion (cm)	Motion in major axis (cm)
1	3.0	2.1	1.6
2	61.0	0.4	0.4
3	12.5	0.5	0.5
4	1.0	0.6	0.6
5	20.4	0.1	0.1
6	5.2	0.4	0.4
7	323.6	0.2	0.2
8	23.0	0.3	0.2
9	6.1	0.2	0.2
10	7.5	0.5	0.4
11	119.2	1.3	1.1
12	7.5	1.1	0.9
Mean (minimum, maximum)	49.2 (1.0, 323.6)	0.7 (0.1, 2.1)	0.6 (0.1, 1.6)

two-dimensional motion in the BEVs of different beam angles (Fig. 2b). On the basis of the target positions in a given BEV, the major axis (dashed arrows in Fig. 2b) of target motion was automatically determined for each beam using a least-squares fit.

Step 2. For the reference phase (end-exhale was used as the most stable phase during respiration [28]), an appropriate IMRT plan was created with the rotated collimator, creating MLC leaf positions for each beam.

Step 3. For each of the other phases, an IMRT plan was created by copying the MLC leaf positions for the reference phase and translating them by the relative displacement of target centroid for each phase, while keeping the collimator angle for each beam the same. For example, for a given phase plan, a beam aperture was shifted from the reference phase (dashed red in Fig. 2c) to the given phase (solid red in Fig. 2c) by the difference in the target centroid position between the two phases, as seen in the BEV. All 10 individual phase plans for a given patient using the deliverable method were exactly the same except for the MLC leaf positions translated.

Step 4. For each patient, a deformable dose-summed 4D plan was created by accumulating the resultant doses from all individual phase plans on the Phase 0 CT image using deformable dose summation (5, 20, 25, 26).

For comparison, the 3D optimal method, which was the same as the deliverable method except for Step 3, was also applied (Fig. 1). For the other phases, with the same IMRT beam angle arrangement and collimator angles as the deliverable plans, the 3D optimal method was to independently optimize an IMRT plan on each phase of the 4D CT images. All 10 individual phase plans for a given patient using the 3D optimal method can be different except for beam and collimator angles.

The deliverable method was compared with the 3D optimal method using composite objective values and dose–volume evaluation metrics derived from the dose–volume histogram (DVH). The composite objective value, a single number, is an indicator of plan quality that takes into account the actually achieved dose distribution for the PTV and organs at risk (OARs) after plan optimization, relative to the initial constraints (23). The smaller the composite objective value, the better the plan. For individual phase plans, the mean and SD of dose–volume metric ratios were averaged over all 10 phases for all 12 patients:

$$\overline{\overline{X_{opt}^{del}}} = \frac{\sum_{i}^{M}\sum_{j}^{N} X_{del}^{i,j}/X_{opt}^{i,j}}{M \cdot N} \text{ and } \sigma_{\overline{\overline{X_{opt}^{del}}}} = \sqrt{\frac{\sum_{i}^{M}\sum_{j}^{N}\left(X_{del}^{i,j}/X_{opt}^{i,j} - \overline{\overline{X_{opt}^{del}}}\right)^2}{M \cdot N}},$$

where X was a dose–volume metric computed from the DVHs of plans using the deliverable (X_{del}) or 3D optimal (X_{opt}) methods, i was a patient number, and j was a phase number. For 4D plans, those were averaged over all 12 patients:

$$\overline{X_{opt}^{del}} = \frac{\sum_{i}^{M} X_{del}^{i}/X_{opt}^{i}}{M} \text{ and } \sigma_{\overline{X_{opt}^{del}}} = \sqrt{\frac{\sum_{i}^{M}\left(X_{del}^{i}/X_{opt}^{i} - \overline{X_{opt}^{del}}\right)^2}{M}}.$$

A one-tailed Student's t-test with the null hypothesis of $H_0 : X_{opt} = X_{del}$ and the alternative hypothesis of $H_A : X_{opt} > X_{del}$ was used to evaluate whether two methods were statistically different (statistically different if $p < 0.05$).

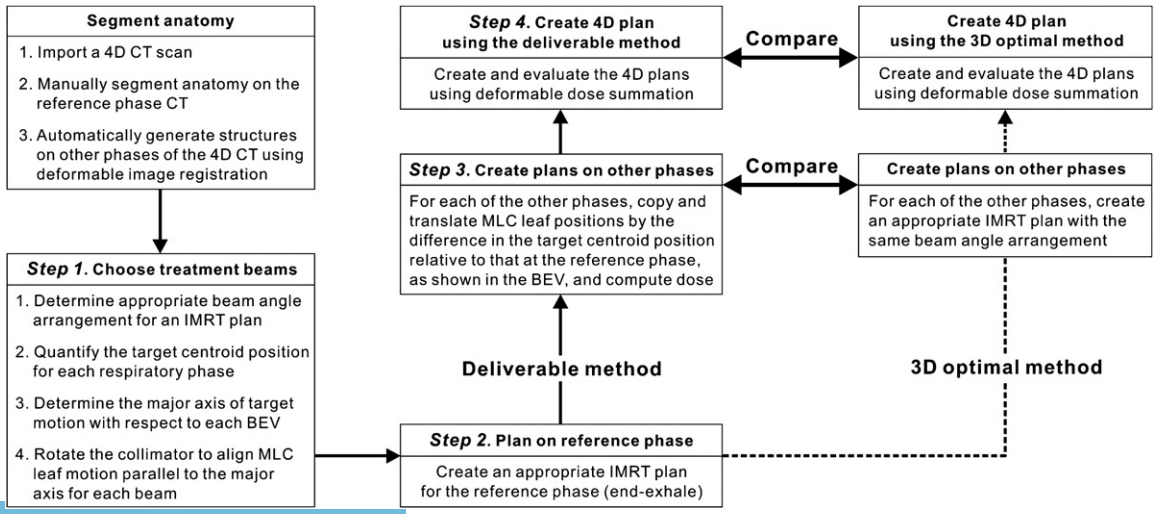

Fig. 1. Flowchart of the methods of deliverable and three-dimensional (3D) optimal intensity-modulated radiation therapy (IMRT) planning on the four-dimensional computed tomography (4D CT) scans. MLC = multileaf collimator; BEV = beam's eye view.

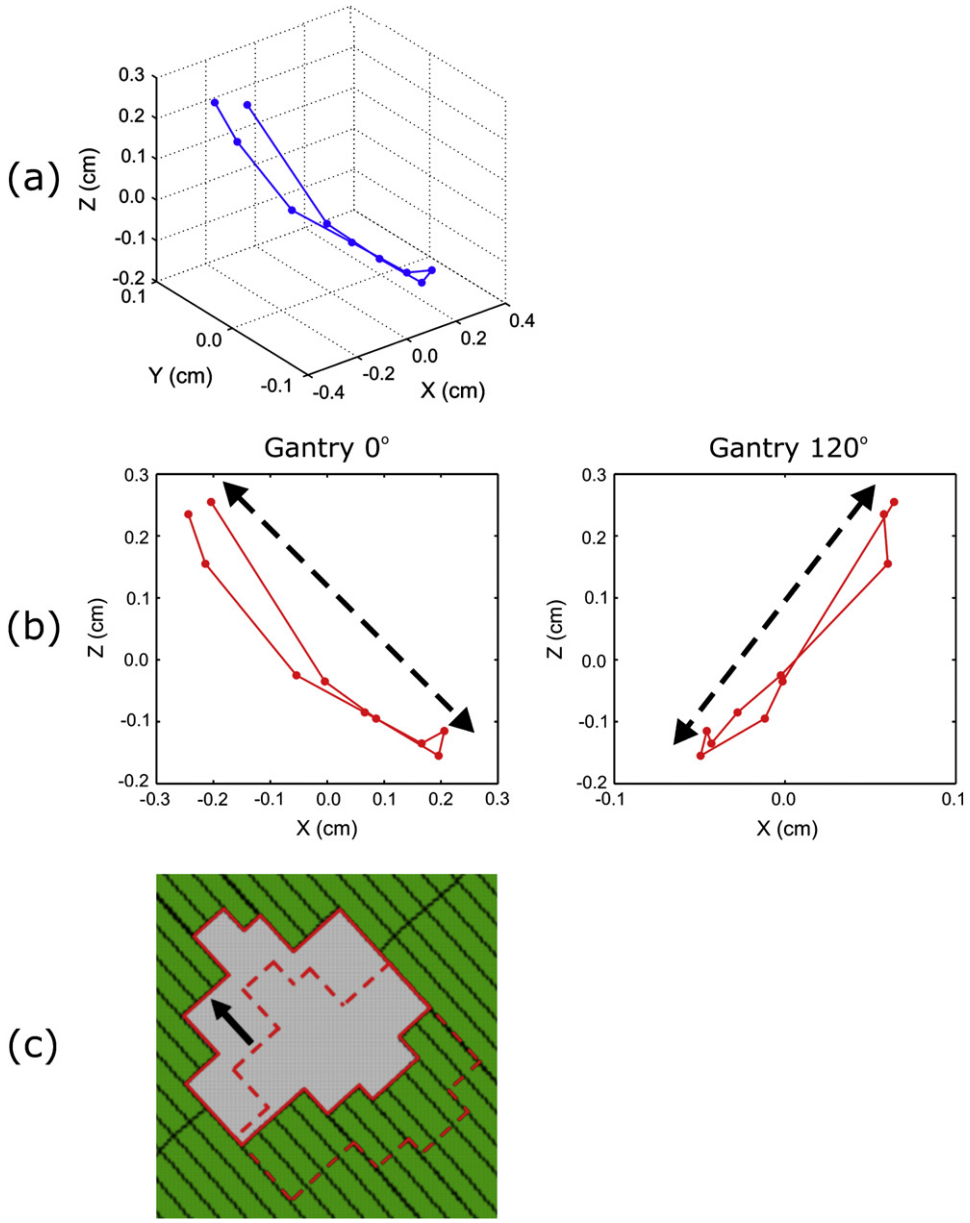

Fig. 2. Determination of the major axis of target motion. (a) The same target motion in three dimensions has (b) different two-dimensional motion in the beam's eye view (BEV) of different beam angles, such as gantry angles of 0° and 120°. On the basis of the target positions in a given BEV, the major axis (dashed arrows) of target motion is automatically determined for each beam: collimator angles are 41° and 106° for the gantry of 0° and 120°, respectively. (c) For the gantry angle of 0° in (b), the collimator is rotated by 41° to align multileaf collimator leaf motion parallel to the major axis. For a given phase plan, a beam aperture is translated from the reference (dashed red) to a given (solid red) phase by the difference in the target centroid position between the two phases, as seen in the BEV.

RESULTS

Individual phase plans

Figure 3 shows the composite objective values of individual phase plans using the deliverable and 3D optimal methods for each patient. The two methods have identical objective values for Phase 5. For the other phases, the 3D optimal method always yields smaller values (better plan quality). Variation in plan quality is generally larger for phase-to-phase compared with that for method-to-method.

Patient 1 shows significant discrepancy in the composite objective values between the two methods for some phases (red in Fig. 3). There are artifacts in the 4D CT image set for this patient, including division of the tumor into two parts for three phases. The artifacts deteriorate target coverage when the deliverable method is used, resulting in discrepancy in both PTV coverage and OAR sparing between the two methods (Fig. 4a). Figure 4a shows the DVHs and isodose distributions for Patient 1, which illustrates the second-worst agreement case in terms of the composite objective values (value ratio of 18.1). Patient 4 also shows significant discrepancies in the composite objective values between the two methods throughout the phases (blue in Fig. 3), which is

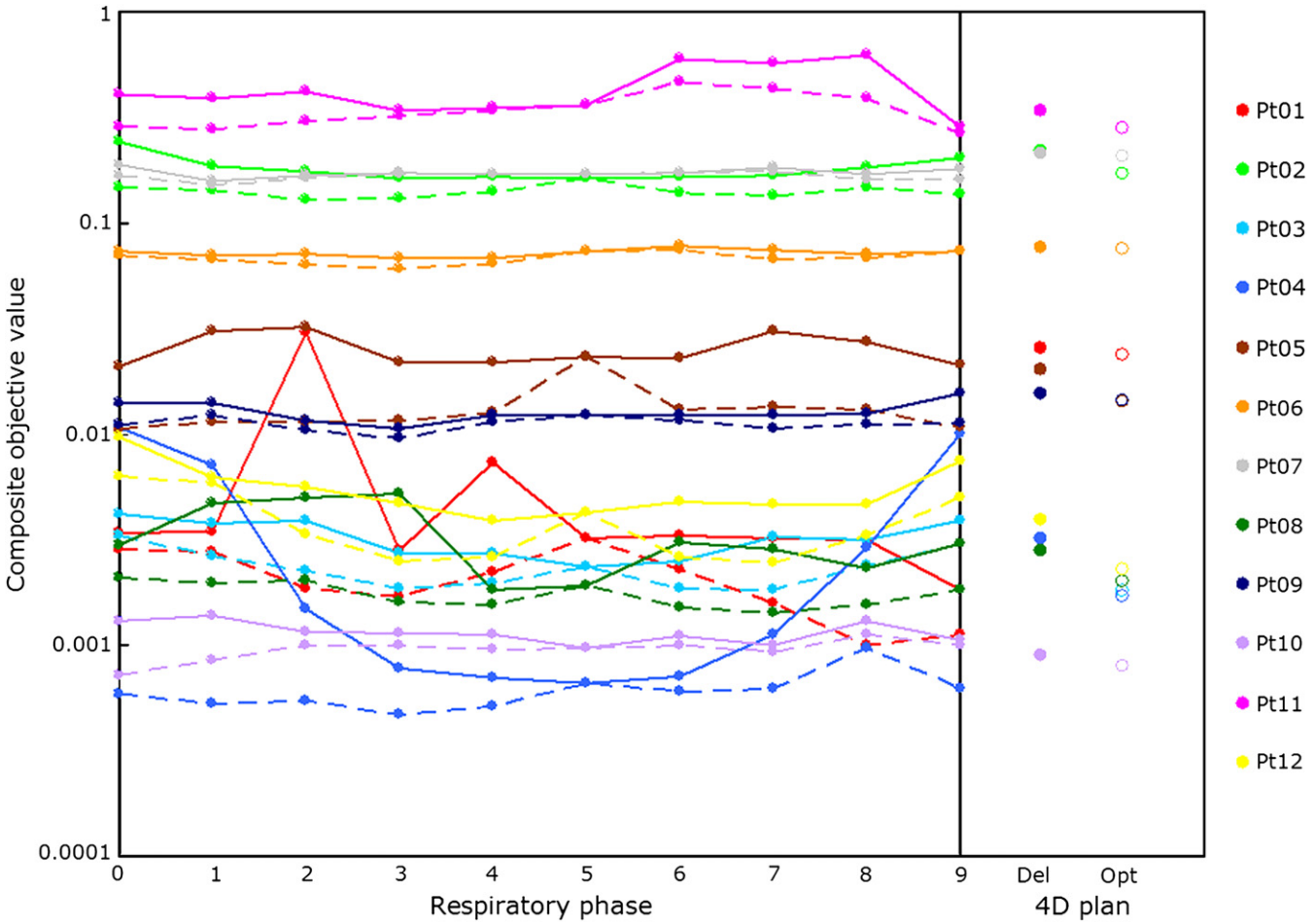

Fig. 3. Composite objective values of individual phase plans using the deliverable (solid) and three-dimensional (3D) optimal (dashed) methods and those of four-dimensional (4D) plans using the deliverable (Del, filled circles) and 3D optimal (Opt, empty circles) methods for each patient. The smaller the value, the better the plan. The two methods have identical objective values for Phase 5. For the other phases, the 3D optimal method always yields better plans. The 4D composite objective values for each method are similar to the average values over individual phase plans per patient.

explained by the largest variation in tumor volume during the respiratory cycle. Even though Phase 0 plans using the two methods for Patient 4 show the worst agreement in terms of the composite objective value (value ratio of 18.4), there is discrepancy only in the DVHs of the PTV (Fig. 4b). The 74-Gy isodose curve (blue) does not cover the whole PTV in the deliverable plan, unlike in the 3D optimal plan. Patient 7, whose tumor has almost no motion during respiration, shows the best agreement of the composite objective values between the two methods for all phases (grey in Fig. 3).

Figure 3 also shows phase-to-phase variation in plan quality. Whereas the composite objective values for the 3D optimal method do not vary much from phase to phase, those for the deliverable method do vary. There is significant phase-to-phase variation in plan quality using the deliverable method for Patients 1 and 4 (red and blue in Fig. 3). Again, Patient 1 has artifacts in the 4D CT images, and Patient 4 has the largest tumor volume variation. Patient 4 also shows a trend in that the farther the respiratory phases are from Phase 5, the worse the deliverable plan quality becomes (blue in Fig. 3). The significant variation in tumor volume causes inferior PTV coverage in the deliverable plans, especially for the phases further away from Phase 5. Figure 5a shows the DVHs of all 10 individual phase plans using the two methods for Patient 1. Although the composite objective values do not vary significantly, there are phase-to-phase variations of the DVHs in the 3D optimal plans, especially for the OARs.

Because the composite objective value is a numeric indicator of plan quality and does not indicate the plan details, a patient showing the most discrepancy in the DVHs between methods and between phases is chosen by visually inspecting the DVHs. Despite relatively good agreement of plan quality (pink in Fig. 3), Patient 11 shows the most discrepancy in the DVHs between methods and between phases (Fig. 5b) because the tumor shows the most hysteresis during respiration (24, 28), the second biggest volume, and the second most motion. These attributes also cause the largest difference in PTV $D_{95\%}$ (dose received by 95% of the PTV) and lung D_{mean} (mean dose to the lungs) between the two methods.

Table 2 shows dose–volume metric ratios of individual phase plans. All mean values of the dose and volume metric ratios are very close to 1.00, indicating that the deliverable

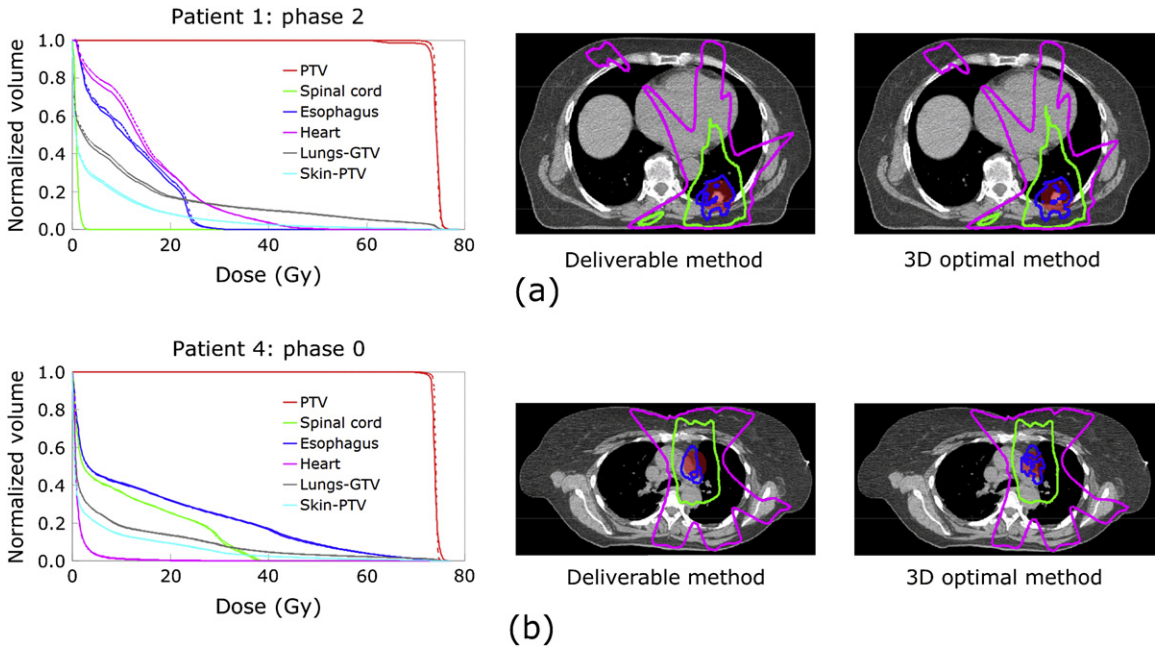

Fig. 4. Dose–volume histograms (DVHs) and isodose distributions of individual phase plans showing discrepancy in the composite objective values between the two methods: (a) the second-worst agreement case (objective value ratio of 18.1) due to the artifacts in the 4D CT scan; and (b) the worst agreement case (objective value ratio of 18.4) due to significant variation in tumor volume during the respiratory cycle. Solid DVHs are for the deliverable method and dashed for the 3D optimal method. The planning target volume (PTV) is shaded in red; blue isodose curves indicate 74 Gy, green 40 Gy, and pink 20 Gy. GTV = gross tumor volume.

and 3D optimal methods yield similar dose–volume characteristics. No evaluated dose–volume metric is statistically different between the methods ($p > 0.05$ for all metrics compared), whereas PTV coverage shows more variation than OARs.

Deformable dose-summed 4D plans (4D plans)

Figure 3 also shows the composite objective values of 4D plans using the two methods for each patient. The 3D optimal method always yields better plans. The 4D composite

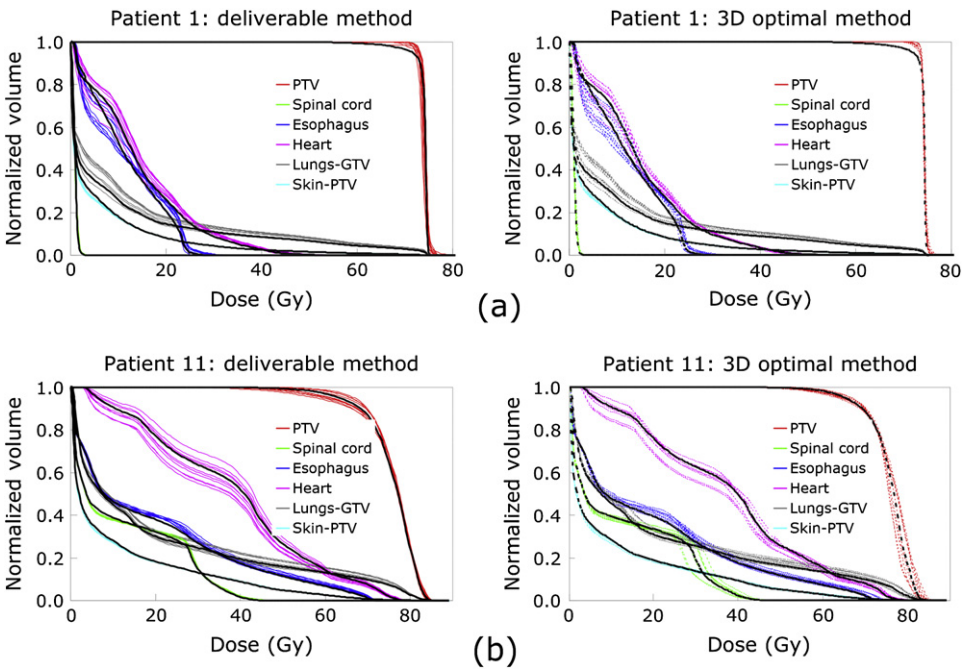

Fig. 5. Dose–volume histograms (DVHs) of all 10 individual phase plans with four-dimensional (4D) plans (black thick curves) for the deliverable (left column) and three-dimensional (3D) optimal (right column) methods: (a) significant phase-to-phase variation with degraded planning target volume (PTV) coverage in 4D plans; and (b) significant phase-to-phase variation, but with reasonable DVHs (about the averages over individual phase plans) in 4D plans. Solid DVHs are for the deliverable method and dashed for the 3D optimal method. GTV = gross tumor volume.

objective values for each method are similar to the average values over individual phase plans per patient.

However, 4D plans for Patient 1 are significantly worse than individual phase plans for both methods (red in Fig. 3). Degraded 4D plans for Patient 1 also are evident in Fig. 5a, mainly owing to inferior PTV coverage. Figure 6 shows the isodose distributions of individual phase plans on Phase 0 and Phase 5, as well as 4D plans for Patient 1. Although the dose distributions for Phase 0 and Phase 5 plans look reasonable (Fig. 6a and b), 4D plans have inconsistent dose distributions (Fig. 6c) for both methods. This is explained by large gradients of the deformation vector field across the PTV. Because the tumor of Patient 1 is next to the chest wall and moves 2.1 cm, the vector field, which differs significantly across the PTV, is used for deformable image registration and dose summation. As shown schematically in Fig. 6d, the vector field tends to be large in the lungs (white arrows) and small in the chest wall (black arrows). As a result, some portion of the PTV (in the chest wall) deforms differently from its other portion (in the lungs). Thus, deforming the PTV differs from deforming the GTV and expanding it to create the PTV, because the former may generate unrealistic appearance of the PTV after deformable image registration (aqua star in Fig. 6d). However, when the dose is deformed back to Phase 0, the latter may result in inconsistent dose distributions after deformable dose summation (green star in Fig. 6d). Because this occurs in both methods, the composite objective values for the two 4D plans are similar (red in Fig. 3), and the DVHs do not show significant discrepancy, especially for PTV coverage (Fig. 7c).

On the other hand, Patient 4 shows the largest difference in the composite objective values between the two 4D plans (blue in Fig. 3), whereas the composite objective value for each 4D plan is an average of individual phase plans, respectively. Again, this is due to the most variation in tumor volume, which results in poor PTV coverage in the deliverable plans (Fig. 7f).

As shown in Fig. 5b, Patient 11 has significant phase-to-phase variation in the DVHs for individual phase plans but shows reasonable DVHs for the two 4D plans, each of which is an approximate average of the DVHs for individual phase plans. The composite objective values for the two 4D plans are better than the average of those values over individual phase plans (pink in Fig. 3). Between the two 4D plans, however, Patient 11 shows the most discrepancy in the DVHs (Fig. 7a). The tumor of this patient has the most hysteresis (0.35 cm) (24), whereas Patient 9 with the least hysteresis (0 cm) shows two DVH sets on the top of each other, indicating good agreement between the two 4D plans (Fig. 7b). Patient 9 actually shows the best agreement between the two methods (Fig. 7b).

In terms of tumor motion, both of the patients with the most motion (2.1 cm) (Fig. 7c) and the least motion (0.1 cm) (Fig. 7d) show discrepancies in the DVHs. In terms of tumor volume, both of the patients with the largest tumor volume (323.6 cm^3) (Fig. 7e) and the smallest tumor volume (1.0 cm^3) (Fig. 7f) show relatively good agreement in the DVHs.

Table 3 shows dose–volume metric ratios of 4D plans. As in Table 2, all mean values are very close to 1.00, indicating

Table 2. A comparison of the dose–volume metrics of individual phase plans using the deliverable and three-dimensional (3D) optimal methods

	PTV		Lungs–GTV		Spinal cord	Esophagus		Heart		Thorax–PTV
	$(D_{mean})^{del}_{opt}$	$(D_{95\%})^{del}_{opt}$	$(D_{mean})^{del}_{opt}$	$(V_{20})^{del}_{opt}$	$(D_{0.1\%})^{del}_{opt}$	$(D_{mean})^{del}_{opt}$	$(V_{55})^{del}_{opt}$	$(D_{mean})^{del}_{opt}$	$(V_{40})^{del}_{opt}$	$(D_{mean})^{del}_{opt}$
Mean ± SD	1.001 ± 0.004	0.992 ± 0.016	1.00 ± 0.02	1.01 ± 0.03	1.00 ± 0.05	1.00 ± 0.03	1.02 ± 0.07	1.01 ± 0.05	0.96 ± 0.20	1.00 ± 0.02
Minimum, maximum	0.988, 1.021	0.916, 1.010	0.93, 1.05	0.90, 1.12	0.88, 1.31	0.88, 1.10	0.96, 1.56	0.87, 1.26	0.00, 1.17	0.93, 1.03
p	0.11	0.09	0.48	0.46	0.48	0.50	0.44	0.49	0.45	0.50

Abbreviations: PTV = planning target volume; GTV = gross tumor volume.
Mean and SD of the dose–volume metric ratios averaged over all 10 phases for all 12 patients; and *p* values testing whether two distributions are statistically different. D_{mean} represents the dose received by mean volume of the PTV or organs at risk (OARs); $D_{A\%}$ the dose received by $A\%$ of volume of the PTV or OARs; and V_B the total volume of OARs receiving at least B Gy.

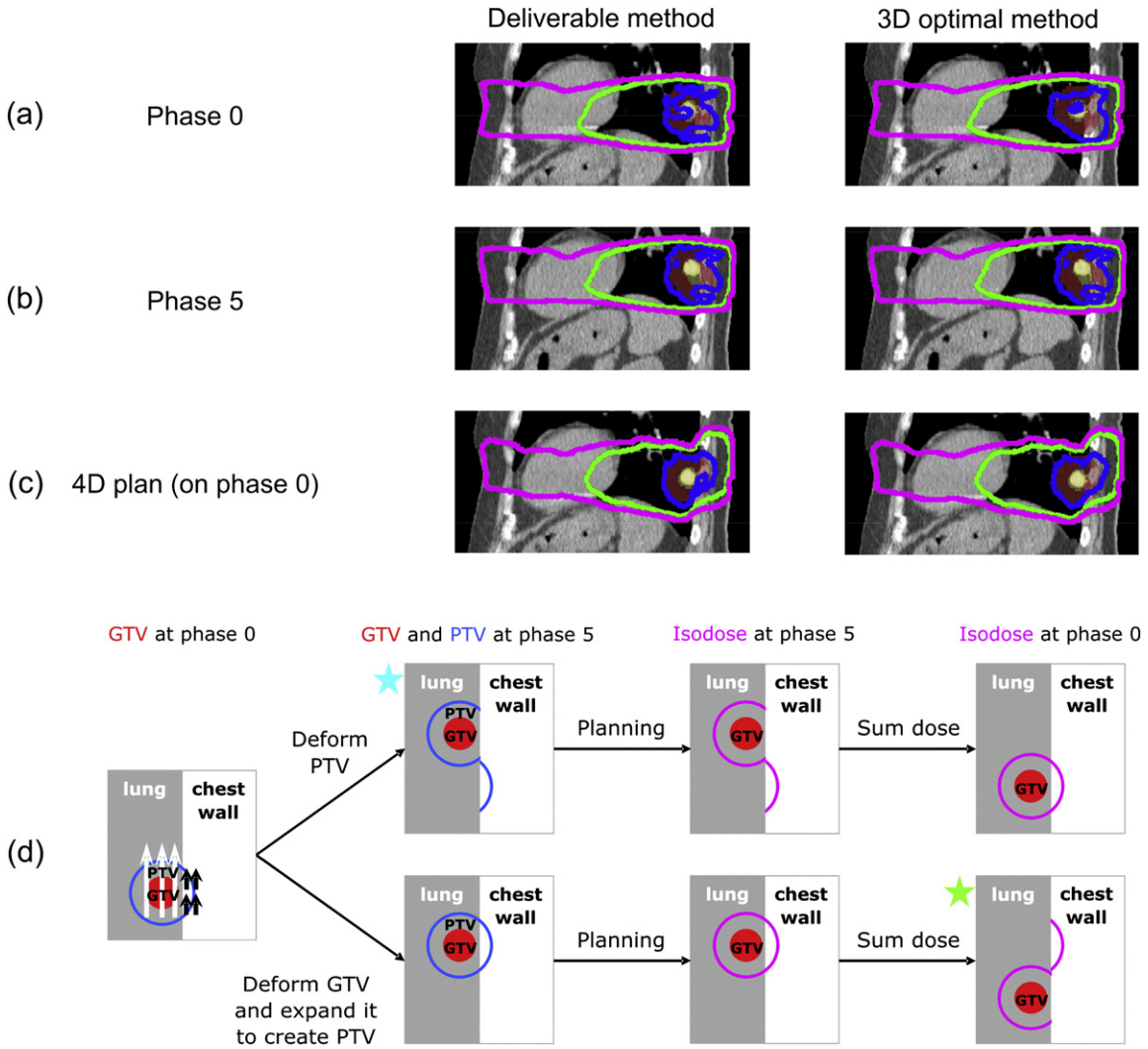

Fig. 6. Isodose distributions for (a) Phase 0 plans and (b) Phase 5 plans, and (c) four-dimensional (4D) plans (on Phase 0 CT image) using the two methods in a sagittal view for Patient 1. Note that Phase 5 plans are identical for both methods. Whereas the dose distributions of Phase 0 and Phase 5 plans look reasonable (a, b), the 4D plans have inconsistent dose distributions (c) for both methods. (d) This is due to large gradients of the deformation vector field across the planning target volume (PTV). Because the vector field is large in the lungs (white arrows) and small in the chest wall (black arrows), deforming the PTV generates unrealistic appearance of the PTV after deformable image registration (aqua star). Deforming the gross tumor volume (GTV) and expanding it to create the PTV results in inconsistent dose distributions after deformable dose summation (green star). See text for more details. In (a–c) the PTV is shaded in red and the GTV in yellow, and blue isodose curves indicate 74 Gy, green 40 Gy, and pink 20 Gy. In (d) the GTV is shaded in red, blue indicates the PTV, and pink illustrates the isodose curves.

that the two methods yield similar dose–volume characteristics. Again, no evaluated dose–volume metric is statistically different between the methods ($p > 0.05$ for all metrics compared), whereas PTV coverage shows more difference than OARs. The difference in PTV coverage between the two methods is smaller than that for individual phase plans.

DISCUSSION

An ''ideal'' 4D IMRT planning would be one optimized over the continuous motion of target and surrounding normal tissues, which may be deliverable; however, there are no solutions for this type of deliverable-based optimization yet. This study proposed a ''deliverable'' 4D IMRT planning method. The reason for taking this approach is that it provides a feasible solution that uses current planning technology and thus has a clear path to clinical application. Though this approach is clearly not optimal, given the assumption made, Trofimov *et al.* (16) showed that tumor tracking yielded better results than the gated technique, and both methods improved treatment compared with the motion-inclusive technique. The planned clinical application involves integrating the linear accelerator with a real-time target position monitoring system. As the target position information is obtained, the appropriate corrections are made to the leaf positions in real time. A ''3D optimal'' method that involved an independent 3D IMRT optimization for each phase of the 4D CT scan also is proposed as a benchmark method. It is important to note that the sum of

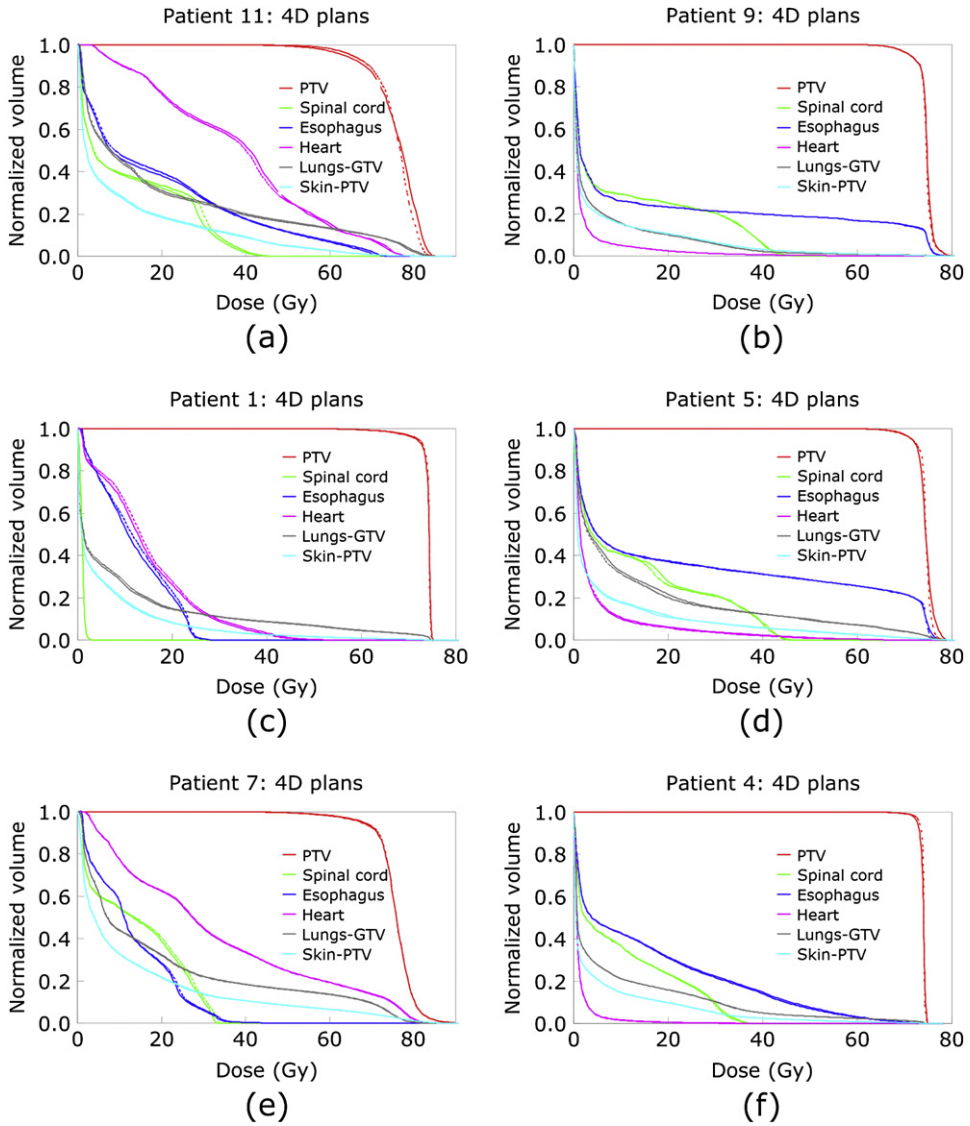

Fig. 7. Dose–volume histograms (DVHs) of four-dimensional (4D) plans using the two methods for the patients with various tumor characteristics: (a) most hysteresis (0.35 cm); (b) least hysteresis (0 cm); (c) most motion (2.1 cm); (d) least motion (0.1 cm); (e) largest volume (323.6 cm^3); and (f) smallest volume (1.0 cm^3). Solid DVHs are for the deliverable method and dashed for the three-dimensional (3D) optimal method.

individually optimized dose distributions does not guarantee an optimal dose distribution because $\min\{f[D(L(MU,\theta))]\}$ is a subset of $\sum_{\theta} \min\{f[D_\theta(L(MU,\theta))]\}$.

"Deliverable" means that the plan does not have MLC leaf motion exceeding the maximum velocity of the MLC leaves. The average maximum leaf velocity at the isocenter plane ranges from 3.3 to 3.9 cm/s (22). In this series of patients, this velocity is exceeded by only 3 of 10 phase transitions in 1 of 12 patients. In Patient 1, the displacement of 2.1, 1.6, and 1.6 cm was observed in subsequent phases (0.4 s apart), corresponding to the velocities of 5.3, 4.0, and 4.0 cm/s for a 4-s period, respectively. A beam hold mechanism will be a part of DMLC tracking implementation. It is not advisable to follow sharp position changes or coughing, providing that the beam hold is not applied so frequently as to significantly affect efficiency, which in this case would be 100% for 11 of 12 patients and 70% for Patient 1. The collimator rotation is not planned to be changed on a daily basis. The deliverable implementation would account for some motion perpendicular to the MLC leaf direction by readjusting the MLC positions on the basis of the plan and the estimated or measured target positions. However, if this algorithm is included in an on-line 4D adaptive therapy strategy, the collimator rotation could be changed day to day. In addition, the algorithm for collimator rotation and MLC shift is not manufacturer specific. Important MLC parameters required to implement this algorithm are a maximum leaf velocity and a fast secondary position feedback system that allows for real-time control of leaf positions.

The deliverable and 3D optimal methods were applied to 12 lung cancer patient 4D CT image sets. Two important findings are as follows. First, the deliverable method is dosimetrically robust to the variations of fractional time spent in respiratory phases on a given 4D CT scan. The deliverable

Table 3. A comparison of the dose–volume metrics of four-dimensional (4D) plans using the deliverable and three-dimensional (3D) optimal methods

	PTV		Lungs–GTV		Spinal cord	Esophagus		Heart		Thorax–PTV
	$(D_{mean})_{opt}^{del}$	$(D_{95\%})_{opt}^{del}$	$(D_{mean})_{opt}^{del}$	$(V_{20})_{opt}^{del}$	$(D_{0.1\%})_{opt}^{del}$	$(D_{mean})_{opt}^{del}$	$(V_{55})_{opt}^{del}$	$(D_{mean})_{opt}^{del}$	$(V_{40})_{opt}^{del}$	$(D_{mean})_{opt}^{del}$
Mean ± SD	1.001 ± 0.002	0.995 ± 0.009	1.00 ± 0.02	1.01 ± 0.03	1.00 ± 0.02	1.00 ± 0.02	1.02 ± 0.05	1.01 ± 0.03	1.00 ± 0.10	1.00 ± 0.01
Minimum, maximum	0.999, 1.007	0.974, 1.009	0.97, 1.03	0.97, 1.08	0.96, 1.04	0.96, 1.03	0.97, 1.11	0.95, 1.05	0.77, 1.20	0.97, 1.02
p	0.32	0.39	0.49	0.49	0.50	0.50	0.48	0.50	0.49	0.50

Abbreviations as in Table 2.

Mean and SD of the dose–volume metric ratios averaged over all 12 patients; and p values testing whether two distributions are statistically different. D_{mean} represents the dose received by mean volume of the PTV or organs at risk (OARs); $D_{A\%}$ the dose received by $A\%$ of volume of the PTV or OARs; and V_B the total volume of OARs receiving at least B Gy.

method has the same λ in Eq. (1) for all phases. Given that the dose distributions of individual phase plans using the deliverable method are very similar to one another (Table 2), the deliverable method would result in the dose distribution close to the planned dose distribution, even when a patient spends more time on one phase (*e.g.,* end-exhale) than other phases during treatment. In addition, for 4D plans, the deliverable method yields dosimetric values statistically similar to those with the 3D optimal method (Table 3). This indicates not only that the deliverable method is dosimetrically robust but also that the target deformation/rotation and hysteresis generally have little dosimetric impact for the 12-patient series studied. For each beam the collimator is rotated to align the MLC leaf motion parallel to the major axis of target motion, which is determined from the target motion in a given BEV. Therefore, the target motion perpendicular to the MLC leaf motion is relatively small (0.13 cm at the most), resulting in negligible impact on plan quality.

However, Patient 11 shows the most discrepancy in DVHs for 4D plans between the two methods (Fig. 7a), indicating that in the presence of hysteresis, the deliverable method is susceptible to plan quality degradation. In terms of target deformation/rotation, Patient 4 shows discrepancy in 4D plans between the two methods, especially for target coverage (Fig. 7f), indicating that target deformation/rotation has some dosimetric impact when the deliverable method is used.

The second important finding is that the PTV concept can cause problems in 4D IMRT planning. The 4D plans for Patient 1 are significantly inferior to individual phase plans for both methods (red in Fig. 3), mostly owing to PTV coverage (Fig. 5a). Large gradients of the deformation vector field across the PTV cause unrealistic appearance of the PTV after deformable image registration and inconsistent dose distributions after deformable dose summation (Fig. 6). This problem occurred in 1 of 12 patients in this study. Therefore, care should be taken when there is a possibility that large deformation gradients across the PTV could occur. Eliminating the PTV by using probabilistic planning approaches (29–31) is one of the solutions.

As for individual phase plans, phase-to-phase variation is generally larger than the difference between the two methods, in terms of plan quality. A more important result is the comparison of 4D plans. The 4D plan quality is similar to average quality over individual phase plans, although 3 patients have issues. Patient 1 shows degraded 4D plans for both methods due to large deformation gradients across the PTV (Fig. 7c), and Patient 4 shows a degraded deliverable 4D plan due to significant tumor volume variation (Fig. 7f). Given that Patient 11 with the most hysteresis shows the most discrepancy in the DVHs between the two 4D plans (Fig. 7a), whereas Patient 9 with the least hysteresis shows the best agreement (Fig. 7b), having motion hysteresis affects deliverable 4D plans. On the other hand, no marked differences between the two 4D plans with tumor motion or volume indicate that both tumor motion and volume do not have a significant effect on 4D plans using the deliverable method (Fig. 7c–f).

CONCLUSIONS

A deliverable 4D IMRT planning method was developed and applied to 12 patient 4D CT image sets. This method yields similar dose distributions for each of the individual phase plans and statistically equivalent dosimetric values compared with the 3D optimal method, indicating that the deliverable method is dosimetrically robust to the variations of fractional time spent in respiratory phases on a given 4D CT scan. Nonlinear target motion and deformation do not cause significant dose discrepancies.

The deliverable 4D IMRT planning method has a clear path to clinical implementation. The clinical application and integration with DMLC tumor tracking delivery research is the subject of ongoing development.

REFERENCES

1. Keall PJ, Chen GTY, Joshi S, *et al*. Time-the fourth dimension in radiotherapy (ASTRO Panel discussion). *Int J Radiat Oncol Biol Phys* 2003;57:S8–S9.
2. Murphy MJ. Tracking moving organs in real time. *Semin Radiat Oncol* 2004;14:91–100.
3. Bortfeld T. IMRT: A review and preview. *Phys Med Biol* 2006; 51:R363–R379.
4. Webb S. IMRT delivery techniques. In: Bortfeld T, Schmidt-Ullrich RK, DeNeve W, editors. Image-guided IMRT. Heidelberg: Springer-Verlag; 2006. p. 73–90.
5. Keall PJ, Siebers JV, Joshi S, *et al*. Monte Carlo as a four-dimensional radiotherapy treatment-planning tool to account for respiratory motion. *Phys Med Biol* 2004;49:3639–3648.
6. McClelland JR, Webb S, McQuaid D, *et al*. Tracking 'differential organ motion' with a 'breathing' multileaf collimator: magnitude of problem assessed using 4D CT data and a motion-compensation strategy. *Phys Med Biol* 2007;52:4805–4826.
7. McMahon R, Papiez L, Rangaraj D. Dynamic-MLC leaf control utilizing on-flight intensity calculations: A robust method for real-time IMRT delivery over moving rigid targets. *Med Phys* 2007;34:3211–3223.
8. McQuaid D, Webb S. IMRT delivery to a moving target by dynamic MLC tracking: Delivery for targets moving in two dimensions in the beam's eye view. *Phys Med Biol* 2006;51:4819–4839.
9. Neicu T, Shirato H, Seppenwoolde Y, *et al*. Synchronized moving aperture radiation therapy (SMART): Average tumour trajectory for lung patients. *Phys Med Biol* 2003;48:587–598.
10. Papiez L. The leaf sweep algorithm for an immobile and moving target as an optimal control problem in radiotherapy delivery. *Mathematical and Computer Modelling* 2003;37:735–745.
11. Papiez L. DMLC leaf-pair optimal control of IMRT delivery for a moving rigid target. *Med Phys* 2004;31:2742–2754.
12. Papiez L, Rangaraj D. DMLC leaf-pair optimal control for mobile, deforming target. *Med Phys* 2005;32:275–285.
13. Papiez L, Rangaraj D, Keall PJ. Real-time DMLC IMRT delivery for mobile and deforming targets. *Med Phys* 2005;32: 3037–3048.
14. Rangaraj D, Papiez L. Synchronized delivery of DMLC intensity modulated radiation therapy for stationary and moving targets. *Med Phys* 2005;32:1802–1817.
15. Schlaefer A, Fisseler J, Dieterich S, *et al*. Feasibility of four-dimensional conformal planning for robotic radiosurgery. *Med Phys* 2005;32:3786–3792.
16. Trofimov A, Rietzel E, Lu HM, *et al*. Temporo-spatial IMRT optimization: Concepts, implementation and initial results. *Phys Med Biol* 2005;50:2779–2798.
17. Webb S. The effect on IMRT conformality of elastic tissue movement and a practical suggestion for movement compensation via the modified dynamic multileaf collimator (dMLC) technique. *Phys Med Biol* 2005;50:1163–1190.
18. Webb S. Quantification of the fluence error in the motion-compensated dynamic MLC (DMLC) technique for delivering intensity-modulated radiotherapy (IMRT). *Phys Med Biol* 2006; 51:L17–L21.
19. Webb S, Binnie DM. A strategy to minimize errors from differential intrafraction organ motion using a single configuration for a 'breathing' multileaf collimator. *Phys Med Biol* 2006;51: 4517–4531.
20. Zhang T, Jeraj R, Keller H, *et al*. Treatment plan optimization incorporating respiratory motion. *Med Phys* 2004;31:1576–1586.
21. Zhang T, Lu W, Olivera GH, *et al*. Breathing-synchronized delivery: A potential four-dimensional tomotherapy treatment technique. *Int J Radiat Oncol Biol Phys* 2007;68:1572–1578.
22. Wijesooriya K, Bartee C, Siebers JV, *et al*. Determination of maximum leaf velocity and acceleration of a dynamic multileaf collimator: implications for 4D radiotherapy. *Med Phys* 2005; 32:932–941.
23. Weiss E, Siebers JV, Keall PJ. An analysis of 6-MV versus 18-MV photon energy plans for intensity-modulated radiation therapy (IMRT) of lung cancer. *Radiother Oncol* 2007;82:55–62.
24. Weiss E, Wijesooriya K, Dill SV, *et al*. Tumor and normal tissue motion in the thorax during respiration: Analysis of volumetric and positional variations using 4D CT. *Int J Radiat Oncol Biol Phys* 2007;67:296–307.
25. Christensen G, Joshi S, Miller M. Volumetric transformation of brain anatomy. *IEEE Trans Med Imaging* 1997;16:864–877.
26. Foskey M, Davis B, Goyal L, *et al*. Large deformation three-dimensional image registration in image-guided radiation therapy. *Phys Med Biol* 2005;50:5869–5892.
27. Giraud P, Antoine M, Larrouy A, *et al*. Evaluation of microscopic tumor extension in non-small-cell lung cancer for three-dimensional conformal radiotherapy planning. *Int J Radiat Oncol Biol Phys* 2000;48:1015–1024.
28. Seppenwoolde Y, Shirato H, Kitamura K, *et al*. Precise and real-time measurement of 3D tumor motion in lung due to breathing and heartbeat, measured during radiotherapy. *Int J Radiat Oncol Biol Phys* 2002;53:822–834.
29. Beckham W, Keall P, Siebers J. A fluence-convolution method to calculate radiation therapy dose distributions that incorporate random set-up error. *Phys Med Biol* 2002;47:3465–3473.
30. Gordon J, Crimaldi A, Hagan M, *et al*. Evaluation of clinical margins via simulation of patient setup errors in prostate IMRT treatment plans. *Med Phys* 2007;34:202–214.
31. Unkelbach J, Oelfke U. Inclusion of organ movements in IMRT treatment planning via inverse planning based on probability distributions. *Phys Med Biol* 2004;49:4005–4029.

Appendix C

FOUR-DIMENSIONAL IMRT TREATMENT PLANNING USING A DMLC MOTION-TRACKING ALGORITHM

Yelin Suh

Amit Sawant

Raghu Venkat

Paul J. Keall

Physics in Medicine and Biology (in press), 2009

4D IMRT treatment planning using a DMLC motion-tracking algorithm

Yelin Suh[1,2], Amit Sawant[2], Raghu Venkat[2], and Paul J. Keall[2]

[1] Department of Radiation Oncology, Virginia Commonwealth University, Richmond, VA;
[2] Department of Radiation Oncology, Stanford University, Stanford, CA

Abstract

The purpose of this study is to develop a four-dimensional (4D) intensity-modulated radiation therapy (IMRT) treatment-planning method by modifying and applying a dynamic multileaf collimator (DMLC) motion-tracking algorithm. The 4D radiotherapy treatment scenario investigated is to obtain a 4D treatment plan based on a 4D computed tomography (CT) planning scan and to have the delivery flexible enough to account for changes in tumor position during treatment delivery. For each of 4D CT planning scans from 12 lung cancer patients, a reference phase plan was created; and with its MLC leaf positions and three-dimensional (3D) tumor motion, the DMLC motion-tracking algorithm generated MLC leaf sequences for the plans of other respiratory phases. Then, a deformable dose-summed 4D plan was created by merging the leaf sequences of individual phase plans. Individual phase plans, as well as the deformable dose-summed 4D plan are similar for each patient, indicating that this method is dosimetrically robust to the variations of fractional time spent in respiratory phases on a given 4D CT planning scan. The 4D IMRT treatment-planning method utilizing the DMLC motion-tracking algorithm explicitly accounts for 3D tumor motion and thus hysteresis and non-linear motion, and is deliverable on a linear accelerator.

1. Introduction

Effective management of intrafraction tumor motion has been one of the outstanding issues in modern radiotherapy, especially for the treatment of thoracic and abdominal tumors. Four-dimensional (4D) radiotherapy to incorporate tumor motion strives to minimize the effect of temporal anatomic changes during irradiation (Keall *et al.* 2006). From an implementation standpoint, 4D radiotherapy consists of three tasks: (1) characterizing anatomic motion, (2) creating a treatment plan that accounts for this motion, and (3) delivering this treatment plan to the moving anatomy optimally. The first task has been greatly facilitated through the increased use of 4D computed tomography (CT) that provides accurate anatomic motion information. The third task has been investigated and/or clinically implemented by breath-hold or respiratory-gating techniques, or tumor tracking using a dynamic multileaf collimator (DMLC) technique or a robotic couch (Keall *et al.* 2006); and repositioning the radiation beam to track the moving tumor using DMLC is shown to be a promising method to deliver a 4D radiotherapy treatment (Webb 2006a). However, creating DMLC leaf sequences to generate a treatment plan that accounts for moving anatomy continues to be a challenge.

Despite its benefit of target dose conformality and normal tissue sparing, intensity-modulated radiation therapy (IMRT) is known to be more susceptible to tumor motion compared with conventional treatment techniques. This is especially the case with an IMRT treatment delivered by a DMLC technique (Bortfeld 2006, Webb 2006b). In addition, a constraint on 4D IMRT treatment planning, which is not found in three-dimensional (3D) IMRT cases, is that leaf sequences need to be specifically designed such that the maximum leaf dynamics (velocity and acceleration/deceleration) are rarely exceeded when tracking anatomic motion with an MLC. This mechanical leaf motion constraint adds additional complexity in IMRT treatment planning on 4D CT data sets.

There have been studies on a 4D IMRT treatment-planning optimization and its delivery using a DMLC technique. Trofimov *et al*. compared different approaches of a 4D IMRT optimization sorted by increasing complexity of delivery, and showed that tumor tracking was better than other techniques (Trofimov *et al.* 2005). They provided a good framework to formulate 4D IMRT treatment-planning optimization problems. However, they did not investigate the robustness of the optimization methods with respect to the delivery methods, thus their study did not create leaf sequences nor include mechanical limitations of a treatment machine, such as MLC leaf motion constraints. Webb *et al*. have developed motion-compensated DMLC techniques to deliver an IMRT treatment. They first proposed a method to account for one-dimensional (1D) rigid body translation, which was based on a modification of the DMLC IMRT technique whereby MLC leaves were arranged to change according to patient breathing (Webb 2005). They then implemented a strategy to minimize the geometric mismatch between MLC leaf and anatomic locations in one dimension and two dimensions, to find the optimal leaf trajectories, including the maximum leaf velocity constraint (Webb and Binnie 2006, McClelland *et al.* 2007). They also investigated a modified DMLC delivery technique for tumor tracking by using a leaf synchronization technique (McQuaid and Webb 2006). Their motion model was constructed from a patient 4D CT scan, but their strategy was not a full 4D optimization, and they did not demonstrate implementation with a cohort of patients. Papiez *et al*. have developed algorithms for optimized DMLC IMRT delivery for mobile and deforming targets. They demonstrated DMLC leaf sequencing for the target motion in real time and when *a priori* motion information was available in one dimension, but as of yet not for three dimensions (Papiez 2003, Papiez 2004, Papiez and Rangaraj 2005, Papiez *et al.* 2005, Rangaraj and Papiez 2005, McMahon *et al.* 2007, Papiez *et al.* 2007). Recently, they applied a real-time DMLC control algorithm for IMRT treatment delivery to targets moving two-dimensionally in a beam's eye view

(BEV), using a leaf-pair shifting technique (McMahon *et al.* 2008, Rangaraj *et al.* 2008). However, their investigations focused on real-time delivery of an IMRT treatment, and thus they did not look at how to create treatment plans for DMLC IMRT. Zhang *et al.* incorporated the respiratory target motion and deformation into a treatment-planning optimization for helical tomotherapy delivery (Zhang *et al.* 2004, Zhang *et al.* 2007). They showed breathing-correlated delivery of radiation for periodic and reproducible breathing patterns, but only for one lung case. Schlaefer *et al.* investigated an approach to consider the relative motion of organs during treatment planning for robotic radiosurgery (Schlaefer *et al.* 2005). However, their study was restricted to a phantom case. Alasti *et al*. suggested a 4D-weighted MLC position as a function of breathing phase and weighting factor (Alasti *et al.* 2006). Their 4D-weighted MLC field was based on the MLC position for the static field combined with the dynamic MLC position for the 4D dynamic field, which allowed MLC leaves to follow a moving tumor. However, they did not consider the mechanical constraints of an MLC, and their study was phantom-based. Tewatia *et al*. proposed procedures of treatment planning for a breathing-synchronized delivery technique and its delivery (Tewatia *et al.* 2006). The motion was directly overlaid to the DMLC leaf position, and violations of the mechanical limitations of the hardware were to be avoided at a treatment-planning stage. However, the motion was incorporated into treatment planning after a plan optimization by superimposing target displacement on the leaf positions, which was not optimal leaf sequencing for 4D treatment planning. This study was also phantom-based. To date, no other groups have reported techniques that develop leaf sequences as a function of respiratory phase. Therefore, an optimal 4D IMRT treatment-planning method that includes MLC leaf motion constraints and is robust to the variations of fractional time spent in respiratory phases within a given 4D CT planning scan has yet to be developed.

In our previous study, a deliverable 4D IMRT treatment-planning method, which

accounted for tumor motion in only one dimension, was proposed (Suh *et al.* 2008b). A treatment plan for each of the respiratory phases was created by shifting leaf positions of the reference phase plan to the given phase (from solid red to dashed red apertures on the left side in figure 1) along the MLC leaf travel direction. The study showed that accounting for 1D tumor translation was not only practical, but also provided a reasonable approximation. In this work, we describe a methodology that accounts for more complex, 3D tumor motion (see the right side of figure 1). This method utilizes an algorithm developed for real-time DMLC motion tracking (Sawant *et al.* 2008) in an offline manner in order to create 4D IMRT treatment plans. Such a plan explicitly accounts for 3D tumor motion and consequently hysteresis and non-linear motion (Seppenwoolde *et al.* 2002, Suh *et al.* 2008a), and it is deliverable on a linear accelerator.

Therefore, the aim of this study is to develop a 4D IMRT treatment-planning method by modifying and applying a DMLC motion-tracking algorithm.

2. Materials and Methods

2.1. Treatment scenario

Three-dimensional IMRT aims to create a treatment plan from one CT image, resulting in MLC leaf sequences as a function of monitor units (MU), $L(MU)$. Four-dimensional IMRT, in which modulating the radiation beam to temporally changing anatomy is explicitly included, aims to create a treatment plan on a CT image set of multiple respiratory phases, resulting in leaf sequences as a function of MU and respiratory phase (θ), $L(MU, \theta)$. Thus, a 4D radiotherapy treatment scenario investigated is to obtain a 4D treatment plan from a 4D CT planning scan and to have delivery flexible enough to account for changes in tumor positions, tumor drift, and/or breathing patterns during treatment delivery.

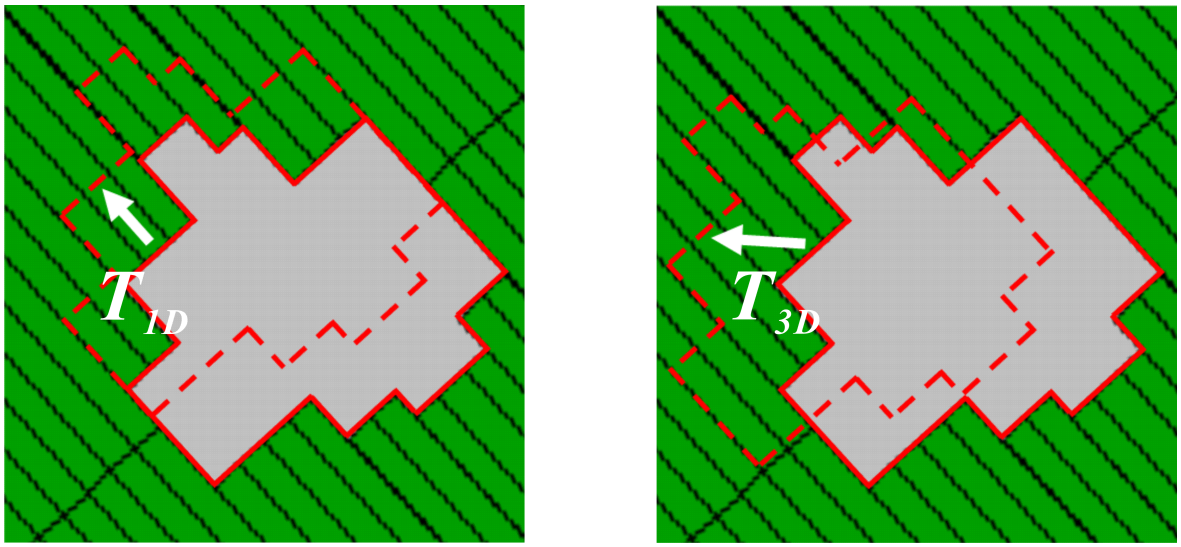

Figure 1. Comparison of the creation of a four-dimensional treatment plan using one-dimensional (1D) translation of multileaf collimator (MLC) leaves from the reference phase (solid red) to a given phase (dashed red) (left) with that using the DMLC motion-tracking algorithm to move MLC leaves to track three-dimensional (3D) tumor motion (right). Only the motion along the MLC leaf travel direction, T_{1D}, is accounted for on the left; whereas 3D tumor motion, T_{3D}, is accounted for on the right side.

2.2. DMLC motion-tracking algorithm

The DMLC motion-tracking algorithm dynamically tracks moving targets in three dimensions using real-time target location data from an independent position-monitoring system to account for tumor motion during treatment (Sawant *et al.* 2008). This algorithm was designed to (a) read initial MLC leaf positions as a function of MU from an MLC leaf sequence derived from a treatment plan; (b) dynamically calculate MLC leaf positions to account for target position changes using real-time 3D target location data from a position-monitoring system; (c) generate new MLC leaf positions as a function of MU and 3D target location by modifying the initial leaf positions in (a) with the calculated leaf positions in (b); and (d) send the generated MLC leaf sequence to a treatment machine to reposition the beam in real time. Further details for this algorithm

are described previously (Sawant *et al.* 2008). For 4D treatment planning, the DMLC motion-tracking algorithm was modified to include the respiratory phase as an additional parameter and to be used in an offline mode.

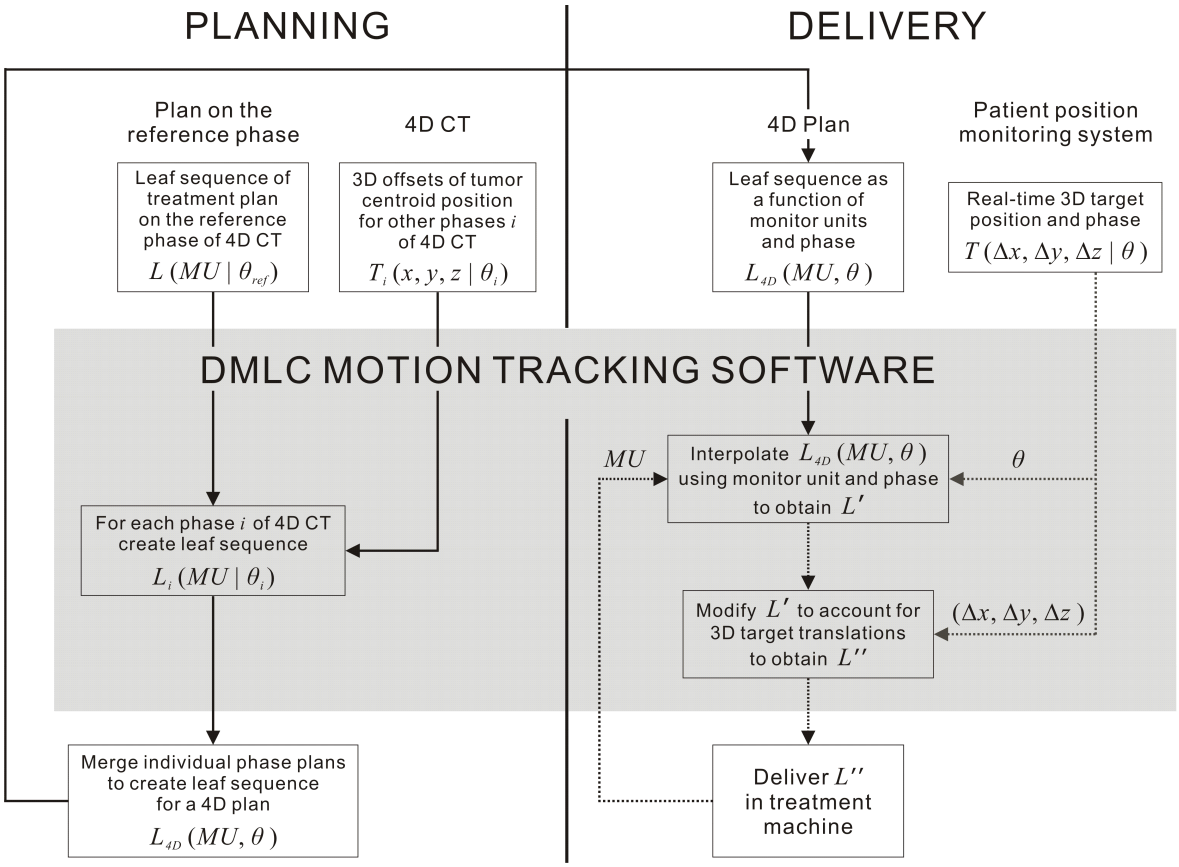

Figure 2. Use of the dynamic multileaf collimator motion-tracking algorithm for both planning and delivery of four-dimensional radiotherapy treatment. Dashed lines indicate real-time processes and solid lines are not real time. CT = computed tomography; L = leaf sequence; MU = monitor units; θ = respiratory phase; T = three-dimensional target position and phase information.

2.3. 4D IMRT treatment planning

The 4D CT image sets used in this study are from 12 lung cancer patients acquired as a part of an institutional review board-approved study (protocol 00-202) at the University of Texas M. D. Anderson Cancer Center. Table 1 shows the volume and the centroid motion range of patients' gross tumor volume (GTV). A commercially available planning system (Pinnacle version 7.9, Philips Medical Systems, Milpitas, CA) was used for contouring, planning, and an IMRT optimization. Using the manually segmented contours on the end-inhale phase of the 4D CT scans and large deformation diffeomorphic image registration (Christensen *et al.* 1997, Foskey *et al.* 2005), contours on the other respiratory phases were automatically generated. The clinical target volume enclosed the GTV with an isotropic 8-mm margin, and then a 5-mm margin was added isotropically to create the planning target volume (PTV). For IMRT treatment planning, the prescribed dose was 74 Gy and beam arrangements were six coplanar, non-opposed, predominantly anterior-posterior fields. Further details for the 4D CT data set, patient characteristics, contouring, planning, and an IMRT optimization are described elsewhere (Weiss *et al.* 2007a, Weiss *et al.* 2007b, Suh *et al.* 2008b).

The DMLC motion-tracking algorithm requires two inputs: an initial MLC leaf sequence and real-time 3D target location and phase information. The input MLC leaf sequence was derived from an IMRT treatment plan that was created on the reference phase 4D CT image. From a delivery perspective, real-time target location and phase information is necessary to reposition the beam in real time; for planning purposes, however, 3D offsets of the tumor centroid position for each phase relative to that for the reference phase were used instead. Figure 2 shows a flow diagram of using the same algorithm for both planning and delivery of 4D radiotherapy treatment.

Table 1. Patient gross tumor volume (GTV), GTV centroid motion range, and three-dimensional (3D) offsets of the tumor centroid position

	Mean (minimum, maximum)		3D offsets of tumor centroid position (cm) Mean (maximum)		
Patient no.	GTV volume (cm^3)	GTV centroid motion (cm)	Parallel to the major axis	Perpendicular to the major axis	Along the beam direction
1	3.0	2.1	0.9 (2.1)	0.1 (0.1)	0.2 (0.4)
2	61.0	0.4	0.2 (0.4)	0.1 (0.1)	0.1 (0.3)
3	12.5	0.5	0.3 (0.5)	0.1 (0.2)	0.1 (0.2)
4	1.0	0.6	0.3 (0.6)	0.1 (0.1)	0.2 (0.4)
5	20.4	0.1	0.1 (0.1)	0.0 (0.0)	0.1 (0.1)
6	5.2	0.4	0.3 (0.4)	0.1 (0.1)	0.1 (0.1)
7	323.6	0.2	0.1 (0.2)	0.1 (0.1)	0.1 (0.1)
8	23.0	0.3	0.1 (0.2)	0.0 (0.0)	0.1 (0.2)
9	6.1	0.2	0.1 (0.2)	0.1 (0.1)	0.1 (0.2)
10	7.5	0.5	0.2 (0.4)	0.1 (0.1)	0.1 (0.1)
11	119.2	1.3	0.7 (1.3)	0.1 (0.2)	0.1 (0.2)
12	7.5	1.1	0.5 (1.1)	0.1 (0.1)	0.1 (0.1)
	49.2 (1.0, 323.6)	0.7 (0.1, 2.1)			

The steps to create a 4D IMRT treatment plan using the DMLC motion-tracking algorithm for each patient are as follows.

(a) For an IMRT treatment plan on the reference phase CT image, an appropriate beam angle arrangement was determined according to the tumor locations. From the tumor centroid position for each respiratory phase, which was quantified from the 4D CT image set, a major axis of tumor motion in each BEV was automatically determined using a least-squares fit (Suh *et al.* 2008b). Then,

the collimator was rotated to align the MLC leaf travel direction parallel to the major axis of tumor motion. Overall mean of the collimator angles calculated was 88°, ranging from 10° to 170° (12 reference plans with 6 beam angles each). This collimator rotation was performed because of the known decrease in delivery efficiency for the motion perpendicular to the MLC leaf travel direction (Sawant *et al.* 2008). As shown by Sawant *et al*., efficiency of IMRT delivery for the motion perpendicular to the MLC leaf travel direction is significantly lower than that for the motion parallel to the MLC leaf travel direction. For each beam, 3D offsets of the tumor centroid position for each phase i relative to that for the reference phase were calculated as the motion parallel to the major axis, the motion perpendicular to the major axis, and the motion along the beam direction, $T_i(x, y, z \mid \theta_i)$ (table 1). With the rotated collimator, an appropriate IMRT treatment plan was created on the reference phase 4D CT image (an end-exhale phase was used as the most stable phase during respiration (Seppenwoolde *et al.* 2002), where an initial MLC leaf sequence, $L(MU \mid \theta_{ref})$, was then derived.

(b) With the MLC leaf positions from the initial leaf sequence and the 3D tumor centroid position offsets, the DMLC motion-tracking algorithm generated a set of MLC leaf sequences for each phase of the 4D CT scan, $L_i(MU \mid \theta_i)$, which then was used to create IMRT treatment plans for individual respiratory phases.

(c) The leaf sequences of individual phase plans were merged to create a leaf sequence for a 4D plan, $L_{4D}(MU, \theta)$. Using a deformable dose summation (Christensen *et al.* 1997, Keall *et al.* 2004, Zhang *et al.* 2004, Foskey *et al.* 2005), the resultant doses from all individual phase plans were accumulated on an end-inhale CT image, and a deformable dose-summed 4D plan was created. A 4D

dose distribution is given by

$$D = \sum_{i=1}^{P} \lambda_i D_i \left(I_i, I_{ref}, u(\theta_i), L_i(MU, \theta_i) \right), \qquad (1)$$

where i is a respiratory phase index from 1 to the maximum number of phases, P ($P = 10$ in this study); λ_i is fractional time spent per phase, which in this study was assumed to be the same for all the phases; and D_i is a dose of a treatment plan for a given phase. D_i was computed on the given phase CT image, I_i, on the basis of leaf sequences as a function of MU and θ_i, $L_i(MU, \theta_i)$, and then deformed to the reference phase CT image used for a dose summation, I_{ref}, by a displacement vector field, $u(\theta_i)$, computed using deformable image registration.

Once the MLC leaf sequence for a 4D plan merging individual phase plans (on the bottom left in figure 2) was created, it was used as an initial leaf sequence on the delivery side as in figure 2. The MU and real-time 3D target position and phase, $T(\Delta x, \Delta y, \Delta z \mid \theta)$, were determined from a treatment machine and a patient position-monitoring system, respectively. The DMLC motion-tracking algorithm software interpolated the initial leaf sequence, $L_{4D}(MU, \theta)$, using both MU and θ to obtain a new leaf sequence, L'; and then modified L' using $(\Delta x, \Delta y, \Delta z)$ to obtain the final leaf sequence, L'', that accounted for 3D target motion. The L'' then was sent to a treatment machine and delivered. The feasibility of delivery of such 4D plans using this method was experimentally validated in a separate work (Keall *et al.* 2008).

It is important to note that it is possible to use the reference phase plan and track the tumor without creating either individual phase plans or a 4D plan. However, the reason we generated individual phase plans was that we wanted to have a plan that was the

best estimate of the dose delivered to the patient, which was a 4D plan merging all individual phase plans. Possibly there is relative motion between the target and surrounding normal tissues from phase to phase (Weiss *et al.* 2007b) that could result in different dose distributions for individual phase plans from those for the reference plan; then a 4D plan also would be different from the reference plan. As shown in our previous study (Suh *et al.* 2008b), a 4D plan was different from the plans for any single phases, at least slightly; and for some patients with bigger target motion or, more importantly, more relative motion between the target and organs, the reference plan was quite different from a 4D plan and also from individual phase plans. Our treatment planning method was developed especially for this type of patients. Therefore, a 4D plan was generated instead of using the reference plan. This 4D plan gives us an estimate of the 4D dose distribution for the patient.

To evaluate the treatment plans generated, the composite objective values (COVs) and dose-volume evaluation metrics derived from the dose-volume histograms (DVHs) were used. The COV, a single number, is an indicator of treatment plan quality that takes into account actually achieved dose distributions for the PTV and organs at risk (OARs) after the plan optimization, relative to the initial constraints (Weiss *et al.* 2007a, Suh *et al.* 2008b). The smaller the COV, the better the treatment plan.

3. Results

Figures 3 and 4 show the DVHs and the COVs, respectively, of all 10 individual phase plans with a deformable dose-summed 4D plan generated using the DMLC motion-tracking algorithm for each patient. The respiratory phase indices of 0 and 5 represent the end-inhale and end-exhale phase, respectively, with a respiratory cycle divided into 10 phases of equal duration. The DVHs of the plans for individual phases of the 4D CT scan

are, in general, similar to those of the reference phase plan, as well as to a deformable dose-summed 4D plan. The target coverage is similar from phase to phase, except for Patients 1 and 11 (whose cases will be discussed later in this section), whereas the DVHs for OARs show variation. This variation is due to an intrinsic drawback of all tumor-tracking methods, which only track the tumor motion, not the motion of whole patient anatomy (Weiss *et al.* 2007b). That is, individual phase plans generated using the DMLC motion-tracking algorithm do not account for the phase-to-phase positional changes of OARs with respect to the tumor and/or to the BEV. In terms of overall plan quality (i.e., COV), most patients show similar plan qualities over individual phase plans (figure 4), except for Patients 1 and 4 (whose cases will be discussed later in this section). Figure 4 also indicates that a COV of a deformable dose-summed 4D plan for each patient is, in general, similar to the average values over all individual phase plans per patient.

There is variation in the COVs of individual phase plans for Patients 1 and 4 (red and blue in figure 4). Figure 5 shows the DVHs of plans for Phases 1, 2, and 4, which have worse plan quality than the other phase plans, compared with the reference phase plan, for Patient 1. The isodose distributions for these phase plans are shown in figure 6. Compared with the Phase 5 plan, plans for Phases 1, 2, and 4 have worse PTV coverage as seen in the transverse, coronal, and sagittal planes. This is due to artifacts in the 4D CT image set of Patient 1 and also tumor volume differences caused by the artifacts (worst for Phase 1 in coronal and sagittal planes as in figure 6). The mean of relative tumor volume of each phase to Phase 5 is 0.96, ranging from 0.79 to 1.07. Patient 4 shows not only phase-to-phase variation in plan quality but also a trend wherein the farther the respiratory phases are from Phase 5, the worse the plan quality becomes (blue in figure 4). This is explained by the tumor volume variation during the respiratory cycle of Patient 4. The mean of relative tumor volume of each phase to Phase 5 is 0.92, ranging from 0.86 to 1.00. The significant variation in tumor volume causes inferior PTV coverage, especially for

plans on the phases further away from Phase 5, as shown in the isodose distributions in figure 7.

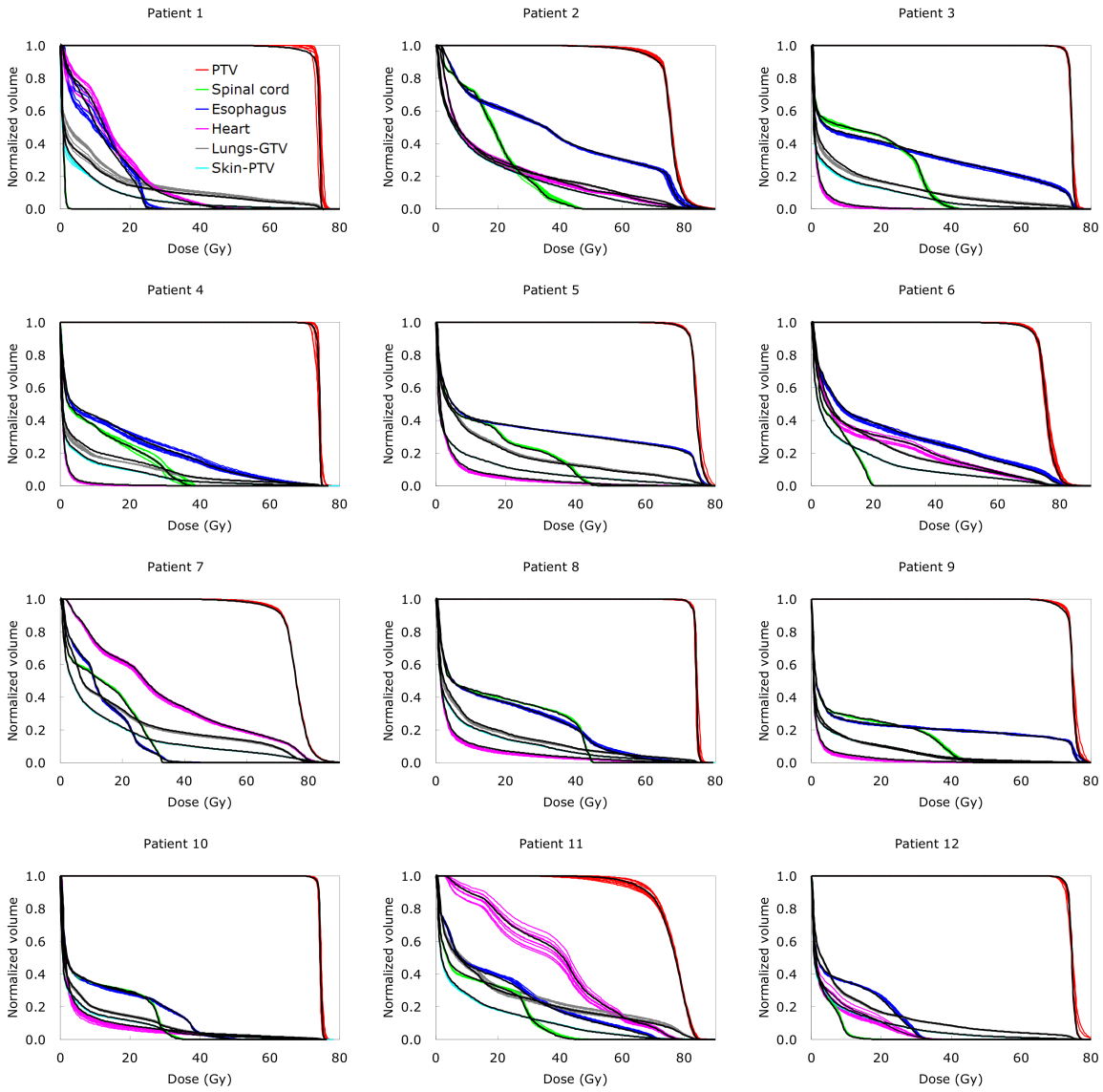

Figure 3. Dose-volume histograms (DVHs) of individual respiratory phase plans (thin colored DVHs) and a deformable dose-summed four-dimensional plan (black thick DVHs) for each of 12 patients. PTV = planning target volume; GTV = gross tumor volume.

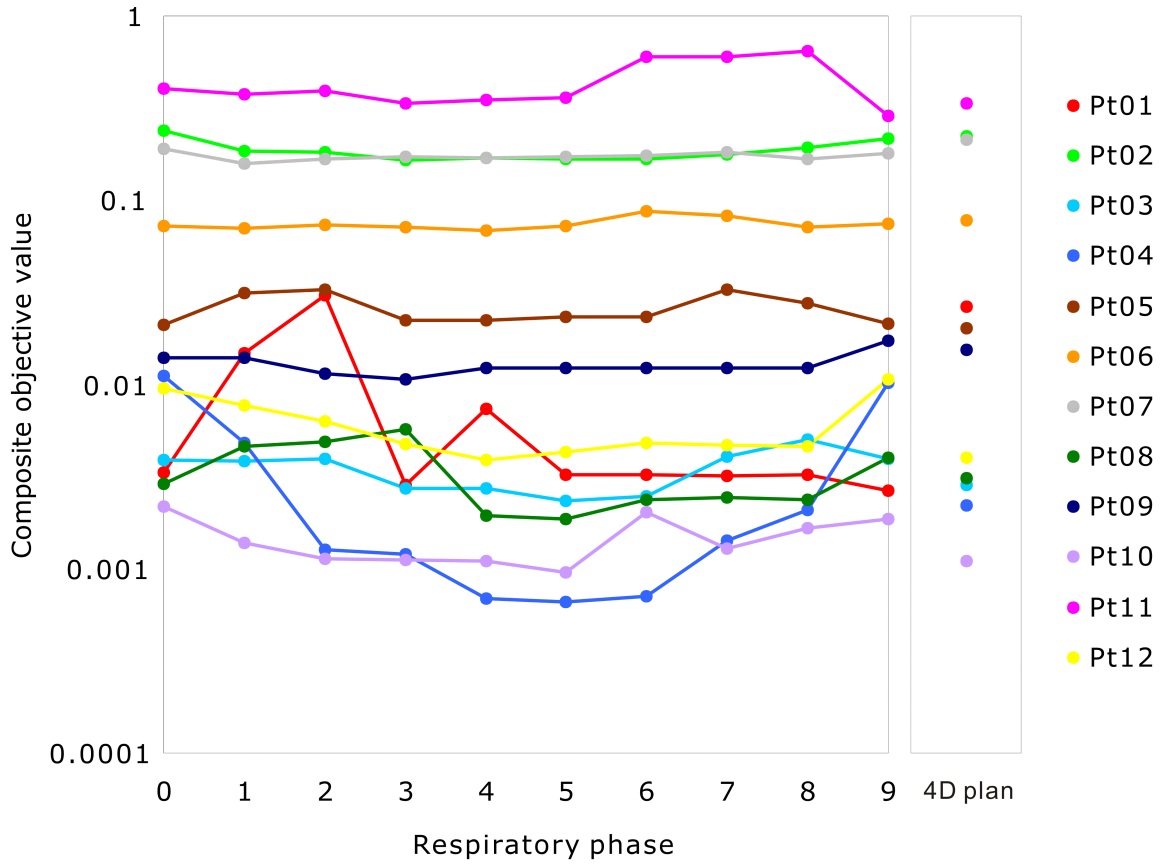

Figure 4. Composite objective values (COVs) of individual respiratory phase plans and a deformable dose-summed four-dimensional (4D) plan for each of 12 patients. The smaller the COV, the better the treatment plan. The COV of the deformable dose-summed 4D plan for each patient is the approximate average value over all individual phase plans per patient.

Whereas Patients 1 and 4 show phase-to-phase variation in both the COVs and the DVHs, the COVs for Patient 11 do not vary significantly from phase to phase (pink in figure 4) but the DVHs do vary (figure 3). Patient 11 actually shows the most discrepancy in the DVHs from phase to phase for both the PTV and OARs. The tumor of Patient 11 shows the second largest volume, the second most motion, and the most hysteresis during respiration (table 1), which all cause phase-to-phase variation in treatment plans. The large tumor volume changes treatment plans from phase to phase due to stressing the optimization algorithm with more constraints to balance; and the motion and hysteresis change treatment plans due to changes in the geometric relation between the tumor and normal anatomy from phase to phase. Nonetheless, the DVHs of the deformable dose-summed 4D plan for Patient 11 show the approximate average of the DVHs for individual phase plans (figure 3).

The deformable dose-summed 4D plan for Patient 1 is significantly worse than all individual phase plans (red in figure 4). The degraded 4D plan for Patient 1 also is evident in the DVHs in figure 3, primarily due to inferior PTV coverage. Large gradients of the deformation vector field, u, across the PTV deteriorate target coverage resulting in the deformable dose-summed 4D plan much worse than all individual phase plans discussed in the previous study (Suh *et al.* 2008b).

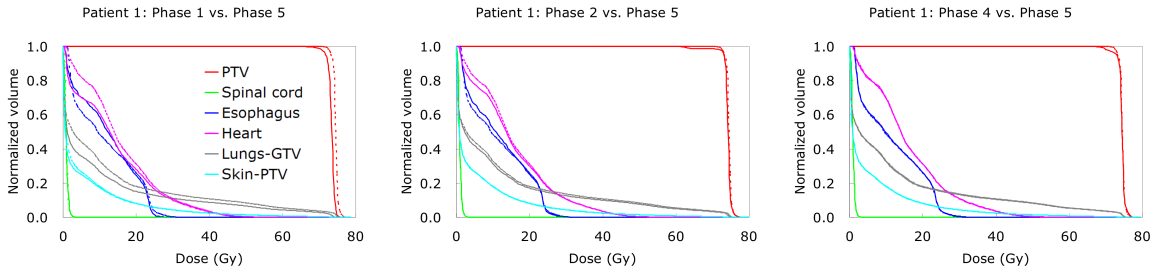

Figure 5. Dose-volume histograms (DVHs) of plans for Phases 1, 2, and 4 (solid DVHs), compared with those of Phase 5 plan (dotted DVHs) for Patient 1. PTV = planning target volume; GTV = gross tumor volume.

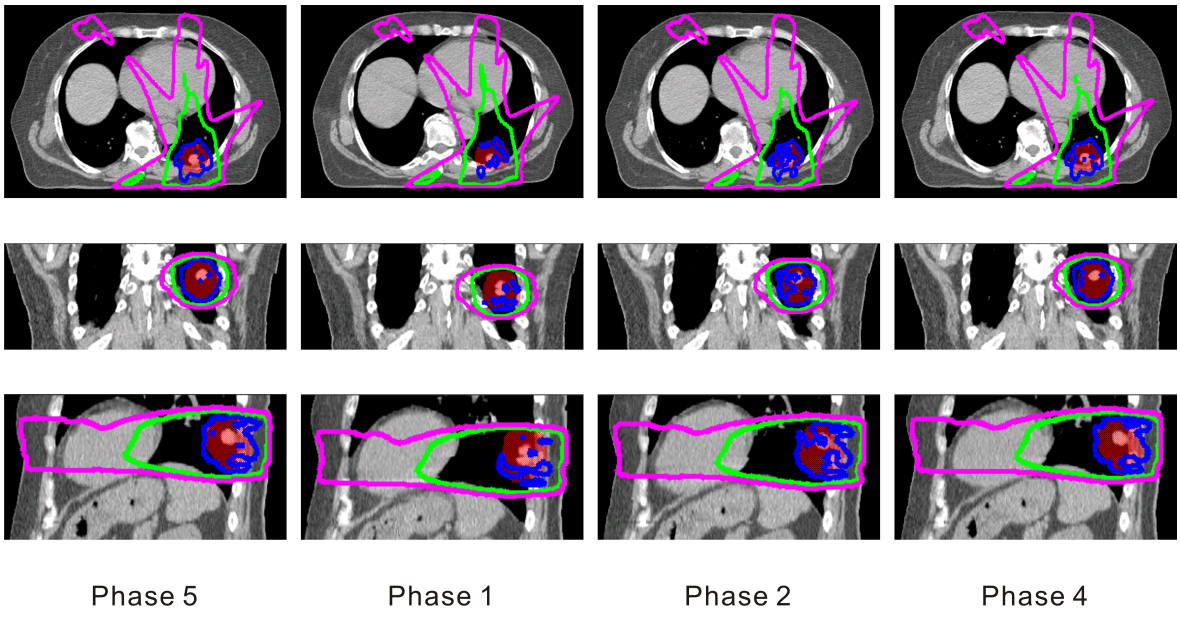

Figure 6. Isodose distributions of plans for Phases 1, 2, 4, and 5 for Patient 1 in transverse, coronal, and sagittal planes. The planning target volume is shaded in red; blue isodose curves indicate 74 Gy, green 40 Gy, and pink 20 Gy.

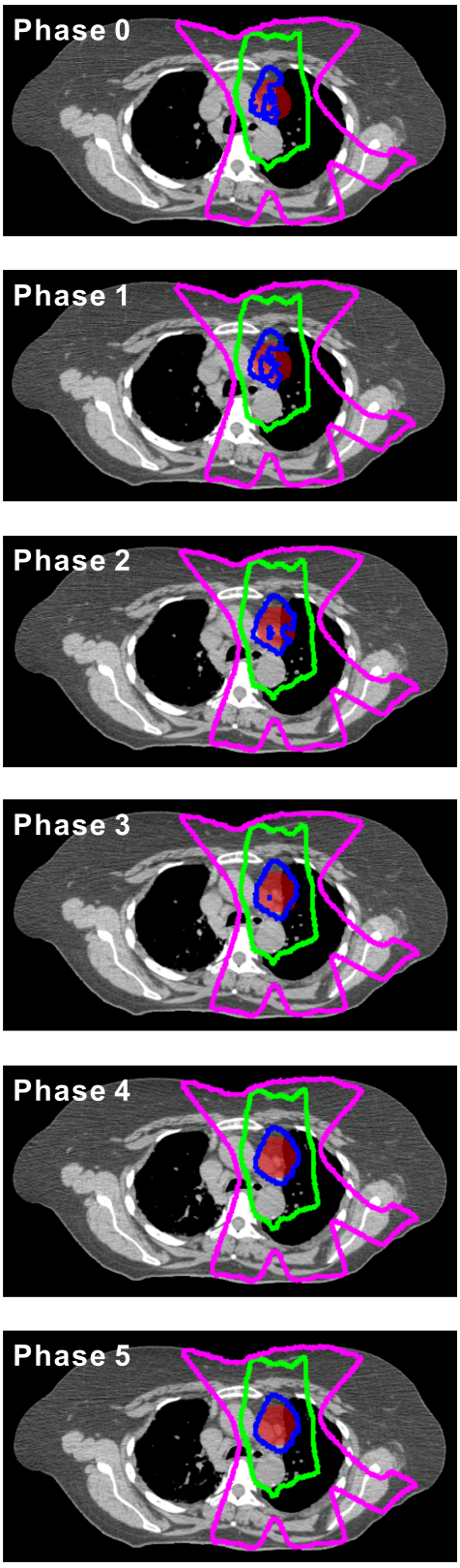

Figure 7. Isodose distributions of plans for Phases 0 to 5 for Patient 4. The planning target volume is shaded in red; blue isodose curves indicate 74 Gy, green 40 Gy, and pink 20 Gy.

4. Discussion

A deliverable 4D IMRT treatment-planning method for DMLC tumor tracking delivery that accounts for 1D tumor translation in the major axis only was previously developed (Suh *et al.* 2008b). It was a proof-of-principal study demonstrating that the deliverable 4D IMRT treatment-planning method is feasible. Though a 1D correction may be better than no correction, tumor motion is known to exhibit hysteresis and non-linear behavior (Seppenwoolde *et al.* 2002, Suh *et al.* 2008a). The current study modified and integrated a DMLC tumor-tracking algorithm (Sawant *et al.* 2008) in the deliverable 4D IMRT treatment-planning method. Thus, 3D translational tumor motion observed during the 4D CT planning scan is explicitly included in 4D treatment planning. Any changes in the motion observed during treatment delivery can be accounted for by using the algorithm during delivery. That is, the same algorithm is called for both planning and delivery of 4D IMRT treatment. This symmetry between planning and delivery for determining leaf sequences lends itself to clinical viability.

The 4D IMRT treatment plans created using the DMLC motion-tracking algorithm account for 3D tumor motion, and thus implicitly account for hysteresis and non-linear motion. However, the rotations or deformations within a respiratory cycle and the differential motion of a tumor and normal tissues are not accounted for, as this algorithm is based on the assumptions that a tumor is rigid and does not undergo in- or out-plane rotations or deformations and the entire anatomy moves. The greater the respiratory tumor motion, the greater the improvement in a resultant treatment plan will be when the off-axis motion of tumor is taken into account. The 4D IMRT treatment-planning method developed in this study creates deformable dose-summed 4D plans with a quality level somewhere between the deliverable and the 3D optimal treatment plans in a previous study (Suh *et al.* 2008b).

Like currently available 3D radiotherapy treatment, some approximations are being made for 4D treatment planning and delivery. The 4D treatment planning is based on a 4D CT planning scan, which is usually taken long before actual delivery. Guckenberger *et al*. showed that respiratory motion assessed by a 4D CT scan was reproducible during a time period corresponding to a high-dose stereotactic treatment, and concluded that for the majority of lung cancer patients studied, treatment planning based on a single 4D CT scan appeared to be reliable (Guckenberger *et al.* 2007). On the other hand, Minn *et al*. showed that a 4D CT planning scan cannot accurately predict pancreatic tumor motion during actual delivery for radiosurgery (Minn *et al.* in press). Thus, it is not always true that the 4D CT image set represents the location and motion of patient's anatomy during treatment delivery; rather, a patient's motion pattern would most likely change between imaging and delivery. Nevertheless, the patient's anatomic motion during imaging is at this time the best possible estimation for what it will be during delivery. As there is no further information on patient's anatomy beyond one single 4D CT planning scan, as is often the case in clinic, this estimation is necessary. If 4D cone-beam CT (Sonke *et al.* 2005, Li *et al.* 2006a, Li *et al.* 2006b) or 4D magnetic resonance imaging (Remmert *et al.* 2007, von Siebenthal *et al.* 2007) is available, the most recent information on the patient's anatomic location is used. Even when the updated information is available, the assumption to correlate the anatomic location during imaging to that during delivery is still required. With a 4D treatment plan, 4D treatment delivery assumes that during delivery there exists real-time information on both 3D target location and respiratory phase, which is from either measurement or estimation.

The 4D IMRT treatment-planning method using the DMLC motion-tracking algorithm was applied to 12 lung cancer patient 4D CT image sets. As for individual phase plans, phase-to-phase variation was generally smaller than patient-to-patient variation, indicating that individual phase plans were similar to one another for each

patient. The deformable dose-summed 4D plan was similar to the average over individual phase plans, except for Patient 1. The DVHs and dose distribution of an IMRT plan for every phase of the 4D CT scan were similar to those of the reference phase plan, as well as the deformable dose-summed 4D plan, for each patient. This indicates that this method is dosimetrically robust to the variation of fractional time spent in respiratory phases on a given 4D CT scan. It also reveals that this method would result in the dose distribution close to the planned dose distribution, even when a patient spends more time on one phase (e.g., the end-exhale phase) than other phases during treatment delivery.

Similar phase-to-phase DVHs are desirable when it comes to target coverage, which in addition to PTV margin reduction is a primary goal of tumor-tracking methods. However, tumor-tracking techniques do not track the surrounding normal anatomy that deforms and/or moves relative to the tumor and/or in or out of BEV. Thus, the DVHs for OARs of some of the plans generated by the DMLC motion-tracking algorithm show more variation from phase to phase than those for the PTV.

In two patients out of twelve, this method was affected by the changes in tumor volume from phase to phase. These tumor volume changes can be attributed to either artifacts in the 4D CT image set as in Patient 1, or tumor volume variation throughout the respiratory phases as in Patient 4. For Patient 1, severe artifacts, which possibly happen in real clinical cases, caused phase-to-phase variation in individual phase plans. In one case, high vector field variation from a deformable registration affected this method (Patient 1). This was discussed in detail in the previous study (Suh *et al.* 2008b).

For each beam in the IMRT treatment plans, the collimator was rotated to align the MLC leaf travel direction parallel to the major axis of tumor motion, which was determined as seen in a given BEV. This makes the tumor motion in the other two directions, the motion perpendicular to the major axis and along the beam direction, relatively small. The tumor motion perpendicular to the MLC leaf travel direction and

along the beam direction is 0.2 and 0.4 cm, respectively, at the most (Table 1). Consequently, the collimator rotation minimizes the decrease in delivery efficiency for the motion perpendicular to the MLC leaf travel direction as much as possible.

5. Conclusions

A 4D IMRT treatment-planning method that accounts for 3D tumor motion was developed and investigated using 12 lung cancer patient 4D CT image sets. A DMLC motion-tracking algorithm previously developed for real-time tumor tracking was modified to allow 4D treatment planning and delivery using the same underlying algorithm. Using this method, the DVHs and isodose distributions of an IMRT plan for every phase of the 4D CT scan were, in general, similar to those of the reference phase plan, as well as the deformable dose-summed 4D plan. This indicates that the method is dosimetrically robust to the variation of fractional time spent in respiratory phases on a given 4D CT scan. This method is affected by 4D CT artifacts and high vector field variation from a deformable registration in one case. Creating 4D IMRT treatment plans using the DMLC motion-tracking algorithm explicitly accounts for 3D tumor motion and thus hysteresis and non-linear motion, and is deliverable on a linear accelerator. This method integrates deliverable treatment planning with DMLC tumor-tracking delivery, and has a clear path to clinical implementation.

Acknowledgements

The authors thank Drs. Lei Dong and Radhe Mohan from the University of Texas M. D. Anderson Cancer Center for the lung cancer patient 4D CT data used for this study; Dr. Elisabeth Weiss for useful discussions; and Devon Murphy for careful editing of the manuscript. This work was supported in part by NCI R01 CA93626 and NCI-NIH P01 CA116602.

References

Alasti H, Cho Y B, Vandermeer A D, Abbas A, Norrlinger B, Shubbar S, and Bezjak A 2006 A novel four-dimensional radiotherapy method for lung cancer: imaging, treatment planning and delivery, *Phys Med Biol* **51** 3251–67

Bortfeld T 2006 IMRT: a review and preview, *Phys Med Biol* **51** R363-79

Christensen G, Joshi S, and Miller M 1997 Volumetric transformation of brain anatomy, *IEEE Trans Med Imaging* **16** 864-77

Foskey M, Davis B, Goyal L, Chang S, Chaney E, Strehl N, Tomei S, Rosenman J, and Joshi S 2005 Large deformation three-dimensional image registration in image-guided radiation therapy, *Phys Med Biol* **50** 5869-92

Guckenberger M, Wilbert J, Meyer J, Baier K, Richter A, and Flentje M 2007 Is a single respiratory correlated 4D CT study sufficient for evaluation of breathing motion? *Int J Radiat Oncol Biol Phys* **67** 1352-9

Keall P, Cho B, Poulsen P, Sawant A, Suh Y, and Venkat R 2008 Simultaneous tracking and four-dimensional radiotherapy delivery: accounting for spatial and morphological tumor changes, *Med Phys* **35** 2913

Keall P J, Mageras G S, Balter J M, Emery R S, Forster K M, Jiang S B, Kapatoes J M, Low D A, Murphy M J, Murray B R, Ramsey C R, van Herk M B, Vedam S S, Wong J W, and Yorke E 2006 The management of respiratory motion in radiation oncology report of AAPM Task Group 76, *Med Phys* **33** 3874-900

Keall P J, Siebers J V, Joshi S, and Mohan R 2004 Monte Carlo as a four-dimensional radiotherapy treatment-planning tool to account for respiratory motion, *Phys Med Biol* **49** 3639-48

Li T, Schreibmann E, Yang Y, and Xing L 2006a Motion correction for improved target localization with on-board cone-beam computed tomography, *Phys Med Biol* **51** 253-67

Li T, Xing L, Munro P, McGuinness C, Chao M, Yang Y, Loo B, and Koong A 2006b Four-dimensional cone-

beam computed tomography using an on-board imager, *Med Phys* **33** 3825-33

McClelland J R, Webb S, McQuaid D, Binnie D M, and Hawkes D J 2007 Tracking 'differential organ motion' with a 'breathing' multileaf collimator: magnitude of problem assessed using 4D CT data and a motion-compensation strategy, *Phys Med Biol* **52** 4805-26

McMahon R, Berbeco R, Nishioka S, Ishikawa M, and Papiez L 2008 A real-time dynamic-MLC control algorithm for delivering IMRT to targets undergoing 2D rigid motion in the beam's eye view, *Med Phys* **35** 3876-88

McMahon R, Papiez L, and Rangaraj D 2007 Dynamic-MLC leaf control utilizing on-flight intensity calculations: A robust method for real-time IMRT delivery over moving rigid targets, *Med Phys* **34** 3211-23

McQuaid D and Webb S 2006 IMRT delivery to a moving target by dynamic MLC tracking: delivery for targets moving in two dimensions in the beam's eye view, *Phys Med Biol* **51** 4819-39

Minn A Y, Schellenberg D, Maxim P, Suh Y, McKenna S, Cox B, Dieterich S, Xing L, Graves E, Goodman K A, Chang D, and Koong A C in press Pancreatic tumor motion on a single planning 4D-CT does not correlate with intrafraction tumor motion during treatment, *American Journal of Clinical Oncology*

Papiez L 2003 The leaf sweep algorithm for an immobile and moving target as an optimal control problem in radiotherapy delivery, *Mathematical and Computer Modelling* **37** 735-45

Papiez L 2004 DMLC leaf-pair optimal control of IMRT delivery for a moving rigid target, *Med Phys* **31** 2742-54

Papiez L, McMahon R, and Timmerman R 2007 4D DMLC leaf sequencing to minimize organ at risk dose in moving anatomy, *Med Phys* **34** 4952-6

Papiez L and Rangaraj D 2005 DMLC leaf-pair optimal control for mobile, deforming target, *Med Phys* **32** 275-85

Papiez L, Rangaraj D, and Keall P J 2005 Real-time DMLC IMRT delivery for mobile and deforming targets,

Med Phys **32** 3037-48

Rangaraj D, Palaniswaamy G, and Papiez L 2008 DMLC IMRT delivery to targets moving in 2D in beam's eye view, *Med Phys* **35** 3765-78

Rangaraj D and Papiez L 2005 Synchronized delivery of DMLC intensity modulated radiation therapy for stationary and moving targets, *Med Phys* **32** 1802-17

Remmert G, Biederer J, Lohberger F, Fabel M, and Hartmann G H 2007 Four-dimensional magnetic resonance imaging for the determination of tumour movement and its evaluation using a dynamic porcine lung phantom, *Phys Med Biol* **52** N401-15

Sawant A, Venkat R, Srivastava V, Carlson D, Cattell S P H, and Keall P J 2008 Management of three-dimensional intrafraction motion through real-time DMLC tracking, *Med Phys* **35** 2050-61

Schlaefer A, Fisseler J, Dieterich S, Shiomi H, Cleary K, and Schweikard A 2005 Feasibility of four-dimensional conformal planning for robotic radiosurgery, *Med Phys* **32** 3786-92

Seppenwoolde Y, Shirato H, Kitamura K, Shimizu S, van Herk M, Lebesque J V, and Miyasaka K 2002 Precise and real-time measurement of 3D tumor motion in lung due to breathing and heartbeat, measured during radiotherapy, *Int J Radiat Oncol Biol Phys* **53** 822-34

Sonke J, Zijp L, Remeijer P, and van Herk M 2005 Respiratory correlated cone beam CT, *Med Phys* **32** 1176-86

Suh Y, Dieterich S, Cho B, and Keall P J 2008a An analysis of thoracic and abdominal tumour motion for stereotactic body radiotherapy patients, *Phys Med Biol* **53** 3623-40

Suh Y, Weiss E, Zhong H, Fatyga M, Siebers J, and PJ K 2008b A deliverable four-dimensional intensity-modulated radiation therapy-planning method for dynamic multileaf collimator tumor tracking delivery, *Int J Radiat Oncol Biol Phys* **71** 1526-36

Tewatia D, Zhang T, Tome W, Paliwal B, and Metha M 2006 Clinical implementation of target tracking by

breathing synchronized delivery, *Med Phys* **33** 4330-6

Trofimov A, Rietzel E, Lu H M, Martin B, Jiang S, Chen G T, and Bortfeld T 2005 Temporo-spatial IMRT optimization: concepts, implementation and initial results, *Phys Med Biol* **50** 2779-98

von Siebenthal M, Székely G, Gamper U, Boesiger P, Lomax A, and Cattin P 2007 4D MR imaging of respiratory organ motion and its variability, *Phys Med Biol* **52** 1547-64

Webb S 2005 The effect on IMRT conformality of elastic tissue movement and a practical suggestion for movement compensation via the modified dynamic multileaf collimator (dMLC) technique, *Phys Med Biol* **50** 1163-90

Webb S 2006a, IMRT delivery techniques, in *Image-guided IMRT*, ed T Bortfeld, R K Schmidt-Ullrich, and W DeNeve (Heidelberg: Springer-Verlag), p 73-90

Webb S 2006b Motion effects in (intensity modulated) radiation therapy: a review, *Phys Med Biol* **51** R403-R425

Webb S and Binnie D M 2006 A strategy to minimize errors from differential intrafraction organ motion using a single configuration for a 'breathing' multileaf collimator, *Phys Med Biol* **51** 4517-31

Weiss E, Siebers J V, and Keall P J 2007a An analysis of 6-MV versus 18-MV photon energy plans for intensity-modulated radiation therapy (IMRT) of lung cancer, *Radiotherapy and Oncology* **82** 55-62

Weiss E, Wijesooriya K, Dill S V, and Keall P J 2007b Tumor and normal tissue motion in the thorax during respiration: Analysis of volumetric and positional variations using 4D CT, **67** 296-307

Zhang T, Jeraj R, Keller H, Lu W, Olivera G H, McNutt T R, Mackie T R, and Paliwal B 2004 Treatment plan optimization incorporating respiratory motion, *Med Phys* **31** 1576-86

Zhang T, Lu W, Olivera G H, Keller H, Jeraj R, Manon R, Mehta M, Mackie T R, and Palowal B 2007 Breathing-synchronized delivery: a potential four-dimensional tomotherapy treatment technique, *Int J Radiat Oncol Biol Phys* **68** 1572-8

Appendix D

GEOMETRIC UNCERTAINTY OF 2D PROJECTION IMAGING IN MONITORING 3D TUMOR MOTION

Yelin Suh

Sonja Dieterich

Paul J. Keall

Physics in Medicine and Biology 52(12), 2007

IOP Publishing Physics in Medicine and Biology

Phys. Med. Biol. **52** (2007) 3439–3454 doi:10.1088/0031-9155/52/12/008

Geometric uncertainty of 2D projection imaging in monitoring 3D tumor motion

Yelin Suh[1,2], **Sonja Dieterich**[3] **and Paul J Keall**[1,2]

[1] Department of Radiation Oncology, Virginia Commonwealth University, Richmond, VA, USA
[2] Department of Radiation Oncology, Stanford University, Stanford, 875 Blake Wilbur Drive, Stanford, CA 94305-5847, USA
[3] Department of Radiation Medicine, Georgetown University Hospital, Washington, DC, USA

E-mail: Paul.Keall@stanford.edu

Received 1 February 2007, in final form 4 April 2007
Published 18 May 2007
Online at stacks.iop.org/PMB/52/3439

Abstract

The purpose of this study was to investigate the accuracy of two-dimensional (2D) projection imaging methods in three-dimensional (3D) tumor motion monitoring. Many commercial linear accelerator types have projection imaging capabilities, and tumor motion monitoring is useful for motion inclusive, respiratory gated or tumor tracking strategies. Since 2D projection imaging is limited in its ability to resolve the motion along the imaging beam axis, there is unresolved motion when monitoring 3D tumor motion. From the 3D tumor motion data of 160 treatment fractions for 46 thoracic and abdominal cancer patients, the unresolved motion due to the geometric limitation of 2D projection imaging was calculated as displacement in the imaging beam axis for different beam angles and time intervals. The geometric uncertainty to monitor 3D motion caused by the unresolved motion of 2D imaging was quantified using the root-mean-square (rms) metric. Geometric uncertainty showed interfractional and intrafractional variation. Patient-to-patient variation was much more significant than variation for different time intervals. For the patient cohort studied, as the time intervals increase, the rms, minimum and maximum values of the rms uncertainty show decreasing tendencies for the lung patients but increasing for the liver and retroperitoneal patients, which could be attributed to patient relaxation. Geometric uncertainty was smaller for coplanar treatments than non-coplanar treatments, as superior–inferior (SI) tumor motion, the predominant motion from patient respiration, could be always resolved for coplanar treatments. Overall rms of the rms uncertainty was 0.13 cm for all treatment fractions and 0.18 cm for the treatment fractions whose average breathing peak–trough ranges were more than 0.5 cm. The geometric uncertainty for 2D imaging varies depending on the tumor site,

tumor motion range, time interval and beam angle as well as between patients, between fractions and within a fraction.

(Some figures in this article are in colour only in the electronic version)

1. Introduction

In order to achieve the goal of radiation treatment, which maximizes dose to the tumor while sparing the normal tissues, target localization is an important task. Tumor motion, however, especially from respiration, challenges the target localization, so that motion compensation has been one of the key issues in radiotherapy (Langen and Jones 2001, Webb 2006).

Compensating for the tumor motion during the course of radiotherapy requires some kind of monitoring methods so that target motion is observed and/or target position is acquired. With the information from monitoring the target, its motion can be compensated for by motion inclusive, respiratory gated (Vedam *et al* 2001, Kubo and Wang 2002, Ozhasoglu and Murphy 2002, Giraud *et al* 2003, Hugo *et al* 2003, Nill *et al* 2005, George *et al* 2006, Jiang 2006), or tumor tracking (Schweikard *et al* 2000, 2004, Keall *et al* 2001, 2005, Murphy 2004, Suh *et al* 2004, Papiez and Rangaraj 2005, Papiez *et al* 2005, Webb 2005b, 2005a, Kamino *et al* 2006, Neicu *et al* 2006, Xu *et al* 2006) strategies. The focus of this study is on the limitation of acquiring target position information with a single two-dimensional (2D) x-ray imager for patients with implanted markers. Examples of 2D imaging methods for target position monitoring are electronic portal imaging devices (EPIDs) (Keall *et al* 2004, Berbeco *et al* 2005), combined kV/MV systems (Oelfke *et al* 2006), Siemens Artiste linac, Varian 21IX and Elekta Synergy linac (Mcbain *et al* 2006). A summary of the application of 2D x-ray imaging for different radiotherapy delivery systems is shown in table 1.

It should be noted that there are several other possibilities for acquiring target position information during a treatment fraction such as real time radiotherapy (RTRT) systems (Shimizu *et al* 2000), Cyberknife (Schweikard *et al* 2000, 2004, Murphy 2004) (of which data were used for the data source in this study), ExacTrac x-ray (Weiss *et al* 2003, Willoughby *et al* 2006a), ultrasound-based systems (Langen *et al* 2003, Scarbrough *et al* 2006), positron emission tomography (Lu *et al* 2006, Xu *et al* 2006), integrated radiotherapy imaging systems (IRIS) (Neicu *et al* 2006) and electromagnetic localization systems (Willoughby *et al* 2006b). Earlier work using orthogonal imaging for determining target position is described in Lam *et al* (1993) and Gilhuijs *et al* (1996).

If 3D tumor motion is monitored with 2D projection imaging, there is unresolved motion because 2D projection is limited in its ability to resolve the motion along the imaging beam axis (Gilhuijs *et al* 1996, Berbeco *et al* 2004, Nill *et al* 2005). This unresolved motion might cause geometric uncertainty in monitoring 3D motion and thus introduce errors in compensating tumor motion. It is assumed that with 2D projection imaging methods resolving the magnification of tumor from the motion in the imaging beam axis is not possible due to the limited resolution and noise, and the ability to resolve the changes of distance between the implanted markers (surrogates for tumor) is less than that to resolve the individual markers. Also it is noted that 3D monitoring systems are not limited to a single 2D projection and thus can resolve the position of tumor or implanted markers in 3D to within measurement errors.

As 2D projection imaging, two different geometric relationships between the imaging beam and treatment beam were considered as shown in figure 1: (1) an inline orientation,

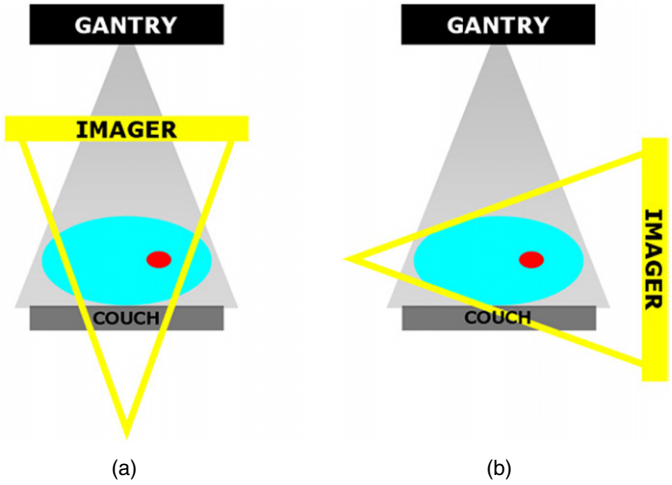

Figure 1. Two different geometric relationships between the imaging beam and treatment beam: (a) an inline orientation, where the imaging beam is parallel to the treatment beam, and (b) an orthogonal orientation, where the imaging beam is orthogonal (by a 90° gantry rotation) to the treatment beam. An electronic portal imaging device (EPID) is similar to orientation (a); however, the imaging detector is below the patient and the treatment beam is used to form the images.

Table 1. Linear accelerator vendors, configuration and comments on the applicability of using a single x-ray imager to determine target position.

Vendor/linac	Configuration	Comments
Accuray/Cyberknife	Dual room-mounted x-ray imagers	Proposed monitoring system can be used to • allow beam positions currently prohibited when robot obscures a single imager • reduce imaging dose in certain situations by using only single imaging mode rather than dual mode
BrainLab/Novalis	Dual room-mounted x-ray imagers	X-ray imagers cannot be used simultaneously due to a single generator
Elekta/Synergy	Single gantry-mounted x-ray imager	Imager orthogonal to MV treatment beam
Siemens/Artiste	Single gantry-mounted x-ray imager	Imager inline with MV treatment beam
Tomotherapy/HiArt	Single gantry-mounted x-ray imager	Original design (Mackie *et al* 1993) though not in current commercial implementation
Varian/Trilogy	Single gantry-mounted x-ray imager	Imager orthogonal to MV treatment beam

where the imaging beam is parallel to the treatment beam (figure 1(a)), such as EPIDs (Keall *et al* 2004, Berbeco *et al* 2005) (note that the detector of an EPID is below the patient and the treatment beam is used to form the images), combined kV/MV systems (Oelfke *et al* 2006), and the Siemens Artiste linac, and (2) an orthogonal orientation, where the imaging beam is orthogonal (by a 90° gantry rotation) to the treatment beam (figure 1(b)), such as Varian 21IX and Elekta Synergy linacs (Mcbain *et al* 2006). When gantry and couch angles are set to 0°, a 2D imager in inline orientation is limited to resolving anterior–posterior (AP) motion as this motion is in the imaging beam axis, while for a 2D imager in orthogonal orientations left–right (LR) motion cannot be resolved. That is, there is always some hidden motion, which

is the limitation of 2D projection imaging systems using only one imaging beam (Gilhuijs *et al* 1996, Berbeco *et al* 2004, Nill *et al* 2005).

Therefore, the aim of this study was to investigate the accuracy of 2D projection imaging methods in 3D tumor motion monitoring by evaluating the motion that 2D imagers in each of the two orientations, inline and orthogonal, failed to resolve, which could be one important error source in tumor motion compensation.

2. Methods and materials

In order to evaluate the accuracy of 2D projection imaging to monitor 3D tumor motion, we needed a 3D tumor motion data source and a method to quantify the unresolved motion due to the limitation of 2D projection when monitoring tumor motion in 3D, as described below. For the purpose of this study, it is assumed that the 3D patient tumor motion data acquired from monitoring implanted markers are the gold standard, though we acknowledge that there can be uncertainty in monitoring the markers and that implanted markers are point surrogates for the anatomy of interest. Furthermore, these markers can migrate with respect to anatomy. Prior to using patient data the unresolved motion of 2D imagers for three sinusoidal motion data sets with only LR, AP and superior–inferior (SI) motion, respectively, was investigated. This study relied on two assumptions, common to the work by Nill *et al* (2005).

- The setup error will be very small since a possible setup correction based on the acquired images could be performed prior to treatment. This assumption is necessary to set a common 2D to 3D framework from which to analyze the limitations of the 2D imaging.
- For a given imaging beam angle, the 2D projection system fails to detect one direction of 3D tumor motion.

2.1. 3D tumor motion data source

The 3D tumor motion information used in this study was from 160 treatment fractions for 46 thoracic and abdominal cancer patients who underwent hypofractionated stereotactic radiotherapy. The tumor locations were lungs (30 patients), liver (2), retroperitoneum (11) and chest wall/internal mammary nodes (3). For each patient, there were one to seven treatment fractions, and the average duration time of the fractions was 31.4 min (ranging from 5 to 106.4 min). The data were acquired under IRB-2005-309 from the Cyberknife system at Georgetown University Hospital from July in 2005 to January in 2006. Synchrony is a subsystem of real-time adaptive motion compensation in the Cyberknife system. In order to compensate for the respiratory tumor motion, the system uses a hybrid tracking model of both the external and internal motion of patients; for the external patient motion, three Flashpoint cameras are used to monitor the multiple light emitting diodes (LEDs) on the patient's chest and/or abdomen and the internal fiducial locations are calculated from orthogonal diagnostic x-ray image pairs of two to four gold implanted markers. At the beginning of the treatment, the system makes a correlation between the external patient motion and the internal fiducial locations. During the treatment, the system continuously (at 32 frames s^{-1}) monitors the external marker motion and estimates the tumor positions at 25 Hz using the current correlation. To update the correlation during the treatment, the system periodically (approximately every 30 s) measures the implanted marker locations by acquiring x-ray images. Thus, the data we had were the estimated 3D tumor positions versus time from the correlation, which are saved in log files of the Synchrony system. The system accuracy is 1.5 mm with uncertainty of 0.3 mm for an end-to-end test on a motion platform, which is the difference between the center of the plan dose distribution and that of the delivered dose distribution measured by film. The

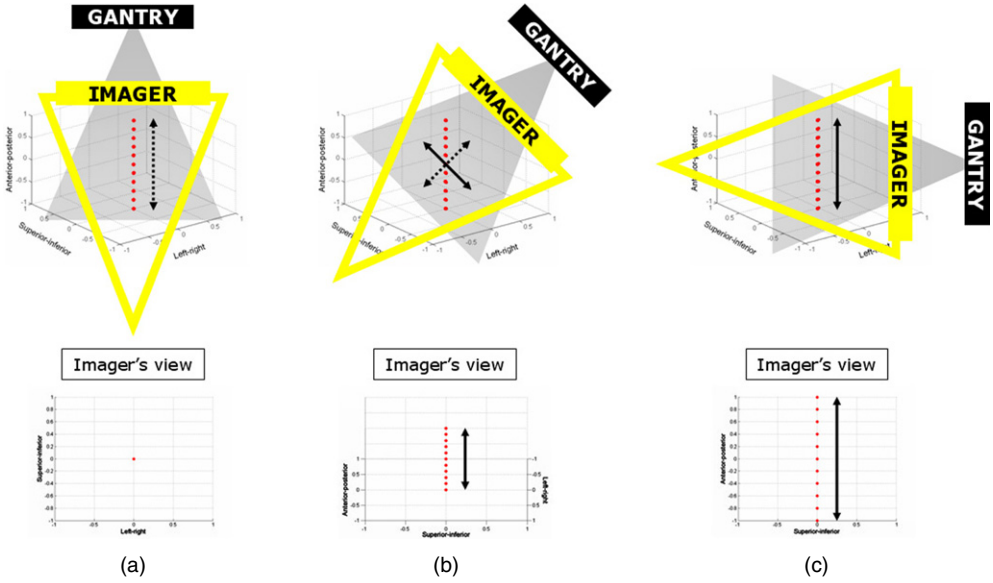

Figure 2. Calculation of the unresolved motion from the limitation of 2D projection imaging to monitor motion in 3D: red dots indicate the tumor motion (only anterior–posterior (AP) motion for example), dashed arrows the unresolved motion, and solid arrows the resolved motion for an inline orientation. (a) When gantry and couch angles are 0°, the tumor looks static for the imager in this orientation as shown in imager's view even though it moves (no solid arrow). However, (c) when the gantry angle is 90° and the couch angle is 0°, the imager resolves the full motion (no dashed arrow). (b) If the gantry angle is 45° with the couch angle 0°, the imager resolves part of the motion (solid arrow) while failing to detect the motion in the imaging beam axis (dashed arrow).

purely technical tracking accuracy is much better, which is on the order of 0.6 mm. Clinically, changes in the patient add much more uncertainty. Typically the correlation starts to be rebuilt if its error is more than 2.9 mm for two images in a row. The detailed information on the Cyberknife Synchrony system is described elsewhere (Schweikard *et al* 2000, 2004, Murphy 2004).

2.2. Calculation of the unresolved motion of 2D projection imaging

From the estimated patient 3D tumor motion data, the unresolved motion (motion in the imaging beam axis) due to the limitation of 2D projection imaging to monitor motion in 3D was calculated. The motion was assumed at the isocenter plane. The geometric uncertainty is shown schematically in figure 2 for a tumor moving only in the AP direction and a 2D projection imager in an inline orientation to monitor the motion. If gantry and couch angles are 0° (figure 2(a)), the tumor looks static for the imager in this orientation as shown in the imager's view even though it is moving. It should be noted that motion in the plane of the imaging beam is theoretically detectable in an ideal situation. However with modern detectors the centroid position of an individual marker can be resolved to within 0.5 mm in the imaging plane. The uncertainty in the imaging plane would correspond to uncertainty of 1 cm along the beam axis for an object of 5 cm lateral to the beam axis at 100 cm from the source. This uncertainty is on the same order of the motion observed, and thus detecting changes along the beam axis is not currently feasible. If the gantry angle is 90° and the couch angle is 0° (figure 2(c)), however, the imager resolves the full motion of the tumor. When the gantry

angle is 45° with the couch angle 0° (figure 2(b)), the imager resolves part of the motion (solid arrow) while failing to detect the motion in the imaging beam axis (dashed arrow). We calculated the magnitude of the unresolved motion of 2D projection imaging in different treatment beam–patient alignments for each of 160 treatment fractions.

As for the different treatment beam–patient alignments, 216 treatment beam angles were considered by varying gantry angles from 0° to 360° in 15° increments (24) and couch angles from −60° to 60° in 15° increments (9). The unresolved motion as a function of only gantry angle while couch angle is 0° was also calculated as most conventional abdominal and thoracic treatments are coplanar. For a given treatment beam angle with a given gantry and couch angle, motion in the imaging beam axis, which is the unresolved motion, was calculated from the 3D tumor motion data assuming that this position of the tumor had not changed from a patient initial setup. Also, to investigate the unresolved motion for different time intervals, 0–1, 0–10 and 0–30 minutes, were considered

2.3. Quantification of the geometric uncertainty of 2D projection imaging

The geometric uncertainty in monitoring 3D tumor motion with a 2D projection imager due to the unresolved motion was statistically quantified using the root-mean-square (rms) uncertainty of the unresolved motion. The rms uncertainty was used to quantify the distribution of the geometric uncertainty since the uncertainty is not normally distributed (determined by using a Kolmogorov–Smirnov test). For the geometric uncertainty of a single patient fraction, the rms uncertainties of the unresolved motion for given treatment beam angles were shown (figures 3–6). To investigate the geometric uncertainty for the cohort of patients studied, let U be the unresolved motion of 2D projection imaging: $U(g, c = 0)$ is the unresolved motion as a function of gantry angle for coplanar treatments (zero couch angle) and $U(g, c)$ is the unresolved motion as a function of gantry and couch angle for non-coplanar treatments, where couch angles vary from −60° to 60°. For each fraction i, the rms uncertainty of $U(g, c = 0)$, which is $R_{g,t,i}$, and the rms uncertainty of $U(g, c)$, which is $R_{g,c,t,i}$, for each of the time intervals t, where t is 0–1, 0–10 and 0–30 min, were calculated. Then, the rms, minimum and maximum values of $R_{g,t,i}$ and $R_{g,c,t,i}$ were calculated, respectively, and these were repeated for the fractions whose average breathing peak–trough ranges were more than 0.5 cm. As shown in figure 3, and obvious from figure 1, the geometric uncertainty of 2D projection imaging in orthogonal orientations from the treatment beam perspective is simply a 90° gantry rotation from that in inline orientations; so $R^{\text{orthogonal}}_{g,c,t,i} = R^{\text{inline}}_{g+90^{\circ},c,t,i}$. Thus the results shown in figure 4 onwards are only for the inline orientation. The dosimetric impact of the geometric uncertainty will be discussed in section 4 and figure 8.

3. Results

3.1. Geometric uncertainty of 2D projection imaging for uni-directional unit amplitude sinusoidal motion with inline and orthogonal orientations

Figure 3(a) shows the rms uncertainty of the unresolved motion as a function of gantry and couch angle, when there is only unit amplitude sinusoidal LR tumor motion for 2D projection imaging in the inline orientation. For the case when gantry and couch angles are 0°, the 2D projection in the inline orientation can resolve LR motion, so there is no uncertainty; but for the case when the gantry angle is 90° while the couch angle is 0°, the 2D projection in this orientation cannot resolve LR motion, so the uncertainty is the highest. Figure 3(b) shows the rms uncertainty of the unresolved motion when there is only AP tumor motion; the highest

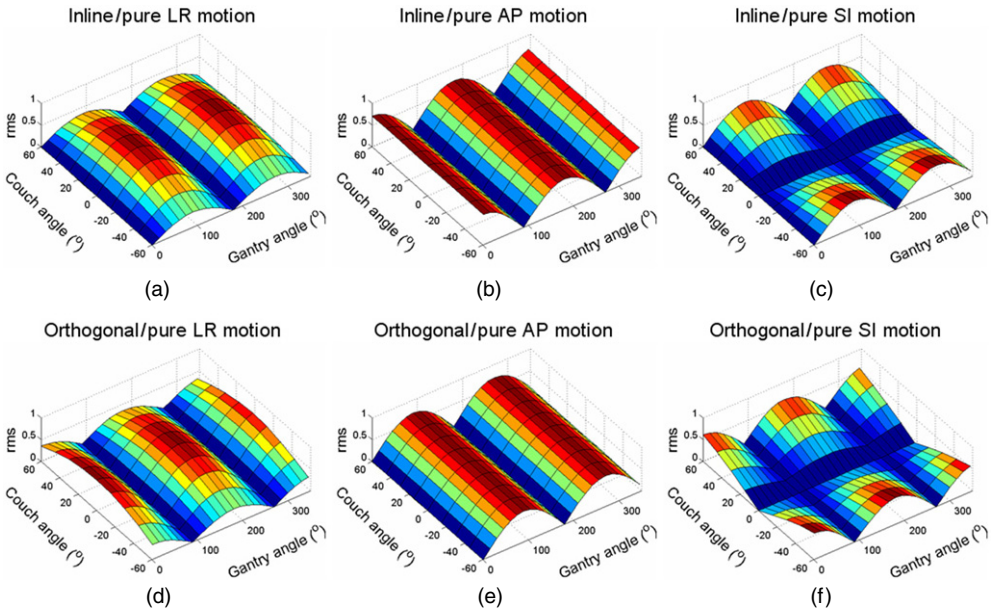

Figure 3. The root-mean-square (rms) uncertainty of the unresolved motion for uni-directional unit amplitude sinusoidal motion: (a) left–right (LR), (b) anterior–posterior (AP) and (c) superior–inferior (SI) motion for an inline orientation and (d) LR, (e) AP and (f) SI motion for an orthogonal orientation. Note that plots for an orthogonal orientation ((d)–(f)) are simply rotated by 90° in the axis of gantry angle from those for an inline orientation ((a)–(c)). The red color indicates the higher value and the blue is the lower value.

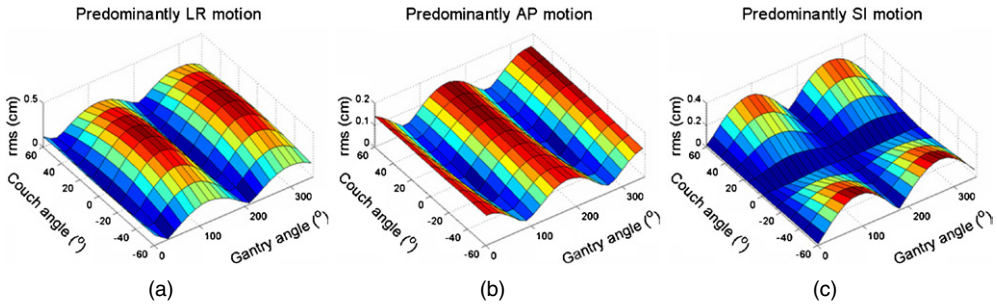

Figure 4. The root-mean-square (rms) uncertainty of the unresolved motion for the patients with (a) predominantly left–right (LR) motion (patient no. 15 (right lower lung lobe), fraction no. 1 for 0–10 min), anterior–posterior (AP) motion (patient no. 42 (right upper lung lobe), fraction no. 3 for 0–10 min), or superior–inferior (SI) motion (patient no. 27 (right lower lung lobe), fraction no. 3 for 0–10 min) for an inline orientation.

uncertainty when gantry and couch angles are 0° and no uncertainty when gantry is 90° with couch 0°. Figure 3(c) shows the rms uncertainty of the unresolved motion when there is only SI motion. For the couch at 0° with SI motion there is no uncertainty at any gantry angles as the motion is perpendicular to the imaging beam. Figures 3(d) and (e) show the same for the orthogonal orientation: pure LR motion (figure 3(d)), pure AP motion (figure 3(e)) and pure SI motion (figure 3(f)). All three plots for the orthogonal orientation are shifted by 90° in the

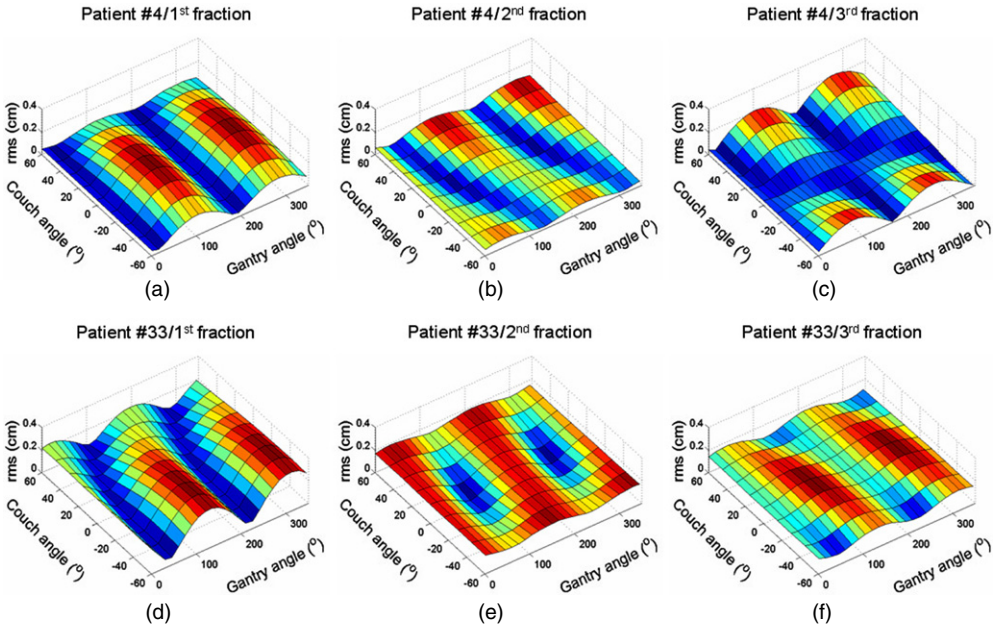

Figure 5. Interfractional geometric uncertainty: the root-mean-square (rms) uncertainty of the unresolved motion for an inline orientation: (a) first, (b) second and (c) third fraction for a single patient (patient no. 4 (pancreas) for 0–10 min) and (d) first, (e) second and (f) third fraction for a single patient (patient no. 33 (hilum) for 0–10 min).

gantry angle axis from those for the inline orientation. Due to this relationship further results will be shown for the inline orientation only.

3.2. Geometric uncertainty of 2D projection imaging for patient motion with inline orientation: patient-to-patient variation

Figure 3 displays the geometric uncertainty for theoretical motion (uni-directional unit amplitude sinusoidal motion). Among the 160 fractions none of the estimated tumor motions were purely uni-directional; however, there were tumor motion data sets showing predominantly uni-directional motion. Examples of the geometric uncertainty for three patients are shown in figure 4: patients with predominantly LR (figure 4(a)), AP (figure 4(b)) and SI (figure 4(c)) motion for 0–10 min.

3.3. Geometric uncertainty of 2D projection imaging for patient motion with inline orientation: interfraction variation

Interfractional geometric uncertainty for the inline orientation is shown in figure 5. Figures 5(a)–(c) show the rms uncertainty of the unresolved motion of the first, second and third fraction for a single patient for 0–10 min, respectively, and figures 5(d)–(f) are the same from another patient. The magnitude and phase of the geometric uncertainty show variation between the fractions for the single patient and also between the patients. Patient no. 4 showed that tumor motion predominantly in the LR direction at the first fraction (figure 5(a)), which changed to AP-like motion combined with LR and SI motion at the second fraction (figure 5(b)), ended up being predominantly in the SI direction at the third fraction

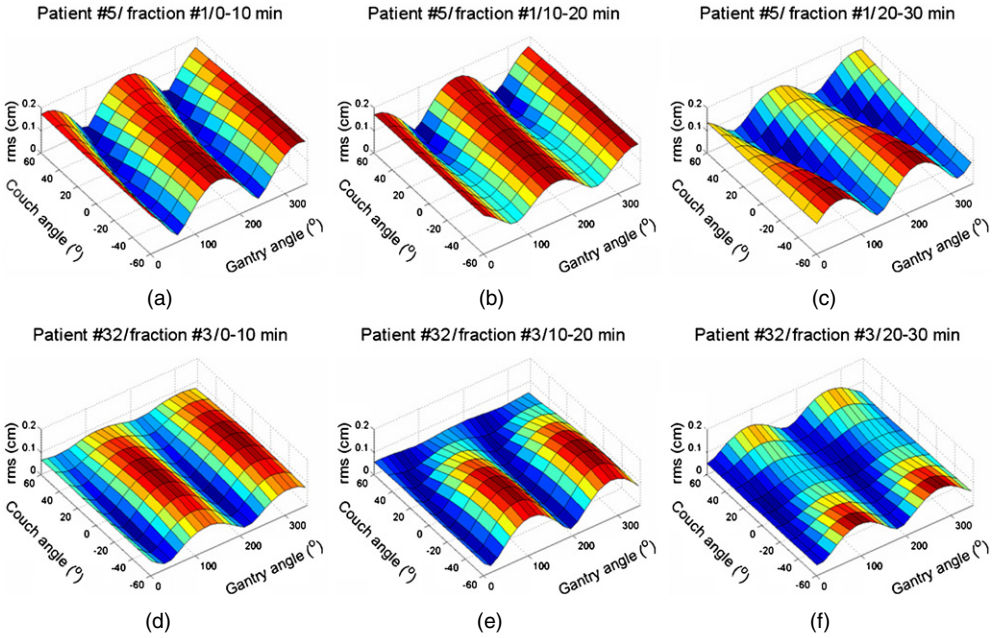

Figure 6. Intrafractional geometric uncertainty: the root-mean-square (rms) uncertainty of the unresolved motion for an inline orientation: (a) 0–10, (b) 10–20 and (c) 20–30 min for a single patient fraction (patient no. 5 (left upper lung lobe), fraction no. 1) and (d) 0–10, (e) 10–20 and (f) 20–30 min for a single patient fraction (patient no. 32 (right lower lung lobe), fraction no. 3).

(figure 5(c)). As for patient no. 33, the second (figure 5(e)) and third (figure 5(f)) fraction showed the opposite phase of the geometric uncertainty; the treatment beam angle with the lowest uncertainty at the second fraction showed the highest at the next fraction.

3.4. Geometric uncertainty of 2D projection imaging for patient motion with inline orientation: intrafraction variation

Figure 6 shows intrafractional geometric uncertainty for the inline orientation. Figures 6(a)–(c) show the rms uncertainty of the unresolved motion for 0–10, 10–20 and 20–30 min for a single patient fraction, respectively, and figures 6(d)–(f) are the same from another single patient fraction. The magnitude and phase of the geometric uncertainty show variation during the single patient fraction and also between the patients. In the case of patient no. 5, for each of 10 min intervals during the single fraction the uncertainty did not show significant changes (figures 6(a)–(c)) unlike interfractional variation: all three time terms showed somewhat AP-like motion. Still, for 10–20 min (figure 6(b)) tumor moved more in the LR direction and for 20–30 min (figure 6(c)) more in the SI direction than for 0–10 min (figure 6(a)). For patient no. 32, tumor motion which was predominantly in the LR direction for the first 10 min (figure 6(d)) changed to predominantly SI motion in 10 min (figure 6(f)).

3.5. Geometric uncertainty of 2D projection imaging for the patient cohort studied

Table 2 shows the rms, minimum and maximum values of $R_{g,c,t,i}$, the rms uncertainty of the unresolved motion for each fraction i and for each time interval t for non-coplanar treatments,

Table 2. The root-mean-square (rms), minimum and maximum values of $R_{g,c,t,i}$ (rms uncertainty of the unresolved motion for each fraction i and for each time interval t for non-coplanar treatments) for 0–1, 0–10 and 0–30 min by sites (cm): rms (minimum, maximum).

Sites	Patient no./fraction no.	0–1 min	0–10 min	0–30 min
Lungs	30/105	0.14 (0.01, 0.64)	0.13 (0.01, 0.43)	0.12 (0.01, 0.24)
Liver	2/8	0.13 (0.04, 0.17)	0.16 (0.05, 0.27)	0.19 (0.14, 0.27)
Retroperitoneum	11/36	0.10 (0.01, 0.22)	0.11 (0.01, 0.25)	0.12 (0.02, 0.24)
Chest wall/internal mammary nodes	3/11	0.04 (0.02, 0.07)	0.04 (0.03, 0.06)	0.05 (0.04, 0.05)
Total	46/160	0.13 (0.01, 0.64)	0.13 (0.01, 0.43)	0.12 (0.01, 0.27)

Table 3. The root-mean-square (rms), minimum and maximum values of $R_{g,t,i}$ (rms uncertainty of the unresolved motion for each fraction i and for each time interval t for coplanar treatments) for 0–1, 0–10 and 0–30 min by sites (cm): rms (minimum, maximum).

Sites	Patient no./fraction no.	0–1 min	0–10 min	0–30 min
Lungs	30/105	0.11 (0.01, 0.46)	0.11 (0.01, 0.35)	0.09 (0.01, 0.24)
Liver	2/8	0.09 (0.03, 0.13)	0.12 (0.04, 0.18)	0.14 (0.11, 0.18)
Retroperitoneum	11/36	0.07 (0.01, 0.21)	0.08 (0.01, 0.19)	0.09 (0.02, 0.18)
Chest wall/internal mammary nodes	3/11	0.04 (0.01, 0.07)	0.04 (0.03, 0.07)	0.05 (0.04, 0.05)
Total	46/160	0.10 (0.01, 0.46)	0.10 (0.01, 0.35)	0.09 (0.01, 0.24)

Table 4. The root-mean-square (rms), minimum and maximum values of $R_{g,c,t,i}$ (rms uncertainty of the unresolved motion for each fraction i and for each time interval t for non-coplanar treatments) for 0–1, 0–10 and 0–30 min by sites whose average breathing peak–trough ranges are more than 0.5 cm (cm): rms (minimum, maximum).

Sites	Patient no./fraction no.	0–1 min	0–10 min	0–30 min
Lungs	16/45	0.19 (0.09, 0.64)	0.18 (0.10, 0.43)	0.16 (0.10, 0.24)
Liver	2/6	0.15 (0.12, 0.17)	0.18 (0.13, 0.27)	0.19 (0.14, 0.27)
Retroperitoneum	8/14	0.14 (0.08, 0.22)	0.15 (0.09, 0.25)	0.16 (0.11, 0.24)
Total	26/65	0.18 (0.08, 0.64)	0.18 (0.09, 0.43)	0.17 (0.10, 0.27)

and table 3 shows those of $R_{g,t,i}$, the rms uncertainty of the unresolved motion for each fraction i and for each time interval t for coplanar treatments, for 0–1, 0–10 and 0–30 min by sites. Overall rms values of $R_{g,c,t,i}$ were 0.13 cm, 0.13 cm and 0.12 cm and those of $R_{g,t,i}$ were 0.10 cm, 0.10 cm and 0.09 cm for each time interval, respectively. As the time interval increases, the rms, minimum and maximum values show decreasing tendencies for the lungs while they show increasing tendencies for the liver and retroperitoneum, in general. For the chest wall/internal mammary nodes, all the values are small and about the same for different time terms. Comparing these two tables demonstrates that most values in table 3, which is for coplanar treatments, are smaller than those in table 2, which is for non-coplanar treatments.

Table 4 shows the rms, minimum and maximum values of $R_{g,c,t,i}$ and table 5 shows those of $R_{g,t,i}$ for 0–1, 0–10 and 0–30 min by sites whose average breathing peak–trough ranges are more than 0.5 cm. Overall rms values of $R_{g,c,t,i}$ were 0.18 cm, 0.18 cm and 0.17 cm and those of $R_{g,t,i}$ were 0.14 cm, 0.13 cm and 0.12 cm for each time interval, respectively. These

Table 5. The root-mean-square (rms), minimum and maximum values of $R_{g,t,i}$ (rms uncertainty of the unresolved motion for each fraction i and for each time interval t for coplanar treatments) for 0–1, 0–10 and 0–30 min by sites whose average breathing peak–trough ranges are more than 0.5 cm (cm): rms (minimum, maximum).

Sites	Patient no./fraction no.	0–1 min	0–10 min	0–30 min
Lungs	16/45	0.15 (0.01, 0.46)	0.14 (0.02, 0.35)	0.12 (0.03, 0.24)
Liver	2/6	0.10 (0.08, 0.13)	0.13 (0.09, 0.18)	0.14 (0.11, 0.18)
Retroperitoneum	8/14	0.10 (0.03, 0.21)	0.11 (0.03, 0.19)	0.12 (0.08, 0.18)
Total	26/65	0.14 (0.01, 0.46)	0.13 (0.02, 0.35)	0.12 (0.03, 0.24)

two tables show the same tendencies as the previous two tables. Again, all values in table 5 are smaller compared to those in table 4.

Figure 7 shows the cumulative probability of the distributions of the rms of $R_{g,c,t,i}$ or $R_{g,t,i}$ for different time intervals of 0–1 (red), 0–10 (blue) and 0–30 (green) min. All four plots show the similar patterns for the different time terms, still showing a tendency that the shorter the time interval the smaller the rms, in general. One noticeable thing is that patient-to-patient variation is much larger than variation from different time terms. Even for the fractions whose average breathing peak–trough ranges are more than 0.5 cm (figures 7(c) and (d)), patient-to-patient variation is still much larger. All the plots show the wide ranges of variation for the rms, and even figures 7(c) and (d), which are for coplanar treatments, show wide variation. Obviously, the geometric uncertainty is larger for non-planar treatments (figures 7(a) and (c)) and for the larger tumor motion (figures 7(c) and (d)).

4. Discussion

With the advance in radiation treatment techniques, more and more highly conformal dose distribution is possible. This also implies that even minor geometric uncertainty can have an effect on the tumor control and normal tissue complications (Stroom *et al* 1999, van Herk 2004). Consequently, target localization is more important than ever before and tumor motion compensation is one of the demanding problems in radiation oncology field especially for thoracic and abdominal tumors. Several techniques have been proposed to compensate for the tumor motion, such as respiratory gating (Vedam *et al* 2001, Kubo and Wang 2002, Ozhasoglu and Murphy 2002, Giraud *et al* 2003, Hugo *et al* 2003, Nill *et al* 2005, George *et al* 2006, Jiang 2006) and tumor tracking (Schweikard *et al* 2000, 2004, Keall *et al* 2001, 2005, Murphy 2004, Suh *et al* 2004, Papiez and Rangaraj 2005, Papiez *et al* 2005, Webb 2005b, 2005a, Kamino *et al* 2006, Neicu *et al* 2006, Xu *et al* 2006). In order to implement these, however, monitoring the target is essential, and 2D x-ray imaging during treatment is a widely available method to quantify internal motion as shown in table 1.

Nill *et al* (2005) compared the imaging systems in two different geometries (figure 1) in their study to look at the possibility of using them for online correction in real-time tumor tracking radiotherapy. They concluded that both systems had the ability to correct for most of the motion, still inline geometry (figure 1(a)) was better. Though they did some dosimetric studies to compare the different systems, they used only one patient with simulated AP tumor motion. In our study, the accuracy of 2D projection imaging methods in 3D tumor motion monitoring has been investigated by quantifying the unresolved motion due to the limitation of 2D projection to monitor the motion in 3D, using the same assumptions as Nill *et al* (2005), but with a tumor motion database of 160 treatment fractions having estimated 3D patient tumor motion.

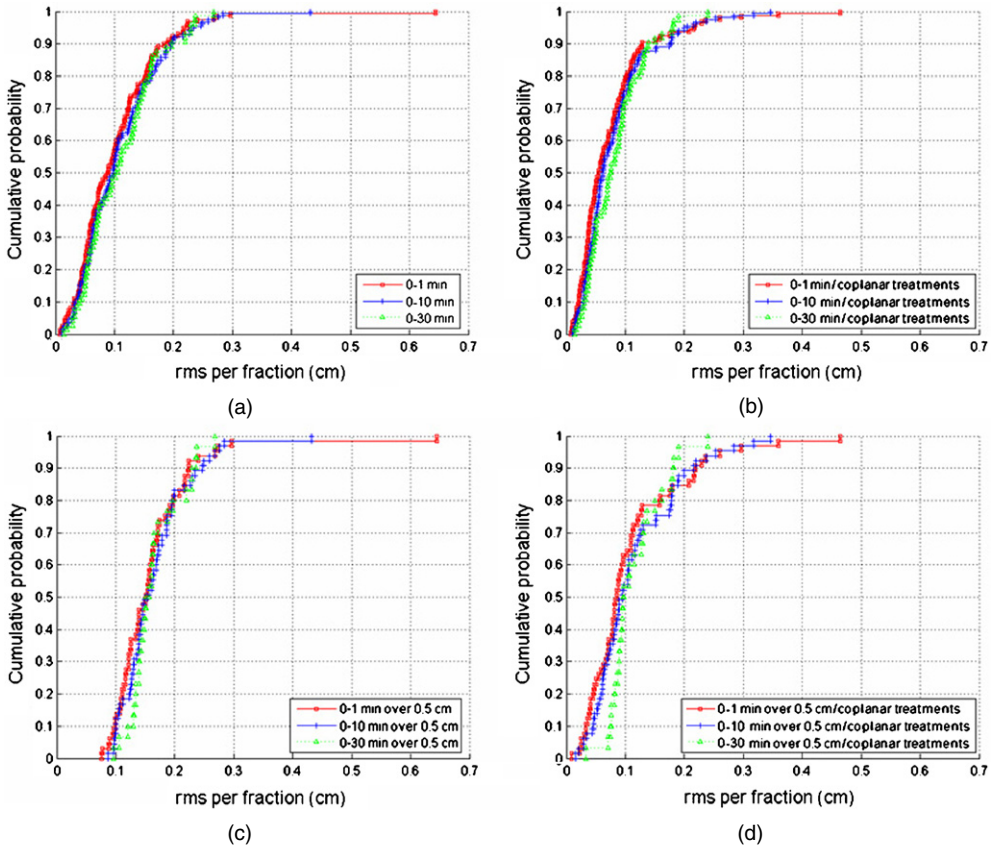

Figure 7. Cumulative probability of the distributions of the rms of ((a) and (c)) $R_{g,c,t,i}$ (rms uncertainty of the unresolved motion for each fraction i and for each time interval t for non-coplanar treatments) or ((b) and (d)) $R_{g,t,i}$ (rms uncertainty of the unresolved motion for each fraction i and for each time interval t for coplanar treatments) for 0–1 (red), 0–10 (blue) and 0–30 (green) min for an inline orientation: (a) all fractions for non-coplanar treatments, (b) all fractions for coplanar treatments, (c) fractions whose average breathing peak–trough ranges are more than 0.5 cm for non-coplanar treatments, and (d) fractions whose average breathing peak–trough ranges are more than 0.5 cm at each time term for coplanar treatments.

Berbeco *et al* (2004) investigated the magnitude of the localization error when a single x-ray imager was used for tumor tracking and determined the optimal geometric configuration of a dual x-ray imaging system. They found out that because tumor motion was 3D and irregular a single source/imager system was 'inadequate' and two source/imager pairs with angles between two imaging beam central axes of 90° were desirable for robust 3D target localization. The findings from the current study agree with Berbeco *et al* in that a single x-ray imaging system is limited; however, the magnitude of geometric uncertainty for a single x-ray imaging system, an overall rms error of 0.13 cm, is not 'inadequate', but will be a useful tool for estimating internal target position during radiotherapy.

In this study, the unresolved motion due to the geometric limitations of 2D projection imaging systems was calculated as displacement in the imaging beam axis for each of given treatment beam angles, assuming that 3D online patient positioning was performed prior to the treatment. As other sources of geometric uncertainty are ignored, such as measurement

Figure 8. Dosimetric impact of the unresolved motion: probability density function (pdf), $p(\vec{r})$, can be divided into (a) the component parallel to the beam (along the dose fall-off), $p(z)$, and (b) the component perpendicular to the beam, $p(x)$. If an anatomic point, r_0, moves with the pdf in dose distribution, $D_{\text{static}}(\vec{r})$, the dose delivered to r_0 is $D_{\text{delivered}}(r_0) = \int p(\vec{r}) D_{\text{static}}(\vec{r})\, \mathrm{d}\vec{r}$; $D_{\text{delivered}} \approx D_{\text{static}}$ for $p(z)$ and $D_{\text{delivered}} \neq D_{\text{static}}$ for some $p(x)$.

uncertainty, imaging/treatment beam alignment etc, the geometric uncertainty quantified in this study represents the lower limits of overall treatment uncertainty possible with a single x-ray imager.

In figure 1, both inline and orthogonal imaging and treatment beam orientations are shown. The geometric uncertainty for the inline and orthogonal orientation is the same; however, how the geometric uncertainty manifests itself as dosimetric uncertainty is different for the two orientations. The dosimetric impact of the unresolved motion is generally higher for the orthogonal orientation (Nill *et al* 2005). Figure 8 shows the dosimetric impact of the unresolved motion by the probability density function (pdf) (Bortfeld *et al* 2002). Let an anatomic point move with the pdf, p, in dose distribution, $D_{\text{static}}(\vec{r}')$; then the dose delivered to any point is $D_{\text{delivered}}(\vec{r}) = \int p(\vec{r} - \vec{r}') D_{\text{static}}(\vec{r}')\, \mathrm{d}\vec{r}'$. Here, $p(\vec{r} - \vec{r}')$ can be divided into the components parallel to beam, $p(z)$ (figure 8(a)), and perpendicular to beam, $p(x)$ (figure 8(b)); $D_{\text{delivered}} \approx D_{\text{static}}$ for $p(z)$ and $D_{\text{delivered}} \neq D_{\text{static}}$ for some $p(x)$. Thus, in the orthogonal orientation the geometric uncertainty from the unresolved motion can be in a high dose gradient direction (figure 8(b)), whereas in the inline orientation it is along the dose fall-off in the beam direction where the gradient is lower (figure 8(a)). Still, the dose delivery is varying temporally as well as spatially, and the beam angles, beam modulation, and order of beam delivery will all affect the dosimetric impact of the unresolved motion from 2D projection imaging.

Considering that most conventional abdominal and thoracic treatments are coplanar, the tumor motion in the SI direction is always resolved in coplanar treatments for both orientations (Nill *et al* 2005) shown in figures 3(c) and (f) and 4(c). This may guarantee the smaller geometric uncertainty from the unresolved motion for 2D projection imaging in both orientations because the patient respiratory tumor motion is usually thought to be the largest in the SI direction. Figure 4(a), however, shows that there are some patients whose tumor motion is the largest in the LR direction, and figure 4(b) the largest in the AP direction, which indicates there could be large uncertainty from LR and AP motion components as well. This reveals that patient-to-patient variation of respiratory tumor motion is substantial, and there is a wide variability of patient respiratory motion patterns (Chen *et al* 2001, Stevens *et al* 2001, Seppenwoolde *et al* 2002, Ahn *et al* 2004, Mageras *et al* 2004). Patient-to-patient variation is also shown in figure 7. The outspread ranges of the rms in cumulative probability of the distributions demonstrate that patient-to-patient variation is more significant than variation with increasing time. It is also evident for the fractions whose average breathing peak–trough ranges are more than 0.5 cm (figures 7(c) and (d)).

Comparing the interfractional uncertainty in figure 5 and the intrafractional uncertainty in figure 6, the changes in magnitude and phase of the geometric uncertainty are more noticeable

for interfractional variation, as the scales in the axis of the rms uncertainty in figure 5 double those in figure 6 and the shapes of the plots vary more in figure 5 than in figure 6.

Tables 2–5 show the geometric uncertainty depending on the tumor sites, tumor motion ranges, time intervals and beam angles. Overall rms values of the rms uncertainty of the unresolved motion was around 0.13 cm for all treatment fractions, 0.10 cm for all coplanar treatment fractions, 0.18 cm for the fractions whose average breathing peak–trough ranges were more than 0.5 cm, and 0.13 cm for the coplanar treatment fractions whose average breathing peak–trough ranges were more than 0.5 cm. As the time interval increases, the rms, minimum and maximum values show decreasing tendencies for the lung patients, but increasing for the liver and retroperitoneal patients. This can potentially be explained by the fact that the lung patients often have limited lung function and thus breathe heavily after physical activity, such as climbing on the treatment couch. They relax after several minutes and finally breathe more quietly. In contrast, the liver and retroperitoneal patients, usually with normal lung function, may be relaxed from the start of the treatment and have abdominal breathing. For the chest wall/internal mammary nodes, all the values are small and about the same for different time terms. This is obvious because in general the motion of those sites is relatively small and so results in small geometric uncertainty. In addition, interpretation of the results is limited by small patient numbers.

The smaller values in tables 3 and 5 than in tables 2 and 4, respectively, and noticeably larger minima of $R_{g,c,t,i}$ in table 4 than those of $R_{g,t,i}$ in table 5 indicate that the geometric uncertainty is smaller for the coplanar treatments than for the non-coplanar treatments. This means that the predominant motion is in the SI direction, which is resolved for coplanar treatments. It also points that for the cohort of patients studied, SI tumor motion, which is resolved in both orientations for coplanar treatments, contributes to the geometric uncertainty most.

Clinical application for the results can be the quantification of geometric uncertainty margins when a single 2D projection imager is used for tumor tracking. The use of a single 2D imager to estimate internal position will require margins of the order of 0.3 cm, which is about twice the rms values of $R_{g,c,t,i}$ or $R_{g,t,i}$.

The results of this study assume the acquisition of continuous x-ray images to monitor the tumor, which would cause high dose to the patient. Alternatively, it is possible to use periodic x-ray images and continuous optical tracking by integrating a single 2D x-ray imaging system and 3D optical monitoring system (the commercially available Cyberknife system (Schweikard *et al* 2000, 2004, Murphy 2004) integrates dual x-ray imaging with 3D optical monitoring in the Synchrony system).

Acknowledgments

This work was supported by grant no. R01CA93626 from the National Institutes of Health. The authors wish to thank Richard Stark, Varian Medical Systems for initial discussions on this study and Dr Elisabeth Weiss for useful discussions and critique of the manuscript.

References

Ahn S, Yi B, Suh Y, Kim J, Lee S, Shin S, Shin S and Choi E 2004 A feasibility study on the prediction of tumour location in the lung from skin motion *Br. J. Radiol.* **77** 588–96

Berbeco R I, Jiang S B, Sharp G C, Chen G T Y, Mostafavi H and Shirato H 2004 Integrated radiotherapy imaging system (IRIS): design considerations ot tumour tracking with linac gantry-mounted diagnostic x-ray systems with flat-panel detectors *Phys. Med. Biol.* **49** 243–55

Berbeco R I, Neicu T, Rietzel E, Chen G T Y and Jiang S B 2005 A technique for respiratory-gated radiotherapy treatment verification with an EPID in cine mode *Phys. Med. Biol.* **50** 3669–79

Bortfeld T, Jokivarsi K, Goitein M, Kung J and Jiang S B 2002 Effects of intra-fraction motion on IMRT dose delivery: statistical analysis and simulation *Phys. Med. Biol.* **47** 2203–20

Chen Q S, Weinhous M S, Deibel F C, Ciezki J P and Macklis R M 2001 Fluoroscopic study of tumor motion due to breathing: facilitating precise radiation therapy for lung cancer patients *Med. Phys.* **28** 1850–6

George R, Ramakrishnan V, Siebers J V, Chung T D and Keall P J 2006 Investigation of patient, tumour and treatment variables affecting residual motion for respiratory-gated radiotherapy *Phys. Med. Biol.* **51** 5305–19

Gilhuijs K G A, van de Ven P J H and van Herk M 1996 Automatic three-dimensional inspection of patient setup in radiation therapy using portal images, simulator images, and computed tomography data *Med. Phys.* **23** 389–99

Giraud P, Reboul F, Clippe S, Garcia R, Carrie C, Campana F, Dubray B, Rosenwald J C and Cosset J M 2003 Respiration-gated radiotherapy: current techniques and potential benefits *Cancer Radiother.* **7** (Suppl. 1) 15s–25s

Hugo G D, Agazaryan N and Solberg T D 2003 The effects of tumor motion on planning and delivery of respiratory-gated IMRT *Med. Phys.* **30** 1052–66

Jiang S B 2006 Technical aspects of image-guided respiration-gated radiation therapy *Med. Dosim.* **31** 141–51

Kamino Y, Takayama K, Kokubo M, Narita Y, Hirai E, Kawawda N, Mizowaki T, Nagata Y, Nishidai T and Hiraoka M 2006 Development of a four-dimensional image-guided radiotherapy system with a gimbaled X-ray head *Int. J. Radiat. Oncol. Biol. Phys.* **66** 271–8

Keall P J, Joshi S, Vedam S S, Siebers J V, Kini V R and Mohan R 2005 Four-dimensional radiotherapy planning for DMLC-based respiratory motion tracking *Med. Phys.* **32** 942–51

Keall P J, Kini V R, Vedam S S and Mohan R 2001 Motion adaptive x-ray therapy: a feasibility study *Phys. Med. Biol.* **46** 1–10

Keall P J, Todor A D, Vedam S S, Bartee C L, Siebers J V, Kini V R and Mohan R 2004 On the use of EPID-based implanted marker tracking for 4D radiotherapy *Med. Phys.* **31** 3492–9

Kubo H D and Wang L 2002 Introduction of audio gating to further reduce organ motion in breathing synchronized radiotherapy *Med. Phys.* **29** 345–50

Lam K L, Ten Haken R K, McShan D L and Thornton A F Jr 1993 Automated determination of patient setup errors in radiation therapy using spherical radio-opaque markers *Med. Phys.* **20** 1145–52

Langen K M and Jones D T 2001 Organ motion and its management *Int. J. Radiat. Oncol. Biol. Phys.* **50** 265–78

Langen K M *et al* 2003 Evaluation of ultrasound-based prostate localization for image-guided radiotherapy *Int. J. Radiat. Oncol. Biol. Phys.* **57** 635–44

Lu W, Ruchala K J, Chen M-L, Chen Q and Olivera G H 2006 Real-time respiration monitoring using the radiotherapy treatment beam and four-dimensional computed tomography (4DCT)—a conceptual study *Phys. Med. Biol.* **51** 4469–95

Mackie T R, Holmes T, Swerdloff S, Reckwerdt P, Deasy J O, Yang J, Paliwal B and Kinsella T 1993 Tomotherapy: a new concept for the delivery of dynamic conformal radiotherapy *Med. Phys.* **20** 1709–19

Mageras G S *et al* 2004 Measurement of lung tumor motion using respiration-correlated CT *Int. J. Radiat. Oncol. Biol. Phys.* **60** 933–41

Mcbain C A *et al* 2006 X-ray volumetric imaging in image-guided radiotherapy: the new standard in on-treatment imaging *Int. J. Radiat. Oncol. Biol. Phys.* **64** 625–34

Murphy M J 2004 Tracking moving organs in real time *Semin. Radiat. Oncol.* **14** 91–100

Neicu T, Berbeco R, Wolfgang J and Jiang S B 2006 Synchronized moving aperture radiation therapy (SMART): improvement of breathing pattern reproducibility using respiratory coaching *Phys. Med. Biol.* **51** 617–36

Nill S, Unkelbach J, Dietrich L and Oelfke U 2005 Online correction for respiratory motion: evaluation of two different imaging geometries *Phys. Med. Biol.* **50** 4087–96

Oelfke U, Tucking T, Nill S, Seeber A, Hesse B, Huber P and Thilmann C 2006 Linac-integrated kV-cone beam CT: technical features and first applications *Med. Dosim.* **31** 62–70

Ozhasoglu C and Murphy M J 2002 Issues in respiratory motion compensation during external-beam radiotherapy *Int. J. Radiat. Oncol. Biol. Phys.* **52** 1389–99

Papiez L and Rangaraj D 2005 DMLC leaf-pair optimal control for mobile, deforming target *Med. Phys.* **32** 275–85

Papiez L, Rangaraj D and Keall P J 2005 Real-time DMLC IMRT delivery for mobile and deforming targets *Med. Phys.* **32** 3037–48

Scarbrough T J, Golden N M, Ting J Y, Fuller C D, Wong A, Kupelian P A and Thomas C R 2006 Comparison of ultrasound and implanted seed marker prostate localization methods: implications for image-guided radiotherapy *Int. J. Radiat. Oncol. Biol. Phys.* **65** 378–87

Schweikard A, Glosser G, Bodduluri M, Martin J M and Adler J R 2000 Robotic motion compensation for respiratory movement during radiosurgery *Comput.-Aided Surg.* **5** 263–77

Schweikard A, Schiomi H and Adler J 2004 Respiration tracking in radiosurgery *Med. Phys.* **31** 2738–41
Seppenwoolde Y, Shirato H, Kitamura K, Shimizu S, van Herk M, Lebesque J V and Miyasaka K 2002 Precise and real-time measurement of 3D tumor motion in lung due to breathing and heartbeat, measured during radiotherapy *Int. J. Radiat. Oncol. Biol. Phys.* **53** 822–34
Shimizu S, Shirato H, Kitamura K, Shinohara N, Harabayashi T, Tsukamoto T, Koyanagi T and Miyasaka K 2000 Use of an implanted marker and real-time tracking of the marker for the positioning of prostate and bladder cancers *Int. J. Radiat. Oncol. Biol. Phys.* **48** 1591–7
Stevens C W, Munden R F, Forster K M, Kelly J F, Liao Z, Starkschall G, Tucker S and Komaki R 2001 Respiratory-driven lung tumor motion is independent of tumor size, tumor location, and pulmonary function *Int. J. Radiat. Oncol. Biol. Phys.* **51** 62–8
Stroom J C, de Boer H C, Huizenga H and Visser A G 1999 Inclusion of geometrical uncertainties in radiotherapy treatment planning by means of coverage probability *Int. J. Radiat. Oncol. Biol. Phys.* **43** 905–19
Suh Y, Yi B, Ahn S, Kim J H, Lee S, Shin S, Shin S and Choi E K 2004 Aperture maneuver with compelled breath (AMC) for moving tumors: a feasibility study with a moving phantom *Med. Phys.* **31** 760–6
van Herk M 2004 Errors and margins in radiotherapy *Semin. Radiat. Oncol.* **14** 52–64
Vedam S S, Keall P J, Kini V R and Mohan R 2001 Determining parameters for respiration-gated radiotherapy *Med. Phys.* **28** 2139–46
Webb S 2005a The effect on IMRT conformality of elastic tissue movement and a practical suggestion for movement compensation via the modified dynamic multileaf collimator (dMLC) technique *Phys. Med. Biol.* **50** 1163–90
Webb S 2005b Limitations of a simple technique for movement compensation via movement-modified fluence profiles *Phys. Med. Biol.* **50** N155–61
Webb S 2006 Motion effects in (intensity modulated) radiation therapy: a review *Phys. Med. Biol.* **51** R403–25
Weiss E, Vorwerk H, Richter S and Hess C F 2003 Interfractional and intrafractional accuracy during radiotherapy of gynecologic carcinomas: a comprehensive evaluation using the ExacTrac system *Int. J. Radiat. Oncol. Biol. Phys.* **56** 69–79
Willoughby T R, Forbes A R, Buchholz D, Langen K M, Wagner T H, Zeidan O A, Kupelian P A and Meeks S L 2006a Evaluation of an infrared camera and x-ray system using implanted fiducials in patients with lung tumors for gated radiotherapy *Int. J. Radiat. Oncol. Biol. Phys.* **66** 568–75
Willoughby T R *et al* 2006b Target localization and real-time tracking using the Calypso 4D localization system in patients with localized prostate cancer *Int. J. Radiat. Oncol. Biol. Phys.* **65** 528–34
Xu T, Wong J T, Shikhaliev P M, Ducote J L, Al-Ghazi M S and Molloi S 2006 Real-time tumor tracking using implanted positron emission markers: concept and simulation study *Med. Phys.* **33** 2598–609

Appendix E

ON THE ACCURACY OF A MOVING AVERAGE ALGORITHM FOR TARGET TRACKING DURING RADIATION THERAPY TREATMENT DELIVERY

Rohini George

Yelin Suh

Martin Murphy

Jeffrey Williamson

Elisabeth Weiss

Paul J. Keall

Medical Physics 35(6), 2008

On the accuracy of a moving average algorithm for target tracking during radiation therapy treatment delivery

Rohini George[a)]
Department of Radiation Oncology, Virginia Commonwealth University, Richmond, Virginia 23298 and Department of Radiation Oncology, University of Maryland School of Medicine, Baltimore, Maryland 21201

Yelin Suh
Department of Radiation Oncology, Virginia Commonwealth University, Richmond, Virginia 23298 and Department of Radiation Oncology, Stanford University, Stanford, California 94305

Martin Murphy and Jeffrey Williamson
Department of Radiation Oncology, Virginia Commonwealth University, Richmond, Virginia 23298

Elizabeth Weiss
Department of Radiation Oncology, Virginia Commonwealth University, Richmond, Virginia 23298 and Department of Radiation Oncology, University of Göttingen, D-37099 Göttingen, Germany

Paul Keall
Department of Radiation Oncology, Virginia Commonwealth University, Richmond, Virginia 23298 and Department of Radiation Oncology, Stanford University, Stanford, California 94305

(Received 17 September 2007; revised 16 April 2008; accepted for publication 17 April 2008; published 19 May 2008)

Real-time tumor targeting involves the continuous realignment of the radiation beam with the tumor. Real-time tumor targeting offers several advantages such as improved accuracy of tumor treatment and reduced dose to surrounding tissue. Current limitations to this technique include mechanical motion constraints. The purpose of this study was to investigate an alternative treatment scenario using a moving average algorithm. The algorithm, using a suitable averaging period, accounts for variations in the average tumor position, but respiratory induced target position variations about this average are ignored during delivery and can be treated as a random error during planning. In order to test the method a comparison between five different treatment techniques was performed: (1) moving average algorithm, (2) real-time motion tracking, (3) respiration motion gating (at both inhale and exhale), (4) moving average gating (at both inhale and exhale) and (5) static beam delivery. Two data sets were used for the purpose of this analysis: (a) external respiratory-motion traces using different coaching techniques included 331 respiration motion traces from 24 lung-cancer patients acquired using three different breathing types [free breathing (FB), audio coaching (A) and audio-visual biofeedback (AV)]; (b) 3D tumor motion included implanted fiducial motion data for over 160 treatment fractions for 46 thoracic and abdominal cancer patients obtained from the Cyberknife Synchrony. The metrics used for comparison were the group systematic error (M), the standard deviation (SD) of the systematic error (Σ) and the root mean square of the random error (σ). Margins were calculated using the formula by Stroom *et al.* [Int. J. Radiat. Oncol., Biol., Phys. **43**(4), 905–919 (1999)]: $2\Sigma+0.7\sigma$. The resultant calculations for implanted fiducial motion traces (all values in cm) show that M and Σ are negligible for moving average algorithm, moving average gating, and real-time tracking (i.e., M and $\Sigma=0$ cm) compared to static beam ($M=0.02$ cm and $\Sigma=0.16$ cm) or gated beam delivery ($M=-0.05$ and 0.16 cm at both exhale and inhale, respectively, and $\Sigma=0.17$ and 0.26 cm at both exhale and inhale, respectively). Moving average algorithm $\sigma=0.22$ cm has a slightly lower random error than static beam delivery $\sigma=0.24$ cm, though gating, moving average gating, and real-time tracking have much lower random error values for implanted fiducial motion. Similar trends were also observed for the results using the external respiratory motion data. Moving average algorithm delivery significantly reduces M and Σ compared with static beam delivery. The moving average algorithm removes the nonstationary part of the respiration motion which is also achieved by AV, and thus the addition of the moving average algorithm shows little improvement with AV. Overall, a moving average algorithm shows margin reduction compared with gating and static beam delivery, and may have some

0094-2405/2008/35(6)/2356/10/$23.00

mechanical advantages over real-time tracking when the beam is aligned with the target and patient compliance advantages over real-time tracking when the target is aligned to the beam. © *2008 American Association of Physicists in Medicine*. [DOI: 10.1118/1.2921131]

Key words: moving average algorithm, tumor tracking, implanted fiducial motion, external respiratory motion, real time tracking, gating

I. INTRODUCTION

Radiation therapy treatment using real-time tumor targeting offers several advantages towards the improvement of accuracy during radiotherapy, especially for lung cancer patients where the tumor moves continuously throughout the treatment.[1–16] During real-time tracking, the treatment beam continuously realigns to the tumor throughout the treatment.[17–38] The advantages to such a treatment technique include improved accuracy of tumor treatment and reduced dose to surrounding tissue by reducing the margin added for tumor motion. However, currently there are certain practical limitations to this technique.

Bortfeld *et al.*[39] showed that if the systematic error component of interfraction motion can be removed; according to margin formulas the residual random error is not significantly deleterious to the dose delivered to the patient. The problem of the above conclusions is that the systematic error component correction, i.e., mean target position of the intrafraction motion, cannot be known *a priori* before commencing each fraction of treatment. Thus, the most accurate static beam delivery scenario of online pretreatment target-beam alignment may still result in systematic errors. However, by tracking using a continuously updated estimate of the mean target position during treatment the systematic error could possibly be reduced to negligible levels.[40] This reasoning prompted the investigation of a moving average algorithm.

Van Herk *et al.*[41] have described systematic errors as errors mainly due to the preparation of the treatment and random errors as errors during the delivery of the treatment on every treatment day. Using patient measurements taken on a daily basis for a number of patients over a number of fractions, three parameters were quantified: group systematic error, systematic error, and random error. Group systematic error, M, is a mean of all the means of the daily measurements and is expected to be very small. It deviates often from mean because of imprecision in equipment and procedure. Systematic error, Σ, is the standard deviation (SD) of the means and is an assessment of reproducibility of the treatment preparation. Random error, σ, is the root mean square of the SD of the daily measurements.[41]

Though motion exceeding mechanical constraints is possible for motion parallel and perpendicular to the leaf motion direction, motion parallel to the leaf direction is clearly the most sensitive. There are several options where multileaf collimator (MLC) tracking in any direction is not possible. An obvious solution is to ignore the motion or use gating. An approach to essentially eliminate the systematic tracking error and treat the respiration motion as residual random error is to use a moving average algorithm with a time scale of several breathing periods. This approach significantly reduces the mechanical requirements on the MLC, and can also be combined with respiration gating.

The moving average algorithm may be appropriate in situations of significant target motion to either:

(1) account for either mechanical limitations of MLC, linac or treatment couch (from a number of manufacturers whose mechanical limitations may vary) to deliver motion compensated radiotherapy where the beam and tumor are continuously aligned, or
(2) for practical considerations, such as for couch tracking, moving the patient with the negative velocity of the tumor motion may be uncomfortable for the patient.

For one MLC type, Wijesooriya *et al.*[42] estimated that target motion *parallel* to leaf motion could be achieved for

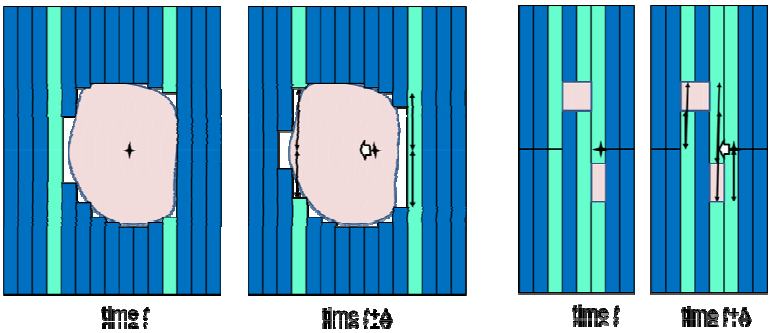

FIG. 1. A demonstration of the challenge of using a multileaf collimator to track motion perpendicular to the leaf direction for conformal radiotherapy (left) and IMRT (right). If a target being tracked at time t moves perpendicular to the leaf motion (in this case ~1.5 leaf widths for the conformal case and 1 leaf for the IMRT case) at time $t+\Delta$, then the target motion can result in a much larger motion of some of the individual leaves. The leaves with the largest motion are light shaded, and the magnitude of motion of these leaves is shown with arrows. This problem can be further exaggerated by IMRT delivery (right), where the leaf sequencing process can result in adjacent leaves having positions several centimeters apart.

up to 97% of respiratory motion, however no attempt was made to investigate the efficiency for motion perpendicular to the leaf direction—or the real case of motion parallel and perpendicular to the leaf direction. A demonstration of the challenge of using a MLC to track motion perpendicular to the leaf direction is shown in Fig. 1. If a target being tracked at time t moves perpendicular to the leaf motion (in this case ~1.5 leaf widths) at time $t+\Delta$, then *a given target motion can result in a much larger motion of some of the individual leaves*. If the difference in position of individual leaves divided by the time to achieve the motion is greater than the maximum leaf velocity (~3.5 cm s^{-1}), a beam hold will occur. Any one leaf not being in position will cause a beam hold, and thus MLC tracking efficiency is governed not by the average maximum velocity of the leaves, but the maximum velocity of an individual leaf. If there are a significant number of beam holds, the delivery efficiency will be substantially decreased, to the point of not being able to complete a given treatment. This problem can be further exaggerated by IMRT delivery, where the leaf sequencing process can result in adjacent leaves having positions several centimeters apart.

The study of Wijesooriya *et al.*[42] was for only one MLC type. It is likely that there will be variability between manufacturers, and even individual MLCs, so that in general it is not valid to state that MLCs are capable of real-time tracking of respiratory-induced target motion.

The moving average algorithm was chosen since, despite its simplicity, the moving average algorithm is optimal for a common task: reducing random noise while retaining a sharp step response. This makes it the premier filter for time domain encoded signals.[43] Though there are other options for such filters, the moving average algorithm achieves the desired goal, to essentially eliminate systematic error caused by any nonstationary signals (e.g., base line drift) and the motion of each respiration cycle is treated as a residual random error. Moving average can be considered as an intermediate state between real-time tumor tracking and static beam delivery. While the moving average algorithm does not follow the tumor on a moment by moment basis it does follow the general trend of the tumor motion. This is an important advantage over static beam delivery especially during period of base line drift where based on the theory of moving average algorithm the beam would follow the general trend of the motion pattern.

The advantages and disadvantages of a moving average algorithm compared with real-time tracking and static beam delivery with pretreatment correction are:

Advantages of moving average algorithm for tracking:

(1) More accurate than pretreatment correction.
(2) Less mechanical motion and therefore possibly longer motor life than real-time tracking.
(3) Less issue of moving MLC leaves,[19,20,22,23] linac[1,17,33,34] or couch[44] at high velocities since an average period is used. The couch motion may also affect patient compliance and secondary-induced skeletal motion.
(4) An additional issue for DMLC IMRT real-time tumor tracking is that the mechanical limitations of MLC[45] motion may be exceeded, and motion perpendicular to the MLC leaf travel direction can also cause beam holds during delivery and therefore the moving average algorithm may be more efficient than real-time tumor tracking in terms of delivery time.

Disadvantages of moving average algorithm for tracking:

(1) Less precise than continuous tracking.
(2) Still requires feedback mechanism for target motion registration to align the beam and the target during treatment.

Given the advantages (and disadvantages) of the moving average algorithm listed above, the aim of this study is to quantify the accuracy and precision of radiation therapy treatment delivery using a moving average algorithm for tracking in comparison with real-time tracking algorithm, gated beam delivery, moving average gating, and static beam delivery with online pretreatment target-beam alignment.

II. METHOD AND MATERIALS

II.A. Data acquisition

Two sets of respiration motion data were used for the purpose of analyzing the accuracy of moving average algorithm.

II.A.1. External respiratory motion

This motion data consisted of 331 4 min abdominal wall (respiratory) anterior-posterior motion traces from 24 lung cancer patients using the Varian RPM system. Each patient was initially asked to breathe without instructions called free breathing (FB) and the respiration motion was recorded. Then audio (A) instructions were given followed by audio-visual (AV) biofeedback based on the frequency and displacement of respiration motion during the FB session. For each type of instruction the respiration motion was recorded. The respiration rate for this set of patients varied between 6 and 24 breaths per minute. The displacement for this set of patients varied between 0.6 and 3 cm peak-to-peak motion. The process was repeated five times for each patient with each session typically spaced a week apart. Further details on the data collected can be found in George *et al.*[46–48] The main application of these data was to study the link between the systematic and random error and the breathing training types, and it is important to note that the data are not tumor motion, for which a separate data set described below was used.

II.A.2. Implanted fiducial motion

This 3D target motion were was acquired from 46 thoracic and abdominal cancer patients treated with stereotactic body radiotherapy using the Cyberknife Synchrony (Accuray Inc. Sunnyvale, CA) system at Georgetown University Hospital and shared under an IRB-approved protocol. Between July 2005 and January 2006 implanted fiducial motion data

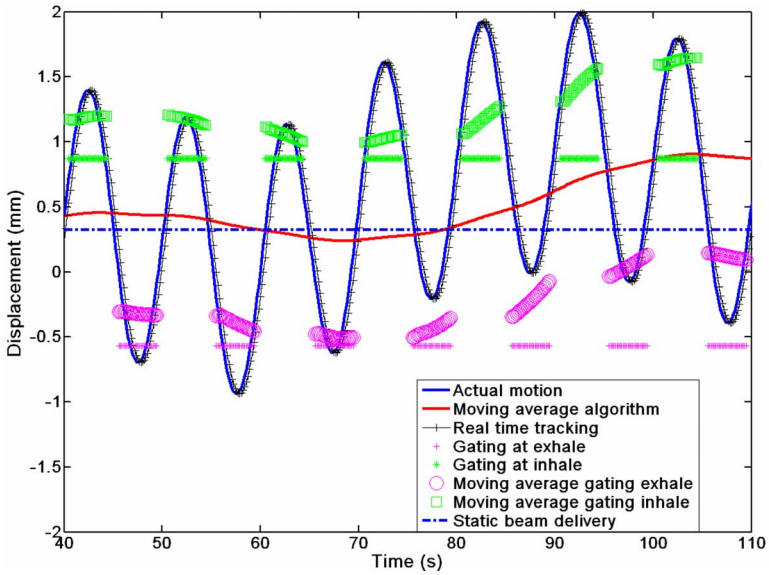

FIG. 2. Five different treatment scenarios are displayed in this figure depicting the comparison performed in this study. Gating and moving average gating were evaluated at both exhale and inhale.

were acquired for patients with the following tumor locations: lung (30 patients), retroperitoneum (11), liver (two), chest wall (two) and internal mammary nodes (one). The number of fractions for each patient was anywhere from one to seven treatment fractions with a total of 160 treatment fractions. The Synchrony system, which was used to acquire the implanted fiducial motion information, is a subsystem of respiration tumor tracking in the Cyberknife system.[33,34,49,50] The Synchrony system estimates the tumor positions by a correlation between the external patient motion and implanted fiducial locations and a prediction algorithm. The data contained patient 4D target motion information (3D target positions versus time) and its duration time was 31.4 min (5.0–106.4 min).[51] For each of 160 treatment fractions, overall mean of the means of motion extent was 0.47 cm (0.02–1.44 cm), and overall means of the means of percent contributions from left-right, anterior-posterior, and superior-inferior motion to 3D motion were 26.6%, 30.5%, and 42.9%, respectively.

II.B. Data analysis

II.B.1. Comparison of treatment scenarios

A depiction of the five treatment delivery scenarios is shown in Fig. 2. The study assumes a real-time target position monitoring system is present for all five delivery scenarios. The target motion information is used to investigate five treatment scenarios:

(*i*) *Moving average algorithm for tracking*: In this case the position of the beam at time t is calculated as the mean of the position during the past m seconds. The value for m is assumed to be 15 s for this analysis. The number of points included in the moving average was $m \times f$, where f is the sampling frequency (30 Hz for the respiratory signals and 25 Hz for the tumor motion data). Thus, for moving average algorithm the equation was

$$x_{\text{est}}(t) = \frac{\sum_{i=t-m\times f-RT}^{t-RT} x_{\text{act}}(i)}{m \times f},$$

where $x_{\text{est}}(t)$ is the estimated position at time t, x_{act} is the actual position, and RT is the number of sample points in the system response time, assumed here to be 0.16 s.[52] From the equation above, the beam position $x_{\text{est}}(t)$ has been calculated as the average of the past 15 seconds of position information.

(*ii*) *Real-time tracking*: The treatment beam responds to the target position after a system response time RT, which is assumed to be 0.16 s as above. No motion prediction algorithm is assumed, and thus the estimated tumor position is

$$x_{\text{est}}(t) = x_{\text{act}}(t - RT).$$

Therefore from the equation for real-time tracking above it can be seen that $x_{\text{est}}(t)$ is the beam position after a system response time of RT.

(*iii*) *Gated beam delivery at inhale and exhale*: Clinically it has been suggested and also studied by various institutions that the standard range of duty cycle for a gated patient should be between 30% and 50%.[48,53] This is in order to provide the benefits of gating while mitigating the effects of intra fraction motion by limiting the treatment time. Thus for the purpose of studying respiration motion gating along with the other techniques, a duty cycle of 40% was utilized. The phase information for the purpose of this analysis was obtained from the RPM phase file for the external respiratory motion data. For the Cyberknife Synchrony data, the phase was obtained by finding the motion peak for each respiratory cycle and linearly assigning phase from 0 to 2π between successive motion peaks. Ruan *et al.*[54] have, however, noted the nonstationary nature of respiration motion. Ruan *et al.*[54] observed that various phases of respiration were predicted with various accuracies. Similarly, in Fig. 2, which displays the effect of the moving average algorithm with respect to other techniques, we can see that during the base line shift the gating window is less accurate (very slightly) as com-

TABLE I. The formalism used to calculate the metrics M, Σ and σ, where Δ is the displacement between the beam and target at a given time, and $\Delta(P_j,F_i)$ is the set of displacements for a given fraction F_i for patient P_j (see Ref. 41) (M: mean; SD: standard deviation; RMS: root mean square).

	Patient 1	Patient 2	…	
Fraction 1	$\Delta(P_1,F_1)$	$\Delta(P_2,F_2)$		
Fraction 2	$\Delta(P_1,F_2)$	$\Delta(P_2,F_2)$		
…				
			↗	$M=\overline{\Delta(P_1\ldots P_M,F_1\ldots F_N)}$
Mean	$\overline{\Delta(P_1,F_1\ldots F_N)}$	$\overline{\Delta(P_2,F_1\ldots F_N)}$	→	$\Sigma=\mathrm{SD}(\Delta(P_1\ldots P_M,F_1\ldots F_N))$
SD	$\mathrm{SD}(\Delta(P_1,F_1\ldots F_N))$	$\mathrm{SD}(\Delta(P_2,F_1\ldots F_N))$	→	$\sigma=\mathrm{RMS}(\Delta(P_1\ldots P_M,F_1\ldots F_N))$

pared to when the base line is constant. In terms of percentage, inhale gating used phases from 80% to 20%, and exhale gating 30%–70%. The real-time calculation of phase has an associated uncertainty, particularly in the presence of varying base line, changing period, and peak-to-trough magnitude, and may not be centered about the peak, but is generally close to the peak.

The position of the beam at time t is calculated as the mean of the position during the first n seconds of gated motion. Gating beam position is calculated at both inhale and exhale. The position of the beam is determined by

$$x_{\mathrm{est}}(t)=\frac{\Sigma_{i=1}^{n\times f}x_{\mathrm{act}}(i)\times H}{\Sigma_{i=1}^{n\times f}H},$$

where H is the Heavyside function that equals 1 when the respiratory phase is within the gate and 0 otherwise. From equation for gated beam delivery at inhale and exhale above, the beam position $x_{\mathrm{est}}(t)$ has been calculated as the average of the first n seconds of beam position within the 40% duty cycle information.

In spite of issues during base line drift, phase-based gating was used in this study for the gating techniques. Displacement-based gating also has a problem with baseline drift, as the gating thresholds need to be adjusted during treatment which takes extra time, particularly if imaging verification is required. In a previous work,[48] we found a slight advantage to displacement-based gating, however the difference was less than 0.5 mm. Hence phase based gating is used as it is the more viable and also currently clinically used with the RPM system. From the study by George *et al.*[48] comparing phase with displacement-based gating, there was little difference in the overall uncertainty of these two approaches thus justifying the use of phase-based gating.

(*iv*) *Moving average gating at inhale and exhale*: The moving average gating technique involves using a moving average algorithm over the respiration motion in the gated window (obtained from *iii* above) and is given by

$$x_{\mathrm{est}}(t)=\frac{\Sigma_{i=t-m\times f-RT}^{t-RT}x_{\mathrm{act}}(i)\times H}{\Sigma_{i=1-m\times f-RT}^{t-RT}H}.$$

In this treatment scenario the position is updated every 15 s similar to moving average tracking algorithm (Sec. II.B.1.i). From equation for gated beam delivery at inhale and exhale above, the beam position $x_{\mathrm{est}}(t)$ has been calculated as the average of the most recent n seconds (i.e., from $t-RT-m\times f$ to $t-RT$) of beam position within the 40% duty cycle information.

This technique will reduce the systematic error and random error. The velocity can be similarly calculated as for the moving average. However, as only respiratory points at a given breathing phase (Fig. 2) are included, the overall velocity will be less for moving average gating than for the moving average algorithm.

(*v*) *Static beam delivery with online pretreatment target-beam alignment*: The first n seconds of target position information is used to align the beam with the target pretreatment, but the beam does not respond to target motion. Thus the position of the beam is determined as the mean of the position during the first n seconds. The position of the beam is determined by:

$$x_{\mathrm{est}}(t)=\frac{\Sigma_{i=1}^{n\times f}x_{\mathrm{act}}(i)}{n\times f}.$$

From equation for static beam delivery with online pretreatment target-beam alignment above, the beam position $x_{\mathrm{est}}(t)$ has been calculated as the average of the first n seconds of position information.

II.B.2. Evaluation metrics

The metrics evaluated for each of the five motion compensation scenarios: the group systematic error, M, the SD of the systematic error, Σ, and the root mean square of the random error, σ, were calculated as shown in Table I.[41]

The displacement of the beam and the target at a given time is indicated as Δ. Δ for the purpose of this analysis was evaluated for a given fraction F_i for a given patient P_j and is represented as $\Delta(P_j,F_i)$. To calculate the group systematic error, M, $\Delta(P_j,F_i)$ was averaged over all fractions and over all patients

$$M=\overline{\Delta(P_1\ldots P_N,F_1\ldots F_M)}.$$

For the SD of the systematic error, Σ, the first SD was obtained over all fractions of each patient $\Delta(P_j,F_i)$, and then SD was obtained over all patients

TABLE II. The values for M, Σ and σ as calculated for the different treatment scenarios for each of respiration motion (see Ref. 41). The table includes the external respiration motion obtained from 24 lung cancer patients. In parentheses are the minimum and maximum values for systematic and random error.

	Group systematic error, M (cm)			
	External			Implanted fiducial motion
Tracking algorithm	FB	A	AV	
Moving average algorithm	−0.01	−0.01	0.00	0.00
Real-time tracking	0.00	0.00	0.00	0.00
Gating exhale	−0.11	−0.05	−0.03	−0.05
Gating inhale	−0.16	−0.12	−0.02	0.16
Moving average gating at exhale	−0.01	−0.01	0.00	0.00
Moving average gating at inhale	−0.01	0.00	0.00	0.00
Static beam delivery	−0.13	−0.17	−0.06	0.02

	SD of systematic error, Σ (cm)			
	External			Implanted fiducial motion
Tracking algorithm	FB	A	AV	
Moving average algorithm	0.01 (−0.03–0.02)	0.01 (−0.03–0.01)	0.01 (−0.03–0.01)	0.00 (−0.01–0.01)
Real-time tracking	0.00 (0.00–0.00)	0.00 (0.00–0.00)	0.00 (0.00–0.00)	0.00 (0.00–0.00)
Gating at exhale	0.18 (−0.52–0.48)	0.12 (−0.28–0.25)	0.06 (−0.18–0.11)	0.17 (−0.73–0.60)
Gating at inhale	0.23 (−0.64–0.41)	0.18 (−0.52–0.21)	0.07 (−0.19–0.15)	0.26 (−0.53–1.23)
Moving average gating at exhale	0.01 (−0.03–0.04)	0.01 (−0.03–0.01)	0.01 (−0.03–0.01)	0.00 (−0.01–0.01)
Moving average gating at inhale	0.02 (−0.04–0.05)	0.01 (−0.03–0.02)	0.01 (−0.02–0.03)	0.00 (−0.02–0.01)
Static beam delivery	0.21 (−0.52–0.45)	0.24 (−0.55–0.36)	0.18 (−0.77–0.12)	0.16 (−0.56–0.84)

	Random error, σ (cm)			
	External			Implanted fiducial motion
Tracking algorithm	FB	A	AV	
Moving average algorithm	0.46 (0.14–0.80)	0.53 (0.22–0.90)	0.54 (0.23–0.88)	0.22 (0.01–0.63)
Real-time tracking	0.13 (0.07–0.25)	0.14 (0.06–0.26)	0.16 (0.08–0.32)	0.07 (0.00–0.18)
Gating at exhale	0.30 (0.11–0.58)	0.29 (0.14–0.50)	0.27 (0.13–0.49)	0.15 (0.01–0.75)
Gating at inhale	0.44 (0.15–0.77)	0.44 (0.21–0.67)	0.36 (0.13–0.68)	0.23 (0.01–0.83)
Moving average gating at exhale	0.21 (0.08–0.43)	0.21 (0.09–0.31)	0.22 (0.12–0.37)	0.10 (0.00–0.53)
Moving average gating at inhale	0.35 (0.13–0.57)	0.35 (0.17–0.58)	0.32 (0.12–0.61)	0.17 (0.01–0.68)
Static beam delivery	0.47 (0.18–0.81)	0.54 (0.21–0.86)	0.55 (0.23–0.88)	0.24 (0.01–0.82)

$$\Sigma = SD[\Delta(P_1 \ldots P_N, F_1 \ldots F_M)].$$

Finally, to obtain root mean square of the random error, σ, the root mean square was calculated overall patients over all fractions

$$\sigma = RMS[\Delta(P_1 \ldots P_N, F_1 \ldots F_M)].$$

These terms were defined by van Herk,[41] however, are clarified here as multiple error values corresponding to each time point instead of single error values for a given treatment.

II.B.3. Margin calculations

Margins were calculated for the implanted fiducial motion data using the formula $2\Sigma+0.7\sigma$ by Stroom *et al.*.[55] The two assumptions were

(1) no other error contributions (optimistic case) and
(2) 0.3 cm systematic and random error contributions from other sources (realistic case). The margins that included the 0.3 cm systematic and random errors were calculated in quadrature $2(\Sigma^2+0.3^2)+0.7(\sigma^2+0.3^2)$.

II.B.4. Averaging period and higher order algorithms

Different choices of windows for averaging between 5 and 25 s were also explored and compared against each other. In addition to the zeroth order (moving average filter), a first and a second order filter were investigated. There are a number of additional filter choices that could be investigated to obtain an algorithm which has the requirements of reducing systematic error and treating the respiratory signal as a random error. These algorithms include adaptive filters, neural networks, and template matching algorithms. However, as the results demonstrate, the simple moving average algorithm fulfils the above requirements.

III. RESULTS AND DISCUSSION

In this study we analyzed the feasibility delivery techniques using a moving average algorithm. Though the results obtained show a potential advantage by using moving average algorithm over static beam delivery, the need for feedback mechanism for target motion registration to align the beam and the target during treatment is a current barrier to the clinical implementation of this algorithm.

III.A. Comparison of treatment scenarios

The results for the five treatment scenarios for both external and implanted fiducial motion are shown in Table II. These results were obtained using $n=15$ s. Table II quantifies the geometric uncertainty using three metrics for the evaluation of the treatment scenarios being investigated.

III.A.1. External respiratory motion

For external respiratory motion, the group systematic error and SD of systematic error are negligible for moving average algorithm, moving average gating, and real-time tracking. For real-time tracking as shown by Murphy *et al.*[56] the errors can be reduced to zero by using a good prediction algorithm. The result of a moving average algorithm over the gated respiration motion, i.e., moving average gating, was an improvement to the gated respiration motion for both inhale and exhale. The random error for real-time tracking and moving average algorithm has a slightly lower random error than static beam delivery. For random error, moving average gating results showed an improvement when compared to the moving average algorithm. AV has a lower group systematic error and SD of systematic error for static beam delivery over the other training types. However, for random errors σ the AV is higher. This result could be explained by the definition of random error which is the root mean square of the SD of all the patients. Hence what we see here could be possibly the variation of respiration motion with AV across the patient population.

III.A.2. Implanted fiducial motion

Implanted fiducial motion data showed similar results to external respiration motion. Moving average results for group systematic error and SD of systematic error are negligible compared to static beams. The trend for the moving average gated respiration motion was also similar to the external respiration motion data where the random error component was a lesser magnitude compared to the moving average algorithm over the entire respiration trace. Values for this data set are listed in Table II.

For implanted fiducial motion, the different treatment techniques can be ranked based on the margin calculation without error as follows:

(1) *Real-time tracking;*
(2) *Moving average gating at exhale;*
(3) *Moving average gating at inhale;*
(4) *Moving average algorithm for tracking;*
(5) *Gated beam delivery at exhale;*

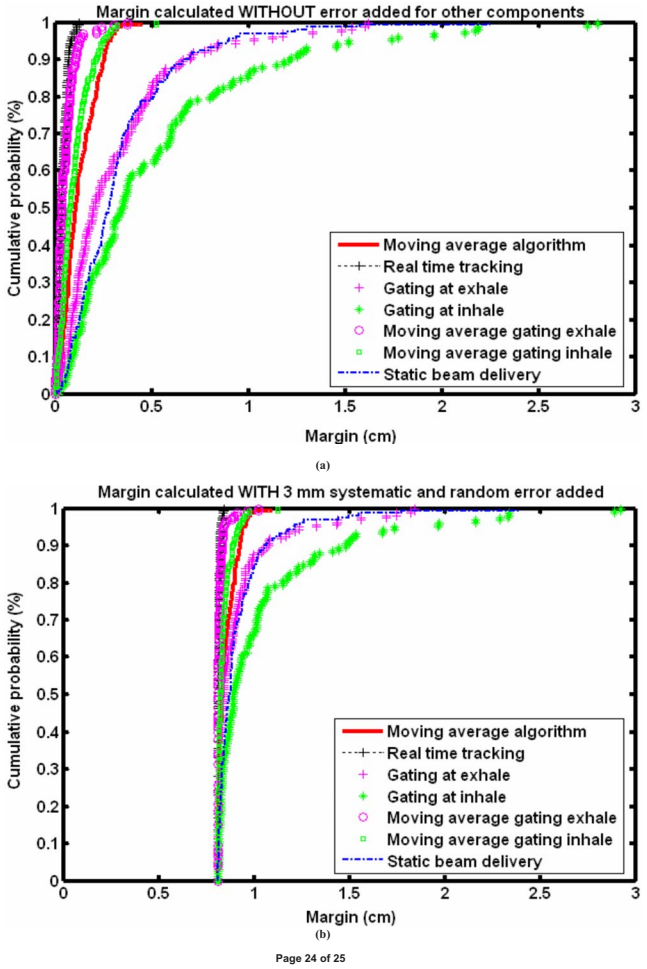

FIG. 3. Margins calculated using the five treatment scenarios for implanted fiducial motion (seven traces because gating and moving average gating are split into inhale and exhale). (a) Indicates margin calculated without other error components while (b) indicates the addition of 0.3 cm systematic and random error contribution from other sources. The x axis is the margin in cm and they y axis is the cumulative probability of the number of patients.

(6) *Static beam delivery with online pretreatment target-beam alignment;*
(7) *Gated beam delivery at inhale.*

The Kuka robot used by the Cyberknife has mechanical specifications exceeding that of respiratory motion, and this has also been the clinical experience in that beam holds are rare during Synchrony treatments. When beam holds occur, it is typically due to an unacceptable variation in the internal-external correlation model from irregular breathing. Thus the moving average algorithm is not recommended for the Cyberknife as real-time tracking works well. Real-time tracking has not been clinically implemented for MLC or couch tracking and there are potential limitations with respect to efficiency and patient motion from these techniques. The moving average algorithm may be an acceptable path to clinical implementation.

III.A.3. Margin calculations

Margins for the implanted fiducial motion are shown in Fig. 3 and quantified in Table III. Table III shows the popu-

TABLE III. Population margins using equation $2\Sigma+0.7\sigma$ (see Ref. 55) (assuming no other error components) and $2\sqrt{\Sigma^2+0.3^2}+0.7\sqrt{\sigma^2+0.3^2}$ (addition of 0.3 cm systematic and random error contribution from other sources) for the implanted fiducial motion obtained from the 46 thoracic and abdominal cancer patients. Individual margins are shown in Fig. 3.

Tracking algorithm	Margin without errors added (cm)	Margins with error added (cm)
Moving average algorithm	0.15	0.86
Real-time tracking	0.05	0.82
Gating exhale	0.45	0.92
Gating inhale	0.68	1.06
Moving average gating at exhale	0.07	0.82
Moving average gating at inhale	0.12	0.84
Static beam delivery	0.49	0.95

lation margins for the implanted fiducial motion obtained from the 46 thoracic and abdominal cancer patients. The overall population Σ and σ values are provided in Table II for the comparison of the various techniques.

Cumulative margins are shown in Fig. 3. These cumulative probability plots indicate the appropriate margin for each individual. The cumulative plots show how appropriate (or in some cases inappropriate) applying a population margin to an individual is. The cumulative probability plots are useful to determine what percentage of the patients fell into a particular margin range.

III.A.4. Averaging period and higher order algorithms

The insensitivity of three errors to different averaging period validates the use of 15 s for the other analyses performed in the study. Since there was no significant differences across these windows 15 s was chosen. Fifteen seconds also represents and average amount of time that the patient takes to settle on the table and breathe normally. Along the same lines, the simplest of the three techniques, i.e., the average of the previous n seconds or moving average, would give the best value for the new beam position as the higher order algorithms did not show any benefit.

IV. CONCLUSIONS

A technique for tumor tracking based on a moving average algorithm for tracking has been investigated. Moving average algorithm has accuracy advantages over online correction with static delivery and practical advantages over real-time tracking as the motion is slower and smoother. This has mechanical advantages when the beam is aligned to the target and patient compliance advantages when the target is aligned to the beam. The main findings of this work can be summarized as:

(1) The moving average algorithm reduces the group systematic error and SD of the systematic error compared with static beam delivery. The random error is modestly reduced.
(2) There is a group systematic error caused by intrafraction motion during FB (1.5 mm) and A (1 mm).
(3) The margins required for moving average algorithm lie between those of real-time tracking and static delivery with pretreatment beam-target alignment. The margin reduction for moving average algorithm compared with online pretreatment correction delivered with a static beam delivery is significant for FB and A, but less noticeable for AV.
(4) The margins required for moving average algorithm are in most cases less than those of gated respiration motion.
(5) For moving average algorithm and static beam delivery the systematic error using AV is less than that for FB and A.
(6) The margins required for real-time tracking as studied here are independent of breathing training type.
(7) AV and the moving average algorithm have a similar characteristic in that they both effectively remove the base line variations or nonstationary signal behavior.
(8) The moving average algorithm can add a further advantage to gated respiration motion by reducing margins making the margin values comparable to real-time tracking.

ACKNOWLEDGMENTS

This research was supported by NCI Grant No. RO1 CA 93626. The authors gratefully acknowledge Dr. Sonja Dieterich who supplied the implanted fiducial motion data from Georgetown University. The authors thank Devon Murphy for carefully reviewing and significantly improving the clarity of this manuscript.

[a]Author to whom correspondence should be addressed. Electronic mail: rgeorge@umm.edu

[1]M. J. Murphy, "Tracking moving organs in real time," Semin. Radiat. Oncol. **14**(1), 91–100 (2004).
[2]E. A. Barnes, B. R. Murray, D. M. Robinson, L. J. Underwood, J. Hanson, and W. H. Roa, "Dosimetric evaluation of lung tumor immobilization using breath hold at deep inspiration," Int. J. Radiat. Oncol., Biol., Phys. **50**(4), 1091–1098 (2001).
[3]G. T. Chen, J. H. Kung, and K. P. Beaudette, "Artifacts in computed tomography scanning of moving objects," Semin. Radiat. Oncol. **14**(1), 19–26 (2004).
[4]Q. S. Chen, M. S. Weinhous, F. C. Deibel, J. P. Ciezki, and R. M. Macklis, "Fluoroscopic study of tumor motion due to breathing: Facilitating precise radiation therapy for lung cancer patients," Med. Phys. **28**(9), 1850–1856 (2001).
[5]L. Ekberg, O. Holmberg, L. Wittgren, G. Bjelkengren, and T. Landberg, "What margins should be added to the clinical target volume in radiotherapy treatment planning for lung cancer?" Radiother. Oncol. **48**, 71–77 (1998).
[6]M. Engelsman, E. M. Damen, K. De Jaeger, K. M. van Ingen, and B. J. Mijnheer, "The effect of breathing and set-up errors on the cumulative dose to a lung tumor," Radiother. Oncol. **60**(1), 95–105 (2001).
[7]I. S. Grills, D. Yan, A. A. Martinez, F. A. Vicini, J. W. Wong, and L. L. Kestin, "Potential for reduced toxicity and dose escalation in the treatment of inoperable non-small-cell lung cancer: A comparison of intensity-modulated radiation therapy (IMRT), 3D conformal radiation, and elective nodal irradiation," Int. J. Radiat. Oncol., Biol., Phys. **57**(3), 875–890 (2003).
[8]J. Hanley, M. M. Debois, D. Mah, G. S. Mageras, A. Raben, K. Rosenzweig, B. Mychalczak, L. H. Schwartz, P. J. Gloeggler, W. Lutz, C. C. Ling, S. A. Leibel, Z. Fuks, and G. J. Kutcher, "Deep inspiration breath-

hold technique for lung tumors: The potential value of target immobilization and reduced lung density in dose escalation," Int. J. Radiat. Oncol., Biol., Phys. **45**(3), 603–611 (1999).
[9]P. Keall, "4-dimensional computed tomography imaging and treatment planning," Semin. Radiat. Oncol. **14**(1), 81–90 (2004).
[10]M. J. Murphy, D. Martin, R. Whyte, J. Hai, C. Ozhasoglu, and Q. T. Le, "The effectiveness of breath-holding to stabilize lung and pancreas tumors during radiosurgery," Int. J. Radiat. Oncol., Biol., Phys. **53**(2), 475–482 (2002).
[11]C. Plathow, S. Ley, C. Fink, M. Puderbach, W. Hosch, A. Schmahl, J. Debus, and H. U. Kauczor, "Analysis of intrathoracic tumor mobility during whole breathing cycle by dynamic MRI," Int. J. Radiat. Oncol., Biol., Phys. **59**(4), 952–959 (2004).
[12]C. S. Ross, D. H. Hussey, E. C. Pennington, W. Stanford, and J. F. Doornbos, "Analysis of movement of intrathoracic neoplasms using ultrafast computerized tomography," Int. J. Radiat. Oncol., Biol., Phys. **18**(3), 671–677 (1990).
[13]Y. Seppenwoolde, H. Shirato, K. Kitamura, S. Shimizu, M. van Herk, J. V. Lebesque, and K. Miyasaka, "Precise and real-time measurement of 3D tumor motion in lung due to breathing and heartbeat, measured during radiotherapy," Int. J. Radiat. Oncol., Biol., Phys. **53**(4), 822–834 (2002).
[14]S. Shimizu, H. Shirato, S. Ogura, H. Akita-Dosaka, K. Kitamura, T. Nishioka, K. Kagei, M. Nishimura, and K. Miyasaka, "Detection of lung tumor movement in real-time tumor-tracking radiotherapy," Int. J. Radiat. Oncol., Biol., Phys. **51**(2), 304–310 (2001).
[15]K. E. Sixel, M. Ruschin, R. Tirana, and P. C. Cheung, "Digital fluoroscopy to quantify lung tumor motion: Potential for patient-specific planning target volumes," Int. J. Radiat. Oncol., Biol., Phys. **57**(3), 717–723 (2003).
[16]C. W. Stevens, R. F. Munden, K. M. Forster, J. F. Kelly, Z. Liao, G. Starkschall, S. Tucker, and R. Komaki, "Respiratory-driven lung tumor motion is independent of tumor size, tumor location, and pulmonary function," Int. J. Radiat. Oncol., Biol., Phys. **51**(1), 62–68 (2001).
[17]Y. Kamino, K. Takayama, M. Kokubo, Y. Narita, E. Hirai, N. Kawawda, T. Mizowaki, Y. Nagata, T. Nishidai, and M. Hiraoka, "Development of a four-dimensional image-guided radiotherapy system with a gimbaled x-ray head," Int. J. Radiat. Oncol., Biol., Phys. **66**(1), 271–278 (2006).
[18]P. Keall, S. Joshi, S. S. Vedam, J. V. Siebers, V. Kini, and R. Mohan, "Four-dimensional radiotherapy planning for DMLC-based respiratory motion tracking," Med. Phys. **32**(4), 942–951 (2005).
[19]P. J. Keall, V. R. Kini, S. S. Vedam, and R. Mohan, "Motion adaptive x-ray therapy: A feasibility study," Phys. Med. Biol. **46**(1), 1–10 (2001).
[20]T. Neicu, H. Shirato, Y. Seppenwoolde, and S. B. Jiang, "Synchronized moving aperture radiation therapy (SMART): Average tumour trajectory for lung patients," Phys. Med. Biol. **48**(5), 587–598 (2003).
[21]L. Papiez and D. Rangaraj, "DMLC leaf-pair optimal control for mobile, deforming target," Med. Phys. **32**(1), 275–285 (2005).
[22]L. Papiez, D. Rangaraj, and P. Keall, "Real-time DMLC IMRT delivery for mobile and deforming targets," Med. Phys. **32**(9), 3037–3048 (2005).
[23]Y. Suh, B. Yi, S. Ahn, J. Kim, S. Lee, S. Shin, and E. Choi, "Aperture maneuver with compelled breath (AMC) for moving tumors: A feasibility study with a moving phantom," Med. Phys. **31**(4), 760–766 (2004).
[24]S. Webb, "Limitations of a simple technique for movement compensation via movement-modified fluence profiles," Phys. Med. Biol. **50**(14), N155–161 (2005).
[25]S. Webb, "The effect on IMRT conformality of elastic tissue movement and a practical suggestion for movement compensation via the modified dynamic multileaf collimator (dMLC) technique," Phys. Med. Biol. **50**(6), 1163–1190 (2005).
[26]T. Xu, J. T. Wong, P. M. Shikhaliev, J. L. Ducofe, M. S. Al-Ghazi, and S. Molloi, "Real-time tumor tracking using implanted positron emission markers: Concept and simulation study," Med. Phys. **33**(7), 2598–2609 (2006).
[27]R. I. Berbeco, T. Neicu, E. Rietzel, G. T. Chen, and S. B. Jiang, "A technique for respiratory-gated radiotherapy treatment verification with an EPID in cine mode," Phys. Med. Biol. **50**(16), 3669–3679 (2005).
[28]P. J. Keall, A. D. Todor, S. S. Vedam, C. L. Bartee, J. V. Siebers, V. R. Kini, and R. Mohan, "On the use of EPID-based implanted marker tracking for 4D radiotherapy," Med. Phys. **31**(12), 3492–3499 (2004).
[29]K. M. Langen, J. Pouliot, C. Anezinos, M. Aubin, A. R. Gottschalk, I. C. Hsu, D. Lowther, Y. M. Liu, K. Shinohara, L. J. Verhey, V. Weinberg, and M. Roach, 3rd, "Evaluation of ultrasound-based prostate localization for image-guided radiotherapy," Int. J. Radiat. Oncol., Biol., Phys. **57**(3), 635–644 (2003).
[30]C. A. McBain, A. M. Henry, J. Sykes, A. Amer, T. Marchant, C. M. Moore, J. Davies, J. Stratford, C. McCarthy, B. Porritt, P. Williams, V. S. Khoo, and P. Price, "X-ray volumetric imaging in image-guided radiotherapy: The new standard in on-treatment imaging," Int. J. Radiat. Oncol., Biol., Phys. **64**(2), 625–634 (2006).
[31]U. Oelfke, T. Tucking, S. Nill, A. Seeber, B. Hesse, P. Huber, and C. Thilmann, "Linac-integrated kV-cone beam CT: Technical features and first applications," Med. Dosim. **31**(1), 62–70 (2006).
[32]T. J. Scarbrough, N. M. Golden, J. Y. Ting, C. D. Fuller, A. Wong, P. A. Kupelian, and C. R. Thomas, Jr., "Comparison of ultrasound and implanted seed marker prostate localization methods: Implications for image-guided radiotherapy," Int. J. Radiat. Oncol., Biol., Phys. **65**(2), 378–387 (2006).
[33]A. Schweikard, G. Glosser, M. Bodduluri, M. J. Murphy, and J. R. Adler, "Robotic motion compensation for respiratory movement during radiosurgery," Comput. Aided Surg. **5**(4), 263–277 (2000).
[34]A. Schweikard, H. Shiomi, and J. Adler, "Respiration tracking in radiosurgery," Med. Phys. **31**(10), 2738–2741 (2004).
[35]S. Shimizu, H. Shirato, K. Kitamura, N. Shinohara, T. Harabayashi, T. Tsukamoto, T. Koyanagi, and K. Miyasaka, "Use of an implanted marker and real-time tracking of the marker for the positioning of prostate and bladder cancers," Int. J. Radiat. Oncol., Biol., Phys. **48**(5), 1591–1597 (2000).
[36]E. Weiss, H. Vorwerk, S. Richter, and C. F. Hess, "Interfractional and intrafractional accuracy during radiotherapy of gynecologic carcinomas: A comprehensive evaluation using the ExacTrac system," Int. J. Radiat. Oncol., Biol., Phys. **56**(1), 69–79 (2003).
[37]R. Willoughby, A. R. Forbes, D. Buchholz, K. M. Langen, T. H. Wagner, O. A. Zeidan, P. A. Kupelian, and S. L. Meeks, "Evaluation of an infrared camera and x-ray system using implanted fiducials in patients with lung tumors for gated radiation therapy," Int. J. Radiat. Oncol., Biol., Phys. **66**(2), 568–575 (2006).
[38]T. R. Willoughby, P. A. Kupelian, J. Pouliot, K. Shinohara, M. Aubin, M. Roach, 3rd, L. L. Skrumeda, J. M. Balter, D. W. Litzenberg, S. W. Hadley, J. T. Wei, and H. M. Sandler, "Target localization and real-time tracking using the Calypso 4D localization system in patients with localized prostate cancer," Int. J. Radiat. Oncol., Biol., Phys. **65**(2), 528–534 (2006).
[39]T. Bortfeld, M. van Herk, and S. B. Jiang, "When should systematic patient positioning errors in radiotherapy be corrected?" Phys. Med. Biol. **47**(23), N297–N302 (2002).
[40]M. J. Murphy, S. D. Chang, I. C. Gibbs, Q. T. Le, J. Hai, D. Kim, D. P. Martin, and J. R. Adler, Jr., "Patterns of patient movement during frameless image-guided radiosurgery," Int. J. Radiat. Oncol., Biol., Phys. **55**(5), 1400–1408 (2003).
[41]M. van Herk, "Errors and margins in radiotherapy," Semin. Radiat. Oncol. **14**(1), 52–64 (2004).
[42]K. Wijesooriya, C. L. Bartee, J. V. Siebers, S. S. Vedam, and P. Keall, "Determination of maximum leaf velocity and acceleration of a dynamic multileaf collimator: Implications for 4D radiotherapy," Med. Phys. **32**(4), 932–941 (2005).
[43]S. W. Smith, *The Scientist and Engineer's Guide to Digital Signal Processing*, California Technical Publishing, San Diego, CA (1997).
[44]W. D. D'Souza, S. A. Naqvi, and C. X. Yu, "Real-time intra-fraction-motion tracking using the treatment couch: A feasibility study," Phys. Med. Biol. **50**(17), 4021–4033 (2005).
[45]K. Wijesooriya, C. Bartee, J. V. Siebers, S. S. Vedam, and R. L. Keall, "Determination of maximum leaf velocity and acceleration of a dynamic multileaf collimator: Implications for 4D radiotherapy," Med. Phys. **32**(4), 932–941 (2005).
[46]R. George, V. Ramakrishnan, J. V. Siebers, T. D. Cnung, and P. J. Keall, "Investigation of patient, tumour and treatment variables affecting residual motion for respiratory-gated radiotherapy," Phys. Med. Biol. **51**(20), 5305–5319 (2006).
[47]R. George, S. S. Vedam, T. D. Chung, V. Ramakrishnan, and P. J. Keall, "The application of the sinusoidal model to lung cancer patient respiratory motion," Med. Phys. **32**(9), 2850–2861 (2005).
[48]R. George, T. D. Chung, S. S. Vedam, V. Ramakrishnan, R. Mohan, E. Weiss, and P. J. Keall, "Audio-visual biofeedback for respiratory-gated radiotherapy: Impact of audio instruction and audio-visual biofeedback on respiratory-gated radiotherapy?" Int. J. Radiat. Oncol., Biol., Phys. **65**(3), 924–933 (2006).

[49]M. J. Murphy, J. R. Adler, Jr., M. Bodduluri, J. Dooley, K. Forster, J. Hai, Q. Le, G. Luxton, D. Martin, and J. Poen, "Image-guided radiosurgery for the spine and pancreas," Comput. Aided Surg. **5**(4), 278–288 (2000).
[50]S. Dieterich, "Robotic radiosurgery," *Dynamic Tracking of Moving Tumors in Stereotactic Radiosurgery*, The CyberKnife Society Press, Sunnyvale, CA (2005), Chap. 6.
[51]Y. Suh, S. Dieterich, and P. J. Keall, "Geometric uncertainty of 2D projection imaging in monitoring 3D tumor motion," Phys. Med. Biol. **52**(12), 3439–3454 (2007).
[52]S. Vedam, A. Docef, M. Fix, M. Murphy, and T. Keall, "Dosimetric impact of geometric errors due to respiratory motion prediction on dynamic multileaf collimator-based four-dimensional radiation delivery," Med. Phys. **32**(6), 1607-1620 (2005).
[53]S. S. Vedam, P. J. Keall, V. R. Kini, and R. Mohan, "Determining parameters for respiration-gated radiotherapy," Med. Phys. **28**(10), 2139–2146 (2001).
[54]D. Ruan, J. A. Fessler, and J. M. Balter, "Real-time prediction of respiratory motion based on local regression methods," Phys. Med. Biol. **51**(23), 7137–7152 (2007).
[55]J. C. Stroom, H. C. de Boer, H. Huizenga, and A. G. Visser, "Inclusion of geometrical uncertainties in radiotherapy treatment planning by means of coverage probability," Int. J. Radiat. Oncol., Biol., Phys. **43**(4), 905–919 (1999).
[56]M. J. Murphy and S. Dieterich, "Comparative performance of linear and nonlinear neural networks to predict irregular breathing," Phys. Med. Biol. **51**(22), 5903–5914 (2006).